FILTRATION AND SOME RELATED PROCESSES
FOR ALUMINUM ALLOYS

by

DIRAN APELIAN

S.B. Drexel University (1968)

Submitted in partial fulfillment of the requirements

for the degree of

DOCTOR OF SCIENCE

at the

Massachusetts Institute of Technology

February, 1973

Signature of Author

Department of Metallurgy and Materials
Science, January 17, 1973

Certified by

Thesis Supervisor

Thesis Supervisor

Accepted by

Chairman, Departmental Committee on
Graduate Students

FILTRATION AND SOME RELATED PROCESSES
FOR ALUMINUM ALLOYS

by

DIRAN APELIAN

Submitted to the Department of Metallurgy and Materials
Science on January 17, 1973, in partial fulfillment of
the requirements for the degree of DOCTOR OF SCIENCE.

. . . .

ABSTRACT

A new type of laboratory filtration apparatus was
designed and built. This apparatus was utilized to study
removal of oxides and "synthetic inclusions" from aluminum
melts and separation of segregated interdendritic liquid from
partially solidified dendritic networks of aluminum alloys.
A new process for production of powders of metal alloys was
also developed. The process called "filatomization" entails
filtration and subsequent atomization of aluminum alloy melts
through sintered ceramic disc filters.

The effectivness of various filter media (i.e. sintered
discs of Al_2O_3, SiO_2 and carbon, granular bed filters, etc.)
in removing oxides and "synthetic inclusions" from aluminum
melts was studied. Platelike $TiAl_3$ particles, 60μ to 1000μ
across by 10μ to 50μ thick, were successfully filtered from
the two phase, $L+TiAl_3$, region of an Al-1% Ti alloy at various
temperatures. Commercial purity aluminums, 99.5% and 99.9%,
were filtered through a combination filter made of 1.5" high
216μ diameter Al_2O_3 granular bed followed by a 40μ pore size
sintered Al_2O_3 disc filter. The tensile properties of both
alloys were improved; reduction in area of the 99.9% Al
increased from 21.6% to 42.0% after filtration. When granular
aluminum was used as initial charge material, Al_2O_3 contents
of the melts were reduced by filtration from ~1.61% to ~0.13%.
TiB_2 "synthetic inclusions" of 2-15μ size range were success-
fully filtered from an Al-0.5% Ti-0.11% B alloy. The majority
of the TiB_2 particles accumulated above the filter beds
forming a "cake". Filtration of the alloy at 750°C through
Al_2O_3 sintered disc filters (1" diameter, 1/4" thick) of
87-100μ and 36-40μ pore sizes reduced the boron content to
0.022% and 0.01%. Boron contents of 0.013% were also obtained
when thick layers of fiberglass cloth ahd carbon felt filters
were used. The boron content of the alloy was further reduced
to 0.006%, when a 1.5" thick granular bed, Al_2O_3 granules
smaller than 200μ, was used above the 36-40μ pore size
sintered Al_2O_3 disc filter. Pressures required for metal flow
through the various filters utilized ranged between 3-60 psi.

Segregated interdendritic liquid was successfully removed from partially solidified Al-4% Si and Al-4% Si-0.25% Ti alloy samples. The impermeable oxide layer above the charge was dissolved with a molten flux. Porous columnar, equiaxed and grain refined dendritic networks of the alloys with actual volume fractions solid, $g_{SA} > 0.628$ were prepared. In equiaxed and grain refined samples, porous channels formed predominately between the primary dendrites (i.e. grains). Specific permeabilities of the porous dendritic networks were measured with a triaxial cell permeameter. Measured values of specific permeability were 1×10^{-9} and 3.5×10^{-11} cm^2 in the Al-4% Si alloy for volume fractions solid of 0.655 and 0.94, respectively. Specific permeabilities in Al-4% Si-0.25% Ti alloy were 5.5×10^{-10} and 7.6×10^{-11} cm^2 for volume fractions solid of 0.628 and 0.837, respectively. These results are in good agreement with previous experimental determinations of permeability of partially solidified dendritic structures. For equivalent volume fractions solid, the measured specific permeabilities were consistently lower for the grain refined samples. This is due to the higher surface area of available channels for flow in the grain refined samples. Flow through the partially solid non-grain refined samples obeys D'Arcy's law and equations derived from the capillaric flow model for volume fraction liquid less than 0.345.

"Filatomization" experiments were carried out with pure aluminum and a 7075 aluminum alloy. The filters used were sintered Al_2O_3 and SiO_2 disc filters with average pore sizes in the range of 40 to 150μ. Size distribution, morphology, and structure of the filatomized powders were investigated. The size range of spherical powders was between ~1700μ and ~150μ. Microstructures and room temperature tensile properties of extruded billets of the filatomized powders of the 7075-T6 alloy were compared with splat cooled powders, commercial powders and bar stock extrusions. The extrusion of filatomized powders had the least oxide and porosity content. The tensile properties of this billet in the T-6 condition were: Y.S. 80,000 psi, U.T.S. 94,300 psi, R.A. 42.4% and Elongation 15.1%. The corresponding values obtained from extrusion of commercial powders were: Y.S. 75,000 psi, U.T.S. 87,500 psi, R.A. 11.5% and Elongation 7.8%. Results of these experiments show that filatomization is a promising process that combines filtration of oxides and/or undesirable second phase particles with atomization.

Thesis Supervisor: Merton C. Flemings
         Title: ABEX Professor of Metallurgy

Thesis Supervisor: Robert Mehrabian
         Title: Assistant Professor of Metallurgy

TABLE OF CONTENTS

LIST OF FIGURES

Figure
Number

Page
Number

LIST OF TABLES

ACKNOWLEDGEMENTS

1. INTRODUCTION

The objectives of this investigation were to study removal of oxide and other particulate materials from molten aluminum by filtration techniques and to apply the latter to practical metallurgical problems.

Impurities in aluminum melts may be characterized as: (i) reaction products formed due to interaction with air or furnace atmosphere, (ii) refractory particles, suspended in the melt, (iii) aluminum oxide that is both suspended on top of the melt and entrapped within the melt due to metal turbulance, (iv) exogeneous inclusions, intermetallic compounds that nucleate and are suspended within the melt.

No mention of type, size and morphology of impurities removed has been made by previous investigators of filtration of aluminum melts. In this study systems were chosen where the particles to be removed were categorized and their size range known. A new type of laboratory filtration apparatus was designed and constructed to study removal of "impurities" from aluminum melts using different types of filter media. Experiments were conducted on Al-Ti alloys, using the precipitated $TiAl_3$ phase as "synthetic inclusions." Various commercial purity aluminums were filtered and filtration effectiveness was determined by mechanical property measurements and chemical analyses.

The effectiveness of various filter media in removing particles less than 20μ in size was investigated by filtering

out TiB_2 "synthetic inclusions" from Al-Ti-B alloys. Pressures required for metal flow through the various filters were measured.

Filtration techniques were applied to partially solidified Al-4% Si alloys, to separate the segregated interdendritic liquid. Columnar, equiaxed and grain refined samples were used. The structure of the remaining porous solid networks were studied, and permeability values were measured.

Filtration techniques were also applied to metal powder production. Exit pores of sintered Al_2O_3 and SiO_2 disc filters were utilized instead of standard orifice type atomization setups. In this manner both filtration and atomization takes place simultaneously. Mechanical properties of powders and flakes produced by this technique were measured and compared with those of powder produced by other methods.

2. LITERATURE REVIEW

2.1   Filtration Processes in the Metallurgical Industry

In metallurgical processes, particularly in casting operations, it is of utmost importance both from a technological and a financial viewpoint to remove impurities from the melt before casting. Technologically, removal of impurities, improves the properties of the cast product. Financially, presence of impurities in the melt may cause production impedances and downtime. For example, in continuously cast fine wires impurities cause an obstruction to metal flow, preventing continuous operation.

The oldest German patent for the filtration of metallic melts by materials of different permeability dates back to 1913(1). The first practical application of filtration was used in the chemical industry in filtering liquid sodium. In the 1930's, the Metallgesellschaft A.G. in Frankfurt introduced filters to separate hypereutectic aluminum-silicon alloys. In this case the segregated precipitate acts as an effective filter layer(2). Chaudron filtered unrefined magnesium through several layers of perforated iron sheet, thus reducing the amount of nitrides and chlorides(3).

An excellent work on the purification of metals by filtration techniques was published in the late forties by Reinacher(4). It seems that Reinacher's work has set the

direction for many of the developments that have appeared since then. The laboratory apparatus used by Reinacher consisted of a vertical iron tube of about 10 cm. in diameter with a circular filter fitted in, 5-10 cm. above its lower end, the tube holding about 1,000 cc. of metal. Reinacher used various types of granular materials for filtration, which were set up above the fitted filter in the vertical tube. The filter consisted of a perforated iron plate with holes 1-3 mm. in diameter. The granular materials used most were aluminum oxide and magnesium oxide. The first layer of granular material above the plate was of 5-15 mm. in diameter, over this a second layer of 2-5 mm. granules were placed such that the coarse grains were completely covered. The finer grains were in turn covered by a layer of 5-10 mm. of granules. It is interesting to note that the granules of 2-5 mm. in diameter do not pass by the 5-15 mm. granules during metal flow because the former are obstructed at the interstices of the latter.

Reinacher purified zinc alloys by removing segregated irion-zinc phases, oxide particles and impurities. Iron contents of .31-1.49% were reduced to 0.02-0.03% by filtration. Lead contents were reduced from 1.25-3.91% to 1-1.20%.

Aluminum alloys were also purified by Reinacher. Hypereutectic iron was removed for Al-Fe alloys, by separating the $FeAl_3$ phase from the liquid phase of eutectic

composition. Samples containing 4.6% and 2.98% iron yielded filtrates of 1.74% and 1.80% iron, respectively. Al-(12-13.6%)Si - (0.79-1.80%)Fe ternary alloys were also filtered to reduce the iron content. Filtrates obtained contained 0.68-0.76% iron.

Successful filtration experiments were also conducted to remove oxide particles from remelted scrap. Subsequently metallic contents were recovered from remelted skimmings(5).

In utilizing filtration procedures in foundry practice, it is important to note that if the outlet side of the filter is below the surface of the filtered bath, then any further surface oxidation is minimized. The use of spun glass fabrics has long been practiced in continuous casting of aluminum. A cloth of this sort should be defined as a sieve and not a filter. In a sieve the mesh size must be smaller than the constituents to be retained.

Weiss, Reinacher and Hansen(6) have used filtration techniques in the foundry by having loose granules of filter materials in front of the tap hole of the hearth furnace. They used filter materials with a higher density than the melt for settling purposes. In the case of aluminum melts, granules of basalt, corundum or magnesite chips were employed.

Halbach has used a casting crucible which is divided into two compartments by a filter plate - one side for the filtered material and the other for the unfiltered(3).

Schneider has filtered out intermetallic compounds in aluminum-magnesium alloys. He did this in a continuous operation by means of a suction filter over basalt chips(7).

Gamber(8) has devised a filtration process which makes use of a porous carbon filter plate rather than a granular filter bed. This setup is very similar to Halbach's. The carbon filter is used to remove finely divided non-metallic particles which are entrapped in the melt.

Spasski(9) has used a filtering graphite crucible, with a perforated base. The filtering crucible contains a 2 in. thick layer of previously melted flux material (52.7% CaF_2 + 47.3% NaF) crushed to 5-7 mm. granules. This filtering crucible is then immersed into the molten bath and metal passes through the flux particles into the filtering crucible. Metal for casting is then taken from this latter crucible. Spaskii reported that by this technique the metal was freed from non-metallic inclusions and suspensions of aluminum oxide, however no quantitative data was presented.

Kalabushkin and Pikunov(10) experimented filtering aluminum through crushed magnesite. Several different diameters of magnesite particles were used, varying from 0.5 to 2 cm. in size. The magnesite was fed into a 5 cm. diameter steel pipe at the bottom of which was a steel wire screen to hold the magnesite. Experiments were conducted to seek a relationship between the rate of filtration and variables such as granular particle size, height of filter, height of

metal head, etc. Both Darcy's formula (for laminar flow),
and others for turbulent flow failed to characterize the
flow of aluminum through the magnesite.

Filter pockets permanently built into the casting
crucible have been used by Spasski(11). The crucibles used
contain a 350 mm. deep pocket on one edge with 30 bottom
holes of 10 mm. each. The pocket is filled with a 60 mm.
thick layer of magnesite brick particles of 12-15 mm. in
diameter. Ladling is done from the filter pocket, and the
crucible is charged outside the pocket.

Brondyke and Hess have developed two processes for
improving the quality of molten aluminum alloys before
casting(12,13). The two processes are, the straightforward
filtration process, and the combination filtration-inert gas
fluxing process. The filtration process involves passing
molten metal through a packed bed of granular filter
(tabular alumina balls or synthetic corundum – size 3 to 14
mesh) material. This process has proven to be a rapid means
of removing finely divided particles from the melt. The
finely divided particles (or inclusions, used equivalently
by Brondyke) are non-metallic particles which are entrapped
in the melt. The major source of these non-metallic
compounds is the metal oxide film which forms on the surface
of the melt and is broken up as the metal is stirred or
agitated. Figure la illustrates this filtration apparatus.
Brondyke and Hess report that by their process the incidence

of inclusions (non-metallic products) has been markedly
reduced. Metal melted in a gas-fired crucible furnace
contained 13.8% inclusions, whereas filtered molten metal
from the same furnace contained 4.1%. The removal of the
non-metallics occurs in the interstitial channels of alumina
granules by settlement and restriction of movement under
conditions of quiescent flow. It is interesting to note
that in this filtration setup the finer granules precede the
coarser ones, this same technique was employed by
Reinacher(4) in his filtration studies during the late
forties.

The combination filtration, inert gas fluxing process,
involves introduction of an inert gas so that it will diffuse
countercurrent to metal flow through the filter bed of
granular materials(14). By this process dissolved hydrogen
is removed from the metal in addition to the removal of
finely divided non-metallic particles. The combination
process is most useful where both inclusion removal and
attainment of consistently low hydrogen content melt are
important. Brondyke(14) reports that up to 76% reduction in
hydrogen content has been attained with this technique.

R. B. Miclot(15) tested several refractory and
metallic media for effectiveness in removing aluminum oxide
from molten aluminum casting alloys 195 and 356. With this
technique the metal sample could be melted, filtered, and
cast entirely in a nitrogen atmosphere. The filter granules

used ranged in size from 1.19 mm. to 4.76 mm. in diameter.
The Al_2O_3 content of each alloy was determined before and
after filtering by chemical analysis. The effectiveness
of the various granular materials differed with the alloys
used. Filter packs of carborundum, porous graphite, and
non-porous graphite decreased the oxide content of 195
alloys; magnesite, alundum, and mullite were most effective
for the 356 alloy.

L. A. Alekseev and I. B. Kumanin have filtered
aluminum AK6 alloy through granular filters(16). The filter
media which they used were: (i) an alloy of potassium and
magnesium fluoride, 1:1 of CaF_2 and MgF_2; (ii) graphite
particles; (iii) magnesite granules. Three sizes of granules
were employed, 1.2, 2.5, and 5.0 mm. The height of the porous
bed was 7 cm. The experimental setup employed is quite
similar to the one used by Miclot(15). Alekseev(16) reports
to have successfully decreased the amount of oxides present
within the filtrate; Figure 1b shows the results. Maximum
removal of oxides was obtained through the fluoride granules.
Alekseev also reports that the maximum drop in the gas
content (H_2) occurred by the fluorides. They also report
that filtration through all three porous media increased the
ductility of the alloy.

A similar method of filtration using metal halides is
that reported by Snow(17). He employed a granular bed
consisting of 52% calcium fluoride and 48% magnesium fluoride,

and the grain size of the bed ranged from 3-6 mm. The metal
was passed through a cast iron cylinder (12 cm. high, 10 cm.
in diameter) fitted with the granular material before
casting. No external force (pressure) was required for this
process, the weight of the metal above the bed was sufficient
for the passage of the metal. Examination of fractured
surfaces of cast billets has shown that untreated metal
contained about 1.17 inclusions/cm^2, whereas filtered metal
contained 0.033 to 0.167 inclusions/cm^2. Snow[17] describes
the inclusions removed by this process; (i) gaseous
inclusions dissolved in the metal and (ii) foreign solid
particles suspended in the metal, such as refractory oxide
particles.

C. A. Sauer of the Dow Chemical Company has obtained
an apparatus patent[18] for filtering light metals, in
particular magnesium alloys. A filter housing (24 in. in
diameter, 7 in. high) is embedded within the casting pot,
and the interior of the housing is divided into three
compartments by a pair of perforated partitions (bores of
3.2 mm.) extending transversely across the housing. The
middle compartment of this housing contains layers of
aluminum oxide granules of 6.3-19 mm. at each end of the
partitions, and between these two layers of coarse granules
exist a layer of fine, 3.2-6.3 mm. in diameter granules of
aluminum oxide.

H. E. Miller[19] reports of the improved mechanical properties in 7075 alloys after filtration. Miller is referring to oxides, carbides, chlorides and borides when using the term inclusion content. Miller used the Plude test to measure "inclusion content". In the plude test, a severe upsetting operation (usually by forging) causes as many inclusions as possible to associate themselves with voids, allowing for ultrasonic detection. Use of a filter with an average effective pore size of 0.233 mm. (233μ) resulted in the reduction of the amount of grain refining nuclei (TiB_2), which ranged in size from 7.6μ to 127μ. Figure 2a shows the variation of short transverse elongation versus average pore diameter. The decrease of short transverse elongation for pore diameters smaller than 0.01 inches (254μ) is due to the coarse grain size of the samples because of the reduction of the grain refining nuclei.

Singleton and Robinson[20] have refined Al-Si hypereutectic alloys by centrifuging a partially crystallized melt, within a removable wall centrifuge. The liquid, rich in aluminum, is separated from the primary solid phase which is concentrated in silicon. The latter crystallizes out in platelet form resulting in many interconnected passageways. Such a structure is desirable for formation of a rigid network form which liquid can be extracted without the requirement of a large pressure differential. On the other hand, in filtration large build up of solid particles causes a rapid

rise in the operating pressure differential. However, substantially higher removal efficiencies are obtained by filtration.

Geiger, Mehrabian and Flemings have recently developed two processes for refining metal alloys by processing the alloy while partially solidified(21). Partially solid, partially liquid slurries of alloys were prepared by vigorous agitation of the melt during solidification. Refining was done either by draining the liquid from a liquid-solid slurry, or by gas atomization of the liquid-solid slurry. The thixotropic nature of liquid-solid slurries permitted Geiger to from a natural filter above the bottom orifice for selective draining of the liquid from the slurry. The atomization experiments resulted in homogeneous powders of metal alloys - free of microsegregation. Al-30%Si-6%Fe-1%Ti alloy, which is the product obtained by the direct reduction of bauxite by coke, was refined by draining the liquid of Al-13.2%Si-1.77%Fe-0.15%Ti at 600°C. Refining by atomization of Al-4.8%Si alloy at 617°C yielded primary solid particles of Al-1.86%Si.

Recently, Brant, Bone and Emley(22) have reported of installing a fumeless in-line degassing and cleaning setup for aluminum between the holding furnace and casting point, Figure 2b. The melt first enters a degassing chamber where it is treated with nitrogen under a liquid flux cover; it then passes through a bed of flux coated (KCl and NaCl

prefused in approximately eutectic porportion with a small addition of CaF_2) coarse refractory granules to complete the cleaning operation. Finally, the melt passes through a bed of uncoated coarse granules to remove entrapped flux. Brant et al(22) report gas and non-metallic inclusion contents equivalent to that obtained by a Brondyke-Hess type filter. The technique used to detect the oxides and non-metallic inclusions was to examine the fractured surface of a notch bar at low magnification using suitable immersion media to suppress unwanted specular reflections.

The Carborundum Company's Metaulics Branch, Refractories Division has developed a molten aluminum filtration system for use in the production line. The system consists of a box-like housing (55 in. by 37 in. by 60 in.); its cover contains a bank of resistance heating elements; and the filter cartridge is made from porous ceramic tubes. In operation, molten metal from the melt furnace is fed into the input trough of the filter, surrounds the parallel tubes of the filter cartridge, and flows inward through the walls to the tube bores. Impurities collect on the outside surfaces of the tubes. With this process, the developers claim that impurities as small as 8μ in size may be screened out. They also report that this system prevents channeling, and eliminates the counter current flow of inert gas.

2.2 Separation Techniques: General Considerations

A. Separation Techniques

Heterogeneous mixtures may be separated by causing
the constituent phases to respond differently to an
externally applied force. This force may be gravitational,
externally applied pressure, magnetic, electrostatic, or
interfacial. The choice of the force and the method by
which the force can be applied are determined by the
heterogeneous system and the characteristics of the
individual phases. The forces used in separation techniques
may be classified into two major categories: electrical
forces and dynamic forces. Electrical forces are used in
air purification techniques. The best example of this is
the electrostatic precipitator, which is used to remove
solid and liquid particles from gases. In liquid,
electrical forces are used to coalesce a certain phase such
as the coalescence of H_2O droplets in oil emulsions.
Inducing an AC or a DC field creates a dipole on the
individual droplets thus causing their coalescence(23).

Dynamic forces, on the other hand, are used in
filtration processes such as sedimentation, pressure filters,
vacuum filters, centifuges and cyclones. One of the "free"
dynamic forces available is gravity. In a liquid-solid
mixture, if there is a density difference between the solid
particles and the liquid, then gravity settling is one way

of separating the two, assuming that the time required for sedimentation is available. The virtue of the sedimentation process is its simplicity and the zero running cost. However, there is a limited driving force available, and bulky equipments are necessary. Other dynamic driving forces commonly used are pressure and vacuum. The former pushing the fluid through the filter and the latter pulling on the fluid from the exit port. Application of a variable pressure differential permits optimization of output in a given set-up. The major drawback here is the difficulty in continuously discharging the cake formed above the filter medium. Vacuum, on the other hand, is costly, and only limited to a driving force of 14.7 psi. This latter imposes less restrictions on the separation equipment than where a positive pressure is used, especially, in the continuous discharge of the cake(23).

The cyclone and the centrifuge employ centrifugal forces to provide the necessary driving force for separation. Centrifugal force is the force which acts radially in an outward direction on a rotating body and which, by balancing the drag force (acting in the inward direction) keeps the body moving in a circular orbit at a certain distance from the center. A cyclone is a device for using the centrifugal force generated by the tangential velocity of a fluid. The particles suspended in the stream, which follows a curved path, are subjected to a centrifugal

force (outward), a drag force (inward), and gravity
(downward). Under the influence of these forces, the
particles separate out(24).

    B.   <u>Mechanisms of Filtration</u>

    There are two distinct mechanisms utilized in
filtration processes; these are: (i) surface filtration, and
(ii) depth filtration(25).

    As solids accumulate on a filter element, different
types of filters behave in very different ways, due to the
distinct mechanism occurring. A surface filter quickly
forms a layer of solids which obstruct further flow.
Whereas, a depth filter disperses the same amount of solids
through part or all of its thickness, and will not obstruct
flow as rapidly as a surface filter does. Surface
filtration is also known as filter medium filtration, in
which the particles (impurities) are retained above the
framework of the filter medium, and in which the hole size
of the filter medium determines the size of particles which
will be retained.

    A filtration process utilizing the depth of the bed
has the advantage of arresting particles much smaller than
the holes in the actual passages through the filter medium.
Whereas, a thin filter medium, such as a fiberglass cloth,
can only arrest particles larger than the actual passages
through the thin medium. A depth filter exhibits increased

retentivity as one goes from the upstream face of the filter
to the downstream side. In this manner, the larger
particles are taken out first followed by the removal of
finer and finer particles by the deeper portions of the
filter. Once the deep filter medium is "contaminated" it
must be replaced. Contamination is used here in the sense
that the medium is completely filled with impurities.

In the case of surface filtration, the cake that
forms above the filter acts as a deep filter in itself.
As the height of the cake film increases, the bed gradually
becomes contaminated, channels becoming clogged, and the
cake must be discharged or removed for further flow to be
possible(25). This type of an arrangement yields
inconsistent results due to the periodic formation and
removal of the cake.

There are several factors which affect the performance
of a filter medium, namely; the structure of the medium,
the mechanism of filtration taking place, the nature of the
liquid, and the permeability of the medium. The latter
factor is an important one, and one that is used frequently
in discussing filtration. Its physical significance is
that it refers to the resistance to flow that the medium
exhibits. Experimental measurement of the permeability of
a filter medium is generally based upon observation of the
rate of flow of a fluid under a defined pressure
differential(26). However, in filtration experiments the

permeability of the medium varies since entrapped impurity particles cause an increase in resistance to flow, which in turn results in a corresponding drop in flow rate at a constant pressure differential.

In general, filtration theories can be classified into two categories: (a) filter medium filtration (surface filtration) and (b) cake filtration (depth filtration).

Filter medium filtration theories describe processes in which the impurities are retained above the framework of the filter medium without the formation of a cake and where the pore spaces do not have the continuity which exists in granular beds. Filtration of liquid metals to remove particles of 1-2μ in size would require media with pores smaller than 1-2μ, and initial operating pressures of the order of 2500-3500 psi. The impracticality of surface filtration processes for liquid metals is evident and therefore will not be discussed here. Hermans and Bredee have studied surface filtration, and theoretical considerations concerning this type of an operation may be found elsewhere(27).

Cake filtration theories are applicable to processes in which the formed cake acts as a filter medium giving rise to an added resistance to flow of the liquid. Cake filtration theories are mostly used to describe the flow of fluids through granular beds. A granular bed is similar to a cake, in the sense that they are both media composed of aggregates.

2.3   Fluid Flow Through Porous Media: Theoretical
       Considerations

A.   Structural Nature of Porous Beds

The parameters describing the microscopic nature of
porous beds are: (i) porosity, (ii) specific surface,
(iii) tortuosity.

(i) Porosity.

Porosity of a porous medium, g, is defined as:

$$g = \frac{\text{volume of pores}}{\text{bulk volume}}$$

Various packing modes of granules effect the porosity of

the aggregate. Graton and Frazer(28) have analyzed the

packing characteristics of granular materials by studying

the ordered geometrical arrangement of spheres. Some values

of void volumes for certain specific arrangements are given

here:

geometry of arrangement	voidage, g	each sphere touching
cubic	47.64%	6
orthorhombic	39.84	8
rhombohedral	25.95	12
tetragonal	30.2	10

In non-spherical random packings, the tendency to
form large voids varies greatly with the shape of the
particles. Thin laminar particles (crushed mica) and thin
needle-shaped particles in a random packing have
porosities in the range of 80-90%, compared with g = 0.385
for uniform size spherical particles (the volume of each
particle being constant). Flat sided particles such as
cubes tend to give values as low as g = 0.34. Jagged
particles of broken or crushed stone give porosities
ranging from 0.45-0.55 (29).

Westmann and Hugill(30) using lead shots have
observed that particles of uniform size and shape could be
packed practically to the same porosity for over a range
of diameters (from 0.312"-0.0035"). Complications arise
if the packing is made up of mixed sizes. For example, if
small spheres are added to a bed of uniformly shaped spheres,
two effects occur:

1. The small spheres increase the porosity content
   by pulling the larger spheres apart from each
   other.

2. The smaller spheres may also fill up the voids
   between the larger spheres, and consequently
   decrease the porosity content.

These two effects cancel each other out, unless a
considerable difference in the particles exist. Coulson(31)

has investigated the proportional difference of various size particles and its effect on porosity content.

Shrinagesh and Ramachandran(32) have studied the packing characteristics of non-spherical homogeneous grains. The effect of shape, size, specific gravity, and angularity of the granules on packing density were investigated. They found that the most important factor which determines the nature of packing is the angularity of the granules, however this is a difficult parameter to measure.

Coulson(31) has investigated the influence of the shape and orientation of the particles on the resistance to flow within granular beds. Coulson has shown that f (Carman's analysis, equation 9) ranges from 3.2-5.8 depending on the shape and orientation of the particles and porosity.

Compaction of packed beds due to an externally applied pressure is a factor that must also be considered in filtration processes. For example, considering cake filtration, the rigidity of the particles making up the cake determines the variation of porosity throughout the cake, and therefore the permeability of the cake. In materials such as cloth and paper, compaction produces a significant change in porosity; however, extremely rigid materials like silica sand, alumina and other refractory materials suffer a slight change in porosity under moderate compaction pressures.

(ii) Specific Surface.

Specific surface, S_o (cm^2/cm^3), of a porous material is defined as the interstitial surface area of the pores per unit volume of solid material. Consequently, finely structured materials exhibit a much greater specific surface area than coarse materials. The specific surface of a porous material may be measured either by statistical methods or through fluid flow techniques(33).

(iii) Tortuosity.

Tortuosity is defined as the ratio of the effective path length, Le, travelled by the fluid flowing through the porous medium, to the apparent length, L, thickness of the medium.

Tortuosity is usually neglected, when considering problems of flow through porous media, probably because of its complex nature, and the difficulties involved in measuring it. The difficulty arises because tortuosity is a function of porosity, and therefore not a constant. Marshall(34) has related tortuosity to porosity by considering the geometrical nature of porous materials.

$$\tau = \frac{Le}{L} = \left(\frac{3g - 2\sqrt{g} + 1}{2g}\right)^{1/2} \tag{1}$$

It can be seen that tortuosity increases with decreasing porosity.

B. Fluid Flow Model

(i) Capillaric Model.

In general, the usual treatment of the problem of flow through porous media, is one in which a large number of parallel capillary tubes, of uniform radius r, are envisioned extending through the solid. Flow is analyzed in one tube and then applied to all. Suitable agreement between calculated and measured values is usually obtained by adjusting the number, or radius of the tubes, and introducing a tortuosity factor(35).

Volumetric flow rate of a viscous fluid (laminar flow) through a single capillary is given by the well known Hagen-Poiseuille equation(35):

$$Q = \frac{\pi r^4}{8\mu} \cdot (\frac{\Delta P}{L}) \tag{2}$$

where: Q = volume flow rate, cm^3/sec

μ = viscosity of the liquid, poise (dyne-sec/cm^2)

$\frac{\Delta P}{L}$ = pressure differential along the capillary length (dynes/cm^3).

For n tortuous capillaries per unit area of cross-section, flow per unit area (superficial velocity), q, will be:

$$q = \frac{n\pi r^4}{8\mu\tau} \cdot \frac{\Delta P}{L} \tag{3}$$

The porosity of the medium, g, is defined as the ratio of total volume of liquid paths through the medium to the total

volume of the medium (unit area):

$$g = \frac{n\pi r^2 \tau \cdot L}{L} \qquad (4)$$

rearranging equation (4)

$$n\pi r^4 = \frac{g^2}{n\pi\tau^2} \qquad (5)$$

Substituting equation (5) into (3), and taking into
consideration the contribution of the gravitational force,
the equation describing fluid flow for the capillaric model
becomes:

$$q = \frac{g^2}{8\pi \cdot \mu \cdot n\tau^3} \cdot (\frac{\Delta P}{L} + \rho_L g_r) \qquad (6)$$

where:

ρ_L = liquid density, gms/cm^3

g_r = acceleration due to gravity, cm/sec^2

(ii) D'Arcy's Law.

D'Arcy proposed an empirical relation in 1856(36) to
describe flow of ground waters through underground strata:

$$q = \frac{Q}{A} = \frac{K}{\mu} (\frac{\Delta P}{L} + \rho_L g_r) \qquad (7)$$

where:

q = superficial velocity, flow per unit area, cm/sec

Q = volumetric flow rate, cm^3/sec

A = porous medium area, cm^2

K = specific permeability, cm^2

ΔP = pressure differential, dynes/cm^2

L = thickness of medium, cm

μ = viscosity of fluid, poise.

Assumptions made in writting equation (7) above are:
(i) permeability of the porous medium is uniform throughout
its depth, and is not dependent on changes in applied
pressure, (ii) the relationship is derived for a single
phase liquid - free of impurity particles(30,31).

> (iii) Modifications of D'Arcy's Law: Kozeny's Theory,
> Kozeny-Carman Equation.

It is evident that one cannot directly simulate flow
of fluids through a porous bed, by flow through a series of
parallel, discrete, capillary channels. The complex nature
of the pore spaces of the medium must be considered. Kozeny
considered(37) the porous medium as a single passage, the
size of which (Kozeny called this the "hydraulic diameter")
corresponds to the volume and surface of the voids in the
medium. Kozeny thus related the permeability of the porous
medium to its geometrical characteristics:

$$K = \frac{cg^3}{s^2} \qquad (8)$$

where S = surface per unit volume of porous medium in cm^2/cm^3

c = Kozeny's constant, ranging from 0.2 to 0.5.

Carman(38) showed that flow through a porous medium is governed by the frictional retarding forces exhibited by the surface of the particles in the bed. Carman used the volume and surface of the voids of the medium as controlling parameters, and considered the particle size as a measure of the specific surface, S_o, available. The specific surface area of the particles is used because the resistance to steady laminar flow of a fluid through the porous medium depends on the extent of the surface in contact with the fluid. The specific surface is a definite geometric quantity, and is calculable for mixtures of shapes and various particle sizes. For uniform spherical particles of diameter d, $S_o = 6/d$; for non-spherical shapes and non-uniform sizes, and effective diameter $d_m = 6/S_o$ is defined. Specific surface, S_o, is the surface exposed to the fluid per unit volume of solid material, whereas S (equation 8) is the surface area of the pores per unit volume of porous material: $S = (1 - g)S_o$.

Kozeny and Carman(38) have modified D'Arcy's law to take into account specific surface, porosity, and tortuosity of the paths of the porous medium. The Kozeny-Carman equation is:

$$q = \frac{Q}{A} = \frac{g^3}{(1-g)^2 f (S_o)^2} \cdot \left(\frac{1}{\mu}\right) \cdot \left(\frac{\Delta P}{L} + \rho_L g_r\right) \qquad (9)$$

where f, is a dimensionless constant, empirically found to have the value of 5.0 when the other terms are expressed in cgs units.

C. Interdendritic Fluid Flow

(i) Relationship Between the Capillaric Flow Model and D'Arcy's Law.

The two different approaches to the problem of fluid flow through porous media result in equivalent equations for q, the superficial velocity:

$$q = \frac{g_L^2}{8\pi \cdot \mu \cdot n \cdot \tau^3} \cdot (\frac{\Delta P}{L} + \rho_L g_r) \qquad (6)$$

$$q = \frac{K}{\mu} (\frac{\Delta P}{L} + \rho_L g_r) \qquad (7)$$

where the porosity g has been replaced by the equivalent porosity within a dendritic network, g_L, the volume fraction liquid. Equating equations (6) and (7), the specific permeability is expressed as:

$$K = \frac{g_L^2}{8\pi \cdot n \cdot \tau^3} = \gamma g_L^2 \qquad (10)$$

For a given dendrite arm spacing: n, τ and thus γ, are constant, and K is directly proportional to the square of the fraction liquid. The mean interdendritic flow velocity(39),

v, can now be expressed as:

$$v = \frac{q}{g_L} = \frac{g_L}{8\pi \cdot n\tau^3} \cdot \frac{1}{\mu} \cdot (\frac{\Delta P}{L} + \rho_L g_r) \quad (11)$$

(ii) Relationship Between Kozeny's Theory and D'Arcy's Law.

Kozeny's analysis and D'Arcy's law result in equivalent equations for q, the superficial velocity:

$$q = \frac{g_L^3}{(1-g_L)^2 \, f \, (S_o)^2} \cdot (\frac{1}{\mu}) \cdot (\frac{\Delta P}{L} + \rho_L g_r) \quad (9)$$

$$q = \frac{K}{\mu} (\frac{\Delta P}{L} + \rho_L g_r) \quad (7)$$

where the porosity g has been replaced by the equivalent porosity within a dendritic network, g_L, the volume fraction liquid. Equating the above two equations, the specific permeability may be expressed as:

$$K = \frac{g_L^3}{(1 - g_L)^2 \cdot f \cdot (S_o)^2} \quad (12)$$

The mean interdendritic flow velocity, v, can now be expressed as:

$$v = \frac{q}{g_L} = \frac{g_L^2}{(1-g_L)^2 \cdot f \cdot (S_o)^2} \cdot (\frac{1}{\mu}) \cdot (\frac{\Delta P}{L} + \rho_L g_r)$$

$$.... \quad (13)$$

Piwonka and Flemings($\underline{40}$) conducted in situ
permeability measurements on an Al-4.5% Cu alloy by flowing
liquid lead (for $g_L < .3$) and gaseous nitrogen (for $g_L > .3$)
through a partially solidified sample of the alloy. They
assumed the capillaric model of flow, where $K = \gamma g_L^2$ (equation
10). The experimental results of Piwonka and Flemings, which
concur with their assumed model for $g_L < .3$, are shown in
Figure 3.

Pielet and Elliott($\underline{41}$) quenched partially solidified
Al-4.5% Cu alloys by a slow freeze transverse quench
technique. They measured volume fractions and specific
surfaces of "liquid channels" (regions which have a
recognizably finer dendrite arm spacing than adjacent
regions) and interdendritic liquid distributed between
tertiary arms via quantitative metallography. These were
used to calculate the permeability of the part solid region
to flow from Kozeny's analysis, equation 8. Pielet and
Elliott report that the interdendritic regions have a much
higher permeability than the channels and thus ignored
contribution of "liquid channels" to the total permeability.

Specific surface and form of porosity have previously
been experimentally measured via permeametry in sintered
copper compacts.($\underline{42}$) However, the literature is void of
any direct experimental permeability measurements of
partially solidified dendritic networks.

D. Cake Filtration

Cake filtration theories generally all stem from Poiseuille's and D'Arcy's laws (43). K from equation (7) may be replaced by $1/\alpha$, where α is the average specific cake resistance.

$$\alpha = \frac{A \cdot \Delta P}{\mu \cdot L} \cdot \left(\frac{dt}{dV}\right) \tag{14}$$

In actual cake filtration, L is continually changing. Assuming that each layer of cake deposited is identical, then L may be replaced as follows: cake volume = $LA = \nu V$, where ν is the volume of cake produced per unit volume of filtrate, and V is total volume of filtrate; therefore, $L = \nu V/A$, and equation (14) becomes

$$\alpha = \frac{A \cdot \Delta P}{\mu \cdot \dfrac{\nu V}{A}} \cdot \frac{dt}{dV} = \frac{A^2 \cdot \Delta P}{\mu \nu V} \cdot \left(\frac{dt}{dV}\right) \tag{15}$$

Considering that the filtration resistance consists of two parts, the cake and the medium, the volumetric flow rate may be expressed as:

$$Q = \frac{\Delta P \cdot A^2}{\mu(\alpha \nu V + R_m A)} \tag{16}$$

where: R_m is the resistance of the filter medium supporting the cake (44). Integration of equation (16) at constant

pressure yields:

$$t = \frac{\alpha \mu \nu}{2 \Delta P A^2} \cdot V^2 + \frac{\mu R_m}{\Delta P A} \cdot V \qquad (17)$$

By plotting t/V vs. V, the values of α and R_m can easily be determined.

From Kozeny's analysis, the specific cake resistance can now be defined as:

$$\alpha = \frac{(1 - g)^2 f S_o^2}{g^3} \qquad (18)$$

2.4   Metal Powder Processing Techniques

The principal methods of powder production are classified as follows:

(1) Chemical reactions and decompositions which involve at least two reactants: A compound of the metal and a reducing agent.

(2) Electrolytic deposition where metals can be made to precipitate on the cathode of an electrolytic cell as a sponge powder.

(3) Mechanical processing of solid materials via ball milling, or fracturing of brittle alloys.

(4) Atomization of liquid metals which entails disintegration and dispersion of a liquid (molten) stream emerging from an orifice or nozzle. Powders with large surface area to volume ratios are produced which consequently experience high solidification rates.

The first three production methods have been reviewed and discussed previously(45-47). Atomization of liquid metals is the principal industrial production technique available at present. Liquid metals have been atomized by the following techniques:

(1) Two fluid jet impingement: powders are produced by disintegrating a stream of metal by another impinging fluid. Water, air, and other gases have been used depending upon the alloy being atomized

and the required purity of the powder(48).
Federal Mogul employs a gas stream atomization
technique to produce a variety of ferrous
alloys(49). If a condensible fluid such as steam
is used together with another cooling fluid, shock
disturbances produced by the condensation process
assists in breaking up the metal stream(50).

(2) Spinning disc (centrifuged) atomization: powders
are produced when the liquid stream is
disintegrated and discharged from the periphery of
a rapidly rotating disc(51-53).
The Reynolds Metals Company(54) produces acicular
and tear-drop shaped powders by centrifuging
(3000 rpm) a porous cylinder containing the melt.
High quality powders are produced by the rotating
electrode process, a variation of centrifugal
atomization(55). A cylindrical electrode of the
desired alloy is rapidly rotated about its axis
as one end of the electrode is melted by an
electric arc. The molten metal is spun off and
solidifies during free fall as nearly perfect
spheres.

(3) Atomization through mechanical vibration:
mechanical vibration is used to disintegrate the
liquid stream. Olin Industries employs a vibratory

atomization process(56) for the production of iron shot particles.

(4) Ultrasonic disintegration: disintegration of the stream is induced by ultrasonic devices. Ultrasonically vibrating beams have been used to atomize a stream of metal poured over them(57) With this technique, particles of a characteristic size range are produced.
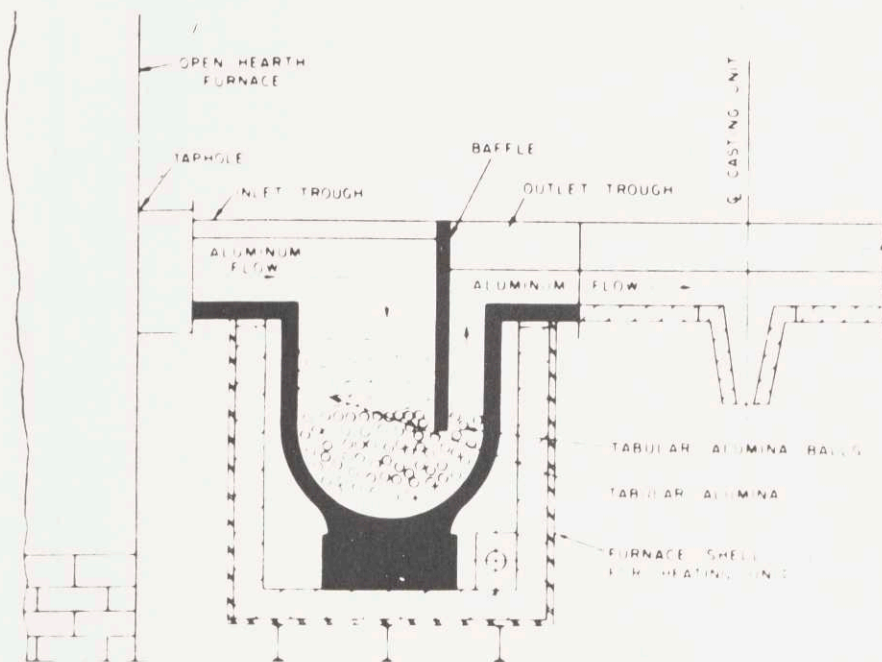
(a)
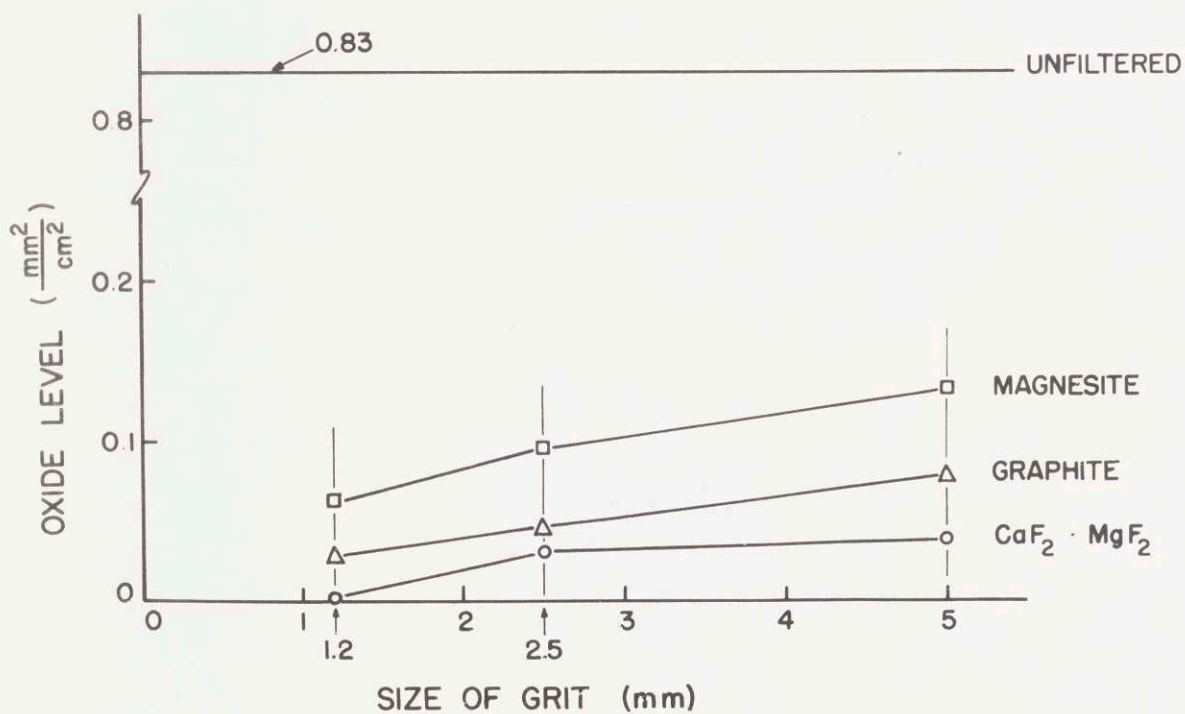
(b)

Figure 1: (a) Filtration setup developed by Brondyke and
Hess employed at Alcoa(13).
(b) Influence of granules size of filter bed and
oxide content in AK6 alloy(16).
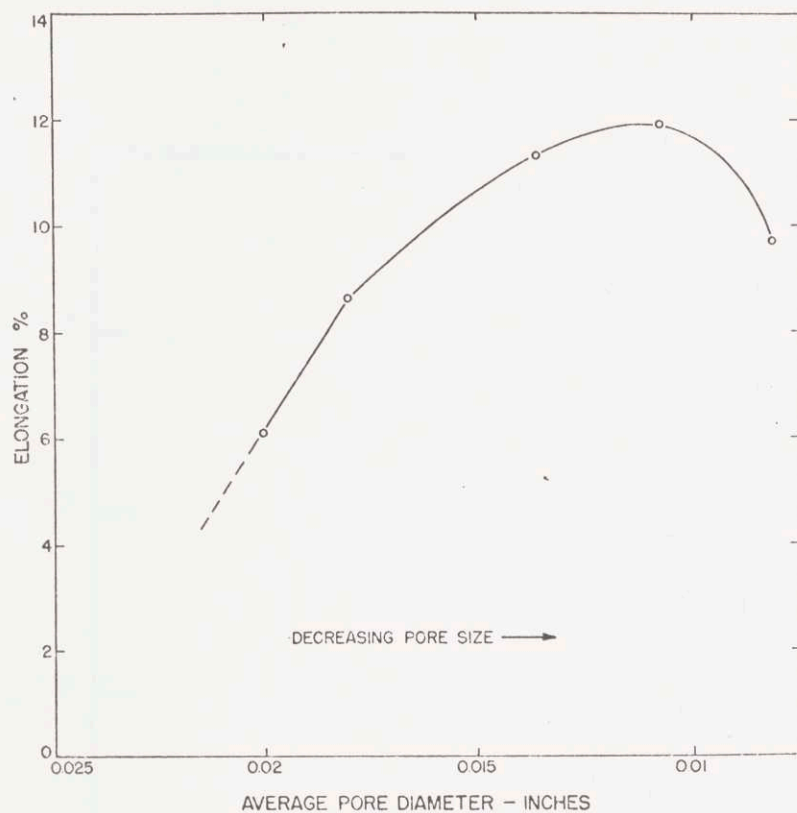
(a)
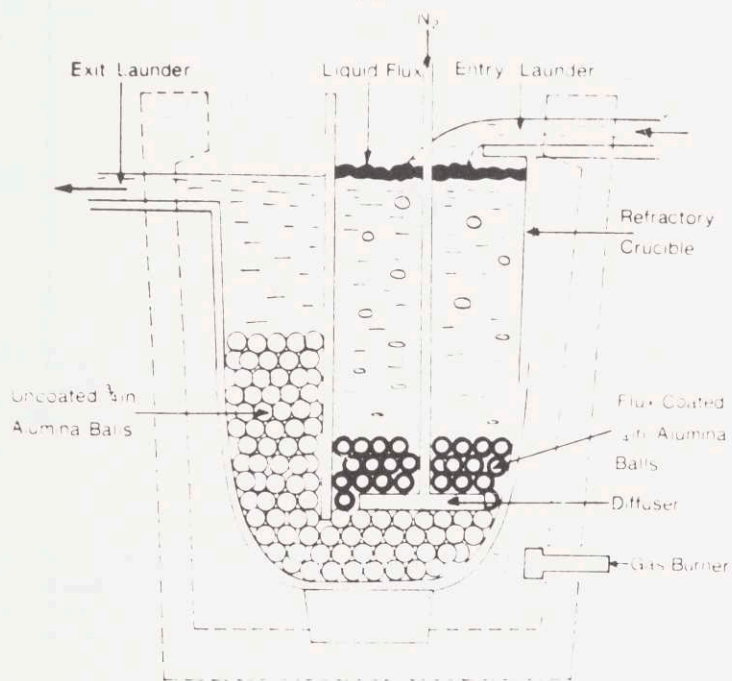
(b)

Figure 2: (a) Effect of filter pore size on elongation of
              filtered aluminum metal(19).
           (b) Experimental setup of Brant, Bone and Emley
              for refining of aluminum(22).
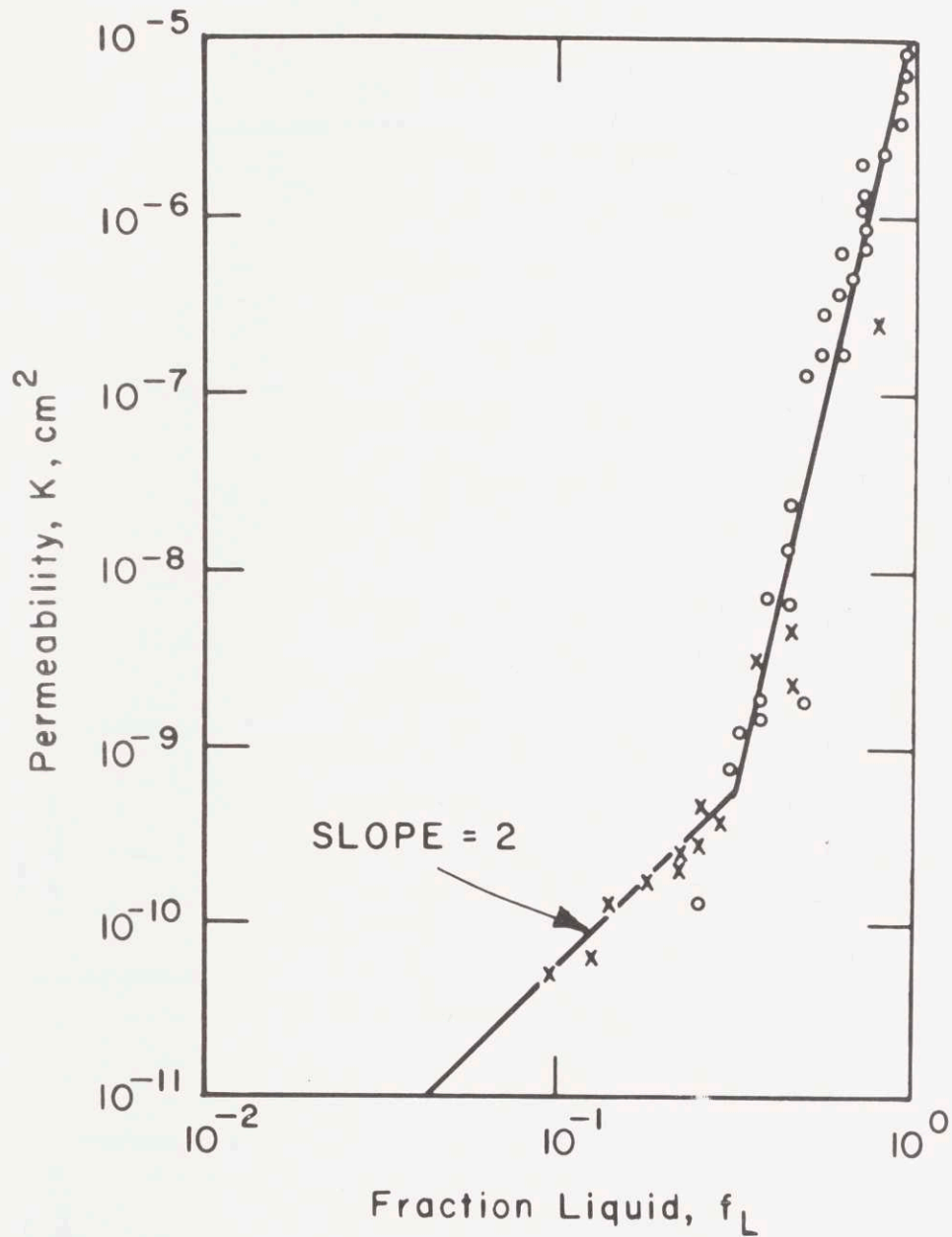
Figure 3: Permeability versus fraction liquid for tests on
aluminum-4.5 per cent copper alloys. Circles
represent data obtained using nitrogen gas;
crosses represent data obtained using molten lead, (40).
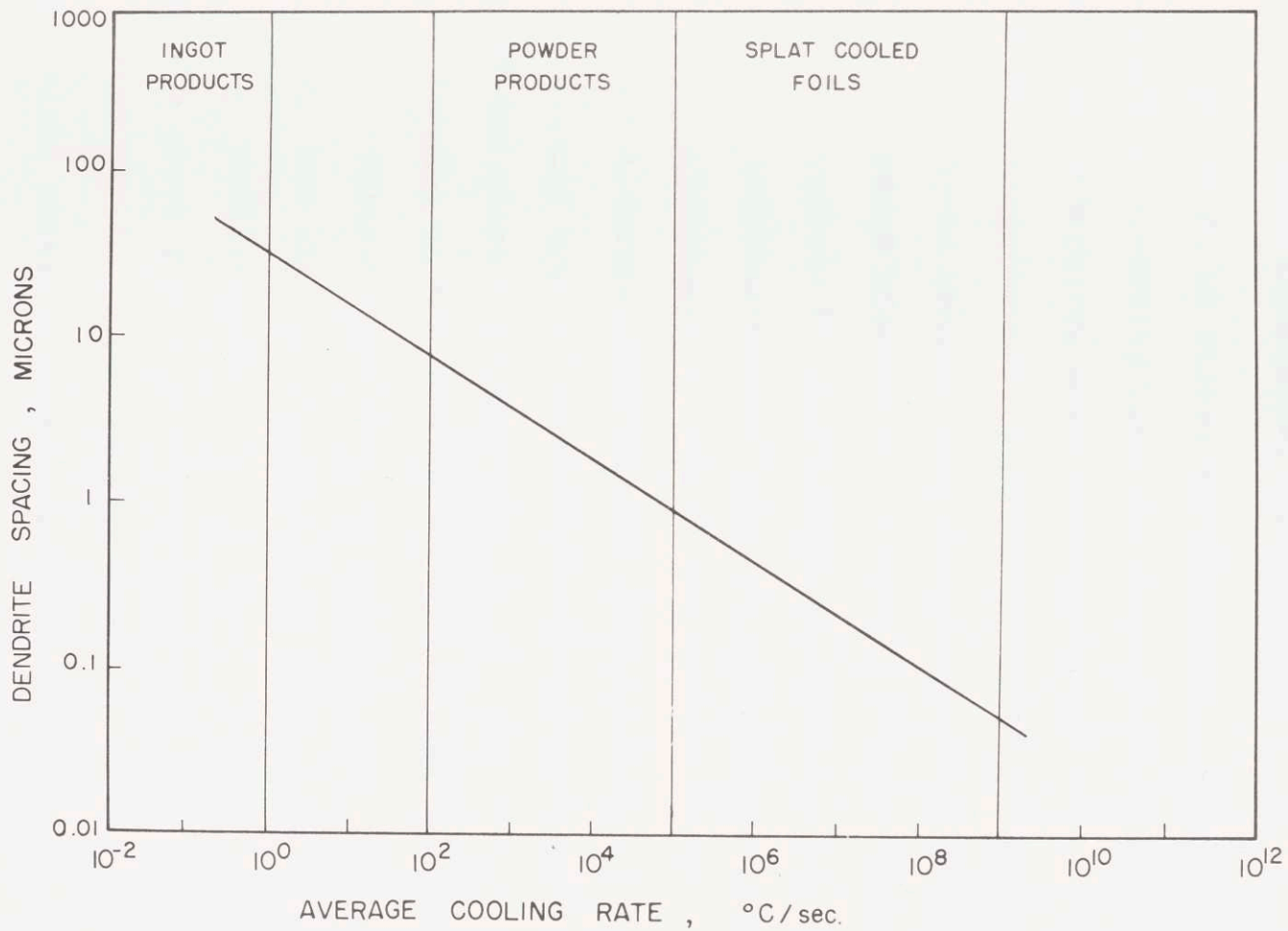
Figure 4: Effect of cooling rate on dendrite arm spacing (79).

3. EXPERIMENTAL APPROACH AND APPARATUS

3.1   Experimental Approach

A. Filtration of Aluminum Alloys

The study of filtration of aluminum alloys was
initiated with certain specific questions and objectives in
mind. The objectives were the following:

1. A system was to be chosen in which the particles
    to be removed were categorized, and their size
    range known.

2. Various filters were to be investigated to
    understand what types of filters are the most
    efficient.

3. A correlation between size of particle removed
    and type of filter used was to be made.

Some of the questions considered were:

1. How do the various particles come out during
    filtration? What is the nature of the separation?

2. How can the separation of these particles be
    facilitated?

Given the above questions and objectives, it was decided that
the system chosen should contain specific inclusions
(impurities) within a particular size range, which could
accurately and easily be detected by available techniques.
This was done by elemental additions to aluminum such that
intermetallic compounds of certain specific particle size and
morphology would form (i.e. $TiAl_3$, TiB_2, $ZrAl_3$ and others).

The independent variables in this series of experiments were:

1. filter material, pore size and filter setup,

2. temperature of filtration,

3. holding time at temperature,

4. additions and alterations to the melt during filtration.

The effect of the above on the following dependent variables was investigated:

1. Inclusion amount, size, and distribution within non-filtered and filtered samples, and within the filter bed.

2. Chemical analysis of all above.

3. Pressure required for filtration.

B. Separation of Interdendritic Liquid from a Partially Solidified Al-Si Alloy

It has been shown that interdendritic fluid flow during solidification of a casting or ingot is the main mechanism responsible for occurence of macrosegregation(58). Theoretical analysis verifying experimental observations of macrosegregation has shown that the nature and extent of segregation is strongly influenced by the resistance of the solid, network in the mushy zone, to the interdendritic fluid flow(59). Calculations of fluid flow velocity have been based on principles of flow through porous media. Thus the

flow velocity, $\vec{v}$, is dependent on the permeability, K, of the solid dendritic network. Previously(40), in absence of experimentally measured values for permeability, estimates were made using a capillaric model for flow through porous media.

In this investigation a series of experiments were carried out to separate the interdendritic liquid from partially solidified Al-4% Si alloys by filtration techniques. Removal of interdendritic liquid from a partially solidified alloy will permit direct observation of the structure and geometry of the porous medium. Furthermore, permeameter testing of samples thus obtained will provide experimental values of permeability previously estimated through calculation(40).

The Al-4% Si system was chosen because the dihedral angle between the interdendritic liquid and the solid is nearly zero(60). This low dihedral angle implies that the liquid completely wets the solid boundaries. Thus liquid entrapment in small pockets by solid is minimal. Filters had to be chosen which did not require terribly high pressures, such that the dendritic network was not compressed and, therefore, deformed. The pore size of the filters used was compatible with the size of the primary dendrites, so that only the interdendritic liquid was separated out.

The independent variables in this series of experiments were:

1. Filter material and pore size

2. Temperature of filtration

3. Local solidification time/holding time at temperature

4. Geometry of setup, type of charge (columnar or equiaxed), and amount of flux used

5. Mode of pressure application.

The effect of the above on the following dependent variables was investigated:

1. Amount of interdendritic liquid removed: efficiency of separation

2. Microstructure, macrostructure, and permeability properties of the dendritic porous medium

3. Silicon composition of the interdendritic liquid and the dendritic network

4. Pressure required for separation.

C. Production of Metal Powders (Filatomization)

Of all the various powder manufacturing processes, this particular process which entails forcing liquid metal through filters is unique for various reasons:
(i) filtration of undesired oxide and foreign particles occurs simultaneously with powder (drop) formation, (ii) the required experimental appratus is not complicated - an

attractive economic advantage, (iii) fairly spherical metal powders are produced, thus minimizing the surface area to volume ratio, (iv) control of powder size is governed by filters used.

A series of experiments were conducted to investigate the governing parameters for the production of metal powders by filters. The independent variables in this series of experiments were:

1. Filter meterial and pore size
2. Temperature at which filatomized
3. Mode of pressure application
4. Geometry of setup - charge composition, and size of opening at filter exit

The effect of the above on the following dependent variables was investigated:

1. Required pressure
2. Size and distribution of powders formed
3. Microstructure of metal powders
4. Mechanical properties of billets made by cold compaction and subsequent hot extrusion of the metal powders.

3.2   Apparatus

An apparatus was designed and constructed to carry out the experiments outlined in the previous section. A schematic of the apparatus for the filtration of aluminum and separation

of interdendritic liquid experiments is shown in Figure 5

A schematic of the apparatus for the production of metal
powders through filters is shown in Figure 6. The overall
experimental setup is shown in Figure 7.

The apparatus consists of a pressure vessel within
which a graphite crucible is placed containing the metal
charge and a filter assembly located below the charge. The
crucible is covered with an insulating shield made out of
fiberfrax. RF induction heating is employed within the
chamber. This upper chamber is 10" in diameter by 8" high.
The lower chamber which is 4" in diameter by 5" high is used
for thermocouple feedthroughs and contains a pressure gauge
to detect any leaks around the upper crucible (gaskets #16
in Figure 5). For the filatomization experiments, the
blind flange of the lower chamber was removed to allow a long
enough free fall distance for the metal powders to solidify.
The whole assembly has been certified to withstand 500 psi
pressure at 600°F. The liquid metal, which is melted in
situ, is filtered by pressurizing the vessel with an inert
gas tank of argon or nitrogen.

Other specific features of the assembly shown in
Figure 5 include:

1. A safety valve, set at 450 psi, located on top of
    the upper chamber.
2. An inflow and outflow valve, incorporating a
    pressure gauge located on top of the upper chamber.

3. Both chambers are connected to a vacuum pump through a 1/2" diameter pipe.

4. Watercooled feedthroughs for the RF coils are located on the side of the upper chamber. These are teflon insulated to electrically isolate the vessel from the RF coils.

5. Two thermocouple feedthroughs are located in the upper and lower vessels respectively. The upper thermocouple is used to measure the temperature of the melt, while the lower thermocouple is located in the bottom of the mold to allow detection of the passage of the liquid metal through the filter. This lower thermocouple was not used for the filatomization experiments.

A tapered graphite crucible was designed and machined as shown in Figure 8a. The crucible is mounted on the base of the upper vessel by six stainless steel bolts utilizing an asbestos insulating gasket. With this construction, upon pressurization, the crucible is under pressure from all sides except the bottom, and a pressure differential is set within the crucible between the melt and the mold or lower chamber.

The filter media employed (sintered discs, granular material, fiberglass cloth, etc.) is completely contained within a graphite filter assembly, which is shown in Figure 8b. This assembly is mounted in the crucible in a tight taper fit, thus blocking any liquid metal travel outside the filter

assembly. The perforated cover of the filter container assembly was not used in the interdendritic separation and filatomization experiments. A copper chill, containing a thermocouple within it, was inserted in a press, fit at the bottom of the graphite crucible. The copper coils for the RF heating, are arranged so that a uniform temperature profile exists along the entire length of the filter container assembly.

The particular design advantages of this apparatus are:

1. Accurate temperature control before and during filtration is possible.

2. The vessel may be pressurized gradually or instantaneously, while the pressure differential is measured continuously.

3. Potential leakage problems around the crucible may be detected before the actual filtration operation.

4. The charge is melted in situ, thus eliminating transporting of liquid metal.

3.3 Filter Media Employed

The various filter media used in the experiments were: granular materials, sintered porous discs, graphite woven felt, fiberglass cloth, and porous carbon plugs.

1. Granular materials:

SiC .... grit size #60 (approximate micron size 406μ)

Al_2O_3 .. grit size #150 (approximate micron size 122μ)

.. grit size #90 (approximate micron size 216μ)

.. grit size #60 (approximate micron size 406μ)

The granular beds used in these experiments were 1.5" high and 1" in diameter. All the granular materials were sized by sieve analysis before insertion in the filter container assembly.

Figures 9a and 9b are scanning electron photomicrographs of the Al_2O_3 and SiC, granular materials of grit size 60, respectively, showing their angularity and mode of packing.

2. Sintered Al_2O_3 porous disc filters; discs with the following pore diameters were used.

Coors P-100-C, diameter range 87-108μ

Coors P-40-C, diameter range 31-36μ

These filters are 1" in diameter and 1/4" thick. Figure 9c, a scanning electron micrograph of the P-100-C filter, illustrates the extreme tortuosity of the flow paths.

3. Sintered quartz (99.8% SiO_2) discs: discs with average pore diameters of 90-150μ, 40-90μ, and 15-40μ were used. These discs were 1" (or 1.18") in diameter by 0.118"

thick. Figure 9d illustrates the flow paths within this filter. Both the Al_2O_3 and the SiC sintered discs were mounted in place by saureisen cement.

4. Porous carbon:

Porous carbon, grade 25, with an average porosity of 48% and an average pore diameter of 120μ was used. Figure 10a illustrates the pore structures of this filter.

5. Fibrous carbon felt:

Fibrous non-woven carbon felt, with densities of 2.0 and 8.0 lbs/yds^2 were used. Figures 10b and 10c are scanning electron photomicrographs, respectively. The morphology of the fibers and their loose packing mode is evident.

6. Graphite and fiberglass cloths:

Both graphite and fiberglass cloths were used. Figure 10d, a scanning electron micrograph, shows the weave style of the fiberglass cloth.

7. Sintered 430 stainless filter discs of 1" diameter and 1/4" thick having a median pore size of 240μ was also used.
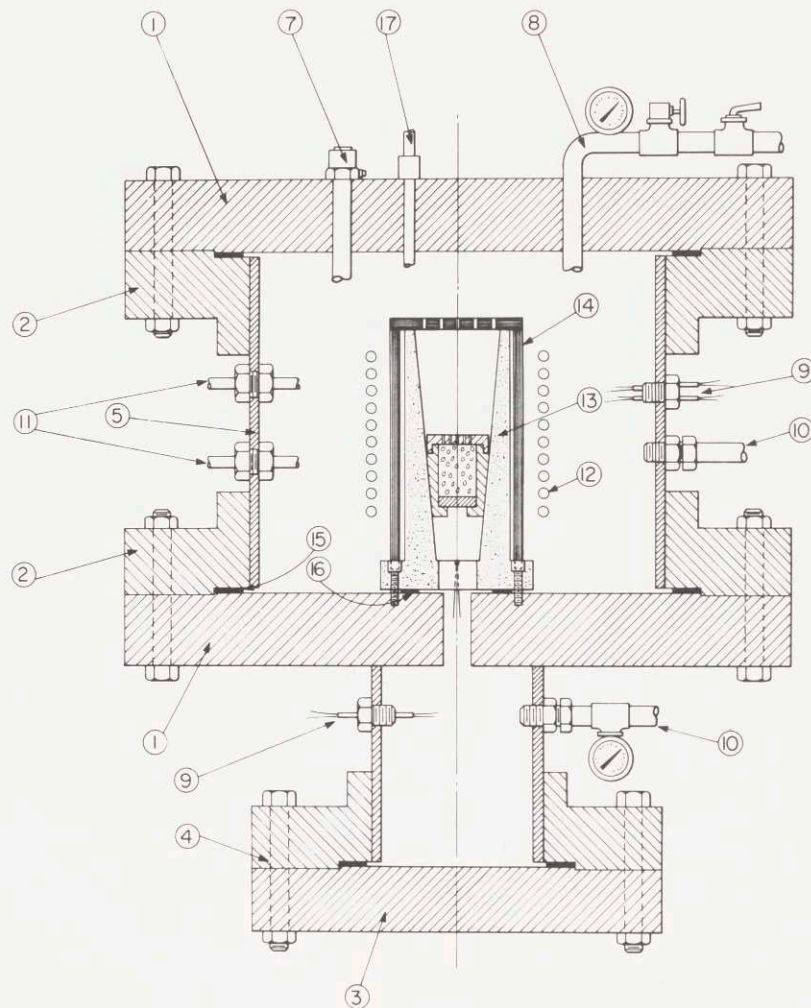
① 10"-300 LB. BLIND FLANGES

② 10"-300 LB. SLIP-ON FLANGES

③ 4"-600 LB. BLIND FLANGE

④ 4"-600 LB. SLIP-ON FLANGE

⑤ 10" SCH. 80 BLK. STEEL SEAM. A-106 PIPE, 0"-8½" PE

⑥ 4" SCH. 40 BLK. STEEL SEAM A-53 PIPE, 0'-5" PE

⑦ SAFETY VALVE

⑧ PRESSURE INFLOW AND OUTFLOW AND PRESSURE GAUGE

⑨ THERMOCOUPLE FEEDTHROUGHS

⑩ ½" PIPE TO VACUUM PUMP

⑪ WATER INFLOW AND OUTFLOW FOR RF COILS

⑫ COILS

⑬ GRAPHITE CRUCIBLE

⑭ FIBERFRAX INSULATING SHIELD

⑮ GASKETS

⑯ INSULATING GASKET

⑰ CHECK VALVE FOR ATMOSPHERE CONTROL

Figure 5:   Schematic of filtration apparatus used in this
study.
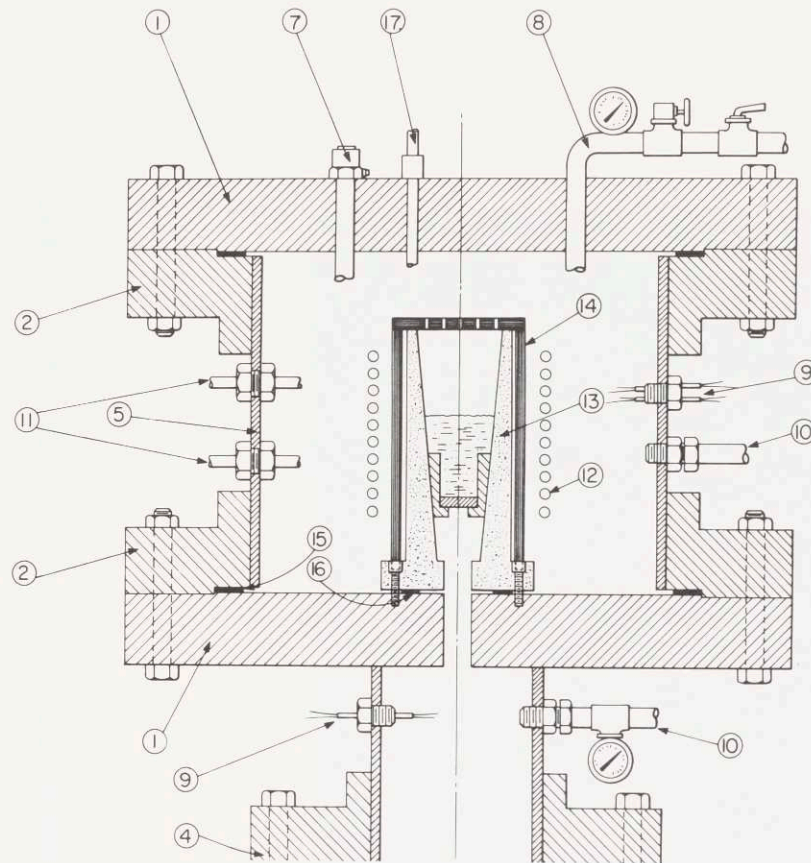
① 10"-300 LB. BLIND FLANGES

② 10"-300 LB. SLIP-ON FLANGES

③ 4"-600 LB. BLIND FLANGE

④ 4"-600 LB. SLIP-ON FLANGE

⑤ 10" SCH. 80 BLK. STEEL SEAM. A-106 PIPE, 0"-8½" PE

⑥ 4" SCH. 40 BLK. STEEL SEAM A-53 PIPE, 0'-5" PE

⑦ SAFETY VALVE

⑧ PRESSURE INFLOW AND OUTFLOW AND PRESSURE GAUGE

⑨ THERMOCOUPLE FEEDTHROUGHS

⑩ ½" PIPE TO VACUUM PUMP

⑪ WATER INFLOW AND OUTFLOW FOR RF COILS

⑫ COILS

⑬ GRAPHITE CRUCIBLE

⑭ FIBERFRAX INSULATING SHIELD

⑮ GASKETS

⑯ INSULATING GASKET

⑰ CHECK VALVE FOR ATMOSPHERE CONTROL

Figure 6: Schematic of filatomization apparatus used in this study.
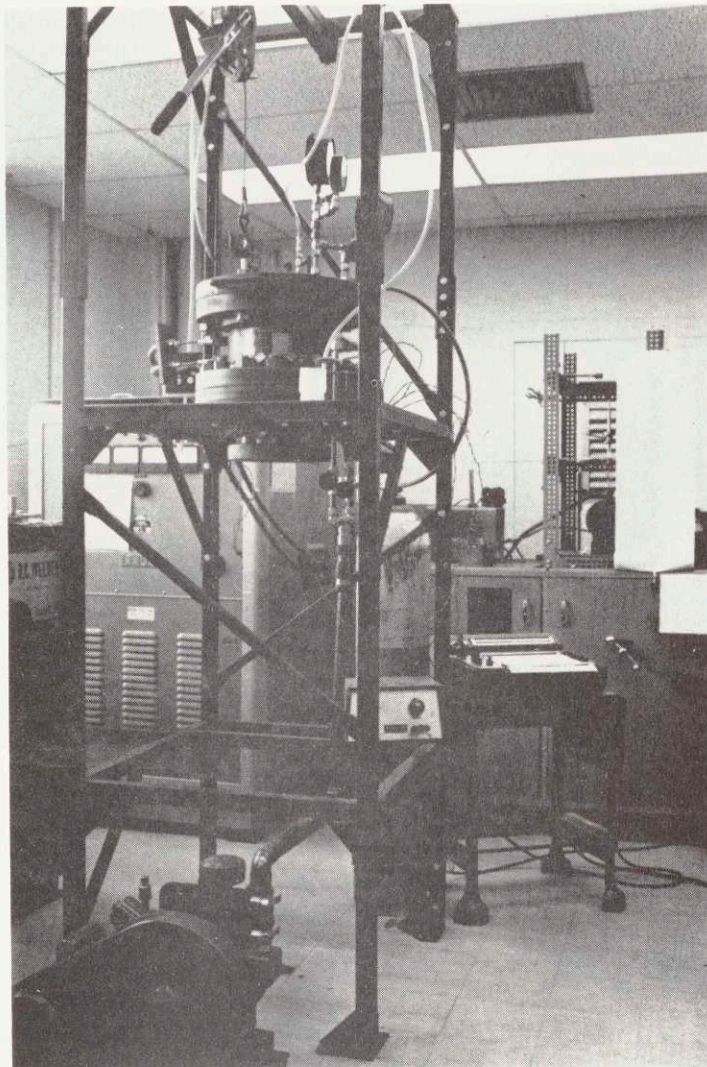
Figure 7: Photograph of experimental setup.
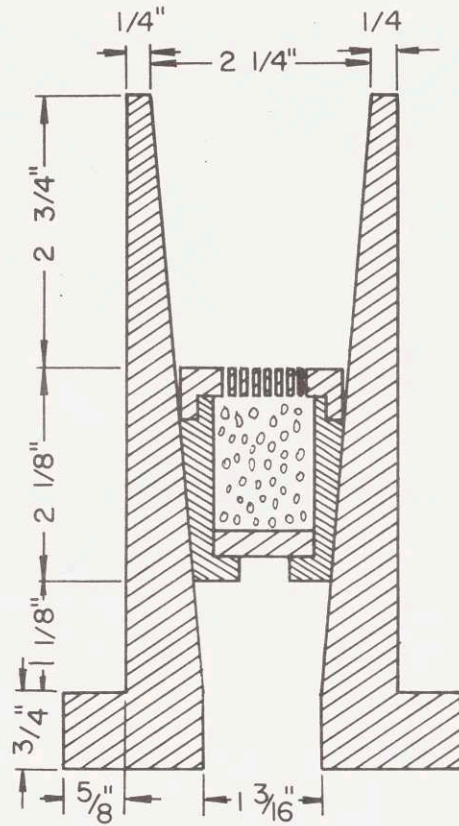
(a)

(b)

Figure 8: Details of experimental setup.
(a) Tapered graphite crucible.
(b) Filter container assembly (0.8X).
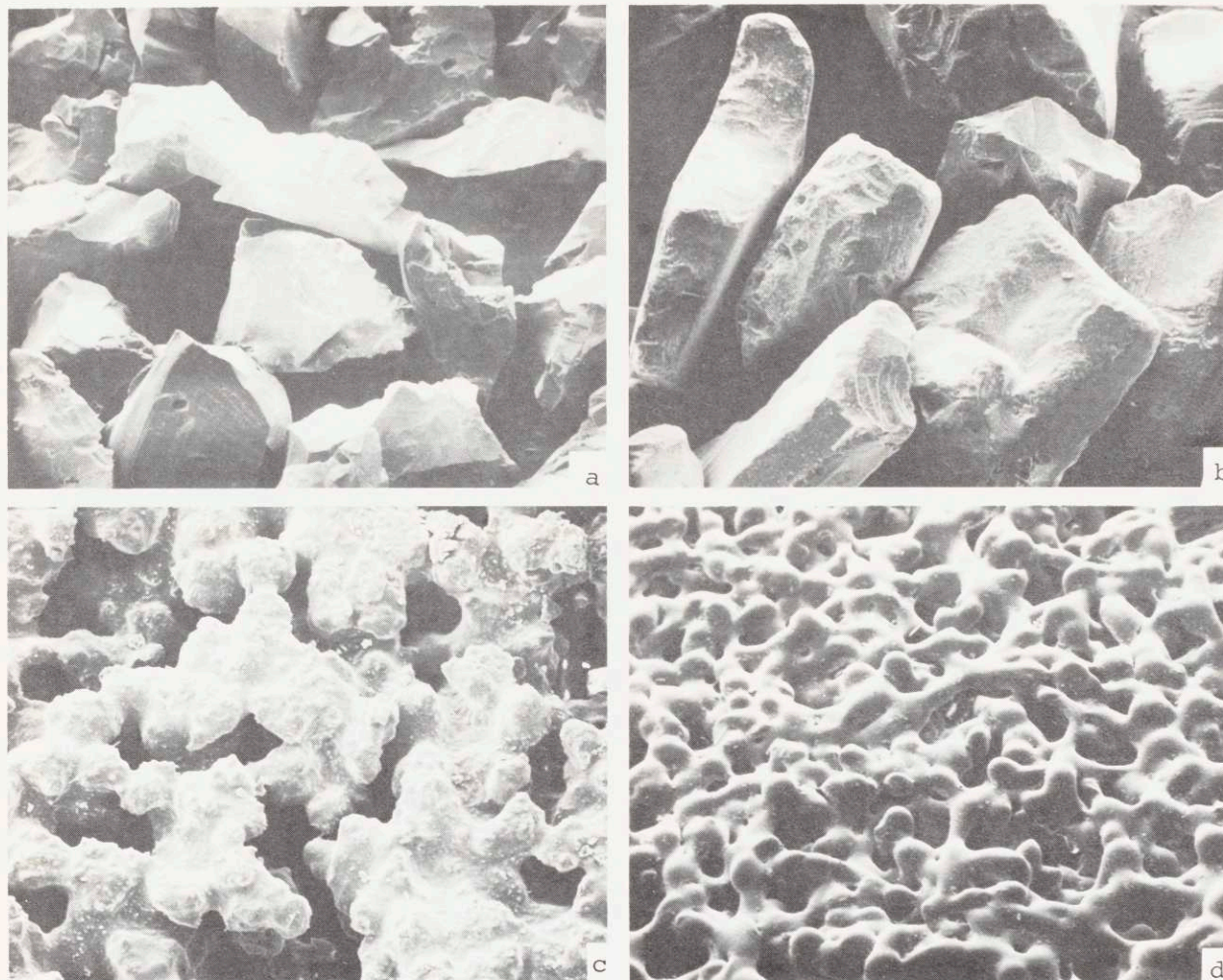
Figure 9: Granular materials and sintered disc filters used in filtration of
aluminum alloys.
(a) and (b), SEM views of the Al_2O_3 and SiC granular materials of
grit size 60 , 63X and 118X, respectively.
(c) and (d), SEM views of the Al_2O_3 and quartz sintered disc filters
of 87-108μ and 90-150μ pore sizes, 102X and 25X,
respectively.
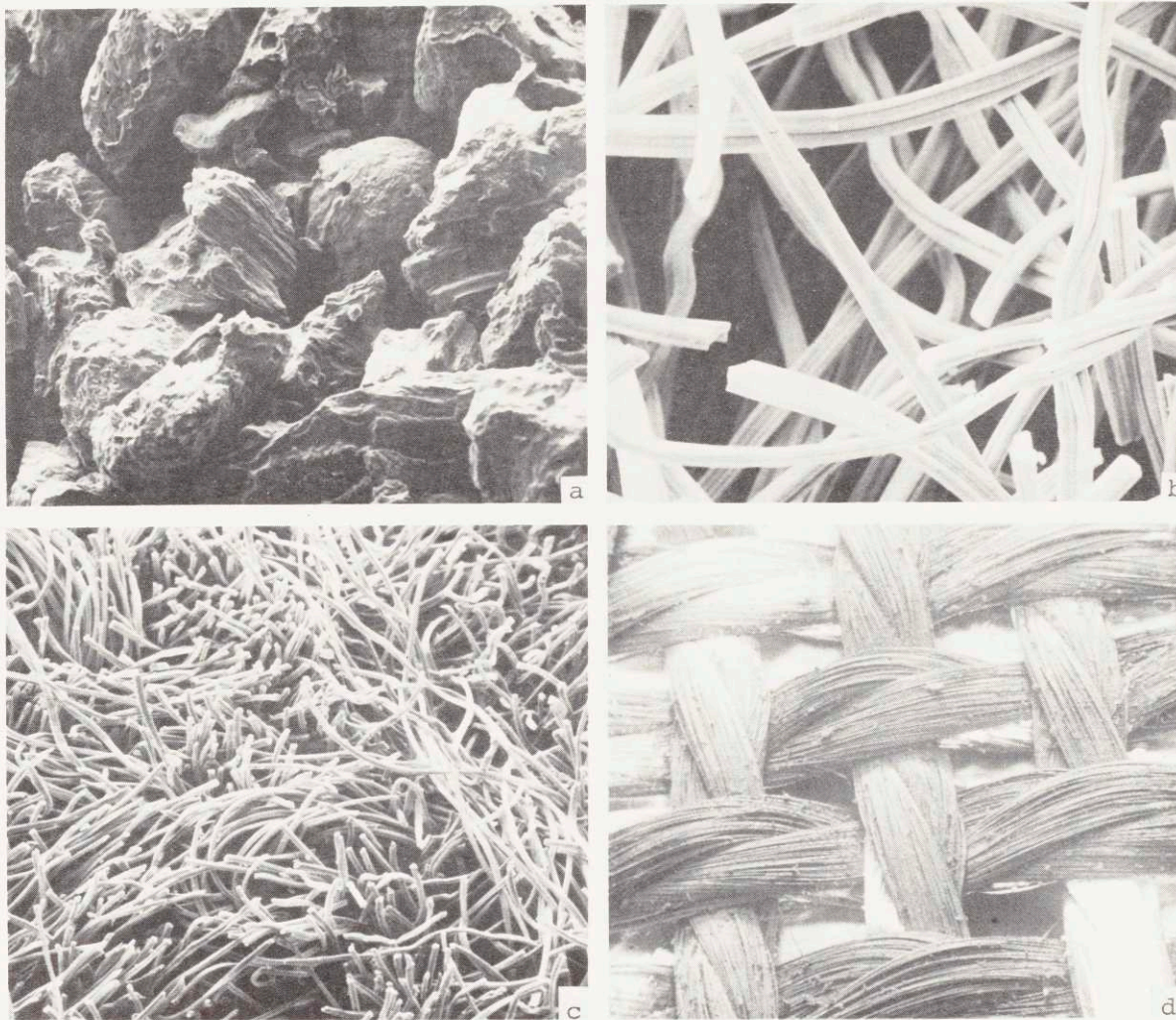
Figure 10: SEM views of filter materials used in filtration of aluminum alloys.
(a) Porous carbon, 68X.
(b) and (c) Fibrous non-woven carbon felt, 263X and 62X, respectively.
(d) Fiberglass cloth, 25X.

4. EXPERIMENTAL PROCEDURE

4.1   Filtration of Al Alloys

The apparatus described in Section 3.2, and shown in Figures 5 and 7, was used in these experiments. The operating procedure was as follows: both the upper and lower chambers were evacuated. The chambers were subsequently backfilled with an inert atmosphere, argon or nitrogen, and the charge was then melted. The melt was superheated to a temperature T_M to insure complete melting. The RF power was then adjusted so that the melt stabilized at the desired filtration temperature, T_F, for a certain time Δt (10-15 minutes). The upper vessel was then pressurized and the metal was pushed through the filter. The time differential between application of the pressure and the first liquid emerging from the exit port of the filter bed was measured using the temperature response of the thermocouple located in the mold, below the filter.

A.   Al-Ti Alloys

$TiAl_3$, synthetic inclusions, were filtered out from the two phase region, liquid + $TiAl_3$, of the Al-Ti system. This system was chosen because the weight fraction of the synthetic inclusions, $TiAl_3$, is quite small, less than 0.015, for an Al-1% Ti alloy at $800^{\circ}C$. This level of impurity content is equivalent to impurity contents in commercially

available aluminum. The aluminum rich corner of the Al-Ti system is shown in Figure 11a.

A 20 pound melt of Al-1% Ti alloy was made using 99.99% purity aluminum and an Al-5% Ti master alloy. The filter bed used in these experiments consisted of 216μ diameter Al_2O_3 granules located on top of a 40μ pore size sintered Al_2O_3 disc filter.

The melting and filtration procedure was as follows: 180 grams of the alloy was superheated in the crucible to 975°C. The melt was subsequently cooled to the desired filtration temperature, T_F, and held for 10 to 15 minutes (Δt). Finally, pressure was applied to initiate filtration. The experiment was repeated at various temperatures in the liquid + $TiAl_3$ range of the phase diagram. The titanium content of the filtered metal, and the unfiltered metal above the filter bed, now enriched in Ti by the presence of excess $TiAl_3$, were chemically analyzed. The exact composition of the initial charge was not analyzed because the composition of the liquid phase at temperature T_F is fixed; it is independent of the initial alloy composition.

The non-filtered metal above the bed and the filtered metal were both metallographically examined. The polishing sequence used on these samples was the following:

1. grind with 80, 120, 240, 320, and 600 grit paper, using water as a lubricant

2. clean the sample in an ultrasonic bath

3. polish using a 6μ diamond paste, and Buehler
    metcloth wheel
4. ultrasonically clean
5. electropolish using the Knuth system and A-2
    solution for 15-20 seconds.

B. Commercial Purity Aluminum

Aluminum of various commercial purities was filtered
to investigate the feasibility of removing aluminum oxide
and other non-metallic inclusions. Ingots of the following
purities were purchased.

ingot	Al	Si	Fe	Mn	Zn	Ga
99.5 Al	99.70	.070	.17	–	–	.024
99.9 Al	99.9	.048	.047	–	–	–

The filter bed again consisted of 216μ diameter Al_2O_3
granules followed by a 40μ pore size sintered Al_2O_3 disc
filter. The procedure during these experiments was as
follows: About 180 gms of aluminum was melted in the
crucible, Figure 8a, and superheated to a certain temperature,
T_F. Melting was carried out in a nitrogen atmosphere. The
melt was held at T_F for a time Δt to equilibrate. Finally,
pressure was applied to initiate filtration.

Filtered aluminum samples, 1/2 in. thick, were rolled
at room temperature. Each rolling pass produced a reduction

in thickness of about 0.050 in. The final thickness of the rolled bars was .05 in. Test bars were taken longitudinal to the rolling direction. The test bar design is shown in Figure 11b. After machining the rolled material, the test bars were annealed (recovered) at 450°F for 1 hour.

Three bars were tested from each as-received and filtered sample of the various purity metals. The bars were tested in tension with an Instron machine at a strain rate of 0.05 inches per minute; the elongation was measuring using a 1/2 in. extensometer.

The non-filtered metal above the bed and the filtered metal were both metallographically examined.

Polishing and etching procedure was the same as that employed on the Al-Ti samples.

Large amounts of aluminum oxide were intentionally added to an aluminum melt to allow metallographic investigation of the efficiency of oxide separation by filtration techniques. Granular (8-20 mesh) purified aluminum was purchased from J. T. Baker Chemical Co. and 180 gms. of this was melted in the crucible. The same melting procedure, as described above, was followed. Various filter media were employed. Flux coated (Klein-Farris, G-61 Al flux) granules of Al$_2$O$_3$ were used along with sintered rigid discs.

The non-filtered metal above the bed and the filtered metal were both metallographically examined. The polishing sequence was the same as before but with a 1/4μ diamond paste

final polish. The Al_2O_3 content of the non-filtered and filtered metal was measured by chemical analysis. 40-60 grams of filtered and non-filtered metal were melted and solidified in a centrifuge* to concentrate the oxide and non-metallic particles. Rotational speeds of 500 rpm were used, corresponding to a nominal 90 g.

C. Al-Ti-B Alloys

In the following series of experiments, Al-Ti-B alloys containing TiB_2 synthetic inclusions were filtered through various filter beds. The objectives here were: (i) to study the filtration process in liquid aluminum with the help of tracer synthetic inclusions, which range from 3-15μ in diameter, and (ii) to evaluate the many different types of filter beds discussed in Section 3. TiB_2 particles were chosen for this study because of their favorable morphology and size range.

A 15 pound melt of Al-Ti-B alloy was made using 99.99% aluminum and an Al-5% Ti-1% B master alloy. The alloy composition ranged from .51% Ti - .11% B to .56% Ti - .15% B. In these series of experiments, the filter bed was varied to evaluate the efficiency of the different filters discussed in Section 3. The procedure for the following experiments was to melt about 180 grams of the prepared Al-Ti-B alloy in a

_____

*   The centrifuge used was that described by Mollard and
       Dore(62). This work was carried out at Olin's
       Research Laboratories, New Haven, Connecticut.

nitrogen atmosphere, superheat it up to 950°C, T_M, which is in the liquid range. The power was then shut off and the melt was cooled down to a predetermined filtration temperature, T_F. The melt was held at T_F for a given time Δt. Finally, the upper vessel was pressurized to initiate filtration. The pressure required for filtration was measured for each different filter bed.

The titanium and boron contents of the filtered metal, the unfiltered metal above the bed, and the initial charge were chemically analyzed by Kawecki Berylco Company's analytical laboratories. The non-filtered metal above the bed, the filtered metal, and the filter bed were metallographically examined. These were polished in the same manner as the Al-Ti alloys. Table I lists the filters evaluated for the removal of TiB_2 "synthetic inclusions." 40-60 grams of filtered and non-filtered metal were heated to 715.5°C (above the peritectic reaction temperature) and were solidified while centrifuged to concentrate the TiB_2 "synthetic inclusions" present in the melt. Rotational speeds of 500 rpm were used corresponding to a nominal 90 g.

4.2 Separation of Interdendritic Liquid from Partially Solid-Partially Liquid Al-Si Alloys

A. Sample Preparation and Procedure

The following series of experiments were designed to separate the interdendritic liquid from a partially solidified

alloy using filters as support for the solidified dendritic
network.

The apparatus shown in Figure 5 was used; however,
the inner crucible was modified as shown in Figure 12a. The
alloys used for these experiments were Al-4% Si and Al-4% Si-
0.25% Ti (grain refined). The Al-Si binary phase diagram
is shown in Figure 12b. A 15 pound melt of each of these
alloys was made using 99.99% purity Al, Al-50% Si and
Al-1% Ti master alloys. After chlorine degassing the melts
for 15 minutes, plugs of these alloys were unidirectionally
cast. These plugs were machined down to a height of 1.5
inches and were placed above the filter mount in a tapered
fit (Figure 12a).

The filters used in this series of experiments were
sintered quartz (99.8% SiO_2) filters with pore size ranging
from 90-150µ, Figure 9d. SiO_2 filters were used because of
the high wettability of aluminum with SiO_2, thus minimizing
the pressure required for filtration.

The procedure was as follows: Two thermocouple holes
were drilled into the alloy plug to accurately monitor the
temperature. Each plug was weighed with a gravimetric scale
and then was inserted into the crucible with the thermocouple
in place. 40 grams of G-61 aluminum flux (Klein-Farris) was
then added to the top of the metal plug to dissolve the
"impermeable" oxide layer above the charge, thus allowing
the pressure forces to act on the interdendritic liquid.

Two types of experiments were carried out: (i) one
in which the plug was completely remelted first and then
cooled to a predetermined temperature in the liquid-solid
range, and (ii) one where the plug was gradually heated from
the solid state to a predetermined temperature in the liquid-
solid range.

The various runs made and their mode of heating are
tabulated below:

Charge remelted then temperature decreased to a predetermined temperature in the liquid-solid range.		Charge directly heated to a predetermined temperature in the liquid-solid range.	
Al-4%Si	Al-4%Si-.25%Ti	Al-4%Si columnar structure	Al-4%-.25%Ti equiaxed temperature
Runs #94 and #95	Runs #96 and #99	Runs #91 and #98	Runs #92 and #97

In both cases, the heating of the charge was done in
a nitrogen atmosphere. The partially frozen charge was held
at T_F for a certain holding time, Δt. Finally, the upper
vessel was gradually pressurized to initiate the separation
of the interdendritic liquid from the solid dendritic network.
The temperature of separation was varied, such that dendritic
networks of .33 to .54* fractions solid were attempted.
A thermocouple inserted in the chill indicated penetration of

---

* Fraction solid at each temperature was calculated from
the Scheil equation (Appendix C).

the interdendritic liquid through the filter, and the necessary required pressure was recorded. Both the filtered interdendritic liquid and the dendritic network above the filter were chemically analyzed for silicon. The micro and macro-structures of these specimens were studied using scanning electron microscopy and metallography techniques.

B. Permeability Measurements

After removal of the interdendritic liquid, the samples of the remaining dendritic network (1.75" in diameter by 1.5" high) were machined down to cylinders of 1.00" in diameter. Both ends of these cylinders were spark cut such that the height of the cylinders ranged between 0.5"-0.9". The spark cutting technique was used to prevent damage to the porous structure.

The permeabilities of these "porous media" were measured by using a triaxial cell permeameter. This equipment shown in Figures 13 and 14a was developed by the M.I.T. Civil Engineering Laboratories. The procedure for the permeability measurements was as follows.

The 1" diameter disc sample was enclosed in a latex impermeable membrane with an excess length of approximately two inches at each end. The lower sintered brass disc was placed on the cell pedestal. The sample along with the membrane was then placed above the brass disc. The lower excess two inches of the membrane was then stretched over the pedestal and secured with rubber "O"-rings in order to

make an impermeable seal. While flushing water through the
upper drainage line, the top cap with a drainage line attached
to it was placed on the sample and the brass disc. The upper
portion of the membrane was then stretched over the top cap,
and the remaining excess water was removed. "O"-rings were
used to seal the membranes to the top cap.

The cell chamber was bolted to the base and the cell
filled with water. A cell pressure of 3 kg/cm^2 was applied
triaxially to seal the latex membrane to the sample. In this
manner flow only through the sample was assured. A pressure
of 2 kg/cm^2 was next applied to both upper and lower drainage
lines. The pressures were kept constant by compensating
mercury pressure systems. The pressure in the upper drainage
line was then increased to establish a pressure difference
across the sample, which caused flow through the sample from
the upper to the lower drainage lines. Volume of flow was
measured through each line by means of paraffin volume change
burettes. By measuring sample dimensions, flow rate, and
head drop across the sample, the coefficient of permeability
was calculated using D'Arcy's equation. For each sample
various heads (pressure gradients) were used to insure laminar
flow through the sample.

4.3 Production of Metal Powders

A. Production Procedure

The apparatus used in this series of experiments is shown in Figure 6. The filter was mounted within a filter container assembly, shown in Figure 8a. The cover of the assembly was not used here. A sensitive pressure gauge, ranging from 0-15 psi was installed and used to record the required pressure for drop formation. The spherical drops (powders) exiting from the filter were exposed to the atmosphere; no inert gas was injected at the exit port. The powders were collected in a can located 5 feet below the filter thus allowing them to completely solidify before reaching the collector can. Sintered Al_2O_3 porous disc filters of 87-108μ and 31-36μ pore sizes, and sintered quartz discs of 90-150μ and 40-90μ pore sizes were used. The alloys used for filatomization were 99.99 aluminum and a 7075 alloy of Al-7.3% Zn - 3.2% Mg-2% Cu-.25%Cr nominal composition. The 7075 alloy was prepared using pure zinc and magnesium, 99.99% Al, Al-50% Cu master, and an Al-20% Cr master. The melt was degassed with chlorine prior to pouring.

The operational procedure for the following experiments was to melt about 200 gms. of the alloy in a nitrogen atmosphere and superheat it to 700°C. The power was then gradually decreased reducing the melt temperature to a predetermined level, T_F. The pressure above the melt

was gradually increased until metal drops (powders) started
to exit from the filter. The procedure employed and the
temperatures and pressures used are listed in Table II.
Size distribution curves of the resulting powders obtained
from the various filters were determined by sizing (sieve
analysis) and weighing of the powders.

The remnant metal above the filter (metal which did
not go through the filter), the powders and flakes produced,
and the filter itself were all metallographically examined.
The polishing procedure was that reported earlier for the
Al-Ti alloys, except that final polishing was done on
microcloth with 0.3 and 0.05μ suspended Al_2O_3 solutions.
Keller's etch was used for the microstructural investigation
of the powders. Macroexamination of the powders and flakes
was done by scanning electron microscopy. The Al_2O_3 content
of the powders, flakes and the remnant metal above the
filter was determined by chemical analysis. Powders and
flakes made by this process were compared with 7075
commercial powders (made by centrifugal atomization) purchased
from Reynolds Aluminum, 7075 (of modified compositions) splat
cooled flakes made by J. P. Durand(63), and 7075 commercial
ingot material.

B. Classification and Processing of Powders

Pound lots of filatomized spherical powders and flakes
were produced using various filters as described above. No

particular powder or flake size was selected for the extrusion process, but rather all the filatomized spherical powders were mixed carefully and used for the extrusion. The size distribution of these powders was measured and calculated. The same was done for the filatomized flakes. The filatomized powders, filatomized flakes, commercial 7075 powders*, and the splat cooled 7075 flakes** were all separately cold compacted under 20,000 psi pressure into two 3 inch O.D. by 2 inch I.D. 6061-T6 aluminum cans. The location of the various powders and flakes in the cans was carefully noted for reference. The above were compacted to 70% density. The top caps of the cans were then welded on, and the cans were leak checked before evacuation.

The extrusion billets were evacuated at the solution-izing temperature of the particular alloy. For the filatomized powders and flakes and the Reynolds' powders a solution temperature of 476.2°C was employed. For the splat cooled flakes of modified 7075 alloy (Al-7.50Zn, 2.4Mg, 1.0Cu, .20Cr, 1.1Fe, 1.0Ni) a solution temperature of 490°C was employed. The billets were heated under vacuum for 2 hours to reach the solution temperature, held at that temperature for an additional hour and furnace cooled. The billets were then sealed, soaked at 300°C for 4 hours and extruded at 300°C at a reduction ratio of 20 to 1. The

---

*   purchased from Reynolds

**   made by J. P. Durand (63)

extruded rods had a final diameter of 0.67" and a core
diameter of 0.41".

The extruded rods were then machined down to the core
diameter, and the as-extruded structure of the various
powders were investigated. Ten 0.75" long samples were cut
from each extruded rod, and the solution temperature and
aging kinetics of the alloys were studied. All the solution
treatments were given in an air furnace equipped with
automatic control. Artificial ageing was done at 121°C
(250°F) for various times.

C. Mechanical Testing

Tensile tests on all materials were performed with a
standard 1/4" - 20 thread tensile specimen, shown in
Figure 14b, with a 1.00" gauge length and a 0.160" diameter.
Several test specimens were machined for each alloy. These
specimens were then radially and longitudinally polished on
a lathe with No. 600 emery paper. After cleaning in Acetone,
the specimens were again radially polished on a lathe with
wenol metal polish. All tensile tests were run on an Instron
machine at a constant crosshead speed of 0.05" per minute.
The elongation, reduction in area, yield strength and ultimate
tensile strength were measured. Finally, the fractured
surfaces of the tensile specimens were studied by scanning
electron microscopy.

Table I

List of Filters Tested for Filtration
of Al-Ti-B Alloys

run	filter description
35	sintered Al_2O_3 disc (2" diameter, 0.25" thick) of 87-100μ pore size
29	sintered Al_2O_3 disc (2" diameter, 0.25" thick) of 87-100μ pore size, preceeded by a granular bed (1.5" high) of Al_2O_3 of #60 grit size (400μ)
41a	sintered Al_2O_3 disc (1" diameter, 0.25" thick) of 87-100μ pore size
41b	sintered Al_2O_3 disc (1" diameter, 0.25" thick) of 87-100μ pore size
42b	sintered Al_2O_3 disc (1" diameter, 0.25" thick) of 36-40μ pore size
42d	sintered Al_2O_3 disc (1" diameter, 0.25" thick) of 36-40μ pore size
44a	5 layers of non-woven carbon felt with a density of 2 lb/yd^2. Each layer is 1/4" thick
44b	2 layers of non-woven carbon felt with a density of 8 lb/yd^2. Each layer is 1" thick
46	9 layers of fiberglass cloth (J. P. Stevens - style #1339), 420 holes/in^2, and 0.00072 in^2/hole
47	porous carbon plug, 1.8" high and having an average pore diameter of 120μ
48	sintered Al_2O_3 disc (1" diameter, 0.25" thick) of 36-40μ pore size, preceeded by a granular bed (1.5" high) of Al_2O_3 of 400μ diameter
49	sintered Al_2O_3 disc (1" diameter, 0.25" thick) of 36-40μ pore size, preceeded by a granular bed (1.5" high) of Al_2O_3 of 200μ diameter
50	sintered Al_2O_3 disc (1" diameter, 0.25" thick) of 36-40μ pore size, preceeded by a granular bed (1.5" high) of Al_2O_3 of 106-148μ in diameter
53	sintered 430 stainless disc filter (1" diameter, 0.25" thick) with a median pore size of 240μ
54	sintered Al_2O_3 disc (1" diameter, 0.25" thick) of 36-40μ pore size, preceeded by a granular bed (1.5" high) of SiC of 400μ in diameter
56	sintered quartz disc (1" diameter, 0.118" thick) of 90-150μ pore size
57	three sintered quartz discs (1" diameter, 0.354" thick) of 90-150μ pore size
58	sintered Al_2O_3 disc (1" diameter, 0.25" thick) of 87-100μ pore size

Table II

List of Filatomization Experiments

run #	sintered filters used	T_F	alloy used	pressure applied (psi)
1	Al_2O_3, 87-100μ	710°C	99.99% Al	7-8 then lowered to 4-5
2	Al_2O_3, 31-36μ	840°C	7075	7-14
3	SiO_2, 90-150μ	756°C	7075	2-4 and 10-15
4	SiO_2, 90-150μ	769°C	7075	10-12
5	Al_2O_3, 87-100μ	756.5°C	7075	3-5
6	Al_2O_3, 87-100μ, previously infiltrated	732.5°C	7075	3-5
7	Al_2O_3, 87-100μ	760°C	7075	3-5
8	SiO_2, 90-150μ	769°C	7075	2-4 and 10-14
9	SiO_2, 90-150μ	650°C	7075	3-4
10	Al_2O_3, 87-100μ	697°C	7075	0-6
11	Al_2O_3, 87-100μ, previously infiltrated	700°C	7075	5-6
12	Al_2O_3, 87-100μ, previously infiltrated	721°C	7075	5-6
13	SiO_2, 90-150μ	685°C	7075	3-5
14	Al_2O_3, 87-100μ, same filter as in runs # 10-12	742°C	7075	5-6
15	Al_2O_3, 87-100μ	742°C	7075	0-7
16	Al_2O_3, 87-100μ, previously infiltrated, filter from run #15	742°C	7075	4-5
17	Al_2O_3, 87-100μ	700°C	99.99% Al	7, then lowered to 4-5
18	SiO_2, 40-90μ	687°C	7075	2-4
19	Al_2O_3, 87-100μ	700°C	99.99% Al	7, then lowered to 4-5
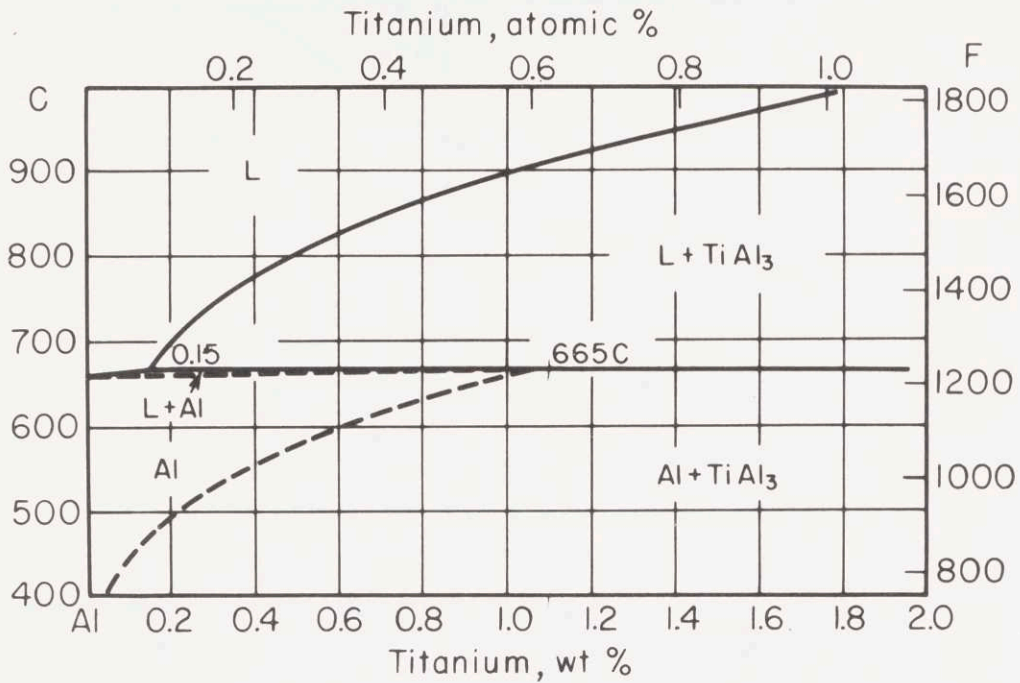
(a)
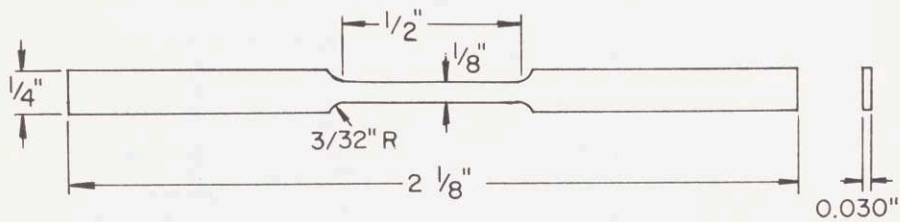
(b)

Figure 11: (a) Aluminum rich corner of the Al-Ti system (61).
(b) Tensile test bar design for filtered aluminum
of various commercial purity.

FLUX

METAL
PLUG

1 1/2"

1 1/2"

1/2"

2 1/2"

SiO₂
FILTER

Cu CHILL

THERMOCOUPLE

(a)

700

650

600

550

500

TEMPERATURE , °C

L

L + Al

Al

577 °C

1.65

11.6

L
+
Si

Al + Si

0   5   10   15

Wt. % SILICON
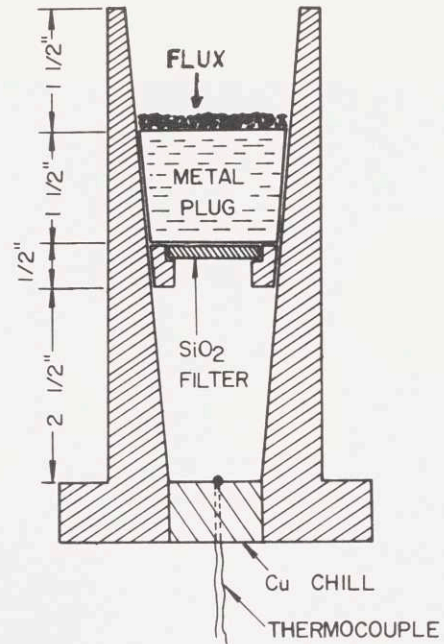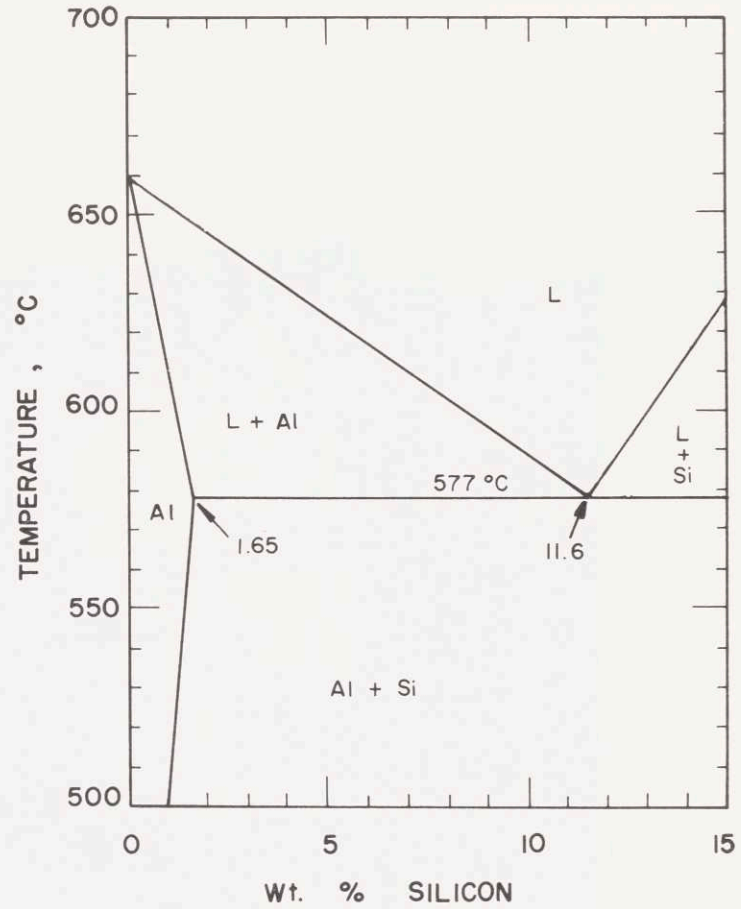
(b)

Figure 12:   (a) Tapered graphite crucible showing details of
                  experimental setup for filtration of
                  interdendritic liquid.
            (b) Aluminum rich corner of Al-Si phase diagram.
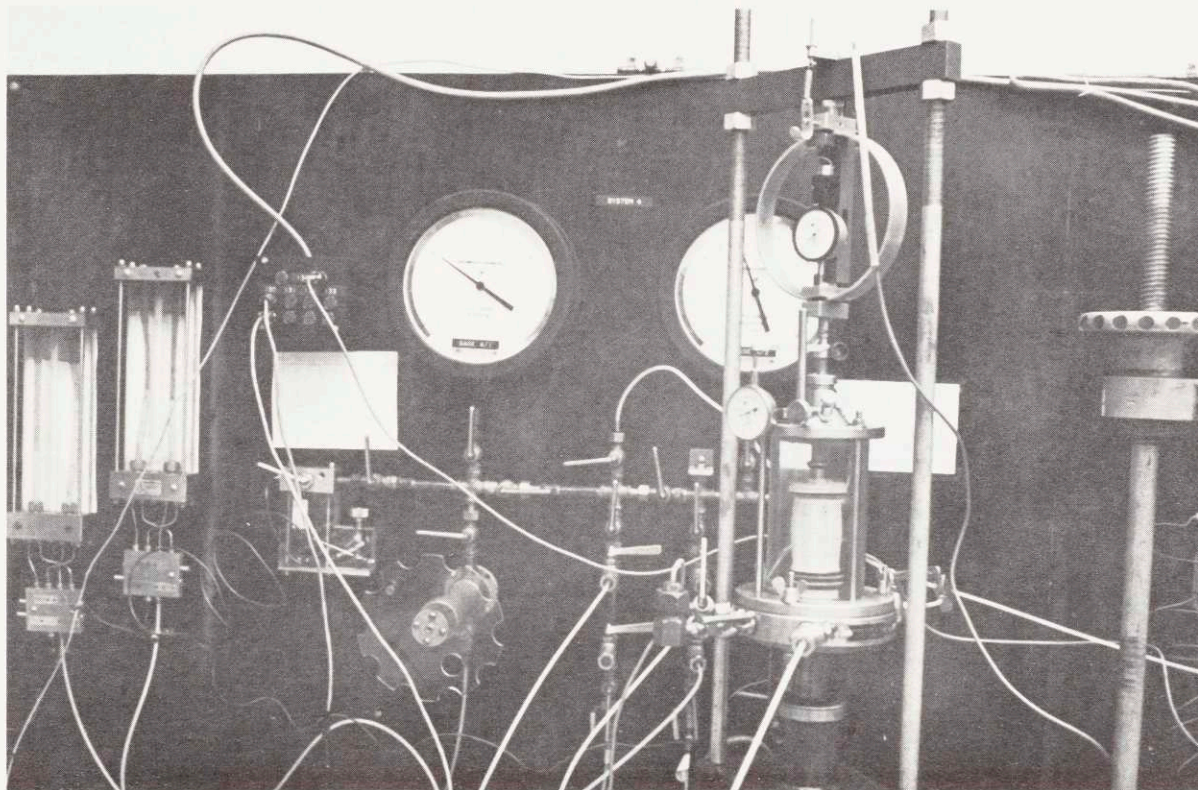
Figure 13: Photograph of permeameter employed.

CELL PRESSURE

DRAINAGE LINE

TOPCAP

SINTERED BRASS
FLUID
DISTRIBUTORS

O – RINGS

IMPERMEABLE
MEMBRANE

PEDESTAL

SAMPLE

TO VOLUME
CHANGE DEVICE
(FLUID OUTLET)
+ PRESSURE H_2

PRESSURE DIFFERENTIAL
= $H_1 - H_2$

TO VOLUME
CHANGE DEVICE
(FLUID INTAKE)
+ PRESSURE H_1

(a)

1/4 - 20   0.20   0.160   1/4 R

0.10   1.000   0.58

2.45

(b)
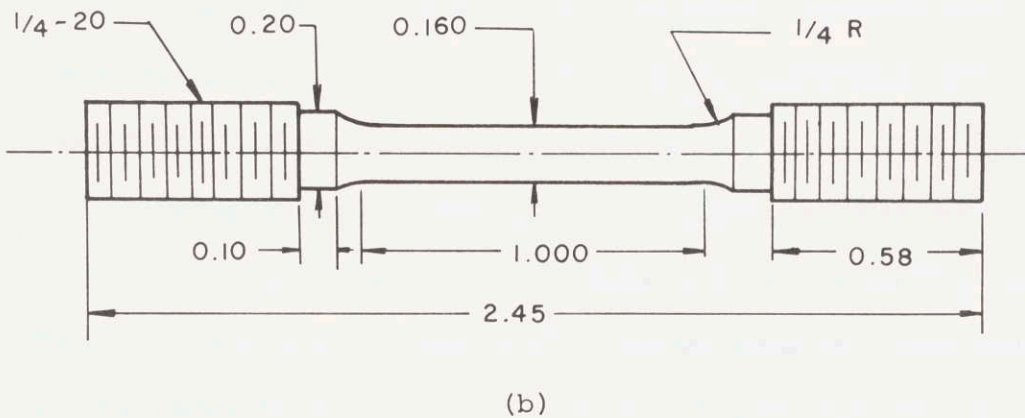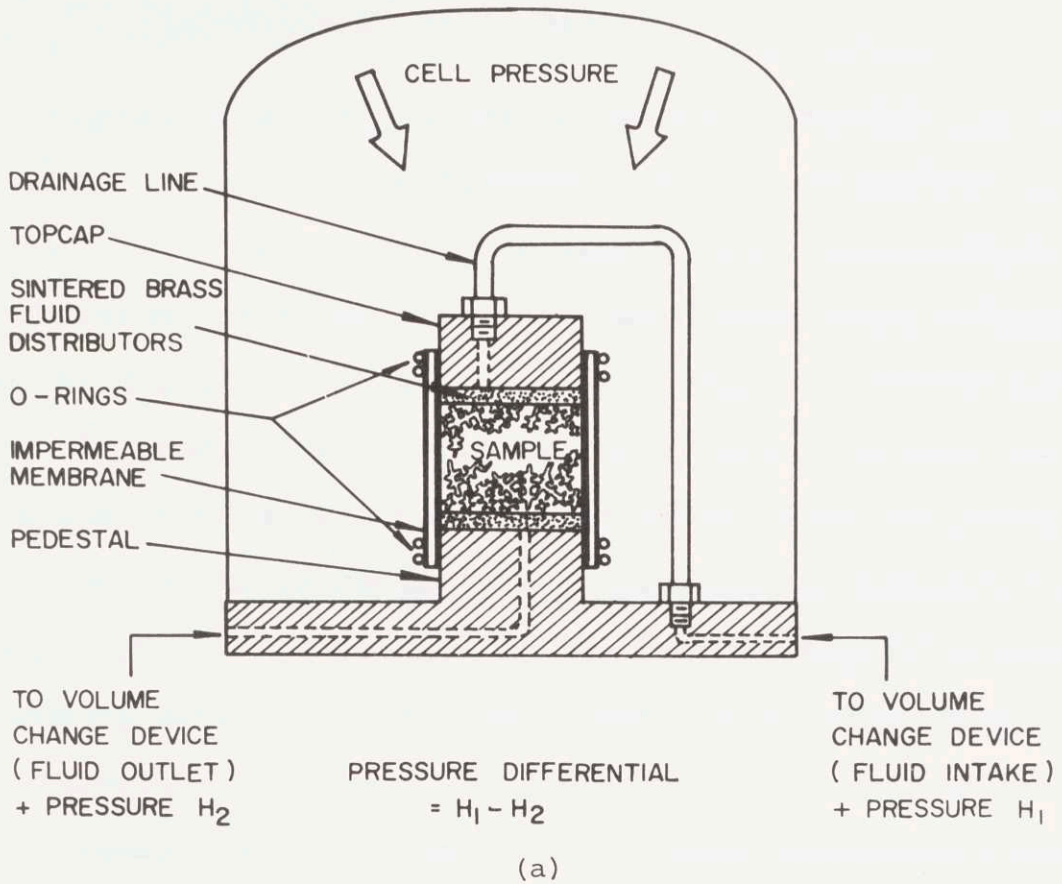
Figure 14:   (a) Schematic of permeameter triaxial cell.
             (b) Schematic of tensile test specimens for
                 filatomized powders.

5.1   Filtration of Aluminum and Its Alloys

A.   Filtration of Al-Ti Alloys

Experiments carried out to separate the $TiAl_3$ phase
from an Al-1% Ti alloy by filtration have been summarized
in Table III. The different variables (i.e. temperature,
filter medium, pressure, etc.) for each experiment are also
listed in Table III. Figure 15a shows the microstructure of
the initial charge used in these experiments. Figure 15b
is a SEM view of extracted $TiAl_3$ particles from the Al-1% Ti
alloy showing the characteristic platelike morphology of
these particles. Extraction of the $TiAl_3$ phase was done at
the Kawecki-Berylco Industries' Laboratories, Bayertown,
Pennsylvania.

Figure 16a shows the charge, filter container assembly,
and the filtered metal of Run #14A. Figures 16b and 16c show
the filters used in these runs. The Al_2O_3 granular bed
impregnated with metal during filtration is shown in Figure
16b. Liquid metal flowing through the granular bed has
uniformly infiltrated the latter. Channeling occurs when the
liquid travels through preferential paths within the granular
bed. It has been found that by efficient packing and
compressing the granules, properly mounting the filters, and
by attaining a uniform temperature across the bed, formation
of large channels can be prevented. Figure 16c shows metal-
droplets exiting from the sintered Al_2O_3 disc filter of 40μ
pore size.

Figure 17 shows a plot of the titanium content of the filtered liquid phase versus filtration temperature. Also, on the same figure the liquidus curve of the Al-Ti system is shown. Correlation between the two curves is good. Figures 18a, 18b and 19a, 19b show photomicrographs of the non-filtered and filtered metal, from Run #11A and #12A, respectively. Comparison of the microstructures in Figures 18a and 18b, shows that separation of the $TiAl_3$ from the liquid phase has occurred. Furthermore, Figure 17 indicates that this separation was quite complete - that is all of the $TiAl_3$ particles present were held above the filter bed. Therefore, a well controlled filtration setup can be utilized to determine certain liquidus curves of phase diagrams.

The microstructure shown in Figure 19a was overetched when electropolishing. The structure indicates that the primary dendrite branches had nucleated around the $TiAl_3$ particles.

Figure 20 shows accumulated $TiAl_3$ particles of various sizes above the granular filter bed. Most of these particles settled on top of the bed during holding time. Appendix A shows calculated settling rates for average size $TiAl_3$ particles. This is analogous to formation of a cake above the bed, discussed previously. This accumulated cake can be thought of as a built-in filter medium within the liquid metal. In other words, the filtered "impurities" can be employed advantageously to remove others. The beer industry has been using diatomaceous earths and expanded pearlite for

many years, as additives to the beer as a "filter-aid" prior to filtration(23 , 26).

Accordingly, if $1-5\mu$ size particles are to be filtered out of aluminum, then intentional additions of inclusions or particles of $20-30\mu$ size (or even larger) to the melt will conceivably yield a more efficient filtration operation. More experimental work is necessary to characterize the role of "filter aids" in liquid metal filtration.

These filtration experiments have shown that the apparatus and experimental approach employed are well suited for investigating filtration of aluminum melts. While $TiAl_3$ particles were successfully filtered out of the Al-Ti system, the size range of these particles was quite large. In subsequent experiments "synthetic inclusions" of a much smaller size range will be used.

B. Filtration of Various Purity Aluminum Melts

Experimental results of filtration of various purity aluminum melts are summarized in Table IV. In the commercial purity aluminum melts (Runs #18A, #24), chemical analyses of the filtered and non-filtered metal indicated no difference in the content of foreign elements (iron, silicon, manganese, and zinc). Figure 21 shows an iron rich intermetallic compound observed in the filtered 99.5% aluminum metal. The extent to which impurities were removed could not be determined by metallographic examination. Electron microprobe

analysis was only instrumental in detection and identification of existing intermetallic compounds. Mechanical property measurements were used to evaluate the effect of filtration.

Averaged results of tensile tests, UTS and elongation data for filtered and non-filtered samples, are plotted in Figure 22. Table V lists all the tensile test results. Figure 22a shows that the filtered aluminum metals have higher ultimate tensile strengths than the as-received samples. Figure 22b shows that total elongation of both 99.5% and 99.9% aluminum increased with filtration. Upon filtration, reduction of area of 99.5% Al melt increased from 21.9% to 32.5%; for the 99.9% Al melt it increased from 21.6% to 42.0% (Table V). This can be attributed to reduction of "second phase" oxide particles. Edelson and Baldwin(64) have shown that ductility (reduction in area) of copper increases exponentially with decreasing volume fraction second phase.

Figures 23a and 23b are SEM fractographs of the as-received and filtered 99.5% purity aluminum, respectively. The fractographs indicate that the filtered metal failed in a much more ductile fashion, as evidenced by the many ductile voids seen in Figure 23b.

Effect of filtration on Al_2O_3 content of the melts could only be successfully measured with melts of high Al_2O_3 content. This was attained by using granular aluminum, with a high surface to volume ratio, for the initial charge material (Runs #51, #100, and #101, Table IV). Figures 24a

and 24b show the microstructure of the remelted granular aluminum with a high Al_2O_3 content and the filtered sample from Run #51, respectively. Al_2O_3 "skins" were not observed upon metallographic examination of the filtered metal. The Al_2O_3 content, determined by wet chemical analysis, was markedly decreased by filtration, from 1.90 to 0.16 wt. %, Table I.

Ten samples, of 20 grams each, of Al-1% Ti alloy were melted in a graphite crucible by induction heating. The surface oxide of the samples was introduced into the melt by stirring the latter immediately after melting (introducing turbulence). The melt was held at $700^{\circ}C$ for 5 minutes and was then let to solidify. Metallographic examination of the ingot showed that the oxide "skins" introduced into the melt by stirring acted as nets, and $TiAl_3$ particles were retained above these nets at various places in the ingot. This is shown in Figure 25.

The Al_2O_3 content of the filtered metal in Run #100 was also decreased from 1.37 to .13 wt %, Table IV.

Microstructure of non-filtered metal, fibrous carbon felt filter infiltrated with the melt, and of the filtered metal from Run #101 are shown in Figure 26. The Al_2O_3 "skins" within the molten charge are shown in Figure 26a. These "skins" do not settle or accumulate above the filter bed since they are all interconnected and thus form a network within the melt. The oxide "skins" retained above the felt

filter are shown in Figure 26b. Figure 26c shows the microstructure of the filtered metal, where no oxide "skins" were observed. The Al_2O_3 content of the filtered metal was decreased from 1.63 to .13 wt %.

The non-filtered and filtered metal were centrifuged, under an applied force of 90 g, to concentrate the oxide "skins", and thus to better determine filtration effectiveness. It was found that the oxide "skins" from the non-filtered metal did not accumulate at the bottom of the centrifuged sample, because they formed a complex network within the melt, and were randomly distributed.

In summary then, the filtered commercial purity aluminum alloys exhibited higher ultimate tensile strengths and total elongation. This can be attributed to removal of oxide particles. With the commercial purity aluminum melts metallographic techniques were not instrumental in detecting filtration effectiveness in removing oxide particles. Filtration effectiveness in removing oxide particles from aluminum was investigated with melts where granular aluminum was used for initial charge material. It was found that by the use of filters described here, the Al_2O_3 content can be markedly decreased.

Table III

Experimental Results of Filtration of Al-Ti Alloys

run	C_o	filter medium	T_M	T_F	Δt	P	C_{NF}	C_F
11A	.79-1.09	216μ diameter	975	800	14	150	.90	.37
12A	.79-1.09	Al$_2$O$_3$ granules, followed	975	739	16	150	1.28	.26
13A	.79-1.09	by a 40μ pore size sintered	975	687	18	150	1.23	.20
14A	.79-1.09	Al$_2$O$_3$ disc	975	860	16	150	1.04	.70

Terminology:

C_o = initial alloy composition, weight percent titanium.

T_M = temperature to which the melt was superheated to, degrees centigrade.

T_F = temperature at which filtered, degrees centigrade.

Δt = local solidification time --- time to reach T_F from liquidus plus holding time to equilibrate at T_F, minutes.

P = pressure applied, psi

C_{NF} = titanium content of non-filtered metal remaining above filter, in weight percent.

C_F = titanium content of filtered metal, in weight percent.

Table IV

Procedure and Experimental Results of Filtered and As-Received 99.5% and 99.9% Al

run	initial charge	filter medium	T_F	Δt	P	C_{NF}	C_F
18A	99.5 Al	216μ diameter Al_2O_3 granules followed by	720	10	200	–	–
24	99.9 Al	40μ pore size sintered Al_2O_3 disc filter	720	10	200	–	–
51	purified granular aluminum, 8-20 mesh	flux coated (G-61) Al_2O_3 granules of 400μ in diameter, followed by 40μ pore size sintered Al_2O_3 disc filter	700	15	110	1.90	0.16
100	purified granular aluminum, 8-20 mesh	P-100C Al_2O_3 sintered disc of 100μ pore size	700	15	70	1.37	0.13
101	purified granular aluminum, 8-20 mesh	fibrous carbon felt filter, 1/4" thick, with a density of 2 lb/yd^2	700	15	40	1.63	0.13

Terminology:

T_F = filtration temperature, degrees centigrade

Δt = holding time at T_F, minutes

P = pressure applied, psi

C_{NF} = Al_2O_3 content of non-filtered metal remaining above filter, weight percent

C_F = Al_2O_3 content of filtered metal, weight percent

Table V

Tensile Test Results of Filtered and As-Received 99.5% and 99.9% Al

sample designation	A_o (10^3 inch^2)	A_f (10^3 inch^2)	max. load (lbs)	UTS (psi)	total elonga- tion %	R.A. %	average UTS (psi)	average total elonga- tion %	average R.A. %
Filtered 99.5% Al									
sample 1	6.27	4.25	132	20,800	11.8	31.8			
sample 2	6.35	4.26	128	20,200	10.0	33.1			
sample 3	6.12	4.10	127.5	20,800	9.8	32.67			
							20,600	10.53	32.52
As-received 99.5% Al									
sample 1	5.56	4.30	96	17,200	7.2	21.8			
sample 2	6.00	4.30	110	18,300	9.8	28.3			
sample 3	5.72	4.85	95	16,600	4.5	15.7			
							17,360	7.2	21.9
Filtered 99.9% Al									
sample 1	5.95	3.8	108.5	18,300	11.6	35.2			
sample 2	6.25	3.67	119.5	19,150	12.6	41.6			
sample 3	6.10	3.13	116.5	19,200	12.6	49.2			
							18,890	12.3	42.0
As-Received 99.9% Al									
sample 1	6.4	4.5	104	16,800	9.4	29.6			
sample 2	6.1	4.91	105	17,200	9.2	19.6			
sample 3	6.4	5.4	117.5	18,400	10.6	15.6			
							17,470	9.73	21.6
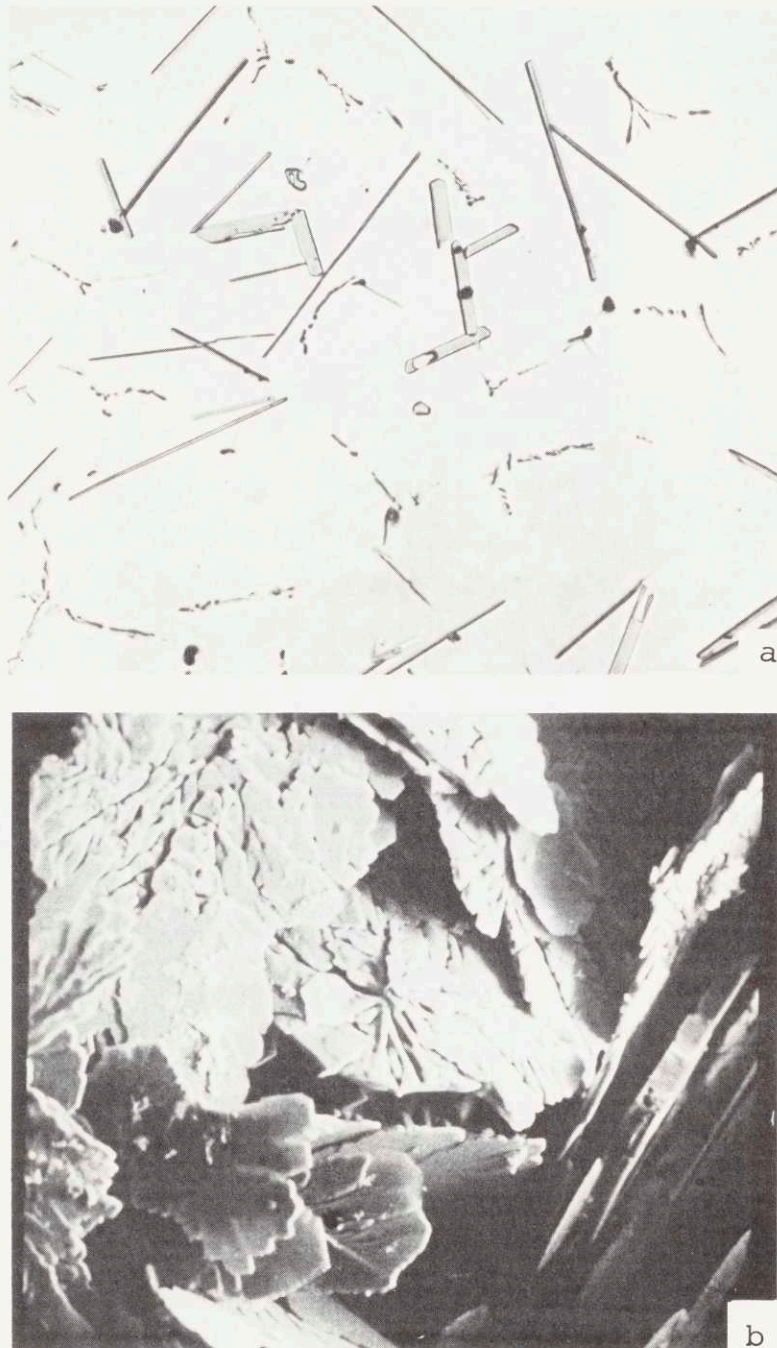
Figure 15: Structure of Al-1% Ti alloy and morphology of
TiAl$_3$ plates.
(a) Microstructure of Al-1% Ti alloy, initial
charge, 150X.
(b) SEM view of extracted TiAl$_3$ particles from
the initial charge, 50X. Note the
characteristic platelike morphology of the
TiAl$_3$ particles.
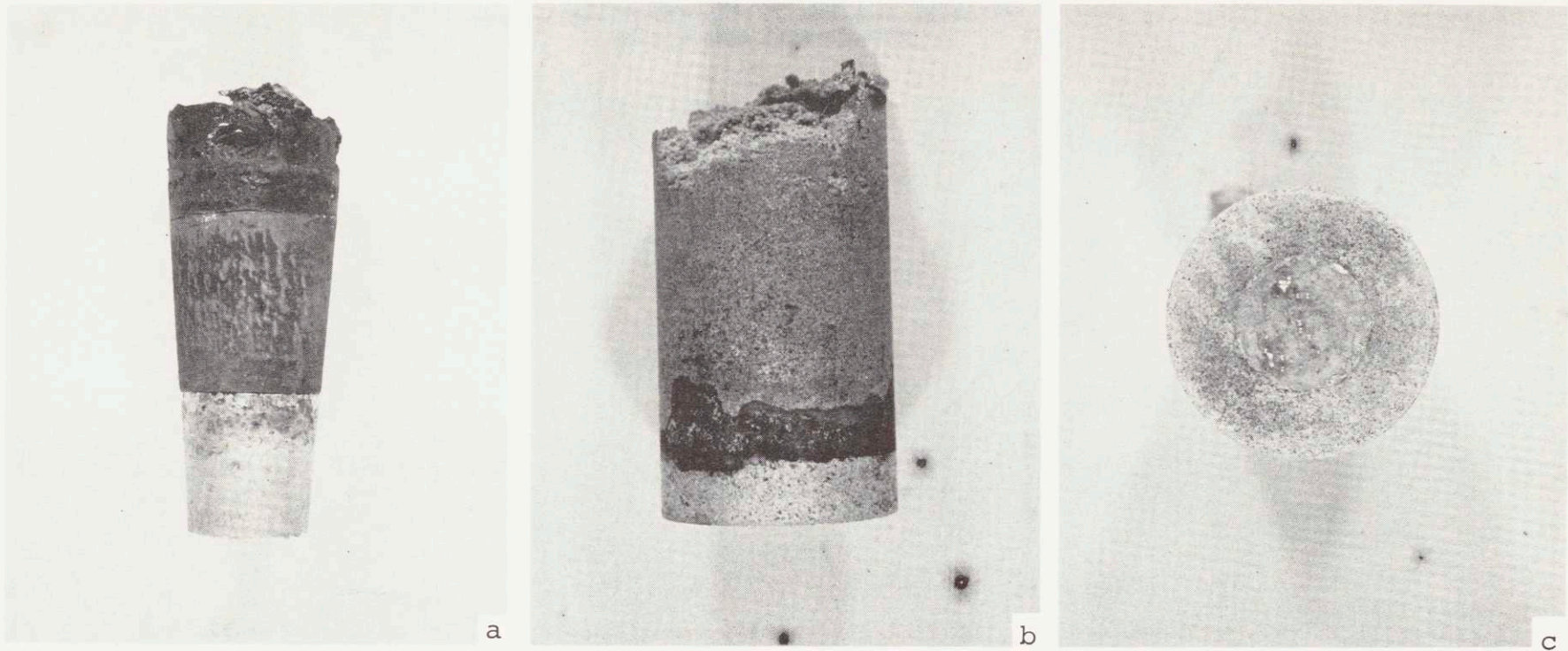
Figure 16: Experimental setup - filter container assembly, infiltrated granular
bed and sintered disc filter.
(a) Filter container assembly with filtered metal below it, 0.4X.
(b) Al_2O_3 (216μ diameter) granular bed impregnated with metal, 1.2X.
(c) Metal droplets exiting from sintered Al_2O_3 disc filter of 40μ pore
size, 1.5X.
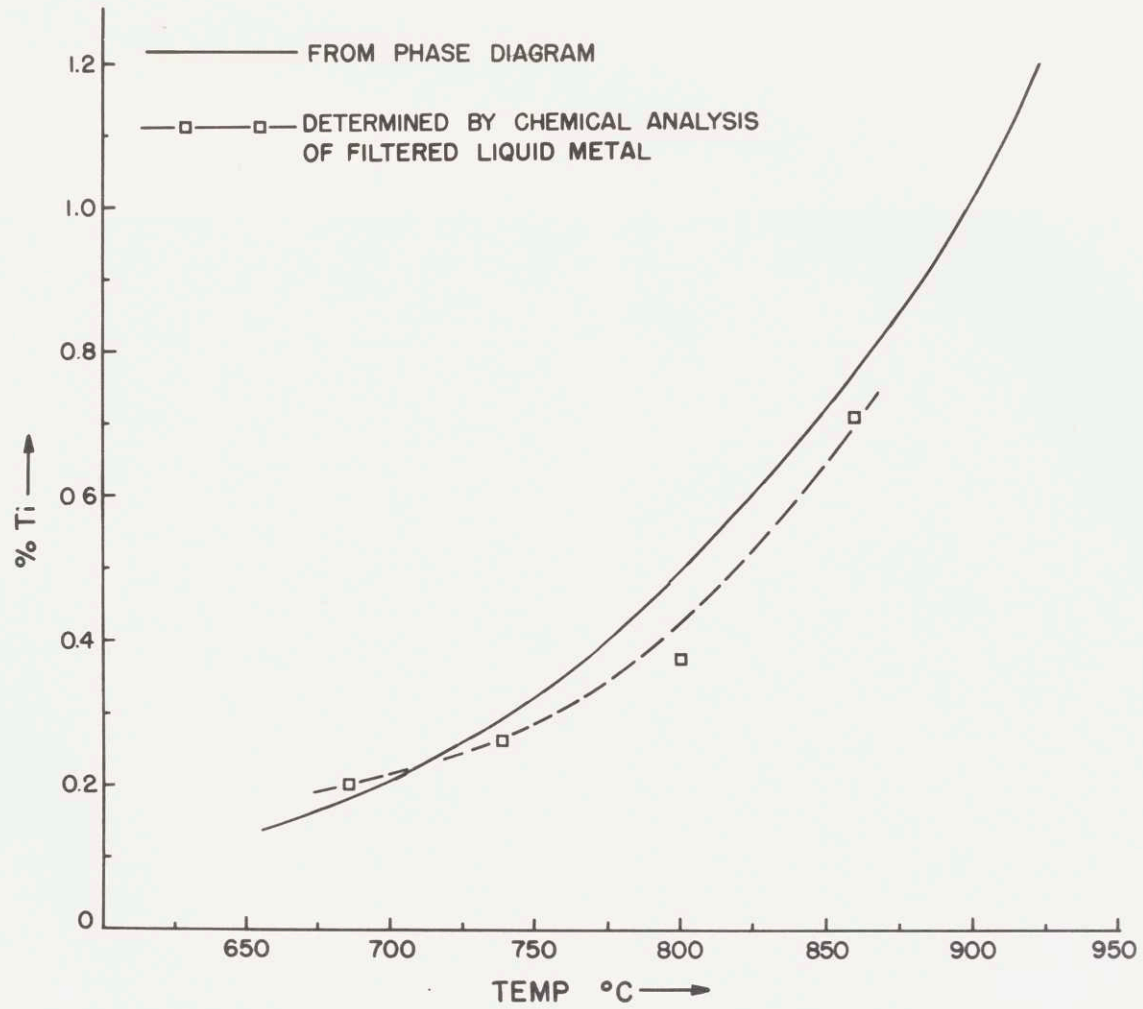
Figure 17: Titanium composition of the filtered liquid, determined by chemical analysis, versus temperature. Solid line represents the liquidus compositions from the phase diagram(61).
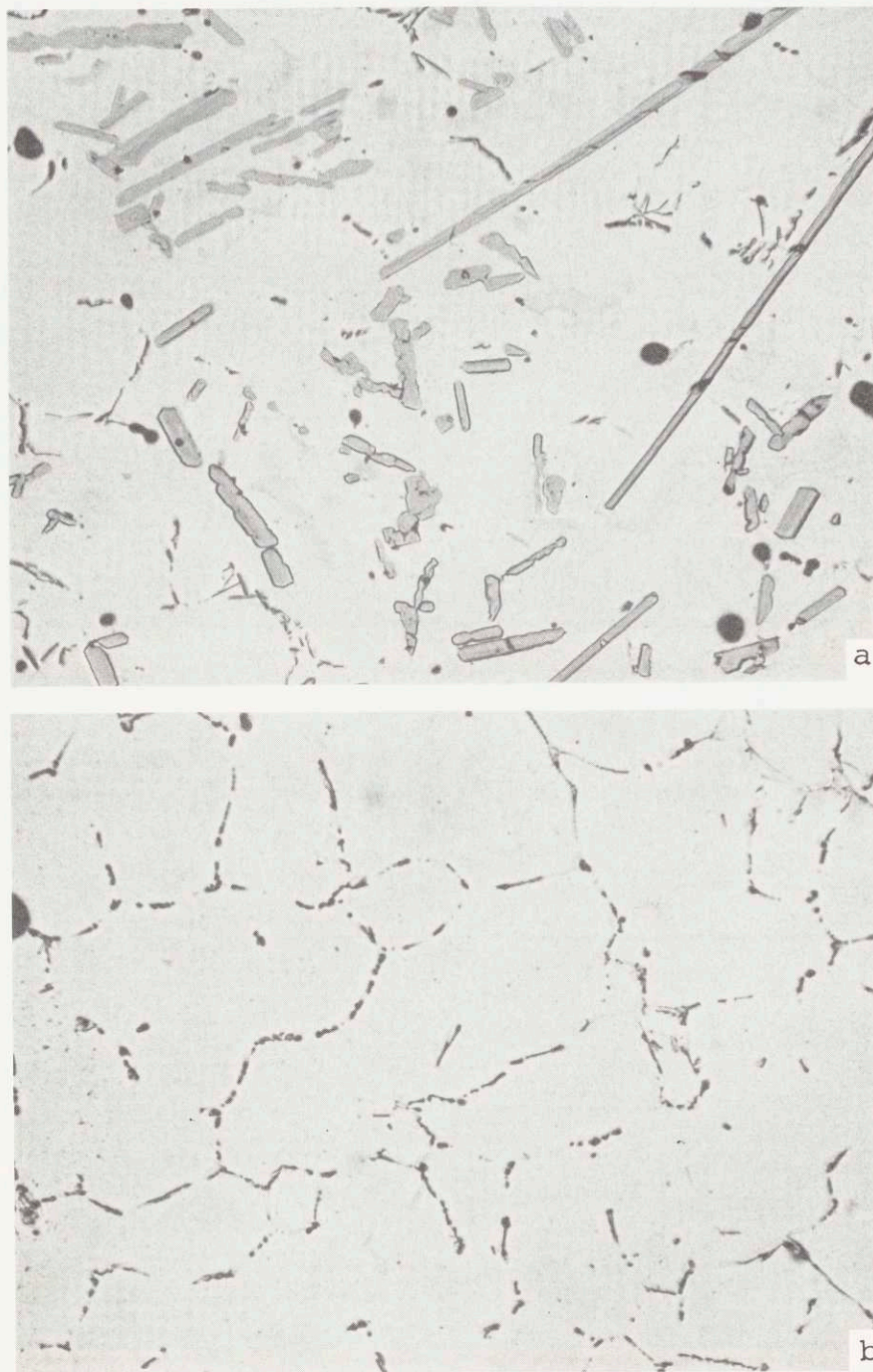
Figure 18: Microstructure of filtered and non-filtered metal
in Run #11A, employing 216μ Al_2O_3 granules
followed by a sintered Al_2O_3 disc filter of 40μ
pore size.
(a) Non-filtered metal above the filter, 150X.
(b) Filtered metal, 150X.
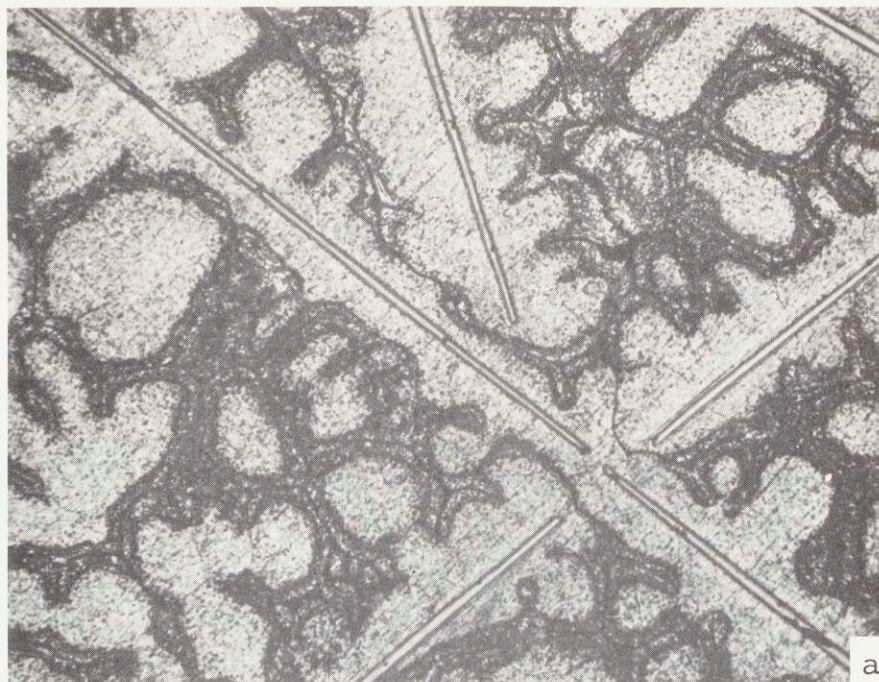
Figure 19: Microstructure of filtered and non-filtered metal in Run #12A, employing 216μ Al_2O_3 granules followed by a sintered Al_2O_3 disc filter of 40μ pore size.
(a) Non-filtered metal, showing the formation of primary dendrites around the $TiAl_3$ plates, 75X.
(b) Filtered metal, 150X.
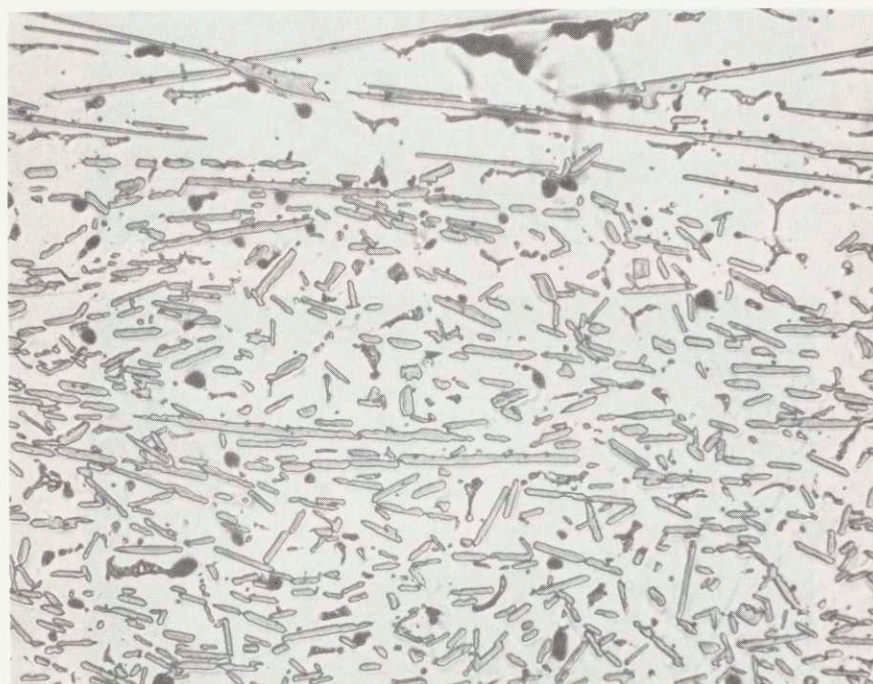
Figure 20:   "Cake" of TiAl₃ particles formed above the filter
bed, Run #13A, 75X.
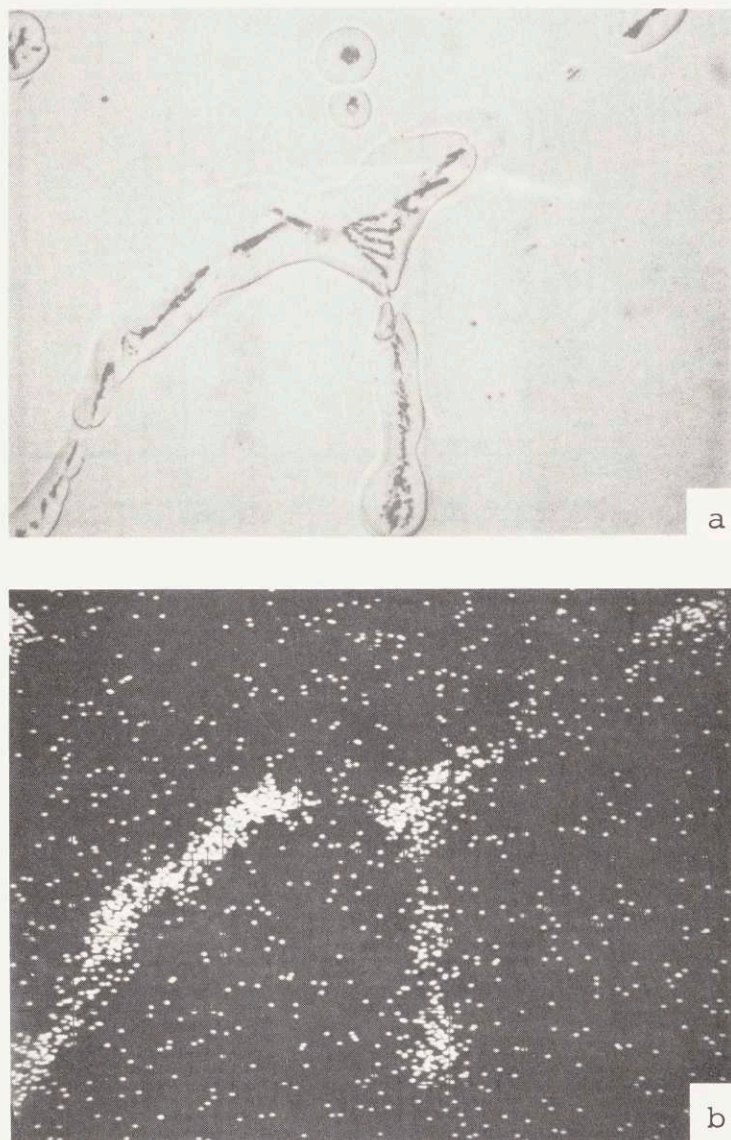
Figure 21:   Intermetallic compound in the filtered 99.5%
              aluminum sample.
              (a) SEM view, 600X.
              (b) Fe X-ray distribution scan of this compound,
                  600X.
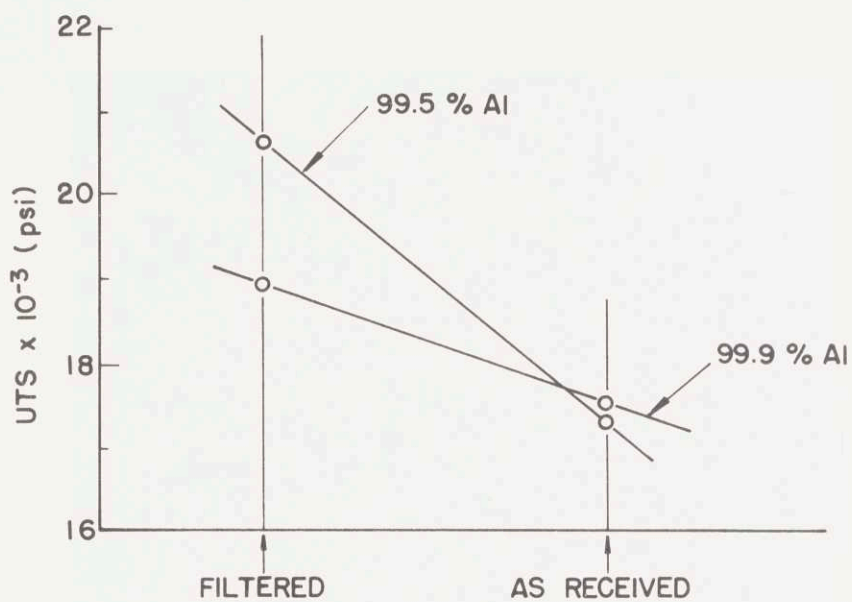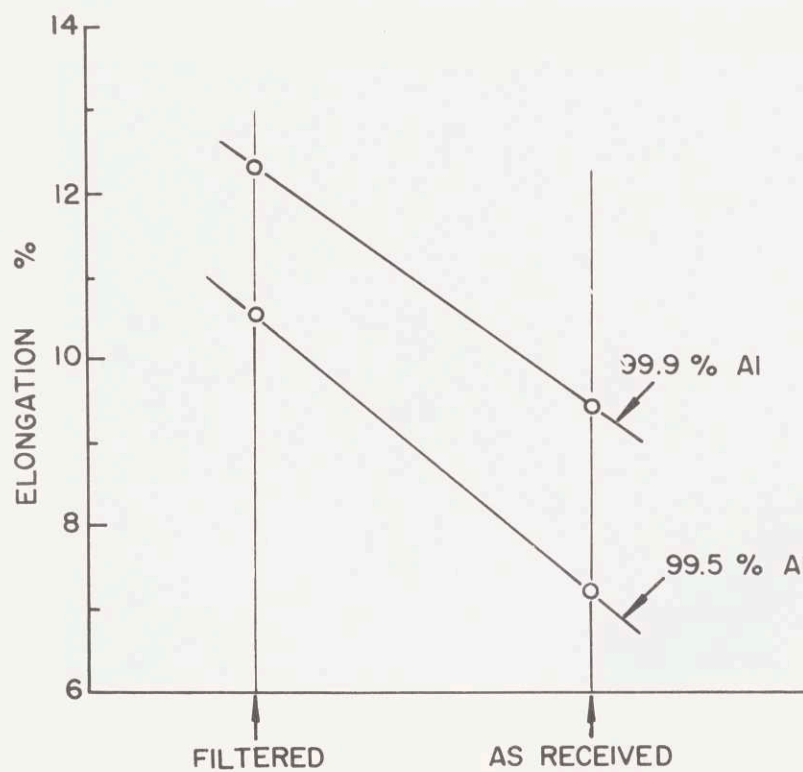
Figure 22: Effect of filtration on the tensile properties of 99.5% and 99.9% Al.
(a) Ultimate tensile strength.
(b) Elongation.
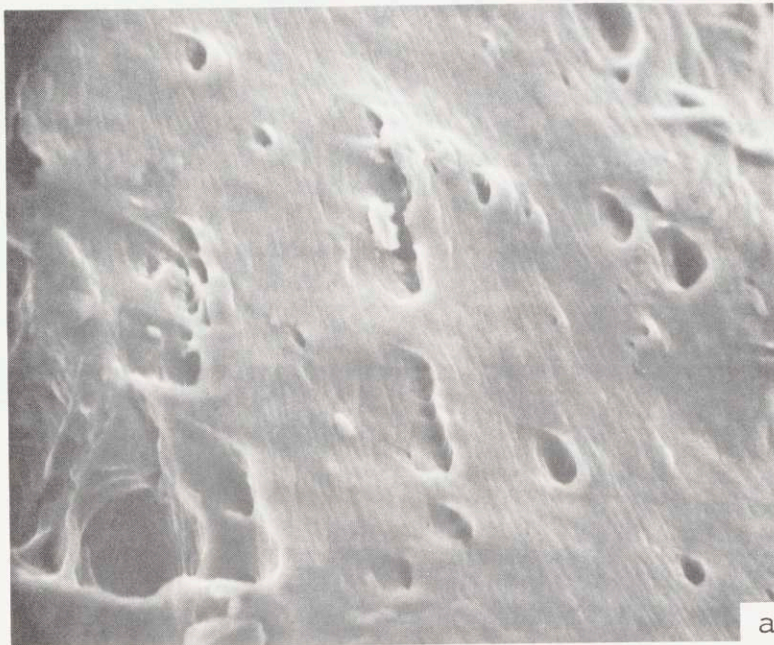
Figure 23:   SEM fractographs of 99.5% aluminum.
             (a) As-received metal, 825X.
             (b) Filtered metal, 1120X.

Figure 24: Microstructure of remelted granular aluminum
before and after filtration, Run #51, Table IV.
(a) Microstructure of metal immediately above
flux coated Al_2O_3 granular bed, 75X.
(b) Microstructure of filtered metal, 80X.
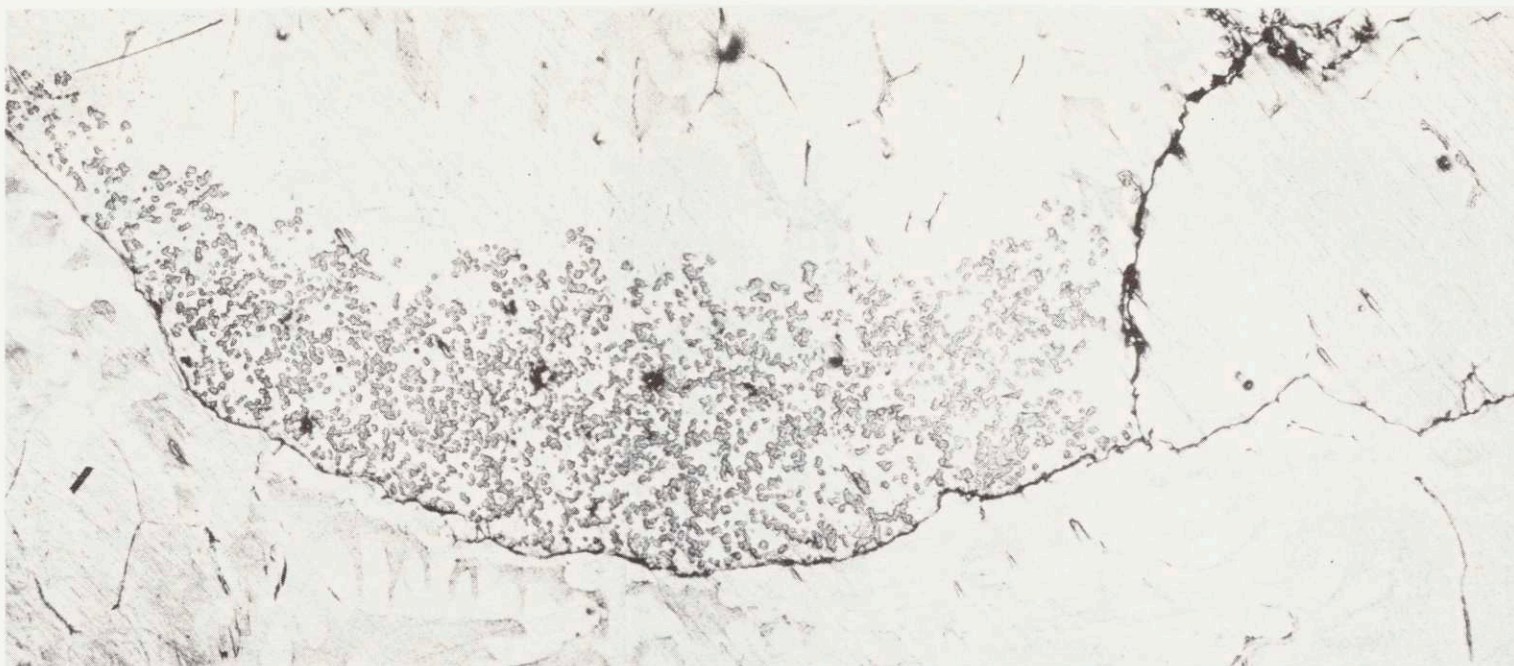
Figure 25: TiAl₃ particles retained by an oxide skin "net" within metal charge of Al-1% Ti alloy, 50X.
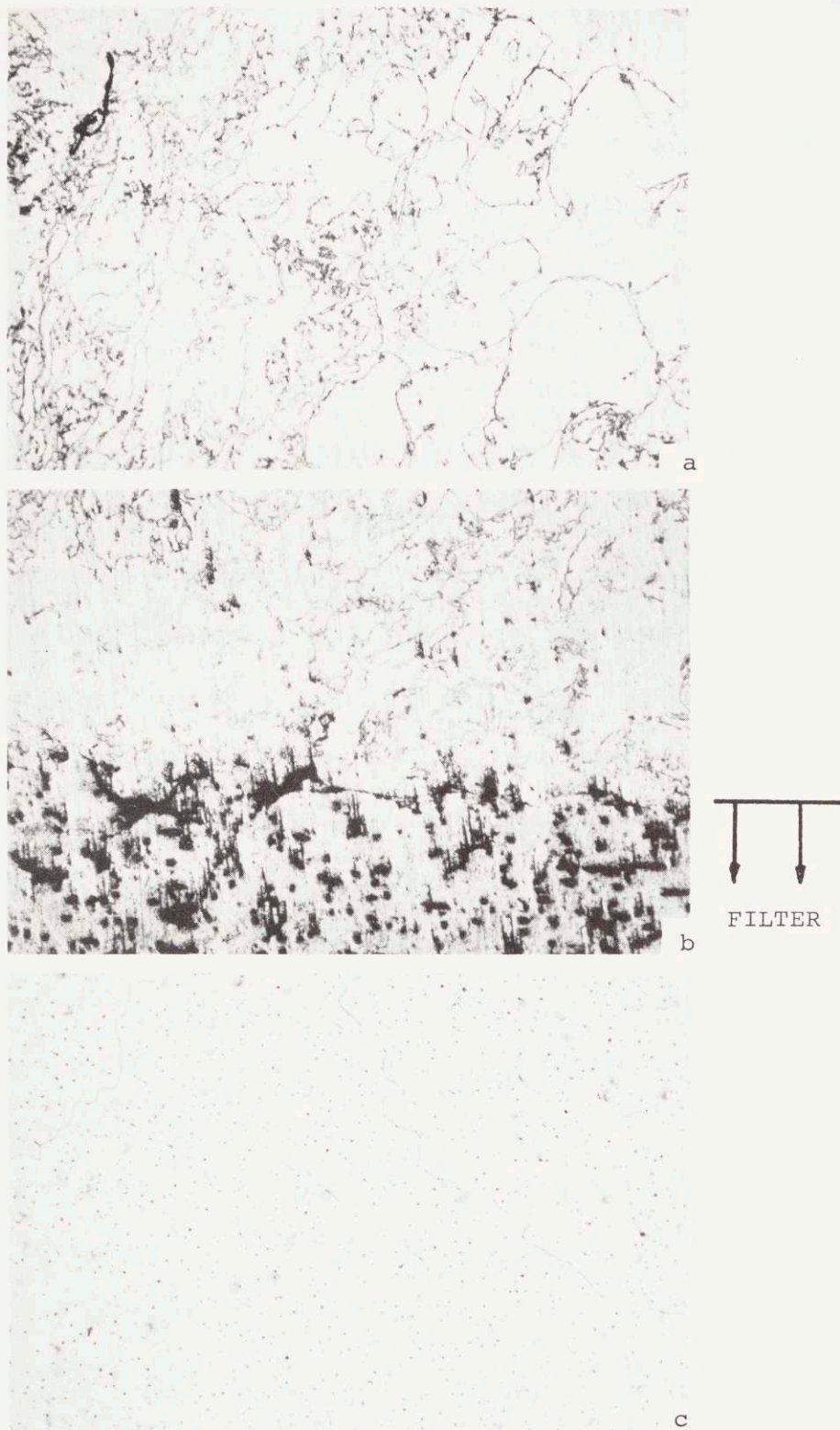
FILTER

Figure 26: Microstructure of remelted granular aluminum
before and after filtration, Run #101, Table IV.
(a) Microstructure of non-filtered metal 2 cm
above filter bed, 50X.
(b) Microstructure of metal immediately above
fibrous carbon felt filter, 50X.
(c) Microstructure of filtered metal, 50X.

C.   Filtration of Al-Ti-B Alloys

In previous experiments, the impurity phases removed, $TiAl_3$ and oxide "skins" were far too large in size. The main objective of this work was to devise a technique to filter out micron size oxide and non-metallic particles from molten aluminum. Therefore, a system had to be chosen in which the particulates to be removed ("synthetic inclusions") were smaller and within a given size range, and where filtration effectiveness could be measured by available techniques.

Several aluminum alloy systems were studied in order to find a suitable system where the precipitated "synthetic inclusions" were fairly uniform in size and smaller than 20μ. Buttons of these alloys were made in an arc melter and their structures studied metallographically. Table VI lists the aluminum systems studied. The Al-Ti-B system was chosen because the platelike TiB_2 precipitates ranged from 2 - 10μ. Figure 27a shows a SEM view of several TiB_2 particles extracted from an Al-5% Ti-1% B* alloy.

In filtration of TiB_2 particles, an understanding of the nature of their precipitation coupled with a knowledge of the liquidus surfaces of the Al-Ti-B phase diagram is necessary. However, the Al-Ti-B ternary phase diagram is not very well established. Phase diagrams for this system

---

*   The extraction work was done by Mr. Peter Sevier of Olin Metals Research Laboratories, New Haven, Conn.

have been published by Mondolfo and Marcontonio(65),
Moriceau(66), and recently by Maxwell and Hellawell(67).

In order to better understand the phase diagram and
the characteristic microstructures of the various phases of
this system, a series of Al-Ti-B alloys of different
compositions were cast and the constituent phases were
established by metallography and electron microprobe analysis.
The alloys were made using Al-5% Ti-1% B and Al-4% B masters,
and KBF_4, K_2TiF_6 salts. Chemical analyses of these alloys
are listed in Table VII. Results of microstructural
investigation correlate well with the phase diagram of Maxwell
and Hellawell(67). This latter phase diagram is assumed to be
correct and will subsequently be used to interpret results of
the filtration experiments.

Figure 28 shows the proposed provisional phase diagram
of Maxwell and Hellawell(67). The TiB_2 liquidus surface rises
very steeply from the aluminum-rich corner. This surface is
closed on the boron rich side by a monovariant reaction such
as: $L \rightleftarrows TiB_2 + AlB_2$, and on the titanium rich side by another,
such as: $L + TiB_2 \rightleftarrows TiAl_3$. These monovarient reactions are
experimentally indistinguishable from the respective binary
liquidus curves(68). For illustration purposes, however, the
difference between the two curves, shown in Figure 28, is
magnified. Thus, on the boron rich side of the $Al-TiB_2$
psuedobinary line, TiB_2 precipitation is followed by AlB_2
while on the other side TiB_2 precipitation is followed by $TiAl_3$.

This Al-TiB$_2$ pseudobinary line is shown as a dotted line in Figure 28.

Figure 27b shows the microstructure of the Al-5% Ti-1% B master alloy, containing the fine TiB$_2$ and coarser TiAl$_3$ precipitates. Figure 29a shows the microstructure of alloy E, Al-0.07% Ti-0.06% B, which lies on the boron rich side of the Al-TiB$_2$ pseudobinary. The two types of precipitates are TiB$_2$ and AlB$_2$. Figure 29b shows the microstructure of alloy J, Al-0.51% Ti-0.11% B, which lies on the titanium rich side of the Al-TiB$_2$ psuedobinary. The TiB$_2$ phase is present at the grain boundaries and was probably pushed there by the growing solidification interface. The TiAl$_3$ phase, however, is present within the grains. Majority of the experiments (Runs #41 to #58) were carried out with this alloy, Table VIII.

Table I lists the filters employed in filtration of the Al-Ti-B alloys. Table VIII summarizes the experimental results. The pressures required (Table VIII) for metal to flow through the filters ranged from 3-60 psi. The titanium and boron compositions of the non-filtered metal above the filter bed increased due to retention of intermetallics precipitated above 750°C. The titanium and boron compositions of the filtered metal decreased to 0.303% Ti and 0.0179% B (averaged values from Runs #41b to #58), Table VIII.

Figure 30 shows a diagramatic representation of the solidification path of alloy J (0.51% Ti - 0.11% B) from above the liquidus (950°C), point L, to the monovariant

reaction line. Only the TiB_2 phase precipitates between points L and M of Figure 30. For alloy J, point M, where the $TiAl_3$ phase begins to precipitate, is at Al~0.30% Ti~0.01% B and 750^OC. Theoretically then, if an Al-.51% Ti-.11% B alloy is successfully filtered at 750^OC, the TiB_2 phase is retained above the filter and the composition of the remaining liquid is that of point M. Excellent agreement exists between the compositions of the filtered metal determined by chemical analyses and the composition of point M determined from the phase diagram.

Figure 31 shows the microstructure of non-filtered and filtered metal from Run #35, where a sintered Al_2O_3 disc filter (87-100μ) was used. The non-filtered metal contains a large concentration of TiB_2 and $TiAl_3$ particles. Figures 32a, 32b and 32c show microstructures of the metal above the cake, in the cake, and the filtered metal from Run #42b (36-40μ Al_2O_3 disc filter), respectively. The randomly distributed particles in Figure 32c are $TiAl_3$ particles precipitated out during solidification of the filtered metal. The dark spots in this microstructure are voids and electropolishing pits. Thus, the TiB_2 particles precipitated above 750^OC were successfully filtered out. The $TiAl_3$ particles shown in Figure 32b have precipitated from the segregated liquid remaining above the filter.

In Run #58, the filtration temperature was decreased to 685^OC. Figures 33a and 33b show microstructures of the

cake formed above the filter and the filtered metal, respectively. As expected, more $TiAl_3$ particles were retained above the filter in this run, due to the lower filtration temperature, as opposed to Run #42 above. Few, if any $TiAl_3$ particles were found in the filtered metal, again due to the lower filtration temperature.

The filtered and non-filtered metals, and the initial charge material of Run #53, where a sintered stainless steel disc filter (Table I) was employed, were chemically analyzed for iron content. The stainless steel filter "contaminated" the melt, and caused a marked increase in the iron content of the filtered metal, Table VIII.

The porous carbon plug used in Run #47 did not contaminate the melt, as indicated by the chemical analyses results of the filtered, non-filtered, and initial charge metal, Table VIII.

Microstructural examination of the non-filtered metal samples above the filter bed revealed formation of cakes of accumulated TiB_2 particles. It was experimentally determined that (at $750^{\circ}C$) the cake thickness increased for increasing holding times of up to 15 minutes. No difference in cake thickness was observed for holding times of 15, 60 and 120 minutes.

TiB_2 particles were retained in the cake above the filter and within the filter itself. Retention sites within filters have previously been characterized(69). These are:

(i) surface sites, schematically shown in Figure 34a, (ii)
crevice sites, Figure 34b, (iii) constriction sites, Figure
34c, and (iv) cavern sites, Figure 34d. Similar retention
sites were observed in the infiltrated filters employed in
this work. Figures 35a and 35b show TiB_2 particles retained
on surface sites. The filter beds shown here are from Runs
#47 (porous carbon plug, 120μ pores) and #56 (sintered quartz
90-150μ pores), respectively. Figure 35c shows TiB_2 particles
retained in a constriction site; the particles cannot
penetrate into a pore of a smaller size than their own. The
filter bed shown here is from Run #57 (sintered quartz,
90-150μ pores). Figure 35d shows TiB_2 particles retained in a
cavern site. These particles are sheltered within a pocket
formed by several grains. The filter bed shown here is from
Run #41b (sintered Al_2O_3, 87-100μ pores).

Figure 36 shows microstructures of the non-filtered and
filtered metal, and the infiltrated filter from Run #44b
(carbon felt of high density, 8 lbs^2/yds). Figure 36a shows
the microstructure of the non-filtered metal above the bed.
TiB_2 particles have again been pushed to the grain boundaries.
Figure 36b and 36c show the infiltrated filter bed at the
entry and exit ports, respectively. Immediately below the
cake, TiB_2 particles are retained on surface sites of the
carbon fibres, Figure 36b. No TiB_2 particles were observed
at the exit port of the filter bed, Figure 36c. Thus, bulk

filtration occurs at the initial stages of metal travel through the bed. Figure 36d shows a representative micro-structure of the filtered metal, where $TiAl_3$ particles have precipitated out during solidification of the filtered melt.

The filtered and non-filtered metals from Runs #41b and #42d were remelted and resolidified in a centrifuge. This technique provided additional qualitative evidence substantiating quantitative data obtained by chemical analyses. Figures 37a and 37b show the $TiAl_3$ and TiB_2 precipitates concentrated at the bottom of the centrifuged sample of the non-filtered metals from Runs #41b and #42d, respectively. The TiB_2 content of the centrifuged filtered sample from Run #41b, Figure 38a, is substantially higher than the sample from Run #42d, Figure 38b. The chemically analyzed boron contents of the two samples were 0.022 and 0.01, respectively, Table VIII. Since both experiments were carried out at the same temperature, the discrepancy between the boron contents must be due to the effectiveness of the filters employed. More of the TiB_2 particles penetrated through the 87-100μ size pores of the filter in Run #41b, Table VIII.

A careful examination of data presented in Tables I and VIII on filters employed, pressures of filtration required, and chemical analyses results of boron content permits the following observations:

(i) Al_2O_3 1" disc filters of 36-40µ pore size were
more effective than the same filters of 87-100µ
pore size. Boron contents of Runs #42b and 42d
were 0.01% for the 36-40µ pore size filter, as
opposed to 0.022% for the 87-100µ pore size filter
of Run #41b. Required pressures for filtration
were slightly higher for the finer pore size
filters (i.e. 40-50 psi as opposed to 30 psi).

(ii)   The use of a granular material above the 36-40µ
pore size Al_2O_3 disc filter can be effective
depending on the size of granules employed. Large
granules, 400µ in diameter, did not increase
filtration effectiveness, Run #48. On the other
hand, granules of 200µ and 106-148µ above the
same filter reduced the level of boron content to
0.006%, Runs #49 and #50. The corresponding
required pressures, due to the addition of the
granular beds, increased by 10 psi.

(iii)   A nine layer fiberglass cloth filter (J. P. Stevens -
style #1339, 420 holes/in^2 and 0.00072 in^2/hole)
and a 2" thick woven carbon felt (density 8 lb/yd^2)
were almost as effective as the 36-40µ pore size
Al_2O_3 disc filters, Runs #46, #44b, respectively.

(iv)   The sintered stainless steel disc filter of Run
#53 was deleterious since it increased the iron
content of the melt. The sintered quartz disc

filters of Run #57 was as effective as the coarse Al_2O_3 disc filter of Run #41b.

In summary then, TiB_2 particles of 2-10μ size range were successfully filtered from an Al-0.5% Ti-0.11% B alloy. The various filter media employed were: sintered rigid disc filters of quartz and Al_2O_3 with and without additional granular beds, and others, Table I. The pressure required for metal flow through these filters was measured and granules of Al_2O_3 required the highest pressures, 60 psi, and a sintered stainless steel filter the lowest, 3 psi. Filtration effectiveness was determined by chemical analyses of titanium and boron contents of the non-filtered and filtered metals, Table VIII, and by examination of samples solidified in a centrifuge. The chemically analyzed compositions (Ti and B) of the filtered metals agreed with the Al-Ti-B provisional phase diagram proposed by Maxwell and Hellawell(67). A combination filter made of a sintered Al_2O_3 disc, 1/4" thick, with 36-40μ size pores, preceded by a 1.5" high granular bed of Al_2O_3 (less than 200μ in diameter) was the most effective media used.

Table VI

Aluminum Systems Investigated
for "Small Synthetic Inclusions"

composition	precipitated phase
Al-30% Si	Al-Si
Al-2.0% Cr	$CrAl_7$
Al-10% Fe	$FeAl_3$
Al-15% Ni	$NiAl_3$
Al-10% Mn	Al_6Mn
Al-12% Ca	$CaAl_4$
Al-20% Co	Co_2Al_9
Al-20% Zr	$ZrAl_3$
Al-6% Sb	AlSb
Al-5% Ti-1% B	TiB_2 $TiAl_3$

Table VII

Al-Ti-B Alloys

alloy	alloying charge*	composition determined** by chemical analysis
A	Al-5Ti-1B master	Al-0.1130Ti-0.011B
B	KBF_4 and K_2TiF_6 salts	Al-0.044Ti-0.023B
C	Al-3% B master	Al-0.018B
D	KBF_4 and K_2TiF_6 salts	Al-0.05Ti-0.03B
E	Al-5Ti-1B and Al-3% B master	Al-0.07Ti-0.06B
F	KBF_4 and K_2TiF_6 salts	Al-0.28Ti-0.20B
G	Al-5Ti-1B master	Al-0.082Ti-0.027B
H	Al-5Ti-1B master	Al-0.44Ti-0.15B
I	Al-5Ti-1B master	Al-1.4Ti-0.41B
J	Al-5Ti-1B master	Al-0.51Ti-0.11B
K	KBF_4 and K_2TiF_6 salts	Al-0.11Ti-0.03B

---

* Master alloys and salts were supplied by Kawecki-Berylco Co., Inc.

** Chemical analyses were done at the Kawecki-Berylco Company's laboratories, Boyertown, Pennsylvania.

Table VIII

Procedure and Experimental Results of Al-Ti-B Alloys

Run no.	C_O-Ti	C_O-B	T_M	T_F	Δt	P_F	C_{NF}-Ti	C_{NF}-B	C_F-Ti	C_F-B	Charge
35	5.0	1.0	980	725	10	30	6.3	1.3	0.3	0.1	Al-5Ti-1B master
29	0.113	0.011	980	735	10	-	0.12	0.025	0.06	0.006	Alloy A
41a	0.11	0.	950	750	15	30	0.165	0.065	0.0083	0.0038	Alloy K
41b	0.51	0.11	950	750	15	30	0.816	0.162	0.318	0.022	Alloy J
42b	0.54	0.13	950	750	15	40-50	1.34	0.34	0.264	0.01	Alloy J
42d	0.54	0.13	950	750	15	40-50	1.56	0.30	0.24	0.01	Alloy J
44a	0.51	0.11	950	750	15	5-10	0.78	0.19	0.30	0.020	Alloy J
44b	0.54	0.13	950	750	15	20-30	0.64	0.17	0.31	0.013	Alloy J
46	0.51	0.11	950	750	15	5-10	0.86	0.22	0.32	0.011	Alloy J
47	0.54	0.11	950	750	15	40	0.69	0.14	0.34	0.028	Alloy J
47	C content = 0.009						C content = 0.010		C content = 0.010		
48	0.51	0.11	950	750	15	50-60	0.71	0.18	0.30	0.010	Alloy J
49	0.51	0.11	950	750	15	50-60	0.78	0.23	0.29	0.0057	Alloy J
49	0.51	0.11					1.45	0.46	0.29	0.0057	(Second analysis)
50	0.54	0.13	950	750	15	50-60	0.64	0.156	0.29	0.006	Alloy J
53	0.54	0.13	950	750	15	3-5	0.63	0.094	0.364	0.037	Alloy J
53	Fe content = 0.031						Fe content = 0.2		Fe content = 0.41		
54	0.54	0.13	950	750	15	45	0.77	0.24	0.29	0.01	Alloy J
56	0.54	0.13	950	750	15	5	0.48	0.06	0.37	0.04	Alloy J
57	0.54	0.13	950	750	15	8	0.63	0.140	0.31	0.023	Alloy J
58	0.54	0.13	950	685	15	30	0.530	0.093	0.24	0.01	Alloy J

Terminology:

C_O-Ti, C_O-B: titanium and boron compositions of initial charge alloy, respectively, weight percent.

T_M: temperature to which melt was superheated to, degrees centigrade.

T_F: temperature at which filtered, degrees centigrade.

Δt: holding time at T_F, minutes.

P_F: pressure required for metal to flow through particular filter, psi.

C_{NF}-Ti, C_{NF}-B: titanium and boron compositions of non-filtered metal above filter, respectively, weight percent

C_F-Ti, C_F-B: titanium and boron compositions of filtered metal, weight percent, respectively.
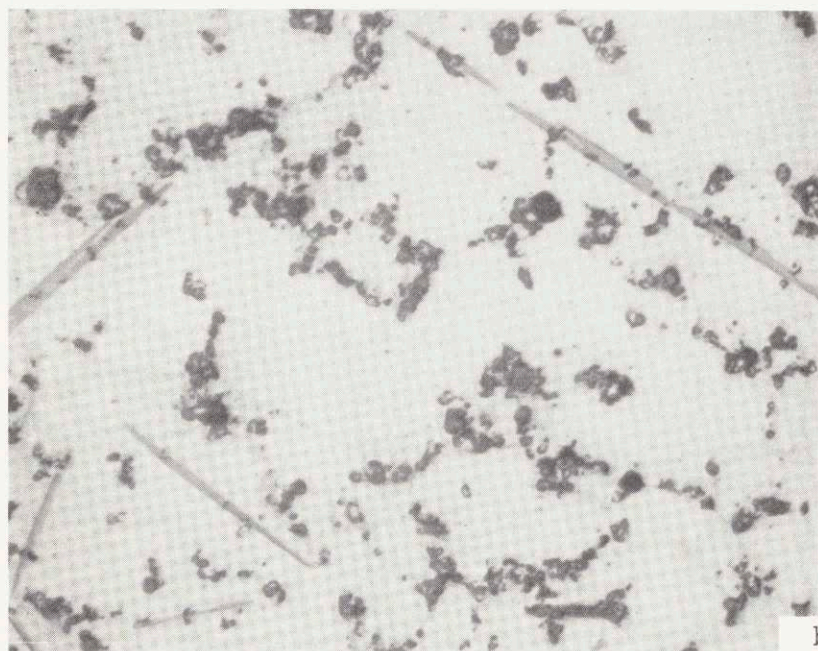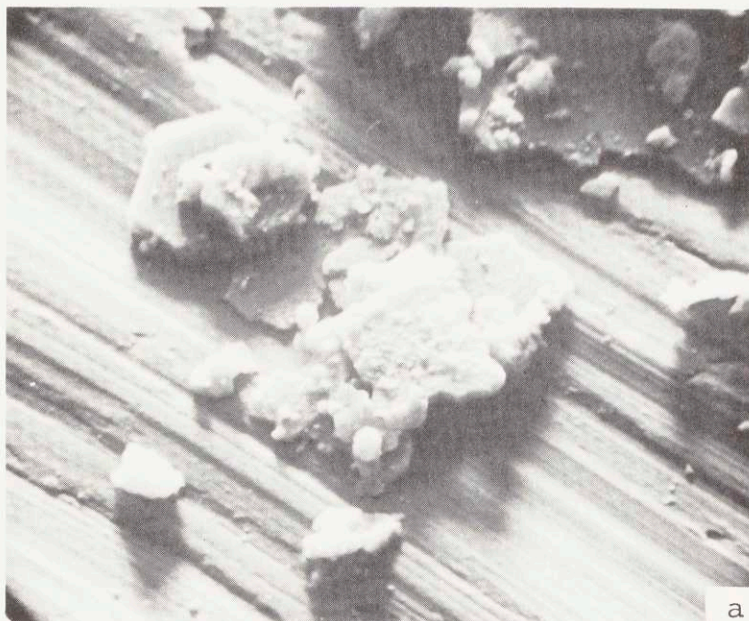
Figure 27: (a) SEM view of TiB$_2$ particles extracted from an
            Al-5% Ti-1% B alloy, 2490X.
            (b) Photomicrograph of Al-5% Ti-1% B showing
            TiB$_2$ and TiAl$_3$ particles.
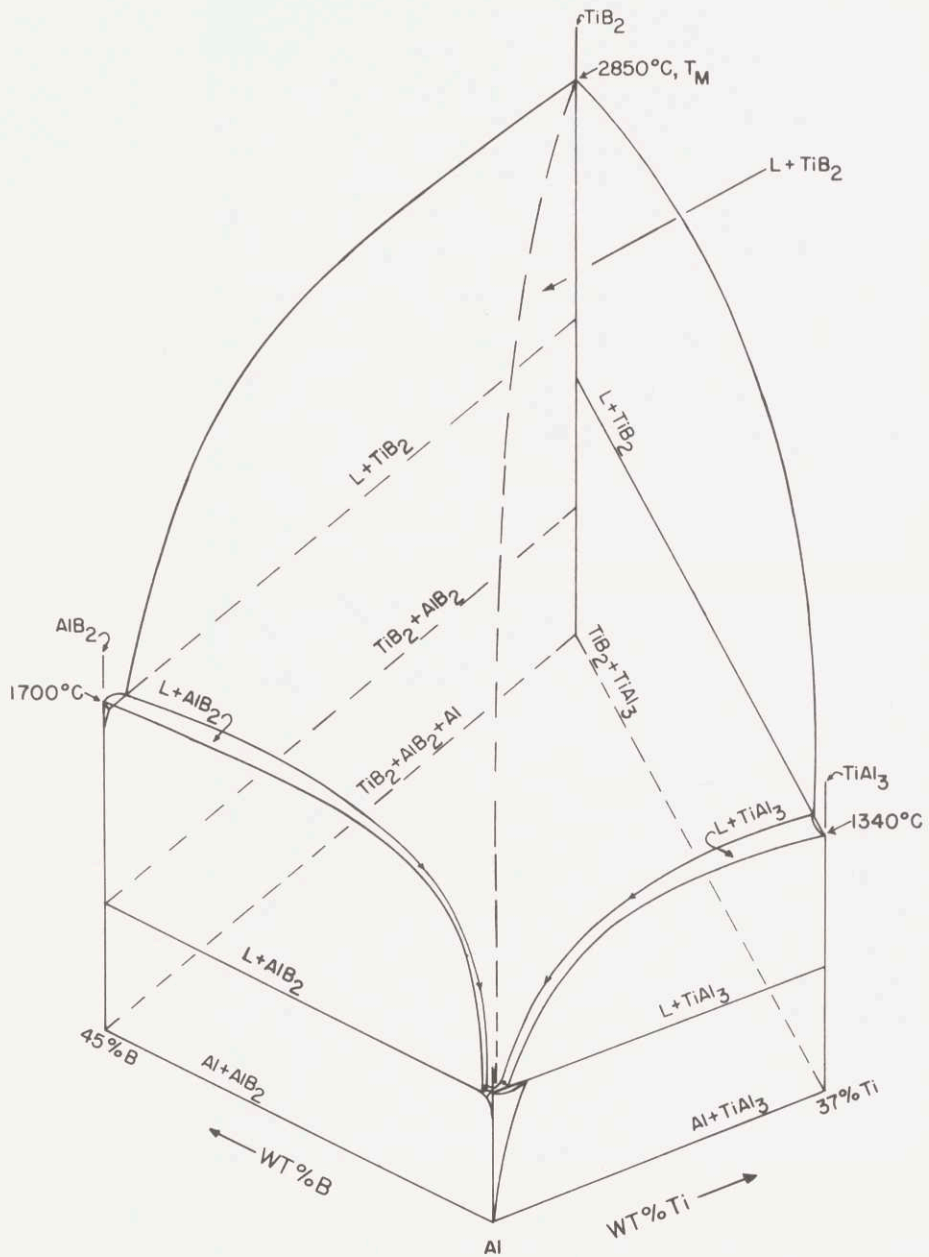
Figure 28: Al rich corner of Al-Ti-B ternary phase diagram(67).
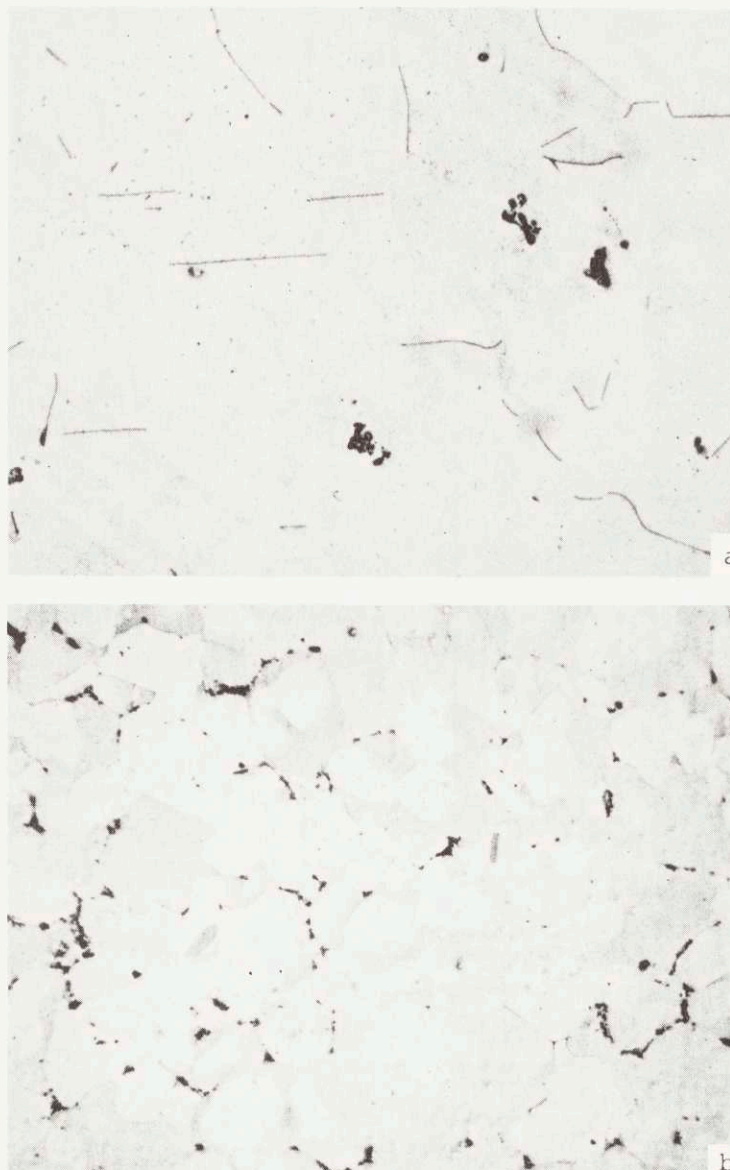
Figure 29: Microstructure of Al-Ti-B alloys prepared:
        (a) Alloy E, Al-0.07% Ti-0.06% B, on the boron
            rich side of the Al-TiB$_2$ pseudobinary, 200X.
            TiB$_2$ particles with AlB$_2$ needlelike
            precipitates can be noted.
        (b) Alloy J, Al-0.51% Ti-0.11% B, on the titanium
            rich side of the Al-TiB$_2$ pseudobinary, 90X.
            TiB$_2$ particles with TiAl$_3$ platelike
            precipitates can be noted.
        This is the microstructure of the initial charge
        used in a majority of experiments.
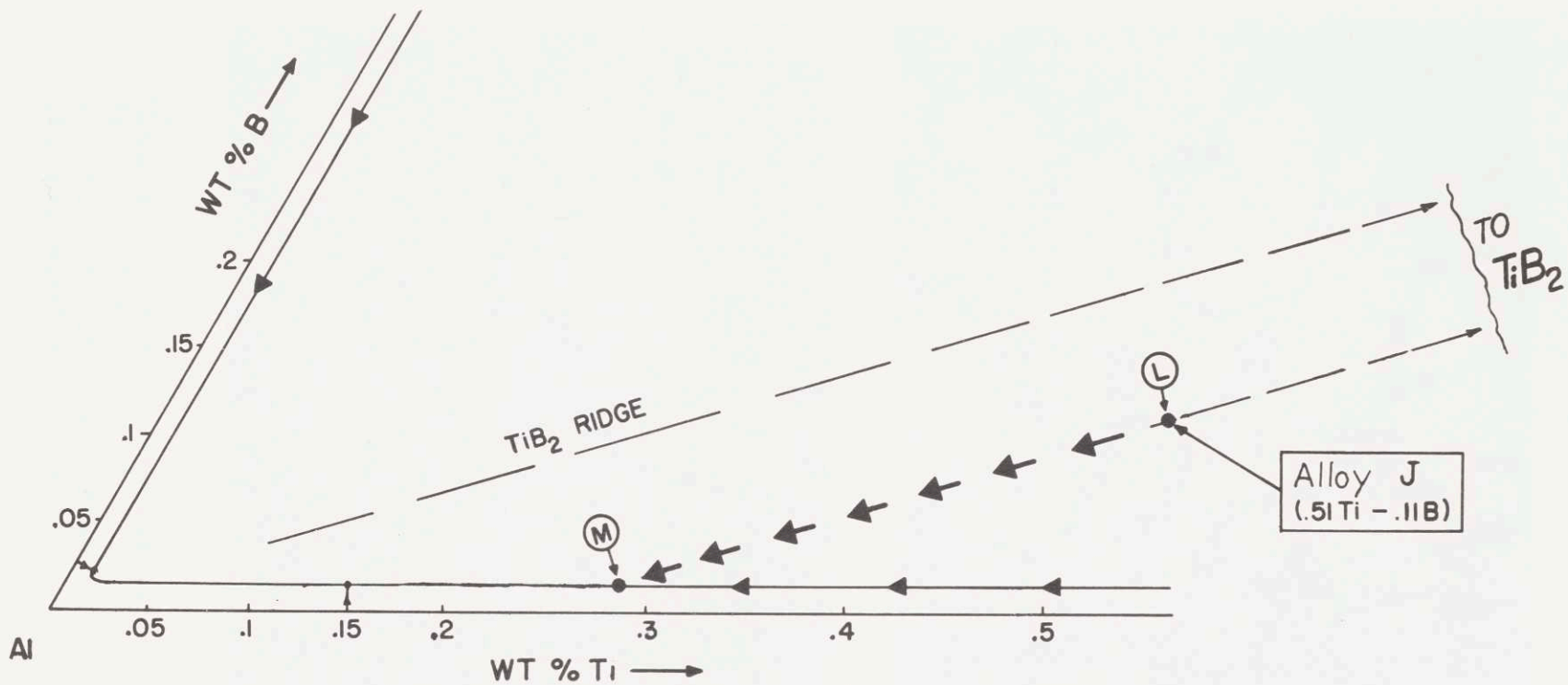
Figure 30: Diagramatic representation of the solidification path of alloy J
(0.51% Ti-0.11% B) from above the liquidus (950°C) to the
monovariant line (750°C)(67).
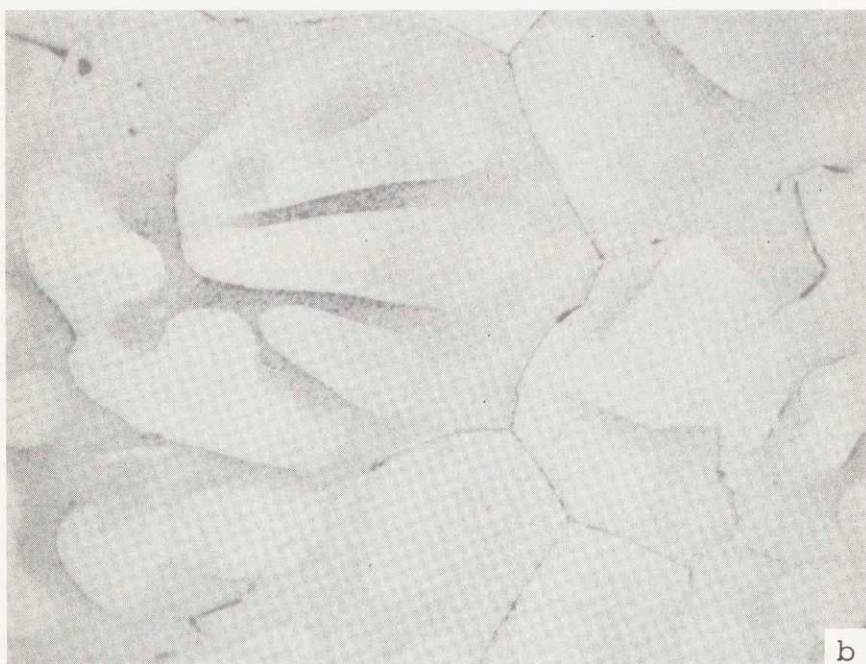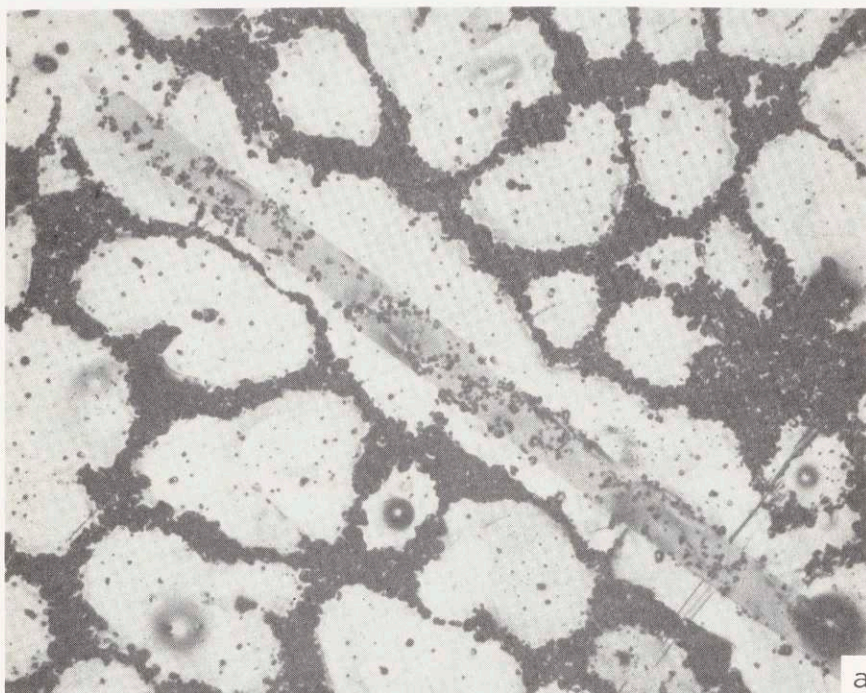
Figure 31:   Microstructure of non-filtered and filtered metal
             from Run #35.
             (a) Non-filtered metal above the filter, 500X.
             (b) Filtered metal, 200X.

131
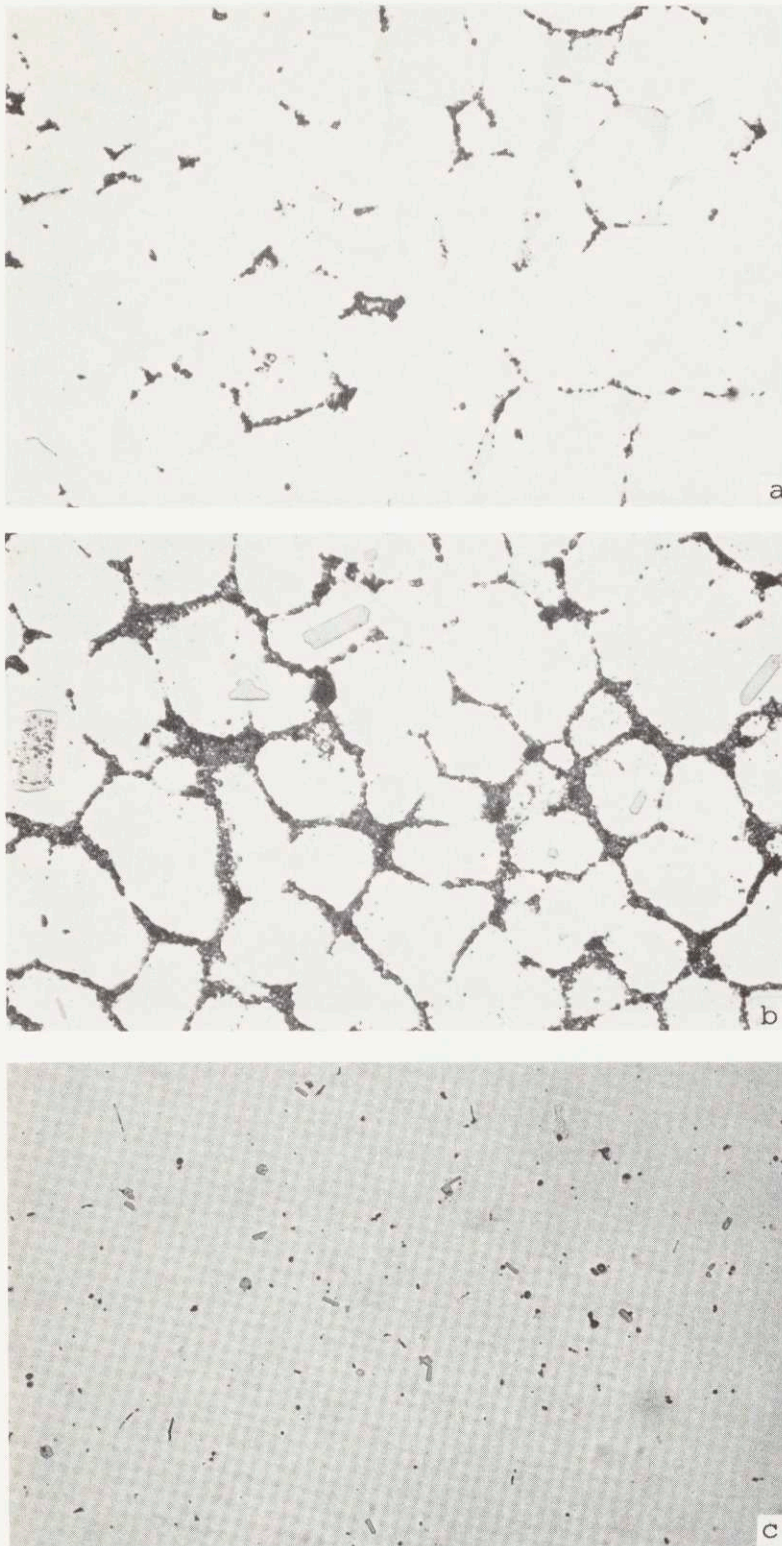
Figure 32: Microstructure of metal from Run #42b.
(a) Metal above cake, 100X.
(b) Cake of TiB_2 particles formed above filter, 100X.
(c) Filtered metal, 100X.
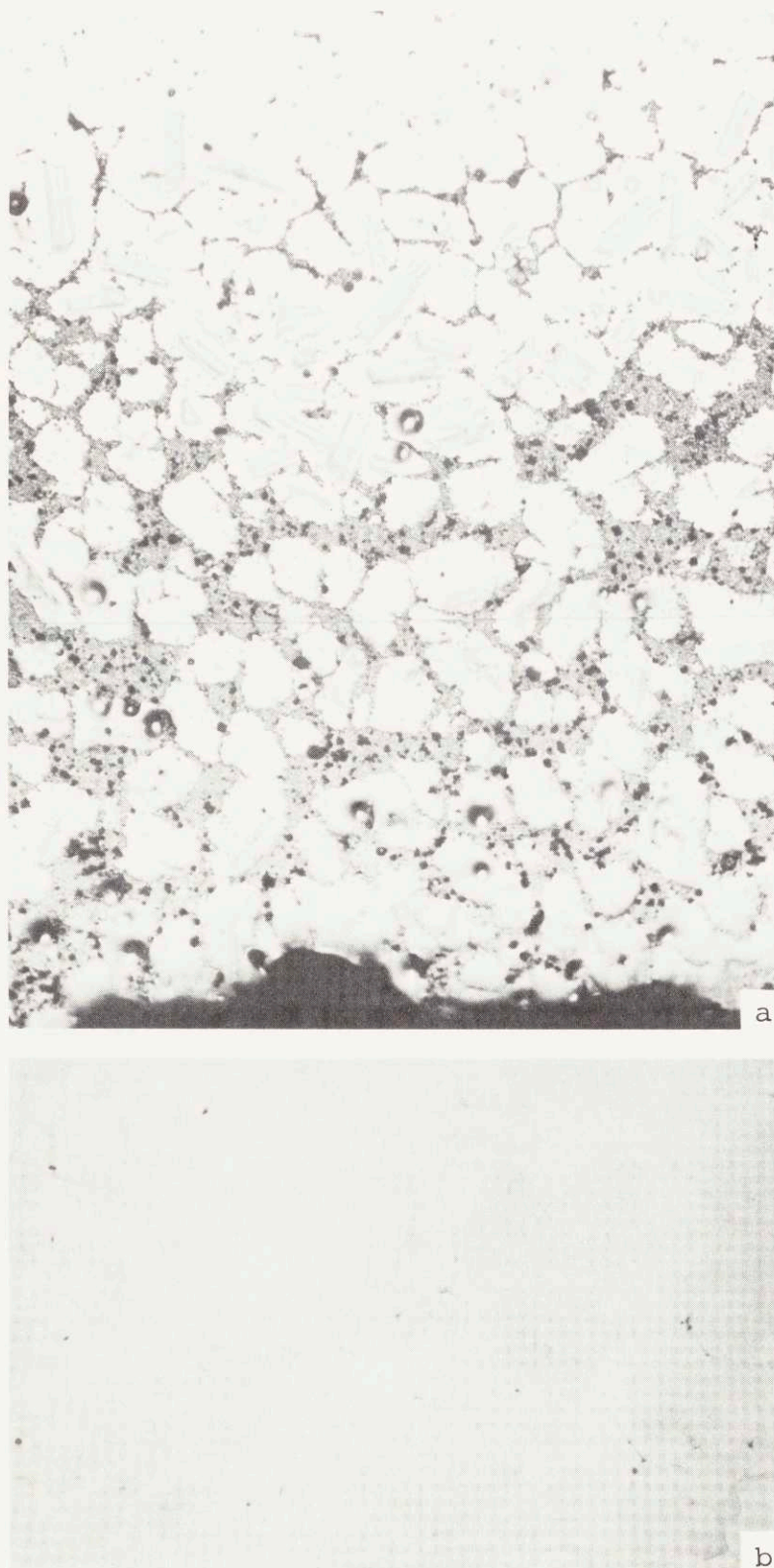
Figure 33: (a) Microstructure of cake formed above bed,
Run #58. TiAl$_3$ particles have settled above
the accumulated TiB$_2$ particles, 75X.
(b) Microstructure of filtered metal, Run #58, 75X.
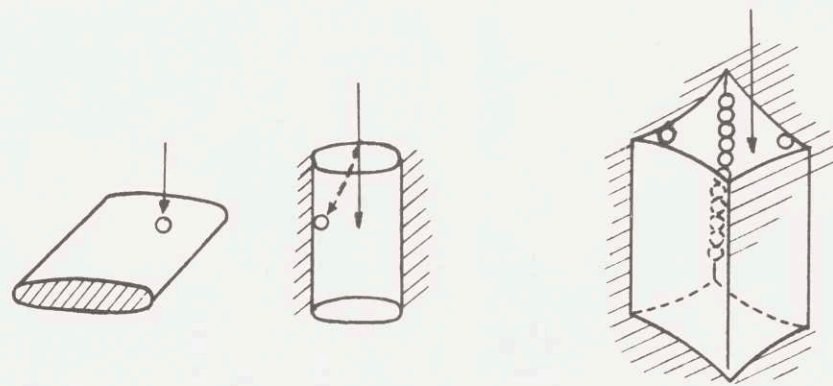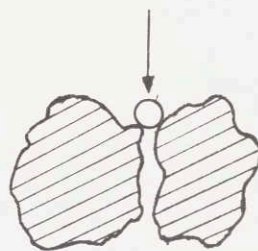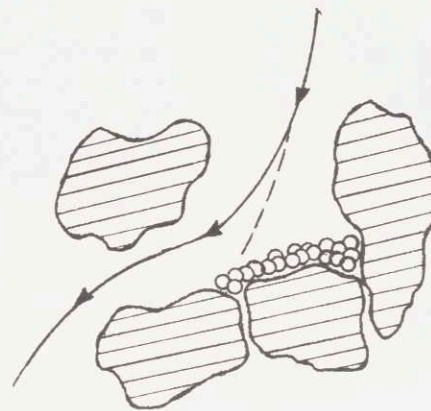
Figure 34: Retention sites (69).

       (a) surface sites, (b) crevice sites

       (c) constriction sites, (d) cavern sites
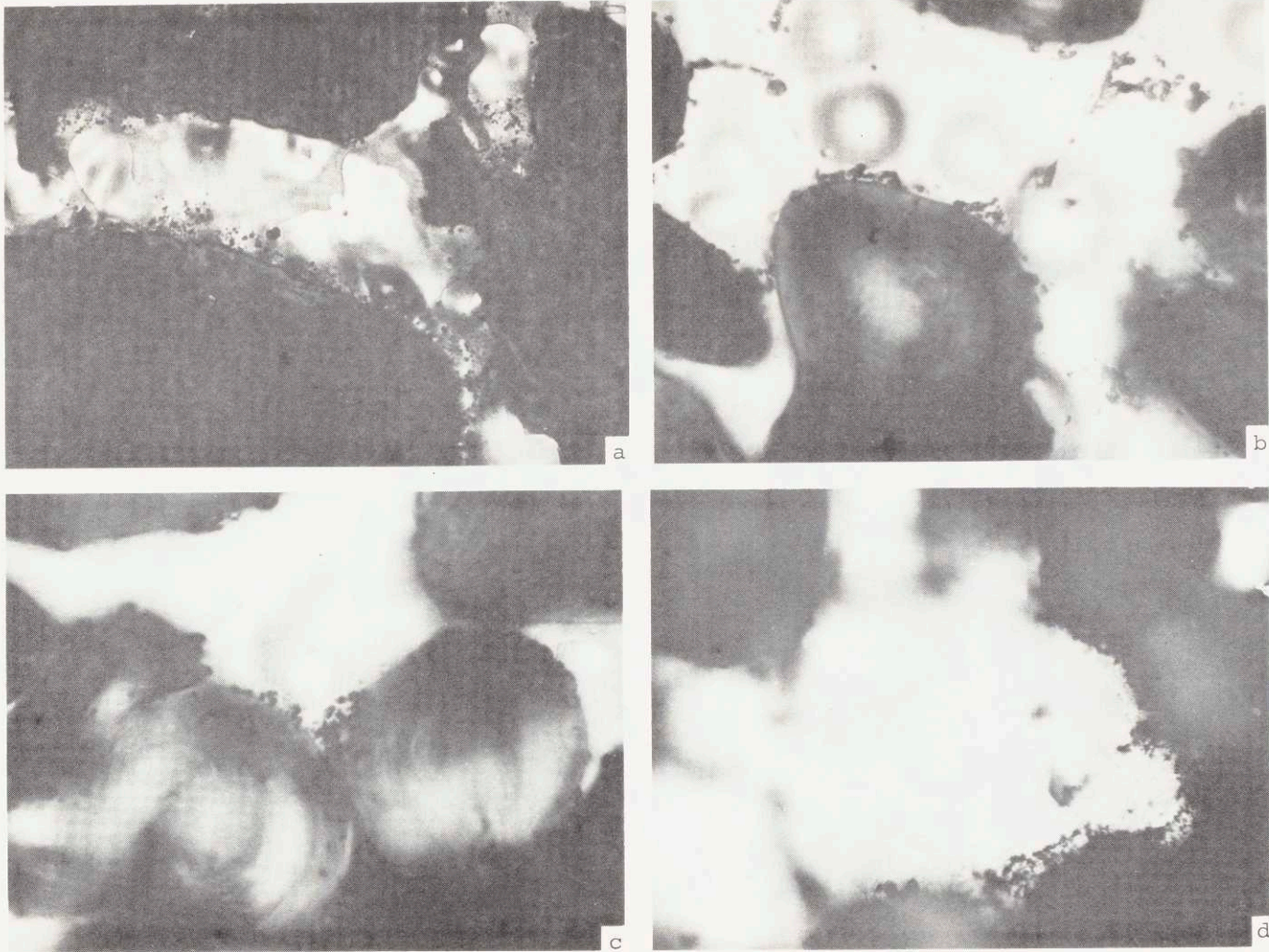
Figure 35:   Retention sites observed in sintered disc filters.
(a) and (b): TiB_2 particles retained on surface sites, Runs
#47 and #56, 200X and 500X, respectively.
(c) TiB_2 particles retained in a constriction site, Run #57, 500X.
(d) TiB_2 particles retained in a cavern site, Run #41b, 500X.

Figure 36: Microstructure of metal from Run #44b.
            (a) Metal above cake, 200X.
            (b) Entry port of filter, 200X.
            (c) Exit port of filter, 200X.
            (d) Filtered metal, 200X.
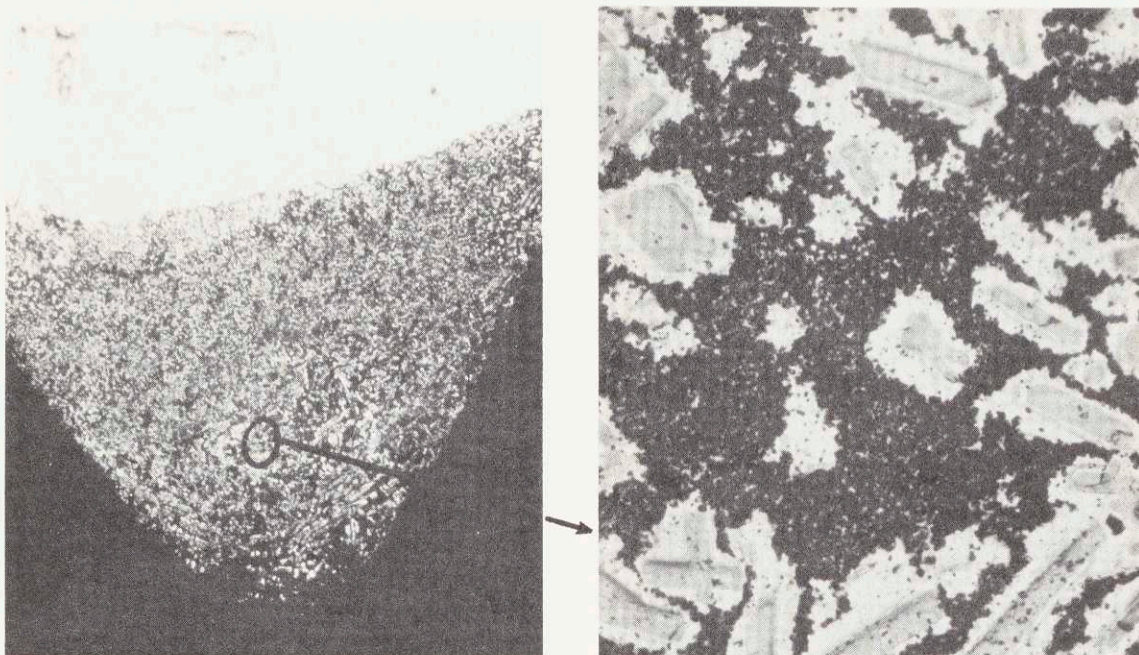
(a)
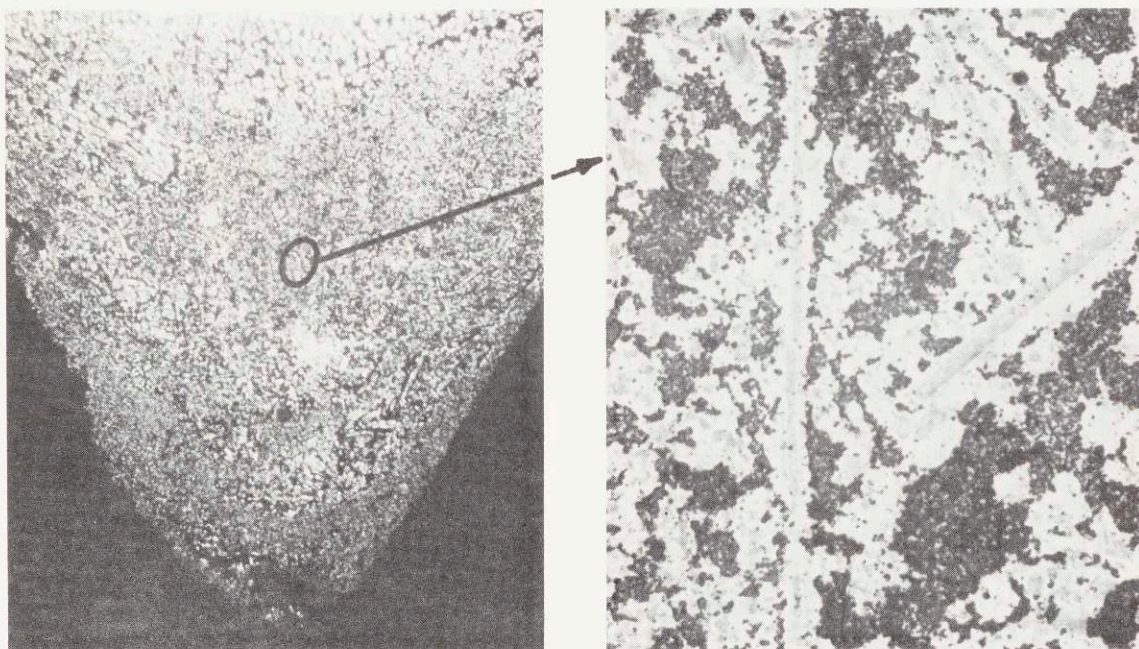
.- (b)

Figure 37:   Microstructure of centrifuged non-filtered metals
             from Runs #41b and #42d.
             (a) Bottom of centrifuged sample of non-filtered
                 metal, Run #41b, 12.5X and 200X, respectively.
             (b) Bottom of centrifuged sample of non-filtered
                 metal, Run #42d, 12.5X and 200X, respectively.
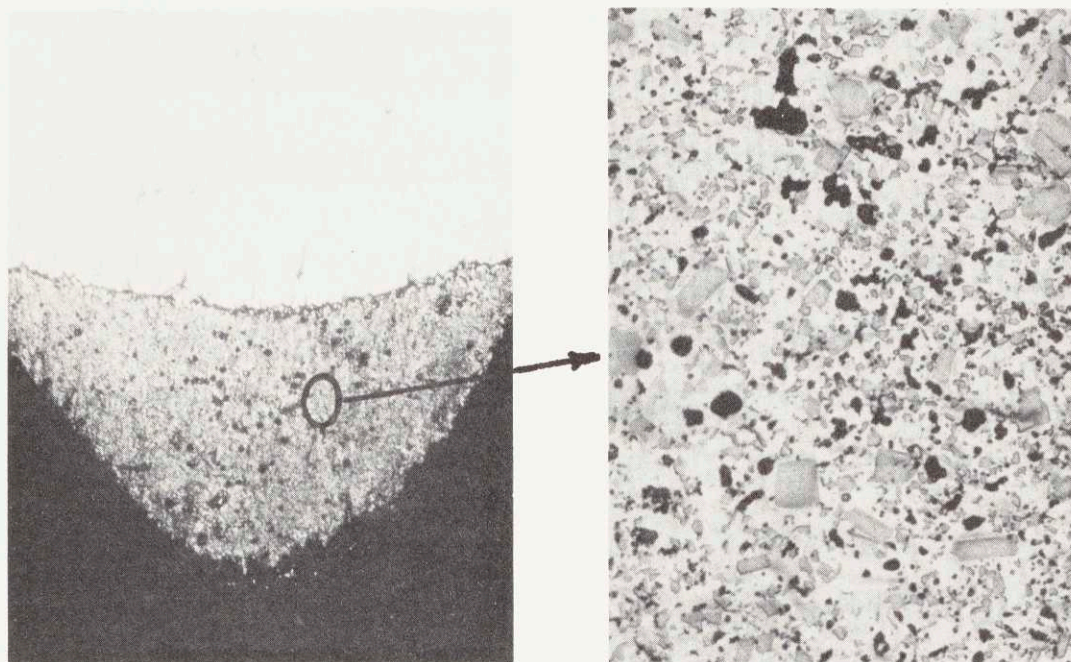
(a)
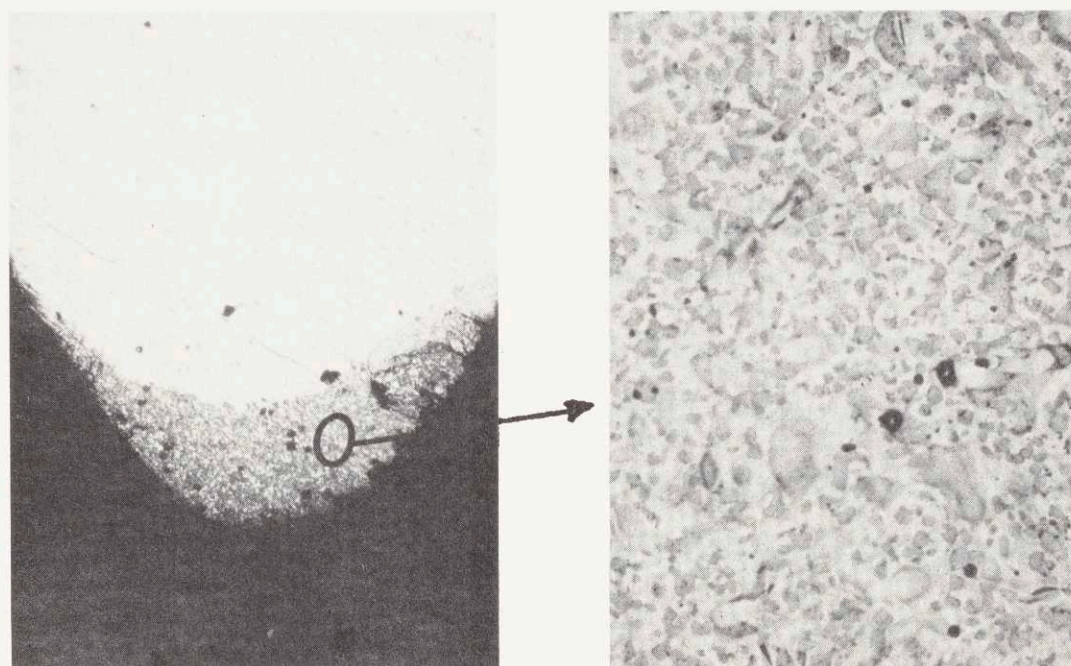
(b)

Figure 38: Microstructure of centrifuged filtered metals from
            Runs #41b and #42d.
            (a) Bottom of centrifuged sample of filtered
                metal, Run #41b, 12.5X and 200X, respectively.
            (b) Bottom of centrifuged sample of filtered
                metal, Run #42d, 12.5X and 200X, respectively.

5.2 Separation of Interdendritic Liquid from Partially Solidified Al-Si Alloys

A. Separation of Interdendritic Liquid

Figure 39 shows the macrostructure of the Al-4% Si-.25% Ti (grain refined) and the Al-4% Si (columnar) unidirectionally cast plugs (starting material) used in these experiments. Figures 39b and 39c show the micro-structures of these two castings, respectively.

The pressures required and the procedure employed to remove the interdendritic liquid from these alloys in the partially liquid-partially solid state, is shown in Table IX Weights of the charge material and liquid removed and calculated efficiencies of removal are shown in Table X.

Figures 40a and 40b show microstructures of the removed interdendritic liquid from Runs #92 (Al-4% Si-.25% Ti alloy) and #93 (Al-4% Si alloy), respectively. Comparing the microstructure of Figures 40a with 39a and Figures 40b with 39b, it can be seen that the removed interdendritic liquid is enriched in silicon - a large volume fraction of eutectic phase is present.

Figure 41 shows chemically analyzed compositions of removed interdendritic liquid from the various runs (data plotted using the method of least squares), and the equilibrium composition of the liquid phase from the phase diagram.

Without the use of a flux above the charge, even pressures in excess of 400 psi were not enough to cause separation of the interdendritic liquid from the solid network. Figures 42a and 42b show the microstructure of an Al-4% Si alloy charge above a SiO_2 filter, where no flux was employed. The applied pressure was 350 psi while the sample was at 610^OC. Figure 42a shows the grooves developed on the oxide layer surrounding the sample (charge). The very high surface tension forces of the oxide layer prevented formation of "capillaries". Consequently, the liquid from the inter-dendritic channels did not drain out. Application of 350 psi pressure above the charge caused solid deformation of the dendrite arms immediately above the filter surface, Figure 42b. Separation of the liquid phase from the solid network required the use of a molten flux above the charge to dissolve the impermeable oxide layer.

The efficiency of removal (weight of liquid removed divided by weight of liquid available) does not depend on the amount of flux used. 30-40 grams of flux was found to be sufficient to dissolve the surface oxide of the charge and to allow formation of "capillaries". 100 grams of flux was used in Run #91, and no noticeable increase in removal efficiency was observed. On the other hand, addition of large amounts of flux (i.e. in excess of 100 grams) was found to be detrimental, since upon separation, the liquid flux became entrapped in the "porous medium". Although the

latter was dissolved away, entrapped flux particles within the extremely tortuous channels were impossible to remove.

For the Al-4% Si alloy, the efficiency of liquid removal was found to be higher when the charge was remelted first rather than directly heated, from the solid state, to the filtration temperature. Comparison of Runs #91 and #94 (Table X) shows that efficiency of liquid removal was increased from 46.7% to 70.4% when the charge was initially remelted. This increase is attributed to the excellent seal that forms between the charge and the crucible walls, thus preventing any pressure losses around the charge.

Higher efficiencies of removal were obtained if, after the initial separation of the bulk liquid, the plug was cooled below the eutectic temperature under pressure (25-30 psi).

Singer and Cottrell(70) measured the mechanical properties of Al-Si alloys in the temperature range of $425^{\circ}C$ to above $610^{\circ}C$. They report that the tensile strength of the Al-4% Si alloy at $575^{\circ}C$ is 600 psi; above $575^{\circ}C$ the strength decreases markedly and loss of all strength occurs above $606^{\circ}C$. Microstructures of Runs #98 ($620^{\circ}C$) and #95 ($618^{\circ}C$), Figures 43a and 43b, respectively, show that the solid network did not buckle under an applied pressure of 25 psi.

Calculations presented in Appendix B show that for the Al-4% Si alloy used here, the difference between weight fractions and volume fractions is very small. In all

subsequent calculations, weight fractions and volume fractions
are assumed to be equivalent.

Volume fractions solid at the separation temperature,
T*, were calculated by the following methods: (i) $\bar{g}_s$ was
calculated from the equilibrium lever rule, where complete
diffusion in the solid is assumed. (ii) g_s was calculated
from the Scheil equation, where no diffusion in the solid is
assumed. Appendix C lists the assumptions and equations
used to calculate $\bar{g}_s$ and g_s.

The "actual" volume fraction solid is the volume
fraction solid remaining in the samples after removal of
the interdendritic liquid. Actual volume fractions solid
remining above the filter, g_{sw}, were calculated from weight
of the liquid removed. Assumptions concerning this latter
method are discussed in Appendix D, section A. Table XI
lists the values of $\bar{g}_s$, g_s and g_{sw}.

Brody et al(71) have shown that during solidification
of aluminum alloys a limited amount of solid diffusion occurs.
Thus, the volume fractions solid existing at temperature T*
range between the values obtained from the Scheil equation
and the equilibrium lever rule. Calculated values listed in
Table X show that the difference between volume fraction
solid from the Scheil equation and that from the equilibrium
lever rule is small compared to the differences between these
values and the "actual" volume fractions solid calculated, g_{sw}.

In subsequent calculations, volume fractions solid at temperature T*, calculated from the Scheil equation will be used.

A second method was also used to determine "actual" volume fractions solid. Slices of the solid dendritic network remaining above the filter were chemically analyzed for silicon content. The compositions determined by chemical analysis, $\bar{C}_S$, are listed in Table XII. g_L^*, the volume fraction liquid remaining in the solid network, after bulk separation of the interdendritic liquid, was calculated from the actual composition (chemical analysis) of the solid network. The following expression was used:

$$g_L^* = \frac{1}{C_L^*} [\bar{C}_S - \int_0^{1-g_L} C_S^* \, dg_S] \qquad (19)$$

where:

C_L^*, C_S^* = equilibrium liquid and solid compositions at the liquid-solid interface

$\bar{C}_S$ = composition of solid network from chemical analysis

g_L = volume fraction solid at temperature T*, from the Scheil equation

The "actual" volume fraction solid remaining above the filter, g_{sA} was then calculated from:

$$g_{sA} = g_s + g_L^* \qquad (20)$$

Derivation of equation (19) is shown in Appendix D, section
B. The calculated "actual" volume fractions solid of the
remaining network, g_{sA}, are listed in Table XII and will be
used in correlation with the measured permeability values.

Calculated values of g_s, $\bar{g}_s$ and g_{sA} are plotted in
Figure 44. As expected the "actual" volume fraction solid is
always larger than the volume fraction solid existing at
temperature T*, because during filtration some of the
interdendritic liquid is invariably entrapped in the solid
network and cannot be removed.

Compositions of the remaining solid networks were
calculated from efficiencies of removal, from the following
expression:

$$\bar{C}_{sc} = \int_0^{1-g_L} C_s^* dg_s + (g_L - g_L \cdot E_{ff}) C_L^* \tag{21}$$

Values of $\bar{C}_{sc}$ are listed in Table XII. Very good agreement
between the calculated compositions from the efficiencies
of removal, $\bar{C}_{sc}$, and from chemical analysis, $\bar{C}_s$, exists.

Interdendritic liquid has been removed from partially
solid-partially liquid Al-4% Si samples (grain refined and
non-grain refined), with up to 70% efficiency of removal.
The separation mode consisted of filtering out the
interdendritic liquid by applying pressure above the flux
coated charge. The filters used supported the solid dendritic
network during separation of the liquid phase. Volume fractions

solid remaining calculated from weight of liquid removed agreed well with those calculated from chemically analyzed composition of the networks. This process could be utilized for refining of alloys by partial solidification. Alternatively, the porous dendritic network remaining above the filter could be used for production of composites by infiltration.

B. Structure of Porous Dendritic Networks

Figure 45 (Run #91, g_{SA} = 0.794) and (Run #99, g_{SA} = 0.783) show a stereo photograph and a SEM view of the top transverse sections of columnar (Al-4% Si) and equiaxed (grain refined, Al-4% Si-0.25% Ti) dendritic networks, respectively. The structure in Figure 45a shows large channels between primary dendrite arms and smaller channels between secondary and a few tertiary arms. The primary and secondary dendrite arm spacings are 1000μ and 280μ, respectively. The structure in Figure 45b shows many small equiaxed crystals surrounded by large channels. Secondary and tertiary arms appear mostly welded together with fewer fine passages as those observed in Figure 45a. The average distance between large channels (grain size) and secondary dendrite arm spacings is about 900μ and 150μ, respectively. The two structures shown in Figure 45 were obtained by different solidification and reheating cycles. The columnar sample, Figure 45a was reheated to the partially solid region from the solid state, while the equiaxed sample, Figure 45b, was

first remelted then partially solidified. The larger channels between primary dendrite arms are similar to those observed in an earlier study by Piellet (41).

Figure 46 shows SEM views of the top transverse section of the equiaxed dendritic network structure (Run #99) at higher magnifications. Again it appears that most of the finer passages between secondary arms are blocked off. This is to be expected since surface tension forces in the finer passages are predominant and draining of the remnant liquid would require high pressures. Figure 46b shows an SEM view of one of the large channels surrounding an equiaxed grain. The rounded tips of the secondary arms protrude into the channel, while entrapped liquid has solidified in the finer passages between the arms.

In two experiments where the non-grain refined Al-4% Si alloy was initially melted then partially resolidified, the equiaxed structures observed were similar to those of the grain refined samples. Figure 47 shows SEM views of the dendritic network of a remelted then partially solidified Al-4% Si alloy (Run #95, g_{sA} = 0.858). Again most of the available passages for flow seem to be the large channels between the equiaxed grains. Secondary dendrite arm spacings are of the same order of magnitude, 140μ, as those observed in the grain refined structure of Run #99, Figure 45b. However, the distance between the large channels surrounding each equiaxed grain is twice as large ~2000μ, as that observed in the grain refined sample of Run #99.

Figures 48 and 49 show longitudinal and transverse structures of ground and polished surfaces of the dendritic network structures from Runs #95 and #98, respectively. The columnar structure shown in Figure 49, (Run #98, g_{sA} = 0.94) deceivingly shows a much larger fraction of voids (i.e. channels) than expected at this high fraction solid. Figure 50b shows a SEM view of the transverse section of this structure demonstrating the fact that most of the dark areas in Figure 49 are filled spaces between secondary dendrite arms. Figure 50a shows the corresponding SEM view of the transverse section of Figure 48.

The samples used in permeability measurements were spark cut to size prior to testing. Figure 51 shows a transverse spark cut cross-section of the sample from Run #94, g_{sA} = 0.655. The dendritic network structure has not been appreciably disturbed or altered due to the cutting.

In summary, the following observations were made. In both the grain refined (Al-4% Si-0.25% Ti) and equiaxed (Al-4% Ti) samples, channels predominately formed between the primary dendrites (i.e. grains) of the samples. Liquid entrappment occurred in the finer passages between secondary dendrite arms, especially in the higher fraction solid equiaxed sample, Run #95, Figure 47. In the columnar sample of Run #91, Figure 45a, channels formed between both the primary and secondary dendrite arms. This could be attributed to the coarser structure of this sample (secondary dendrite arm spacing ~280μ).

C. Specific Permeabilities of Partially Solid
     Al-Si Alloys

Table XIII lists results of the permeability tests
conducted on the dendritic networks. Flow rate for a certain
pressure gradient was measured, and having the sample
dimensions, the coefficient of permeability was calculated
from D'Arcy's law (equation 7).   Applicability of D'Arcy's
law was verified by measuring flow rates through the porous
dendritic networks for various pressure gradients. The linear
plot obtained between flow rate, Q, and pressure drop, ΔP,
across the sample from Run #94 is shown in Figure 52.

The viscosity of Al-5 to 8% Si (composition of the
segregated liquid in this study) at the temperatures of
interest is not known. The viscosity of the segregated
liquid of Al-4.5% Cu alloy varies from 0.0165 to 0.015 poise
in the temperature range of 600 to 625°C ($\underline{72}$,$\underline{73}$). It can be
assumed that the viscosity of the Al-Si alloy is of the same
order of magnitude as the Al-Cu alloy. Thus, the use of
distilled water at room temperature (viscosity ~0.01 poise)
is a reasonable substitute.

Measured specific permeability values versus "actual"
volume fraction liquid are plotted in Figure 53. In the
non-grain refined samples of Al-4% Si, for both the columnar
and equiaxed samples studied, the plot of log K versus log g_{LA},
yields a straight line with a slope of 2 as predicted by the
following equation:

$$K = \gamma g_{LA}^2 \qquad (10)$$

Also plotted in Figure 53 are results of experiments carried out by Piwonka(40) on partially solidified Al-4.5% Cu alloys. The results plotted are for $g_{LA} < 0.3$, which also yields a slope of 2 as predicted by equation (10) above.

Hence, the basic model of capillaric flow through partially solid "mushy freezing" alloys appear to be applicable in the later stages of solidification, $g_{LA} < 0.345$, of the Al-4% Si alloy.

Specific permeabilities for the grain refined dendritic networks have also been plotted in Figure 53. The plot again yields a straight line. The slope of the line is 2.4 which is at variance with the predicted capillaric flow model, equation (10). The highest fraction liquid was in the sample from Run #97, $g_{LA} = 0.372$. Piwonka's measurements of permeabilities in Al-4.5% Cu alloy for all fractions liquid are shown in Figure 3. The plot shows that for fractions liquid larger than ~0.3, a new line with a higher slope was obtained. It is possible that the same phenomenon would have been observed in the grain refined samples of this study if more data points were obtained in the fraction liquid ranges of Runs #99 and #97. It is evident from Figure 53 that the data for the lower fractions liquid again yields a slope of 2, dotted line.

The constant γ in equation (10) from the capillaric flow model is:

$$\gamma = \frac{1}{8\pi \cdot n\tau^3} \tag{22}$$

Where n is the number of flow channels per unit area, and τ is the tortuosity factor to account for the fact that the channels are neither straight, nor perfectly symmetrical.

The values of γ calculated from the plots of Figure 53 are:

γ for Al-4% Si, this work = 8 x 10^{-9} cm^2

γ for Al-4.5% Cu from Piwonka's data = 5.7 x 10^{-9} cm^2

γ^* for Al-4% Si-0.25% Ti, this work = 2.9 x 10^{-9} cm^2

Mehrabian, Keane, and Flemings([74]) previously estimated values of ~10^{-7} cm^2 for calculations of interdendritic fluid flow during columnar solidification of Al-4.5% Cu castings. In that work it was assumed that the value of γ stays constant throughout solidification (i.e. $0 < g_L < 1.0$). They also showed that interdendritic flow velocity, hence macrosegregation, increases with increasing values of γ (i.e. specific permeabilities). It has been shown earlier by Piwonka([40]) and in this work (in the case of the grain refined Al-4% Si-0.25% Ti alloy) that at volume fractions liquid in excess of 0.3 the slope of the log K versus g_{LA} is larger than 2. Hence, specific permeabilities are much higher for corresponding values of fraction liquid than those that would be obtained from values of γ calculated here.

---

*   The values of γ is calculated here from the dotted line shown in Figure 53.

Measured permeabilities of the dendritic networks are comparable to permeabilities of other metallic porous media. Measured permeability values of loosely sintered copper compacts made from -300 mesh spherical powders(42) range between 1 x 10^{-9} and 3.5 x 10^{-9} for interconnected porosities of 0.2 to 0.3, respectively. These values are higher than those of the dendritic networks of the same porosity.

The Kozeny-Carman(38) modification of D'Arcy's law yields the following expression for coefficient of permeability:

$$K = \frac{g_{LA}^3}{(1 - g_{LA})^2 \, f \, (S_o)^2} \qquad (12)$$

Where S_o is the surface of the porous media exposed to the fluid divided by volume of the solid in the media. f is a dimensionless constant, empirically found to have a value of 5.0.

Applicability and verification of Kozeny's analysis to fluid flow through partially solidified dendritic networks requires independently measured values of specific surface, S_o. Piellet(41) has determined permeability values during solidification of Al-4.5% Cu alloys using an equivalent version of equation (12). Utilizing a slow freeze-transverse quench technique, he calculated surface areas of porous media by quantitative metallography. The values of permeability thus obtained were an order of magnitude higher than those of Mehrabian, Keane, and Flemings(74), and two to three orders

of magnitude larger than values shown in Figure 53. Calow
and Tottle(42), on the other hand, have determined surface
areas of sintered copper powders utilizing a BET gas adsorption
technique.

Figure 53 shows that for equivalent volume fractions
liquid, or volume fractions solid, the measured coefficients
of permeability were consistantly lower for the grain refined
samples. This observation is in qualitative agreement with
equation (12) above, where for a given value of g_{LA}, increasing
the surface area S_o results in lower values of K. As shown
earlier, for the range of fractions solid studied, large
channels surrounding equiaxed grains are the predominate
passages open to flow. The smaller grains of the grain
refined samples have a higher surface area and thus lower
permeabilities at equivalent volume fractions.

Table IX

Mode of Pressure Application and Required Pressures for Separation of Interdendritic

Liquid from Partially Solid-Partially Liquid Samples

run	alloy	filter	mode of heating to T*	holding time at T*	pressure required psi	mode of pressure application
94		sintered SiO_2 disc 90-150μ pores	remelted, cooled to 609.25°C	17 mins	12 - 13	gradually increased to 13 psi, sample cooled under 25 psi
91	Al-4% Si	sintered SiO_2 disc 90-150μ pores	directly heated to 604.5°C	18.4 mins	13 - 14	gradually increased to 14 psi, sample cooled under 25 psi
95		porous carbon grade 25, 120μ pores	remelted, cooled to 620°C	20 mins	16 - 18	gradually increased to 18 psi, sample cooled under 30 psi
98		sintered SiO_2 disc 90-150μ pores	directly heated to 618°C	22 mins	13 - 14	gradually increased to 14 psi, sample cooled under 25 psi
97	Al-4% Si-.25 Te	sintered SiO_2 disc 90-150μ pores	directly heated to 616°C	19 mins	13 - 14	gradually increased to 14 psi, sample cooled under 25 psi
99		sintered SiO_2 disc 90-150μ pores	remelted, cooled to 611°C	26 mins	12	gradually increased to 12 psi, sample cooled under 25 psi
92		sintered SiO_2 disc 90-150μ pores	directly heated to 604.5°C	20 mins	14	gradually increased to 14 psi, sample cooled under 25 psi
96		sintered SiO_2 disc 90-150μ pores	remelted, cooled to 616°C	17 mins	13	gradually increased to 13 psi, then released pressure

Table X

Efficiencies of Interdendritic Liquid Removal

run	T*	g_L	w_o	w_L	E_{ff} %
94	609.25	.506	124.5	44.34	70.4
91	604.5	.458	169.6	36.27	46.7
95	620.0	.667	140.0	24.00	25.7
98	618.0	.632	157.0	16.87	17.0
97	616.0	.6	150.0	50.7	56.3
99	611.0	.528	151.5	38.1	47.7
92	604.5	.458	141.9	26.45	40.7
96	616.0	.6	127.0	26.00	34.1

Terminology:

T* = separation temperature, in degrees centigrade

g_L = volume fraction liquid at T* determined from the Scheil equation (Appendix C)

w_o = weight, in grams of initial charge

w_L = weight, in grams of removed liquid

E_{ff} = calculated efficiencies of liquid removal, 100% efficient if $w_L = g_L \cdot w_o$

Table XI

Calculated Volume Fractions Solid

run	T^*	C_S^*	C_L^*	$\bar{g}_s$	g_s	g_{sw}
94	609.25	1.016	7.18	.51	.494	.65
91	604.5	1.11	7.85	.57	.542	.79
95	620.00	.80	5.68	.34	.333	.83
98	618.00	.84	5.95	.38	.368	.89
97	616.00	.88	6.22	.41	.4	.67
99	611.00	.98	6.92	.49	.472	.75
92	604.5	1.11	7.85	.57	.542	.82
96	616.00	.88	6.22	.41	.4	.80

Terminology:

T^* = separation temperature, in degrees centigrade

C_S^*, C_L^* = equilibrium solid and liquid compositions, determined from phase diagram

$\bar{g}_s$ = volume fraction solid at T^* calculated from equilibrium lever rule (Appendix C)

g_s = volume fraction solid at T^* calculated from Scheil equation (Appendix C)

g_{sw} = volume fraction solid after bulk separation of liquid, calculated from weight of liquid removed (Appendix D)

TABLE XII

"Actual" Volume Fractions Solid Determined
Using Chemically Analyzed Compositions

run	T*	g_L	C_L^*	$\bar{C}_s$	$\bar{C}_{sc}$	g_{SA}
94	609.25	.506	7.18	1.53	1.44	.655
91	604.5	.458	7.85	2.4	2.34	.794
95	620.0	.667	5.68	3.21	3.04	.858
98	618.0	.632	5.95	3.66	3.37	.94
97	616.0	.6	6.22	1.7	1.91	.628
99	611.0	.528	6.92	2.5	2.26	.783
92	604.5	.458	7.85	2.69	2.55	.830
96	616.0	.6	6.22	3.0	2.74	.837

Terminology:

T* = separation temperature, in degrees centrigrade

C_L^* = equilibrium liquid composition determined from phase diagram

g_L = volume fraction liquid at T*, from Scheil equation (Appendix C)

$\bar{C}_s$ = composition of solid network after filtration, determined by chemical analysis

$\bar{C}_{sc}$ = composition of solid network after filtration, calculated from efficiencies of liquid removal

g_{SA} = "actual" volume fractions solid (Appendix D, Section B)

Table XIII

Specific Permeability Values

run	g_{SA}	g_{LA}	Q	L	ΔP	μ	A	K
94	.655	.345	.0197	1.746	6.8×10^4	10^{-2}	5.062	1×10^{-9}
91	.794	.206	.047	2.47	5.79×10^5	10^{-2}	5.0126	4×10^{-10}
95	.858	.142	.0146	1.409	2.33×10^5	10^{-2}	5.268	1.68×10^{-10}
98	.94	.06	.00561	1.902	6.025×10^5	10^{-2}	5.063	3.5×10^{-11}
97	.628	.372	.0289	1.41	13.3×10^4	10^{-2}	5.58	5.5×10^{-10}
99	.783	.217	.01173	1.633	2.33×10^5	10^{-2}	5.67	1.45×10^{-10}
92	.830	.170	.01534	1.69	6.075×10^5	10^{-2}	5.063	8.5×10^{-11}
96	.837	.163	.00541	1.706	2.4×10^5	10^{-2}	5.063	7.6×10^{-11}

Al-4% Si (runs 94, 91, 95, 98)

Al-4% Si-0.25% Ti (runs 97, 99, 92, 96)

Terminology:

g_{SA}, g_{LA} = "actual" volume fractions solid and liquid, respectively (Appendix D)

Q = volumetric flow rate, cm^3/sec

L = height of sample, cm

ΔP = applied pressure differential in permeameter, $dynes/cm^2$

μ = viscosity of distilled water, poise

A = cross sectional area of sample, cm^2

K = specific permeability, cm^2
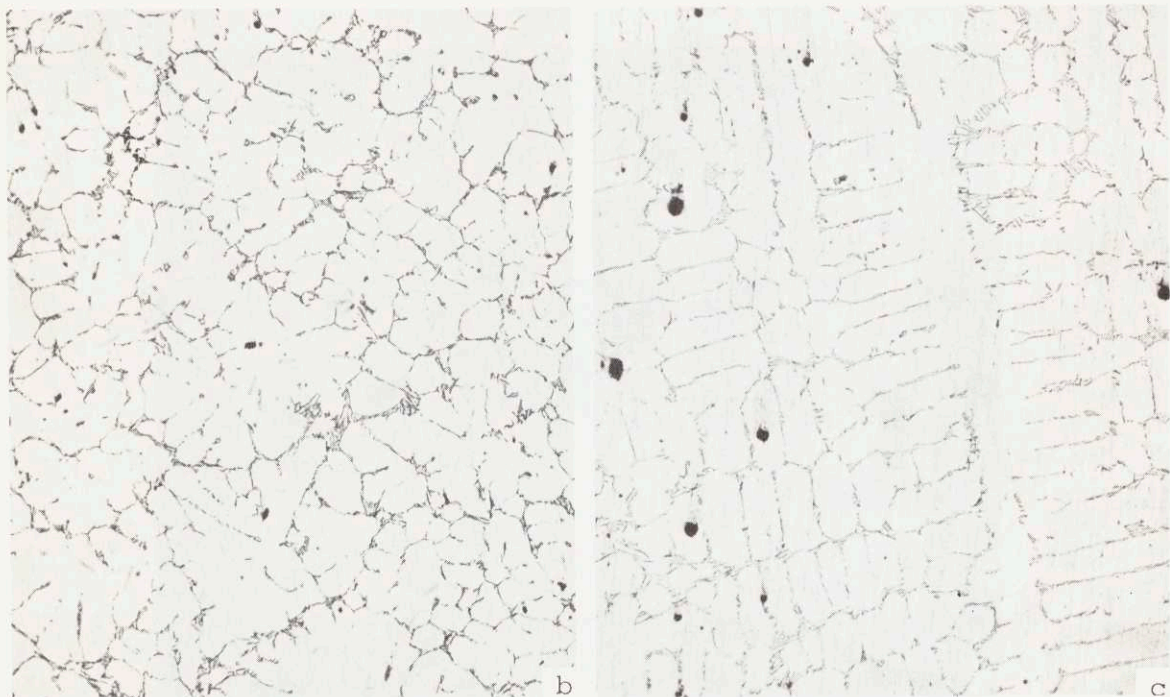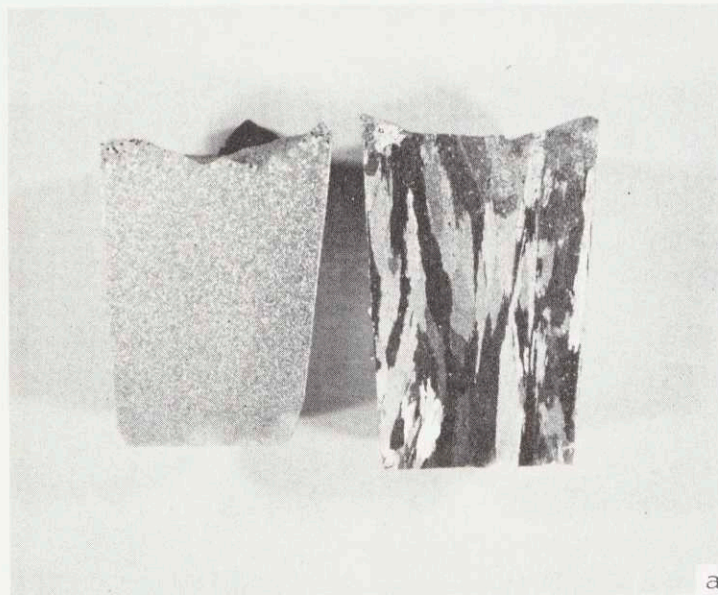
Figure 39: Structure of the samples prior to removal of the
            interdendritic liquid.
            (a) Microstructure of Al-4% Si-.25% Ti alloy, 100X.
            (b) Microstructure of Al-4% Si alloy, 100X.

Figure 40: Structure of removed interdendritic liquid.
            (a) From Run #92, Al-4% Si-0.25% Ti alloy, 100X.
            (b) From Run #94, Al-4% Si alloy, 100X.
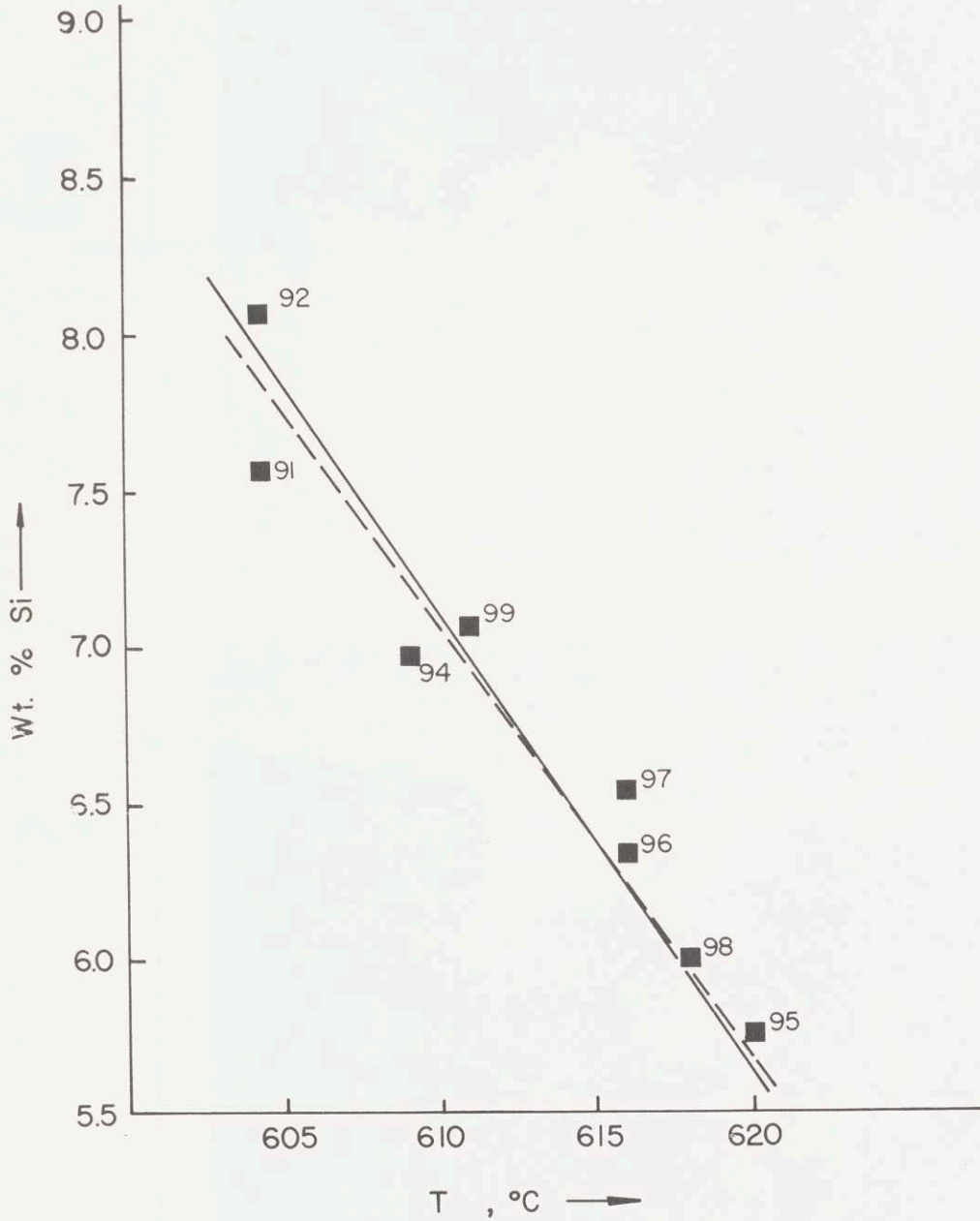
Figure 41: Silicon composition of the removed interdendritic
liquid, determined by chemical analysis, versus
temperature. Dotted line represents the liquidus
compositions from the phase diagram.

TOP
OF
PLUG
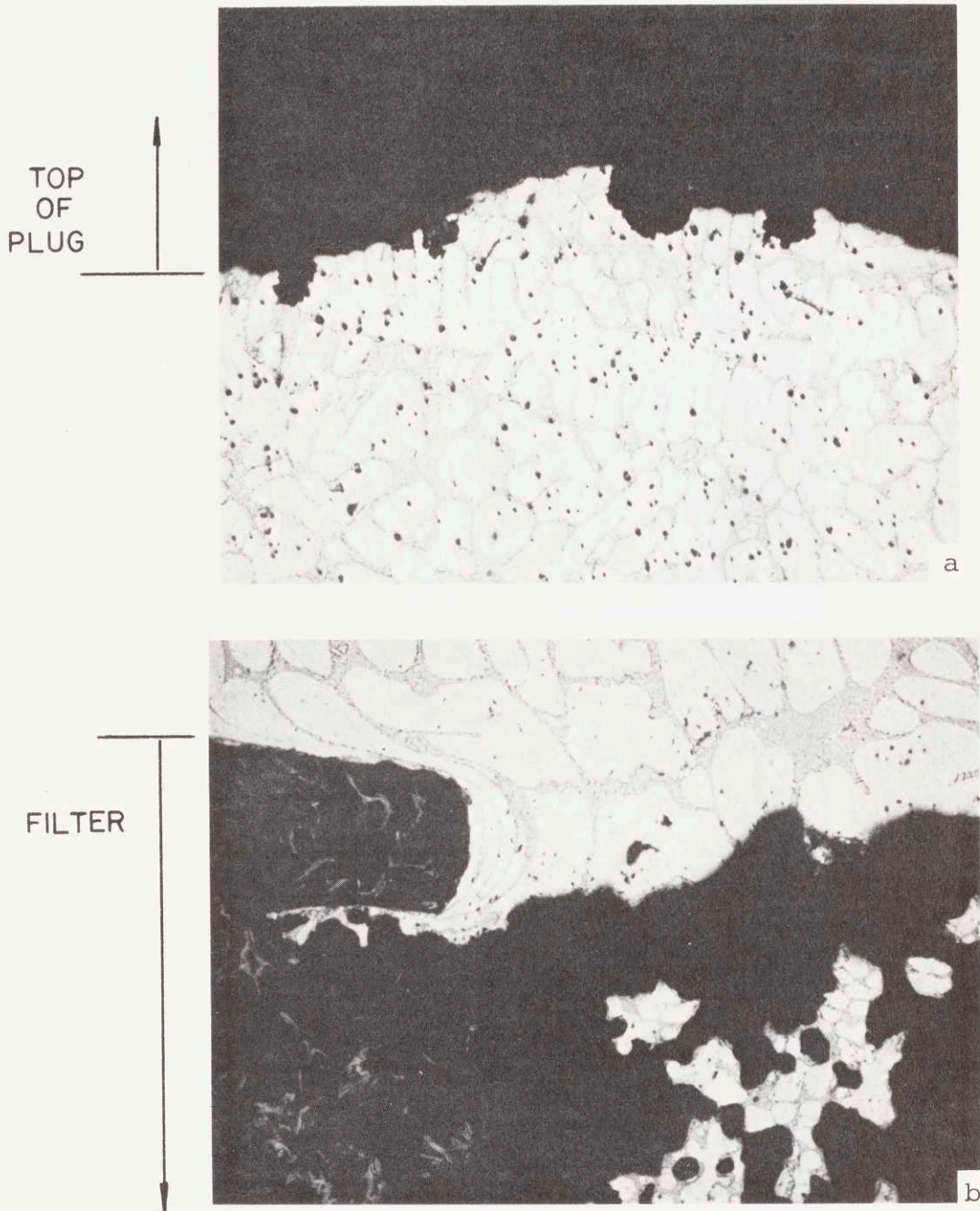
FILTER

Figure 42:   Structure of a sample after application of 350 psi
             at 610°C. No flux was used above the sample:
             (a) Top of the sample, 50X.
             (b) Bottom of the sample, located above the filter,
                 note some penetration and deformation of the
                 charge into the filter pores.
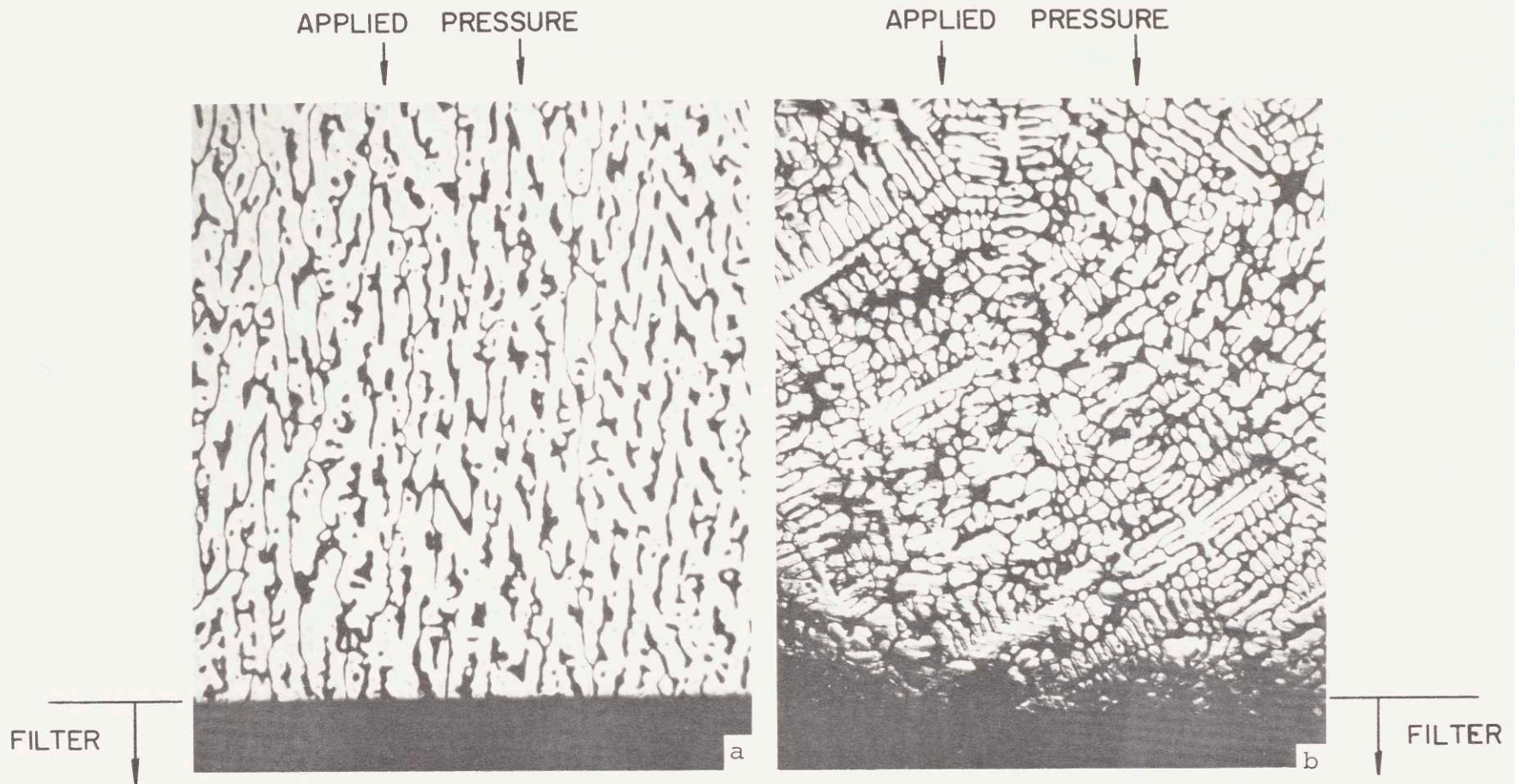
Figure 43: Structure of Solid dendritic network remaining after removal of
interdendritic liquid. Initial alloy composition was Al-4% Si.
(a) Run #98, pressurized at 618°C, $g_S = 0.368$ and $g_{SA} = 0.95$,
12.5X.
(b) Run #95, pressurized at 620°C, $g_S = 0.333$ and $g_{SA} = 0.858$,
12.5X.
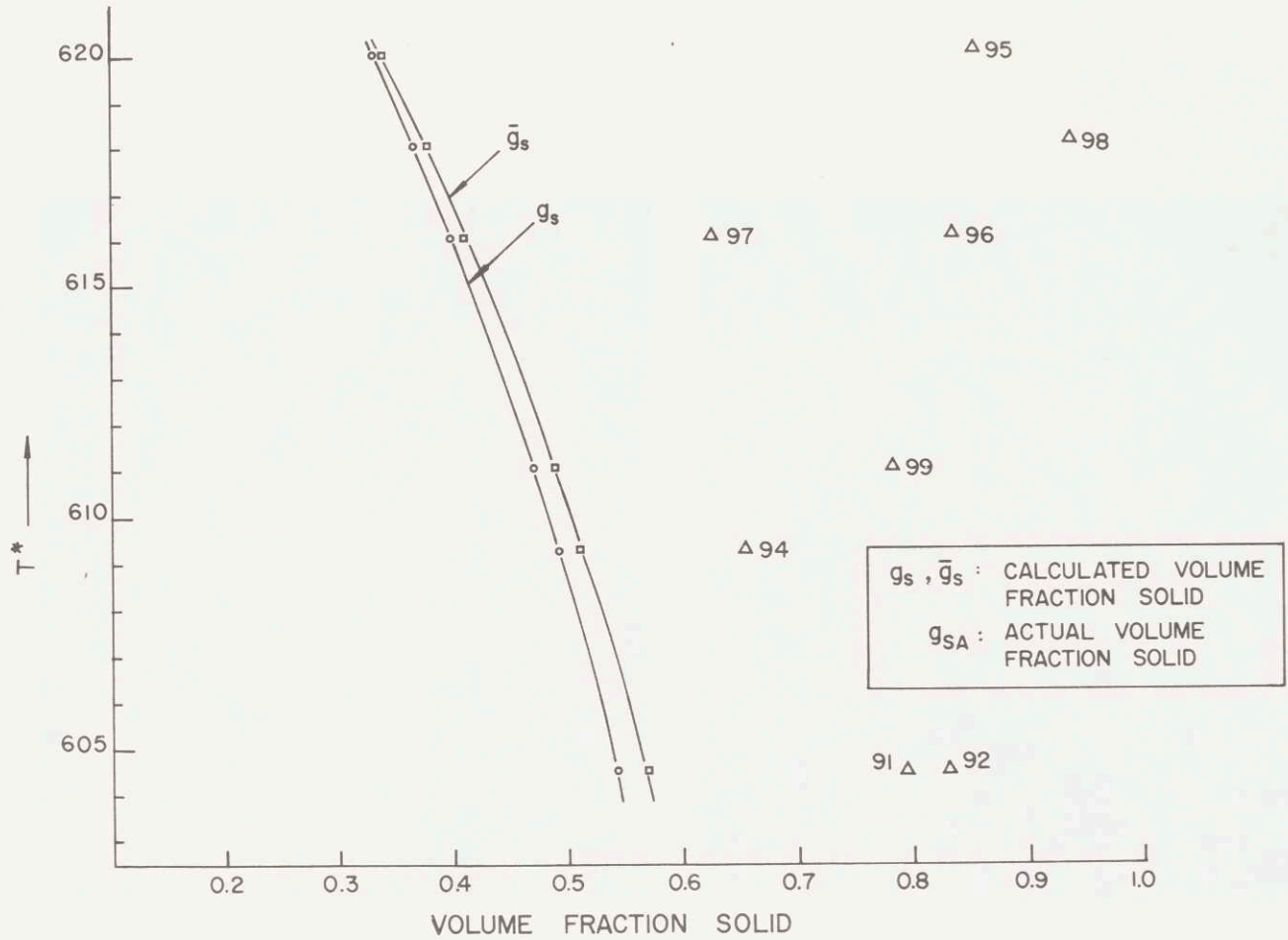
Figure 44: Calculated and "actual" volume fractions solid versus
temperature. g_S, $\bar{g}_S$, g_{SA} are volume fractions solid
calculated from the Scheil equation, equilibrium lever rule
and from compositions of the remaining dendritic networks,
respectively.
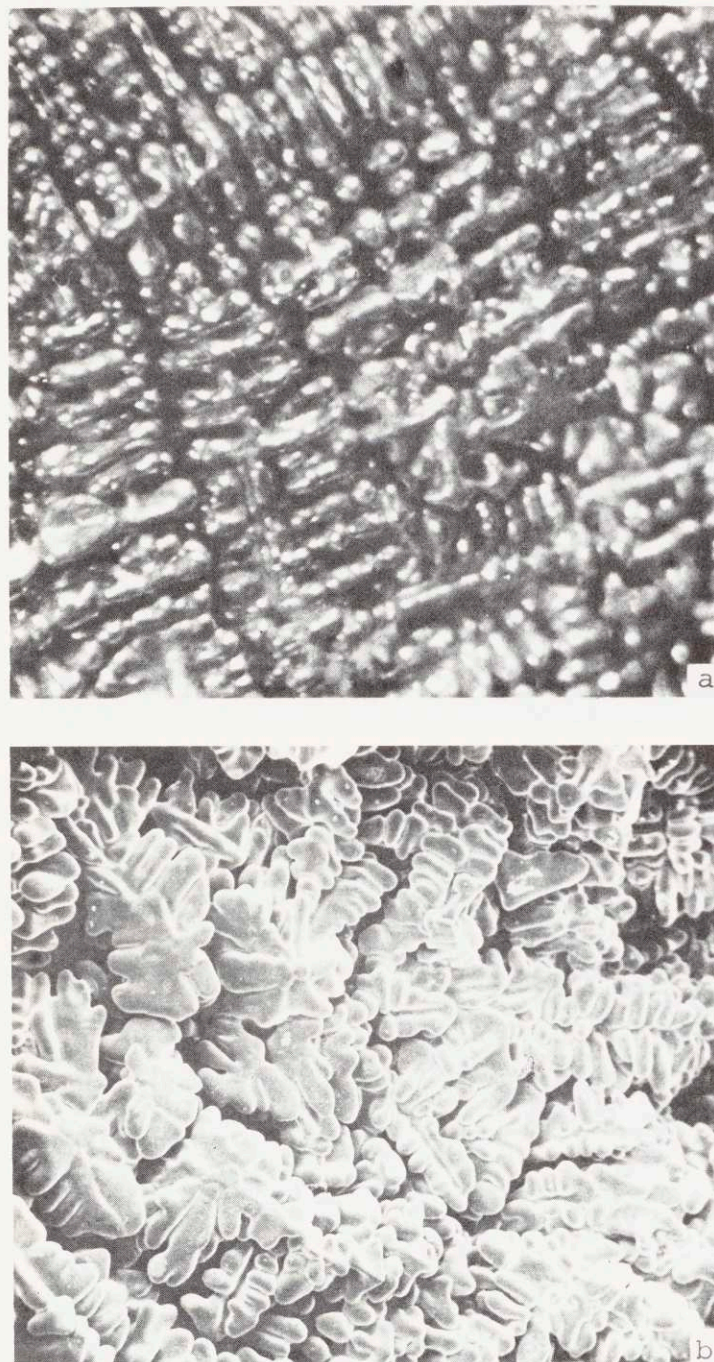
Figure 45: Views of the top transverse sections of porous
            dendritic networks of Al-4% Si and Al-4% Si-0.25% Ti
            samples.
            (a) Stereo photograph of the columnar network
                structure from Run #91, g_{SA} = 0.794, 15X.
            (b) SEM view of equiaxed, grain refined, network
                structure from Run #99, g_{SA} = 0.783, 22X.
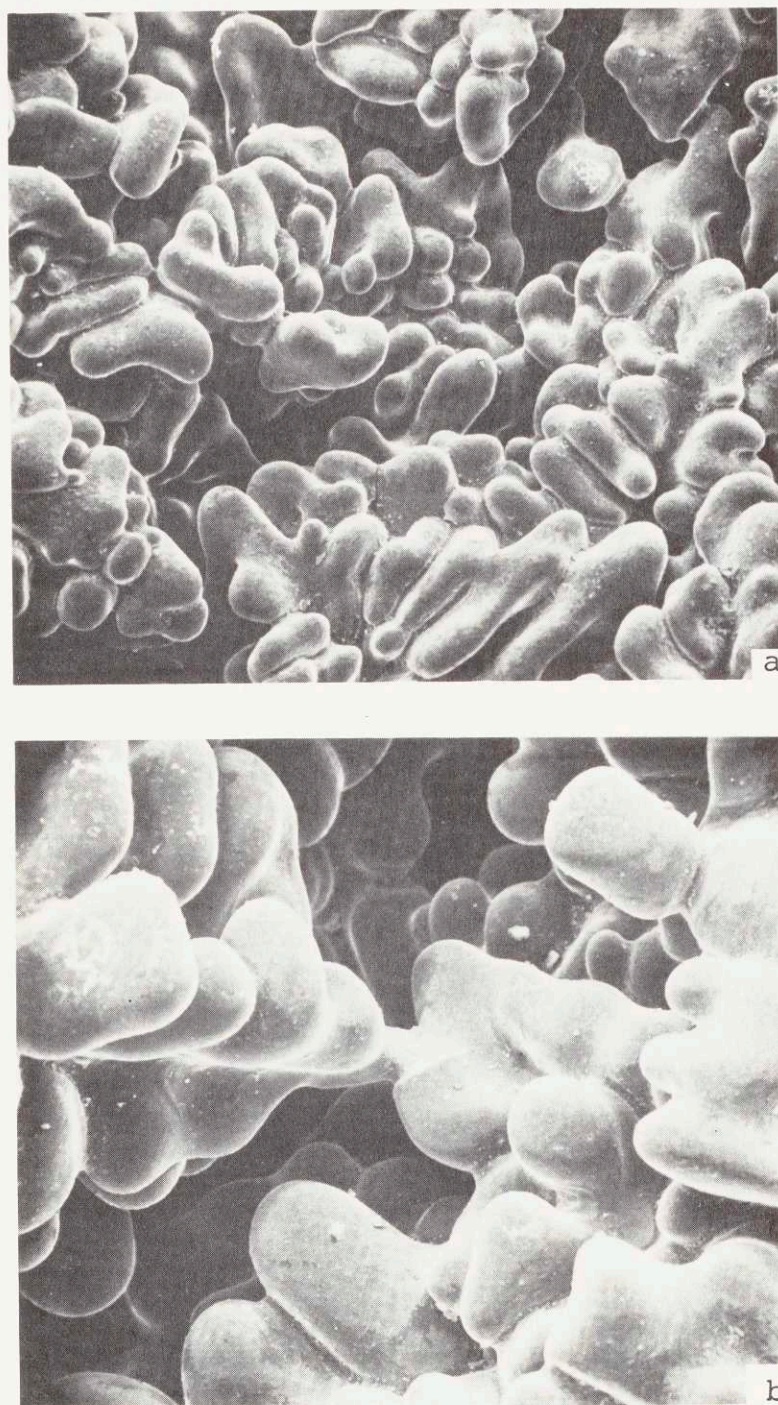
Figure 46:   SEM views of the top transverse section of the
             porous dendritic network of Al-4% Si-0.25% Ti
             sample from Run #99, g_{SA} = 0.783;
             (a) 50X
             (b) 100X.
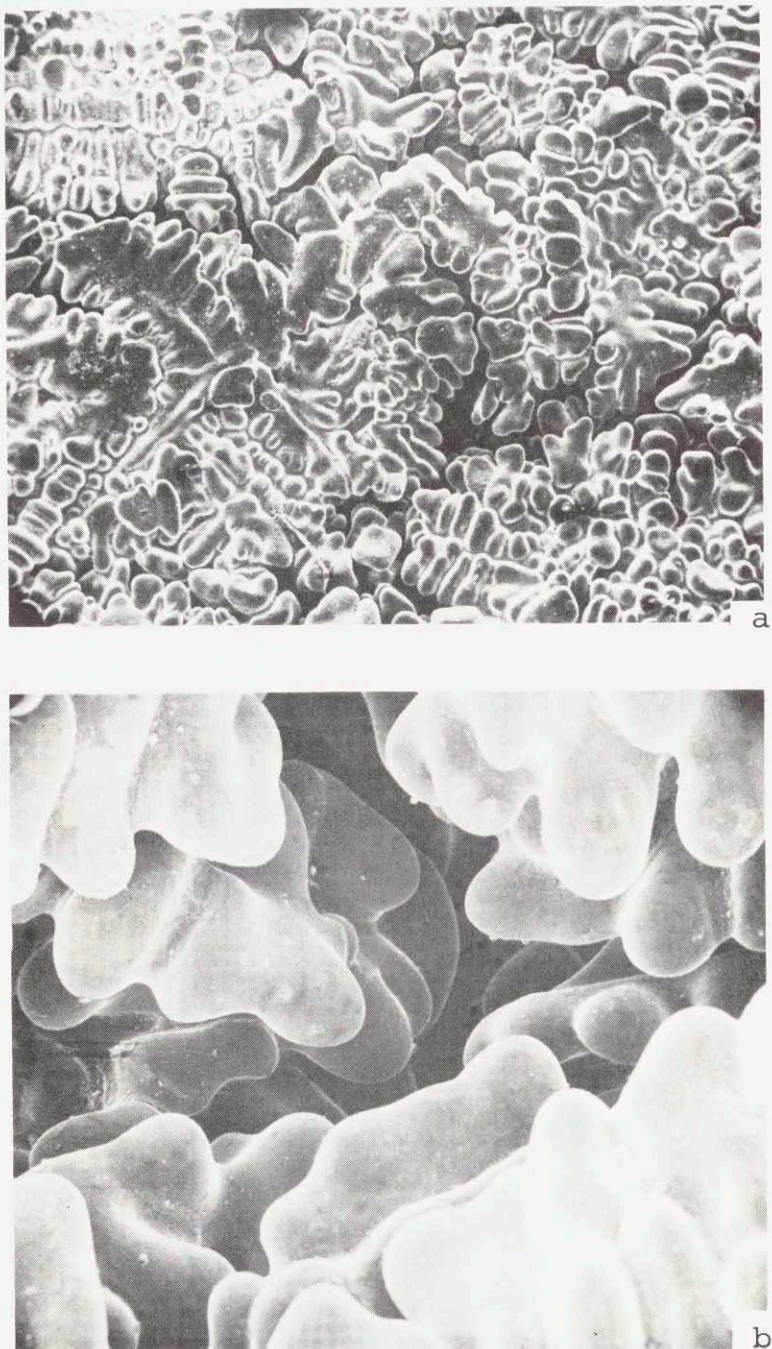
Figure 47: SEM views of the top transverse section of the porous dendritic network of the equiaxed Al-4% Si sample from Run #95, g_{SA} = 0.858;
(a) 19X
(b) 100X
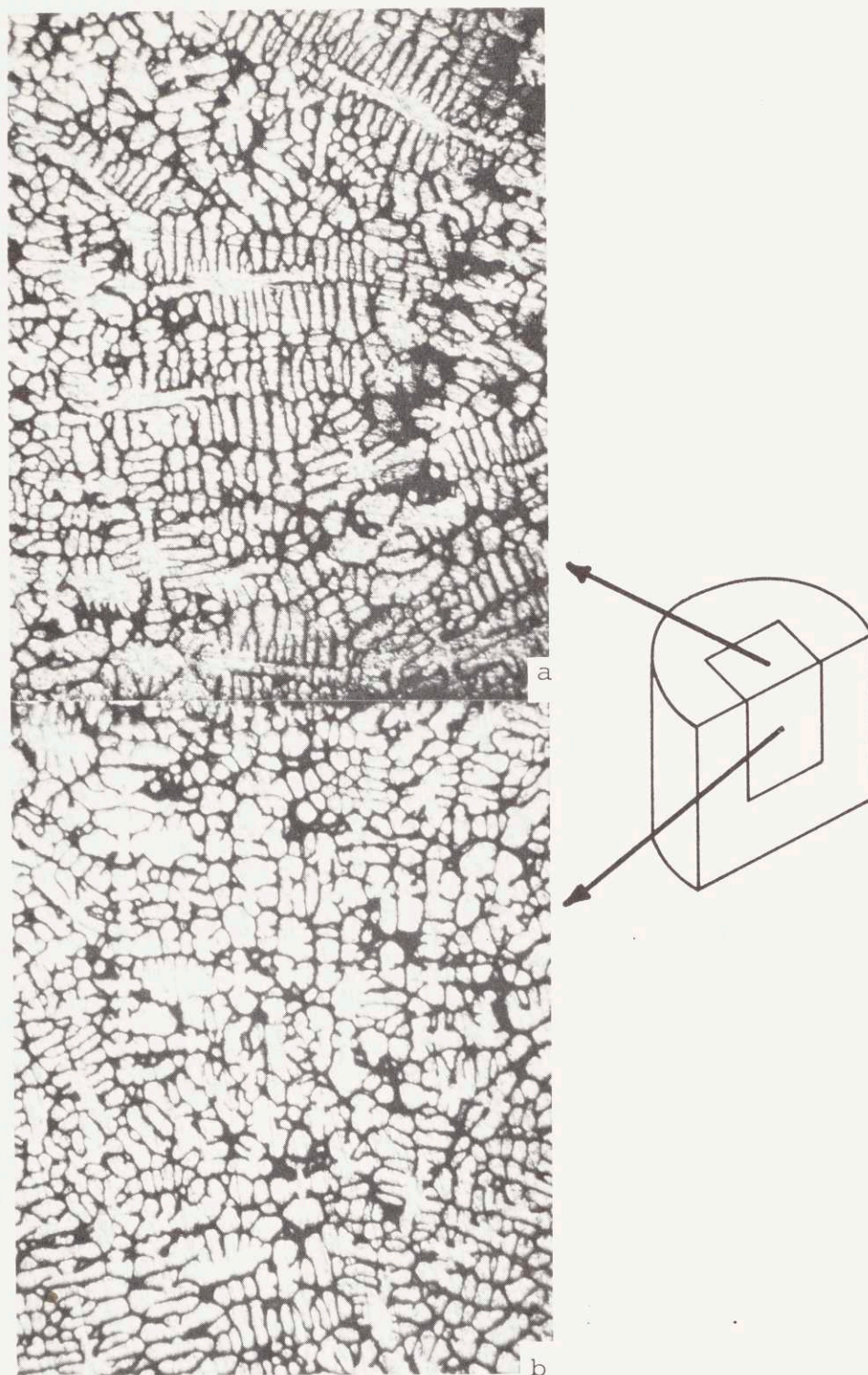
Figure 48: Photomicrographs of the polished porous dendritic
            network of equiaxed Al-4% Si sample from Run #95,
            g_{SA} = 0.858, 15X.
            (a) Transverse section.
            (b) Longitudinal section.
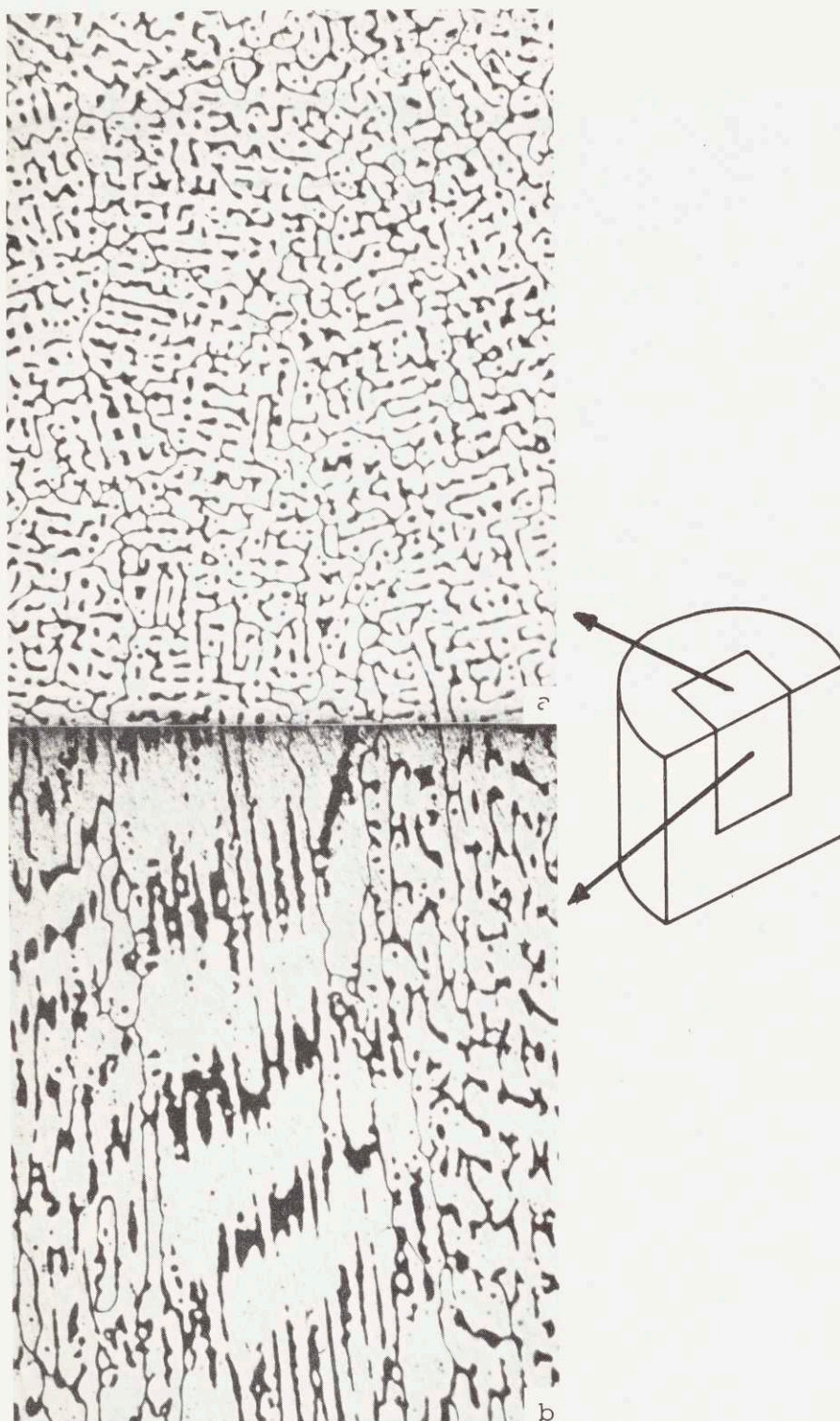
Figure 49: Photomicrographs of the polished porous dendritic
network of columnar Al-4% Si sample from Run #98,
g_{S_A} = 0.94, 15X.
(a) Transverse section.
(b) Longitudinal section.
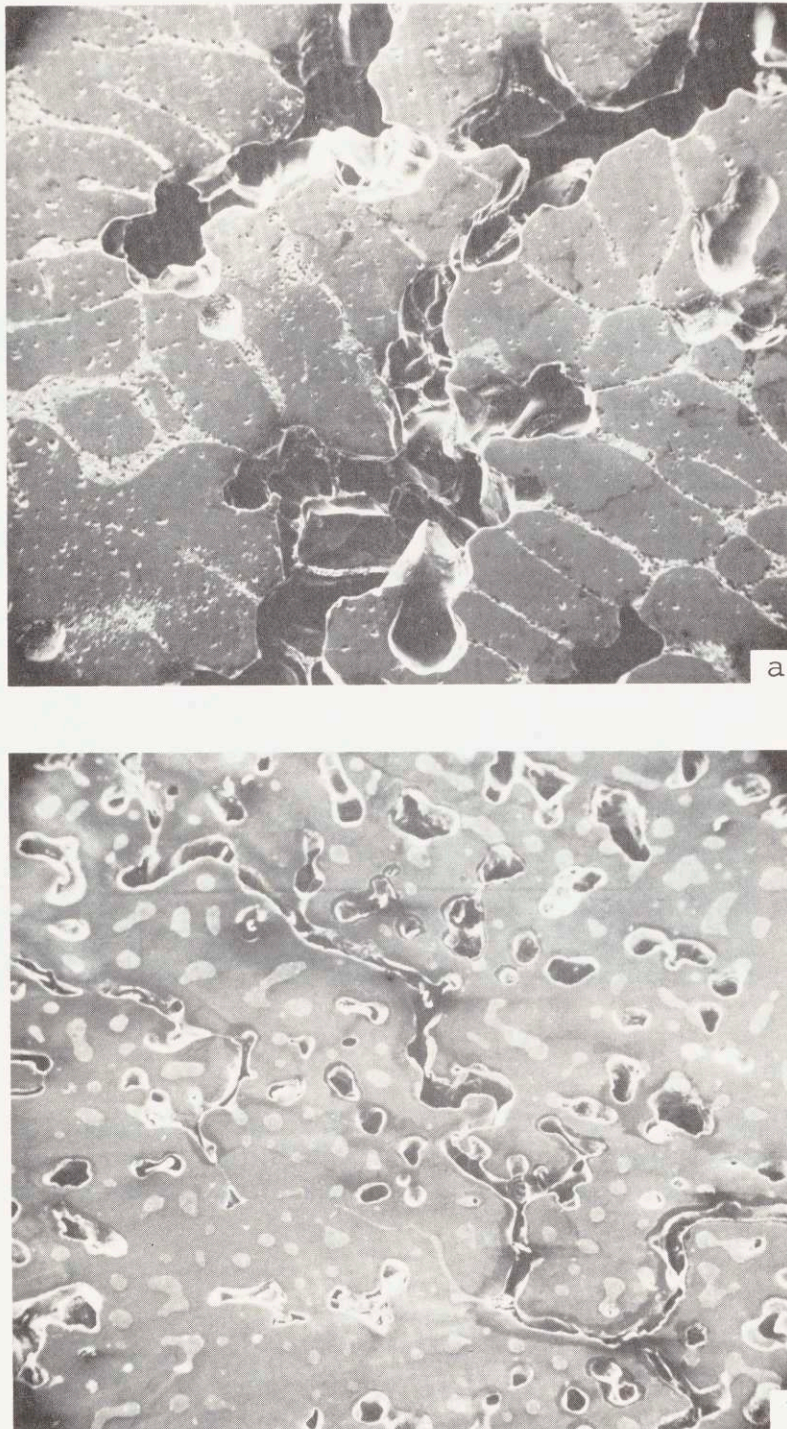
Figure 50: SEM views of the polished transverse sections of porous dendritic networks of Al-4% Si samples.
(a) Equiaxed sample from Run #95, $g_{SA} = 0.868$.
(b) Columnar sample from Run #98, $g_{SA} = 0.94$.

Figure 51: SEM view of the spark cut transverse section of
the porous dendritic network of equiaxed Al-4% Si
sample from Run #94, g_{SA} = 0.655, 20X.
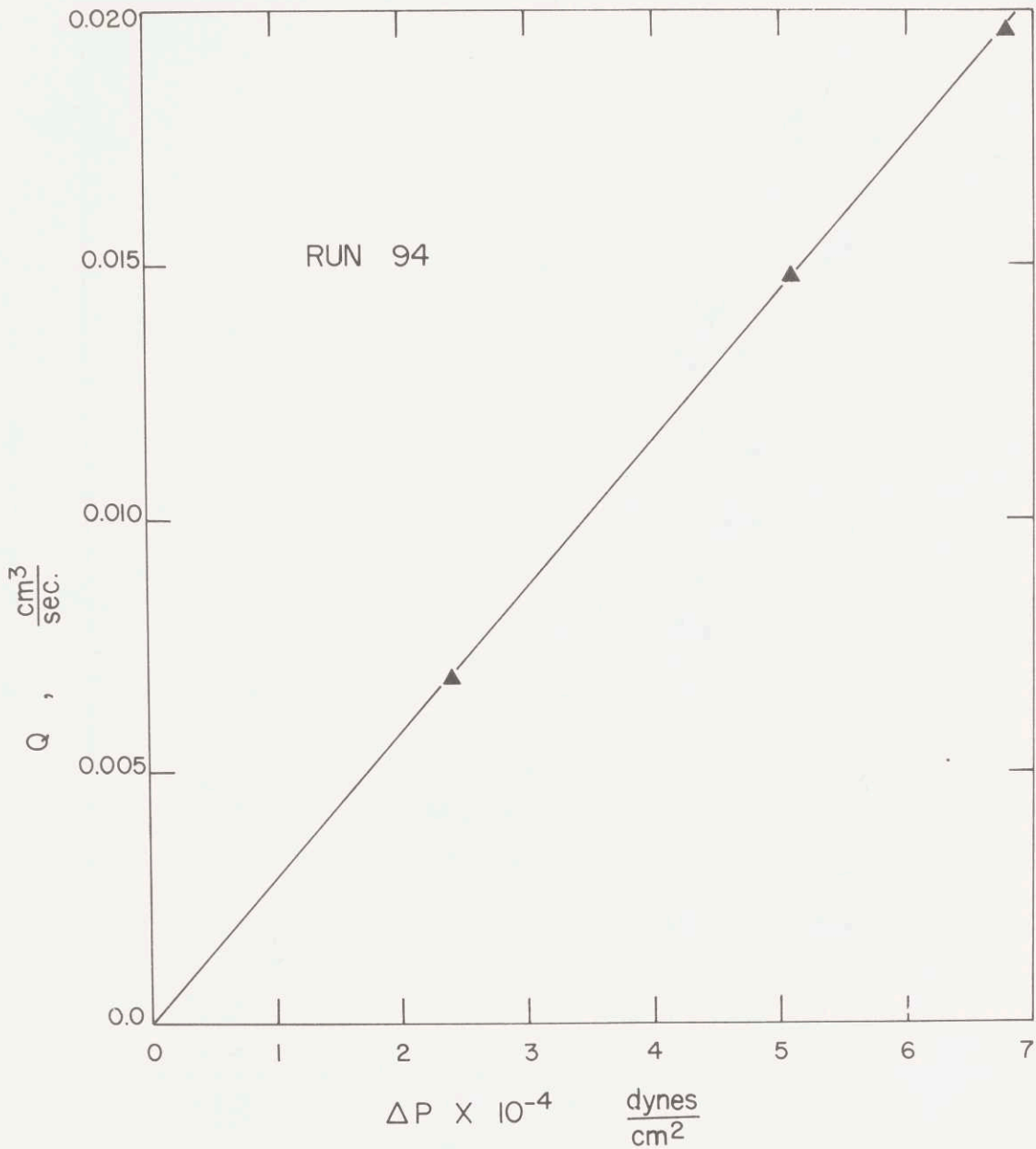
Figure 52: Verification of applicability of D'Arcy's law to
flow through a porous dendritic network (Run #94,
Table IX), Q is volumetric flow rate and ΔP is the
pressure drop across the sample.
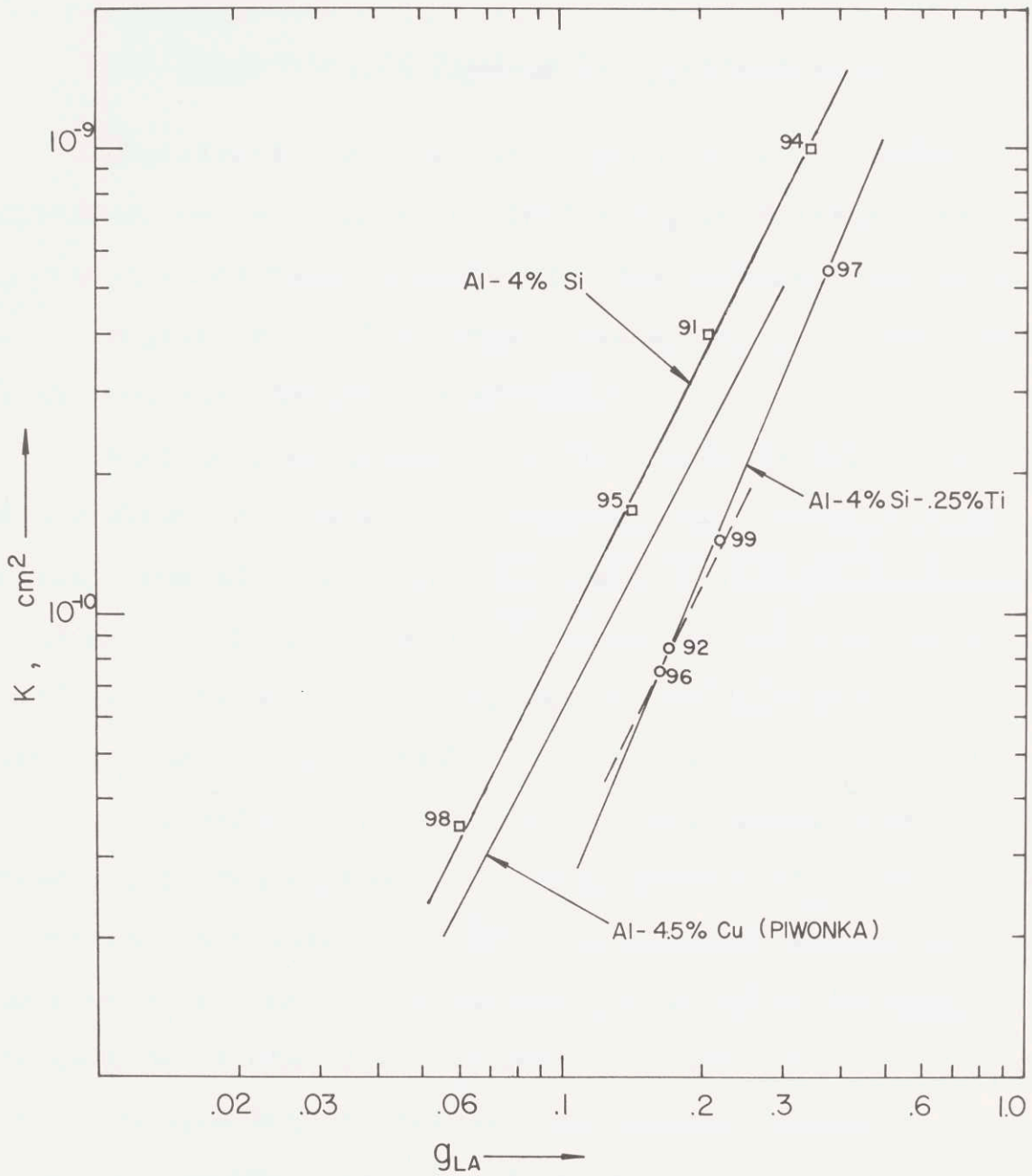
Figure 53: Measured specific permeabilities versus "actual" volume fraction liquid, for Al-4% Si and Al-4% Si-0.25% Ti alloys, and permeabilities of Al-4.5% Cu measured by Piwonka and Flemings(40).

5.3   Production of Metal Powders

A.   Production of Powders by Filatomization

Experiments carried out in production of powders of pure aluminum and a modified 7075 alloy by filatomization have been summarized in Table II. The different variables (i.e. temperature, filter media, pressures, etc.) for each experiment are listed in Table II.

Various size spherical powders made in Runs #1 and 18 are shown in Figure 54. Occasionally, liquid streams exiting from adjacent pores coalesced to form large liquid metal drops. Large drops thus formed did not completely solidify in flight and "splatted" in the collector container, forming flakes, Figure 54e.

A scanning micrograph of spherical metal drops (powders) formed at the pores of a sintered Al_2O_3 disc, with an average pore size of 87-100μ, is shown in Figure 55a. The neck region of one of the powders is shown in Figure 55b. The exiting stream of liquid metal becomes spherical in shape due to surface tension forces, and subsequently drop detachment occurs. Hauser and Edgerton(75) have investigated the steps of formation and detachment of drops from the end of vertical tubes. They show that a waist forms first and rapidly necks down into a stem which then breaks off close to the top of the drop. Harkins and Brown(76) have derived

an expression for drop formation using a force balance

between gravity and surface tension:

$$mg = \pi d\sigma f(d \cdot V^{-1/3})$$ (23)

where:

mg = weight drop

d = tip or orifice diameter

σ = surface tension

V = drop volume

$f(d \cdot V^{-1/3})$ = an empirical correction factor that takes into account the shape of the drop. In case of an ideal spherical drop the value of this function becomes unity

This type of analysis does not take into account (i) the formation of an oxide layer around the exiting drop, (ii) initiation of solidification, and (iii) large temperature gradients that exist below the filter.

A large number of available pores in the bottom of the filter are not utilized during drop (powder) formation, Figures 56a and 56b. Liquid metal preferentially flows through paths of least resistance, causing a channeling phenomenon to occur. Increasing filatomization pressures leads to utilization of a greater number of pores, which in turn can cause consolidation of drops from adjacent pores (i.e. less than one drop diameter apart), Figure 56c. In the extreme case, consolidation of many liquid drops results in formation of large drops which

upon encountering a solid substrate form the flakes shown in Figure 54e.

The temperature of the melt above the filter influences the size of the drops formed. If the melt contains a large superheat, then the surface tension forces have more time to act on the emerging drop, and therefore larger drops are formed. Whereas, if the temperature of the melt is only 20-30°C above the melting temperature, then as the drops are formed at the pore interface, solidification is initiated preventing any further enlargement of the drops. Size distribution curves of powders formed in Runs #11 (T_F = 700°C) and #16 (T_F = 742°C) are shown in Figures 57a and 57b, respectively. With the exception of the filatomization temperatures, both of these runs were conducted under the same conditions. It can be seen that in Run #11 a much larger percentage of drops in the -20+30 and -30+50 size range were obtained, whereas in Run #16 a large percentage (41%) of -10+12 size range powders were formed.

It was found that Al_2O_3 filters were more amenable to filatomization than the SiO_2 filters. SiO_2 filters of 90-150μ pore size were used in Runs #8 (T_F = 769°C) and #9 (T_F = 650°C). In both runs large drops of the 7075 alloy were formed, which in turn splatted against the collection container below. Size distribution analysis of spherical drops formed through an SiO_2 filter, Run #4 (769°C) is shown in Figure 58a.

Liquid Al wets SiO_2 much more readily than it does Al_2O_3 (77). Hence, in cases where drops of metal consolidate below the filter, large drops can easily spread out on the SiO_2 filters, leading to formation of the flakes described above. It is also possible that in SiO_2 filters the molten aluminum penetrates through more pores (i.e. less channeling occurs). This in turn would result in increased consolidation of drops, subsequent spreading, and thus formation of large drops.

Pressure control is an important variable for successful filatomization. Surpassing the critical pressure (the one required for drop formation through preferential channels) results in the formation of continuous and consolidated streams. Keith and Hixson (78) investigated the effect of pressure and flow rate on formation of drops at the tip of a vertical tube, Figure 58b. At low flow rates, drops form individually at the pore tip and grow in size until the weight overcomes the interfacial tension and drop detachment occurs. This mechanism pertains to filatomization.

With increasing flow velocities, a point is reached where a very short continuous neck of liquid exists between the pore tip and the point of drop detachment. This velocity is called the jetting point. At high flow rates, the jet breakup point retreats to the pore tip and a nonuniform spray of drops results - point of atomization.

In these experiments, the produced powders exiting from the filters were exposed to the atmosphere. It is conceivable that a setup for filatomization can be designed using reduced pressure by having the area below the filter exposed to a vacuum, rather than applying pressure above the melt.

One of the attractive features of filatomization is that filtration and drop (powder) formation occur simultaneously. Figure 59a shows the oxide "cake" retained above the sintered SiO_2 disc filter, Run #4. Figure 59b shows the oxide skins connected with porosity found above the sintered Al_2O_3 disc filter employed in Run #16. Thus it should also be possible to filter out undesirable secondary phases (exogenous inclusions) from a melt prior to powder formation, by adjusting the temperature of filatomization.

In usual atomization processes, the emerging liquid is disrupted either by applying a large pressure above the melt (very large flow rates) or by impinging the emerging liquid from the orifice. In the filatomization setup, an additional setup below the filter which impinges a jet of gas towards the exiting liquid metal jet may be employed, instead of using a single hole orifice atomizer. In this manner, both filtration and atomization occur in one final operation.

The filter used in Run #14 had also been used in the four preceeding runs. Size distribution of powders obtained

from Runs #14 (T_F = 742°C) and #16 (T_F = 742°C, new filter)
are shown in Figures 60 and 57b respectively. In Run #14 a
larger percentage -16+20 and -20+30 mesh powders were
formed. Clogging of the interstices occurs as a filter is
used successively. Thus leading to liquid flow through
other finer pores and resulting in the formation of finer
powders. In Run #14 slightly larger pressures were required
for flow of liquid metal (ΔP for fine pores > ΔP for larger
pores).

B. Structure of Filatomized and Commercial Powders

1. Spherical Powders

Figure 61a and 61b show scanning electron micrographs
of pure aluminum powders of 300μ and 150μ size range obtained
in Run #1. The powders are generally spherical in shape.
Occasionally powders with stems or tips not completely
detached were also observed, Figure 62a. At a higher
magnification, surface irregularities such as ripples, folds,
and waves are observed, Figures 62b, 62c. These are caused when
the initial oxide layer tries to accommodate deformation
experienced by the drop as solidification, shrinkage, and
flight instabilities occur. Figure 61c shows a representa-
tive microstructure of the pure aluminum powders obtained
in this study. All the pure aluminum powders obtained in
this study had the one general type of structure described
above.

Filatomized spherical powders made from a modified
7075 aluminum alloy, on the other hand, varied in their
structure. Two distinct types of spherical powders were
observed, Type (i) powders possessed a fine dendritic
structure, and Type (ii) powders had no apparent dendritic
structure.

Figure 63 shows SEM views of Type (i) powders. These
are representative structures of the filatomized powders cold
compacted and hot extruded into a billet. The different
dendritic microstructures of these powders are shown in
Figure 64. There is no evidence of porosity here, and the
measured dendrite arm spacings were between 4-8μ, indicating
cooling rates ranging from 10^2 to 10^4 $^{\circ}$C/sec, Figure 4(79).

Figure 65a shows an SEM view of a Type (ii) 7075
aluminum alloy powder. This powder has a smooth surface with
no apparent dendritic structure, and contains second phase
particles that have precipitated throughout the structure.
The microstructure of these powders are shown in Figures 65b
and 65c. It can be seen that what appears to be a fine
dendritic structure at low magnifications, Figure 65b, is
really a distribution of second phase particles within the
matrix, Figure 65c. The absence of dendritic structures is
due to the higher cooling rates experienced by these smaller
Type (ii) powders. Some of the Type (ii) small powders
(25-50μ diameter) have oscillatory nodes around their
circumference, Figure 66. These particular powders are

attached to each other by a cup-like layer. This may be due to collision and subsequent attachment during flight of two or more drops; the surface ridges being caused by aerodynamic rippling(80).

The filatomized spherical powders reported above were chemically analyzed, and the Al_2O_3 content ranged between 0.07-0.12 wt. %.

2. Flakes

Figure 67a shows an SEM view of the fine dendritic structure on a filatomized flake of 7075 aluminum alloy. The dendritic arm spacings of the flakes ranged between 2-4μ, corresponding to relatively high cooling rates of 10^4-10^5 °C/sec(79).

The flakes generally have a "duplex" structure composed of fine and coarse dendrites, Figure 67b. The coarse dendrites form during the flight of a large drop. While the higher cooling rates experienced by the drop upon "splatting" against the collector can result in the finer structure.

The Al_2O_3 content of the filatomized flakes, determined by chemical analysis, ranged between 0.15-0.57 wt. %. As expected, the flakes had a much higher oxide content because of the large surface area to volume ratio.

3. Commercial 7075* Powder

SEM views of 7075 aluminum alloy powders produced by a centrifugal atomizer are shown in Figures 68a and 68b.

*   Obtained from Reynolds.

The powders are acicular in shape and are enveloped by a thick oxide layer. The shape of these powders is quite heterogeneous, and their size varies from 1 mm. to 5 mm.

The microstructure of the powders is shown in Figures 68c and 68d. Excessive porosity resulting from the atomization process is evident. Measured dendrite arm spacings are of the order of $7-8\mu$, corresponding to cooling rates of 5×10^2 to 10^3 $^{o}C/sec$ (79). Comparing the microstructures of these powders with those of the filatomized powders, Figure 64, the superiority of the latter both in lack of porosity and fineness of structure is evident.

C. Processing and Structure of 7075-T6 Extrusions

1. Processing

The filatomized spherical powders and flakes of the 7075-aluminum alloy were cold compacted and hot extruded into two separate billets. Size distribution of the spherical powders obtained using the Al_2O_3 filters is shown in Figure 69. The filatomized flakes, 5-10 mm. in length and $1250-500\mu$ thick, were obtained with SiO_2 filters.

Extrusion billets of the filatomized and commercial powders, and a commercial bar of 7075 aluminum alloy were made under conditions shown in Table XIV. All powder compacts except D, Table XIV, were preheated to $475^{o}C$ for 1 hour to lower gas content of the compact and prevent subsequent blistering and delamination during solution heat

treatment(81). All the billets were soaked at $300^{\circ}C$ for 4 hours and extruded at a reduction ratio of 20 to 1.

The transverse and longitudinal macrostructures of the as-extruded spherical filatomized powders are shown in Figures 70a and 70b respectively. The structure is fibrous with no observable porosity. Hardness measurements along the transverse (average R_B = 30.18) and longitudinal (average R_B = 44.78) sections of the bar differed consistently, caused by the texture developed during the extrusion. Figures 70c and 70d show the same structures at a higher magnification, the second phase particles are aligned along the extrusion axis.

The transverse and longitudinal macrostructures of the as-extruded filatomized flakes are shown in Figures 71a and 71b respectively. The structure is again fibrous with definite evidence of porosity. Figures 71c and 71d show the transverse and longitudinal structures of extruded commercially produced 7075 powders. The structure is fibrous with no observable porosity. All of the 7075 extrusions were heat treated to a T6 condition, which consists of a solution heat treatment to maximize solid solubility of the alloying elements and artificial ageing to cause precipitation hardening.

Samples of the extruded billet (filatomized spherical powders) were heat treated for various times and temperatures to determine the optimum solutionization temperature. Peak

aged condition was determined by following the solution heat treatment with natural ageing for 24 hours and artificial ageing at 129°C for 24 hours. A solution heat treatment of 2 hours at 475°C was found to maximize solid solubility of the alloying elements as shown in Figure 72. Also, the best hardness values were obtained for this solution treatment followed by the ageing condition reported above, Table XV. A scanning micrograph of a sample solutionized at 475°C for 2 hours, Figure 72e, illustrates the minimal distribution of a second phase particle. Figure 72f reveals that at higher temperatures, 490°C coarsening and liquation have occurred. Ageing kinetics data of the filatomized powders is given in Appendix E.

The solutionizing temperature of the commercial 7075 powder and ingot material with a nominal composition of Al-5% Zn-1.45% Cu-2.69% Mg-.17% Cr has previously been established(82) and, accordingly, these billets were solution heat treated for 2 hours at 460°C.

Billet E (Table XIV) was made from splat cooled flakes with a nominal composition of Al-7.5% Zn-2.4% Mg-1.0% Cu-.20% Cr-1.1% Fe-1.0% Ni and was included here for comparison.

2. Structure of Extruded 7075-T6 Billets

The structure of the commercial 7075-T6 billet F, Table XIV, is shown in Figure 73a. Large and well defined grains with a distribution of coarse (8-10μ) second phase particles are seen. The transverse microstructures of

extruded 7075-T6 powders are shown in Figure 73. Figures 73b
and 73c show the structures from billets D and C (Table
XIV), respectively. The marked difference in porosity
content of the two billets is evident(81). Structure of
extrusion of filatomized flakes, billet B, is shown in
Figure 73d. Finally, the transverse and longitudinal micro-
structures of the extrusion made from filatomized spherical
powders, billet A (Table XIV) are shown in Figure 74.

Although both flakes and powders were preheated at
$890^{\circ}F$ (1 hour) prior to extruding, it can be seen comparing
Figures 73d and 74 that the filatomized flakes contain a
large amount of porosity, whereas the spherical powders do
not. The resulting porosity in the filatomized flakes
(billet #B) can be caused by (i) the large surface oxide
content of the flakes which causes poor bonding and thus
acts as crack initiation sites, and/or (ii) the
characteristic morphology of the flakes which causes
inefficient and poor compaction.

It can be seen that the spherical filatomized powders
which possess a minimum surface area to volume ratio, (i.e.,
minimum amount of oxide and surface contaminants) and have
favorable packing characteristics, gave the soundest extrusion
billet.

Metallographic investigation of the extrusions of
commercial 7075 powder has revealed that porosity appeared
immediately after the water quench and remained during the

subsequent ageing treatments, Figures 73b and 73c. This

porosity (blistering) is believed to be caused by the gas

content of the extrusion. The gas present is predominantly

hydrogen dissolved or adsorbed during the filatomization

process (from H_2O and hydrates on surface of powders) and

subsequent handling. The hydrogen remaining after the

extrusion is (i) dissolved in the matrix, and/or (ii) adsorbed

at grain boundaries and original pore sites. Upon quenching,

the solubility of the gas is suddenly decreased markedly,

hence causing the formation of gas pockets between the grains.

It has been shown(81) that preheating the billet prior to

extrusion can lower the gas content of the compact to prevent

subsequent blistering and delamination, the amount of

hydrogen remaining being inversely proportional to the preheat

temperature.

A marked difference in porosity (blistering) content

can be seen between samples #D (no preheat) and #C (with

preheat), as illustrated in Figures 73b and 73c. The small

amount of porosity observed for the preheated billet, (#C,

and Figure 73c) is believed to be caused by either

(i) insufficient thermal activation (low preheat temperature),

thus resulting in incomplete removal and inefficient lowering

of H_2 content, and/or (ii) deposition of Al_2O_3 at the grain

boundaries due to decomposition of $Al_2O_3 - 3H_2O$ to $\gamma-Al_2O_3$

thus causing weak bonding sites.

D. Mechanical Properties

The room temperature longitudinal tensile properties of the 7075-T6 extrusions are given in Table XVI. The values listed are average values from multiple tests*. All tests were run at a cross-head speed of 0.05 inch/minute. The following observations can be made from Table XVI:

(i) The highest reduction in area (42.4%) and elongation (15.1%) values were obtained in the extrusion made from filatomized spherical powders.

(ii) The best corresponding values for the extruded billet made of commercial powders were 11-14% and 7-9%, respectively.

(iii) The 7075-T6 extrusion made of round bar stock had a slightly higher yield stress, but lower ductility than the filatomized powder extrusion.

(iv) The filatomized flake and splat cooled flake extrusions had relatively lower ductilities. However, the extrusion of splat cooled flakes had the highest strength properties.

Figures 75a-c show SEM fractographs of the 7075-T6 extrusion of filatomized spherical powders, billet A, (Table XIV). The fracture is ductile without any

---

*   Table XVII lists tensile test results of all the samples.

delaminations, Figure 75a, with the second phase particles attached to the ductile voids, Figures 75b and 75c. Figures 75d-f show SEM fractographs of the 7075-T6 extrusion of the filatomized flakes, billet B, (Table XIV). Severe delaminations associated with porosity are observed. Figures 75e and 75f are high magnification fractographs of a ductile region and surface of the delaminations, respectively.

SEM fractographs of the 7075-T6 extrusion of commercial powders, billet C, (Table XIV), are shown in Figures 76a-c. Delaminations accompanied by large regions that have fractured in a ductile manner are shown in Figure 76c. Second phase particles which have remained within the voids are shown in Figure 76c.

SEM fractographs of the 7075-T6 extrusion of splat cooled flakes, billet E (Table XIV), are shown in Figures 76d-f. Figure 76d shows few delaminations accompanied by large regions fractured in a ductile manner. The fibrous nature of the delamination wall, and the fine constituent second phase particles within the voids are shown in Figures 76e and 76f, respectively.

The filatomized spherical powders and flakes had undergone the same thermomechanical processing. However, the properties obtained differ markedly due to the oxide content and morphology of these powders. More specifically:

(i) The flakes have a higher surface area to
volume ratio, and thus a higher oxide content.

(ii) During compaction, the surface oxide on the
walls of the flakes causes weak bonding. The
poor bonding of the oxide walls accompanied
with longitudinal porosity, caused by the heat
treatment, results in coarse fibrous
delaminations.

(iii) Spherical powders pack more efficiently than
do the flakes, sinter more completely, and
contain a lower amount of porosity.

The superior ductilities measured in the extrusions
made from filatomized spherical powders can be attributed
to removal of oxide particles during "filatomization" and to
the spherical morphology of the powders.

E. Summary

Pure Al and 7075 powders of spherical and flake
morphology were made using Al_2O_3 and SiO_2 filters with
40-150μ pore size ranges. The range of metal drops forming
below the filter is governed by (i) pore size and composition
of the filter material, (ii) the temperature of filatomization,
and (iii) the applied pressure.

(i) Channeling within the filter permits formation
of drops without consolidation of the emerging
streams. The extent of wetting between the
liquid metal and the filter employed is important.

(ii) Size range of powders is influenced by the amount
of superheat in the melt. Increasing superheat
results in formation of larger drops.

(iii) The pressure range required for filatomization
(i.e., 2-6 psi) can easily be accommodated by a
hydrostatic head on the melt.

An alternative method is one where the area below the
filter is exposed to a partial vacuum. One attractive aspect
of this process is that filtration of undesirable second
phases and oxides occurs simultaneously with powder formation.

In all the experiments reported herein, aluminum oxide
skins and "cakes" were found immediately above the filter.
This is an important advantage of this process, since the
presence of oxides has detrumental effects on the properties
of the material. An alternative process is one in which
filtration is combined with inert gas atomization. In this
process, higher pressures would be employed to form
consolidated metal streams below the filter. One or more
inert gas jets directed toward the exiting liquid metal
streams would then cause atomization.

The microstructures of the spherical powders produced
by filatomization were found to be superior to the commercially
produced powders, in particular, for their lack of porosity,
fineness of structure, favorable morphology, and low oxide
content. An extruded billet of this powder in T6 condition
was prepared to investigate the feasibility of using

filatomized spherical powders for conventional PM processing operations. The structure of the billet after a T6 treatment was superior to all the other materials used. As a consequence, the extruded billet of this powder had a comparable strength and much higher ductility than all other extrusions used in this study.

Table XIV

Processing of 7075-T6 Extrusions

billet designation	starting material	treatment prior to extrusion	extrusion	solution heat treatment	ageing
A	filatomized 7075 spherical powders	1 hour at 475°C under vacuum + 4 hours at 300°C	20:1 at 300°C	2 hours at 475°C	24 hours at 129°C
B	filatomized 7075 flakes	"	"	"	"
C	commercial 7075 powder	"	"	2 hours at 460°C	"
D	commercial 7075 powder	4 hours at 300°C	"	"	"
E*	modified 7075 splat cooled flakes	1 hour at 490°C under vacuum + 4 hours at 300°C	"	2 hours at 490°C	"
F	7075-T6 round bar	4 hours at 300°C	"	2 hours at 460°C	3 days at room temperature + 24 hours at 129°C

---

*   From J. P. Durand (63)

Table XV

Hardness Measurements after Different Heat Treatments
of Extruded Billets of Filatomized Powders

heat treatment	after water quench		after natural ageing: (24 hours at R.T.)		after artificial ageing (24 hours at 129°C)	
	R_B(long)	R_B(trans)	R_B(long)	R_B(trans)	R_B(long)	R_B(trans)
2 hours at 470°C	28	16.5	42.5	26	51	48
2 hours at 475°C	30	17	61	41	78	68
4 hours at 475°C	34	14.5	61.5	39	72	59
2 hours at 480°C	30.5	13	61	44	77	64
4 hours at 480°C	33	17	68	42	77	61
2 hours at 485°C	31	4	64.5	50	71	49
4 hours at 485°C	15	off scale	57	52	70	53
2 hours at 490°C	26	9	55	48	72	53
4 hours at 490°C	7.5	off scale	42	12	71	46

Table XVI

Tensile Test Results

sample	yield stress (psi)	UTS (psi)	elongation %	reduction of area %	remarks
A	80,000	94,300	15.1	42.4	Filatomized 7075-T6 spherical powders ductile fracture with no delaminations
B	78,000	90,200	8.2	12.0	Filatomized 7075-T6 flakes many fine delaminations accompanied by regions of ductile fracture, few coarse delaminations
C	75,000	87,300	7.8	11.5	Commercial 7075-T6 powder few delaminations with large regions fractured in a ductile m nner
D	68,200	81,900	9.0	13.9	Commercial 7075-T6 powder severe delaminations accompanied by regions of ductile fracture
E*	90,750	102,000	8.6	17.5	Splat cooled flakes of a modified 7075-T6 alloy ductile fracture with few fine delaminations
F	86,200	93,000	11.2	32	7075-T6 round bar

*   from J. P. Durand (63)
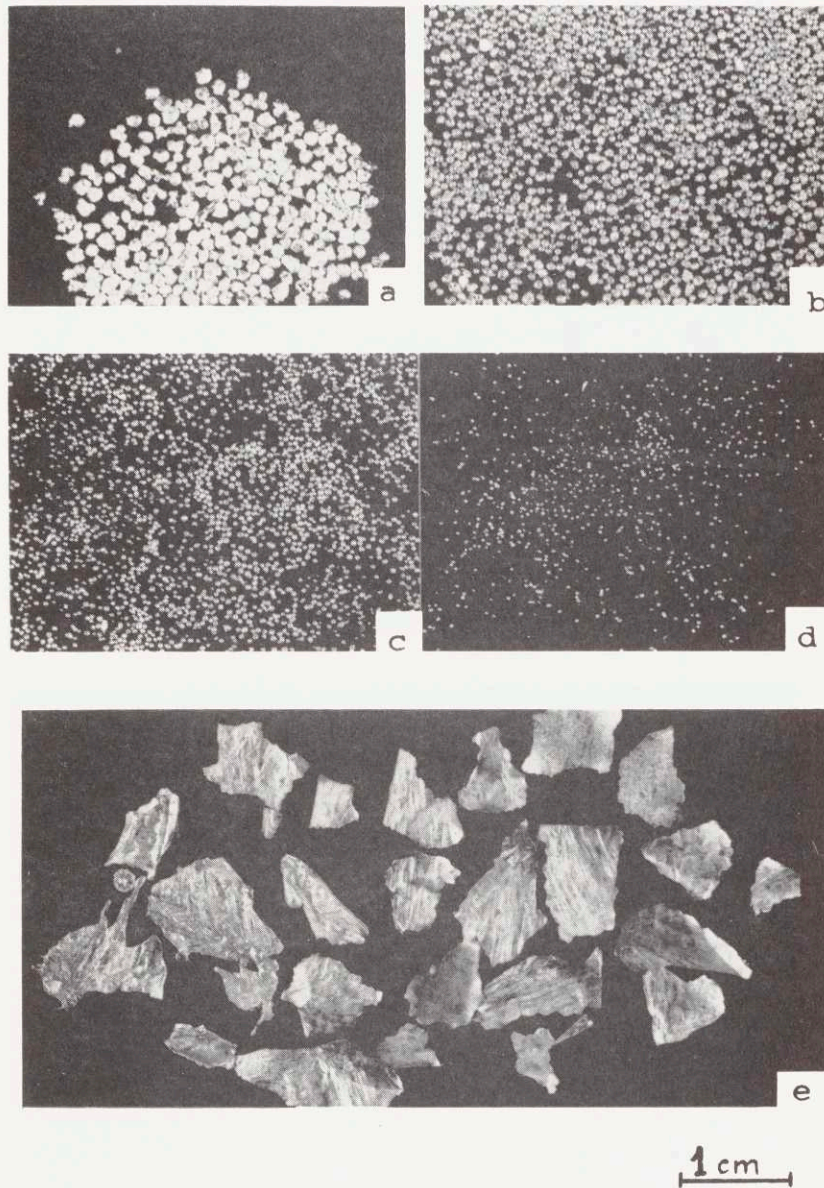
Figure 54: Filatomized powders of pure aluminum and 7075
aluminum alloy; (a) through (d) show pure
aluminum powders produced by utilizing an Al_2O_3
filter, Run #1, mesh sizes are −16+20, −20+30,
−30+50, and −50+100, respectively, (e) flakes of
7075 alloy produced utilizing a SiO_2 filter,
Run #18, mesh size is −8+14.
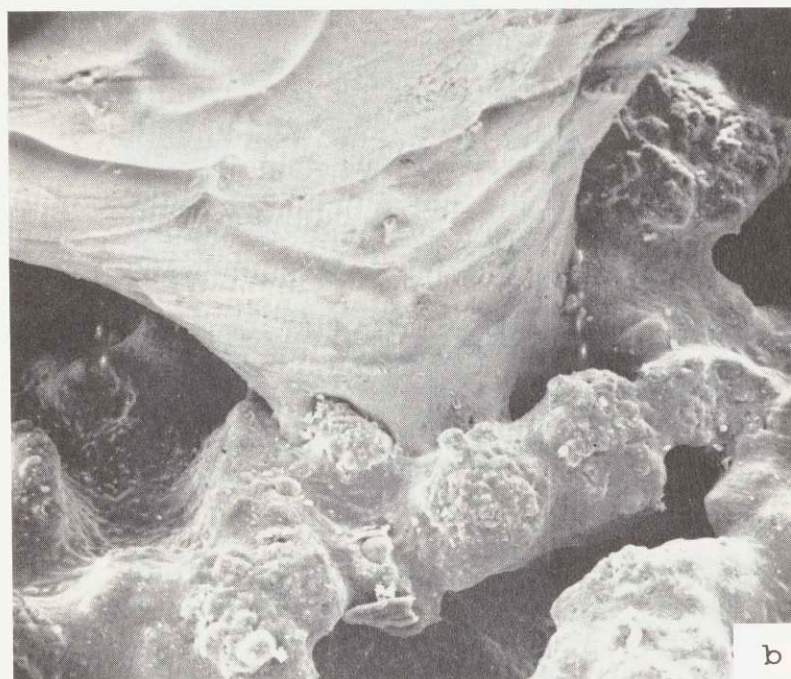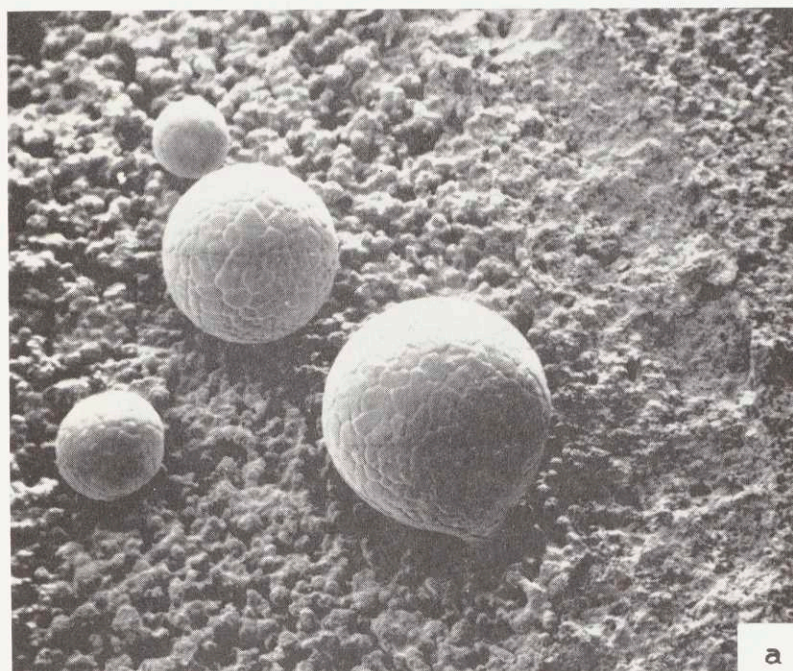
Figure 55: SEM view of pure aluminum powders emerging from
a sintered Al_2O_3 filter, Run #1; (a) 23X, (b) 208X.
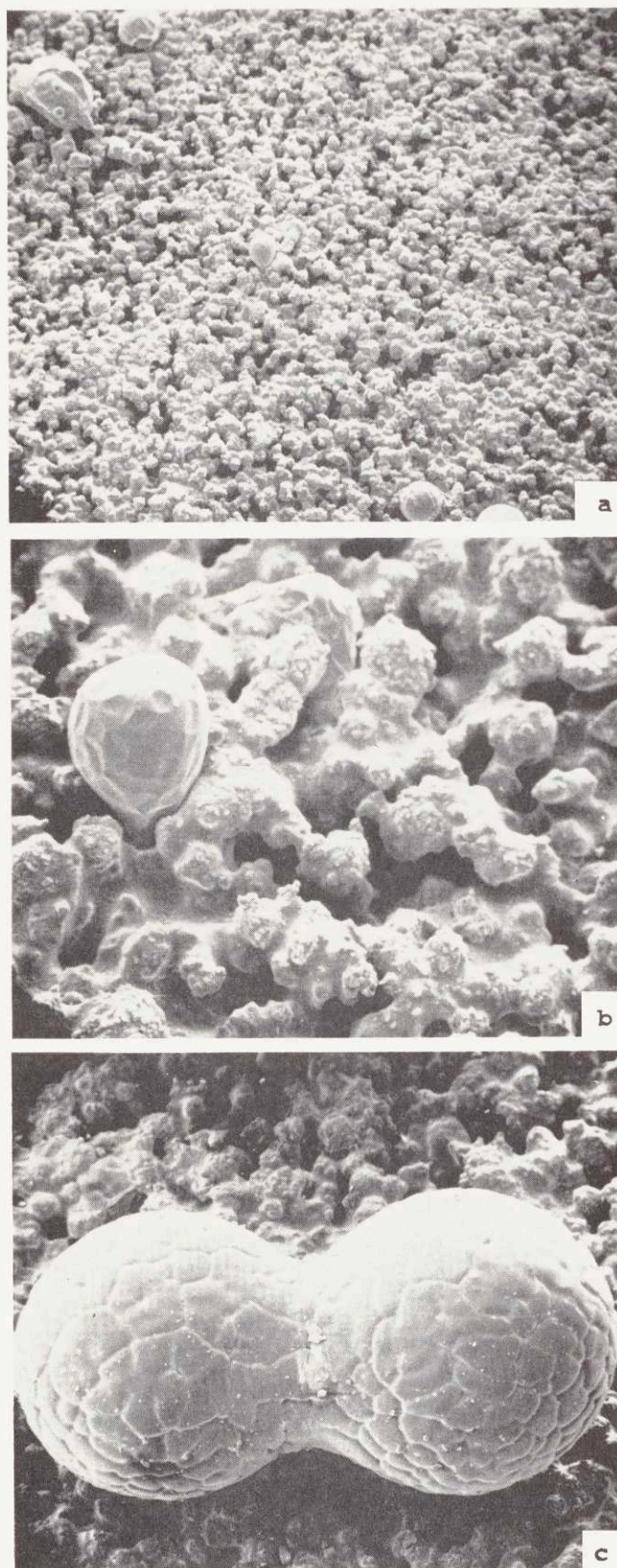
Figure 56. SEM view of pure aluminum powders emerging from
a sintered Al_2O_3 filter; (a) and (b) are from
Run #17 at 20X and 90X, respectively, (c) is from
Run #19 at 75X.
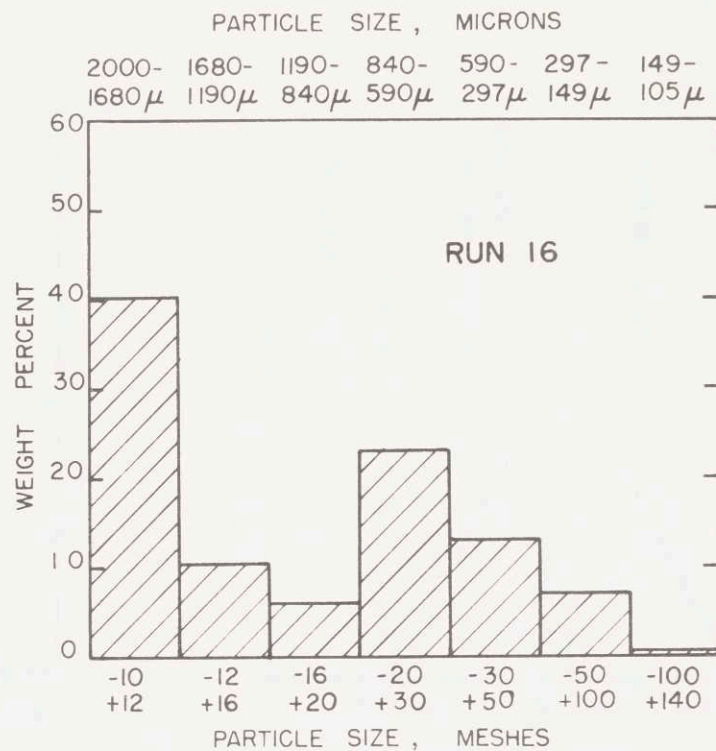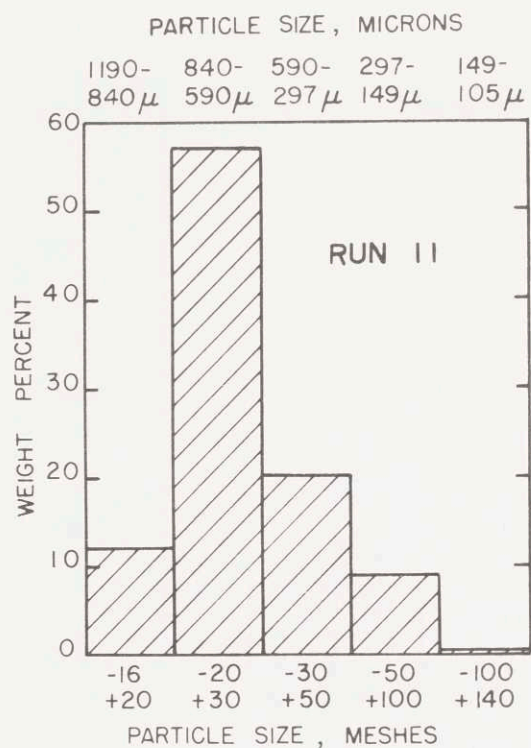
Figure 57   Size distributions of spherical 7075 aluminum alloy
powders made utilizing Al_2O_3 filters; (a) Run #11,
$T_F=700°C$, (b) Run #16, $T_F=742°C$.
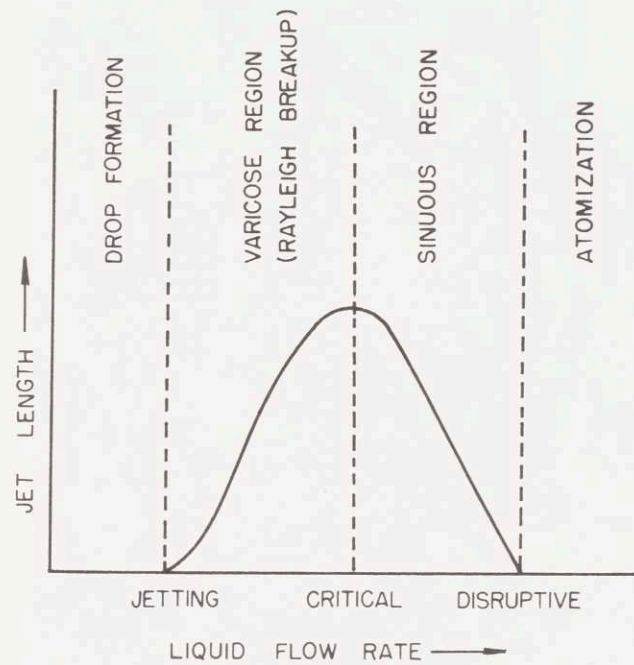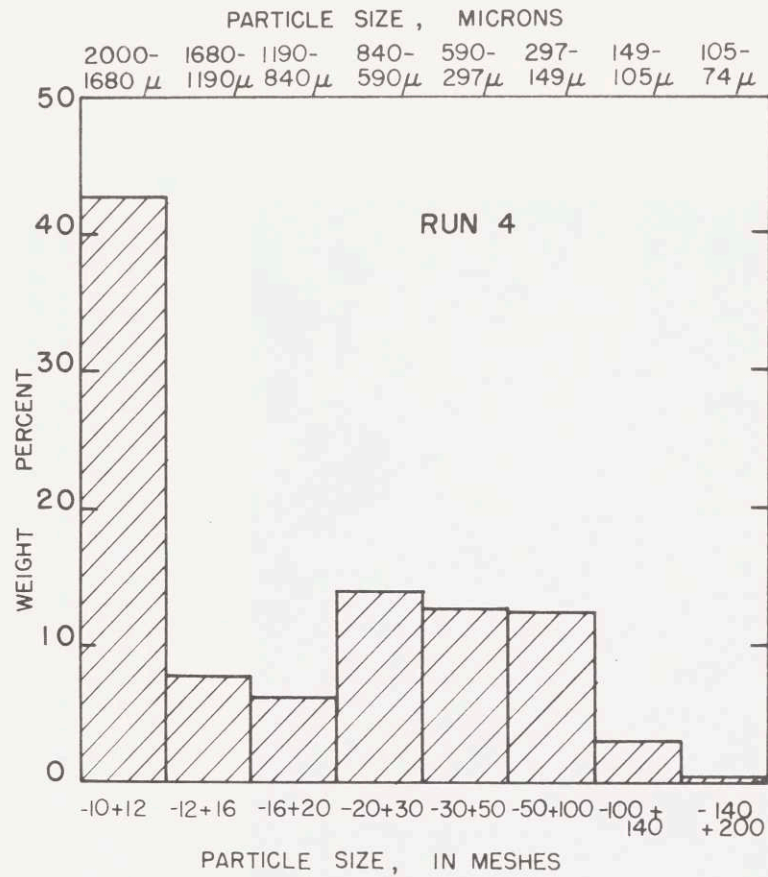
Figure 58   (a) Size distribution of spherical 7075 aluminum alloy powders made utilizing an SiO$_2$ filter, Run #4; (b) effect of flow rate on formation of drops at the tip of a vertical tube.[5]
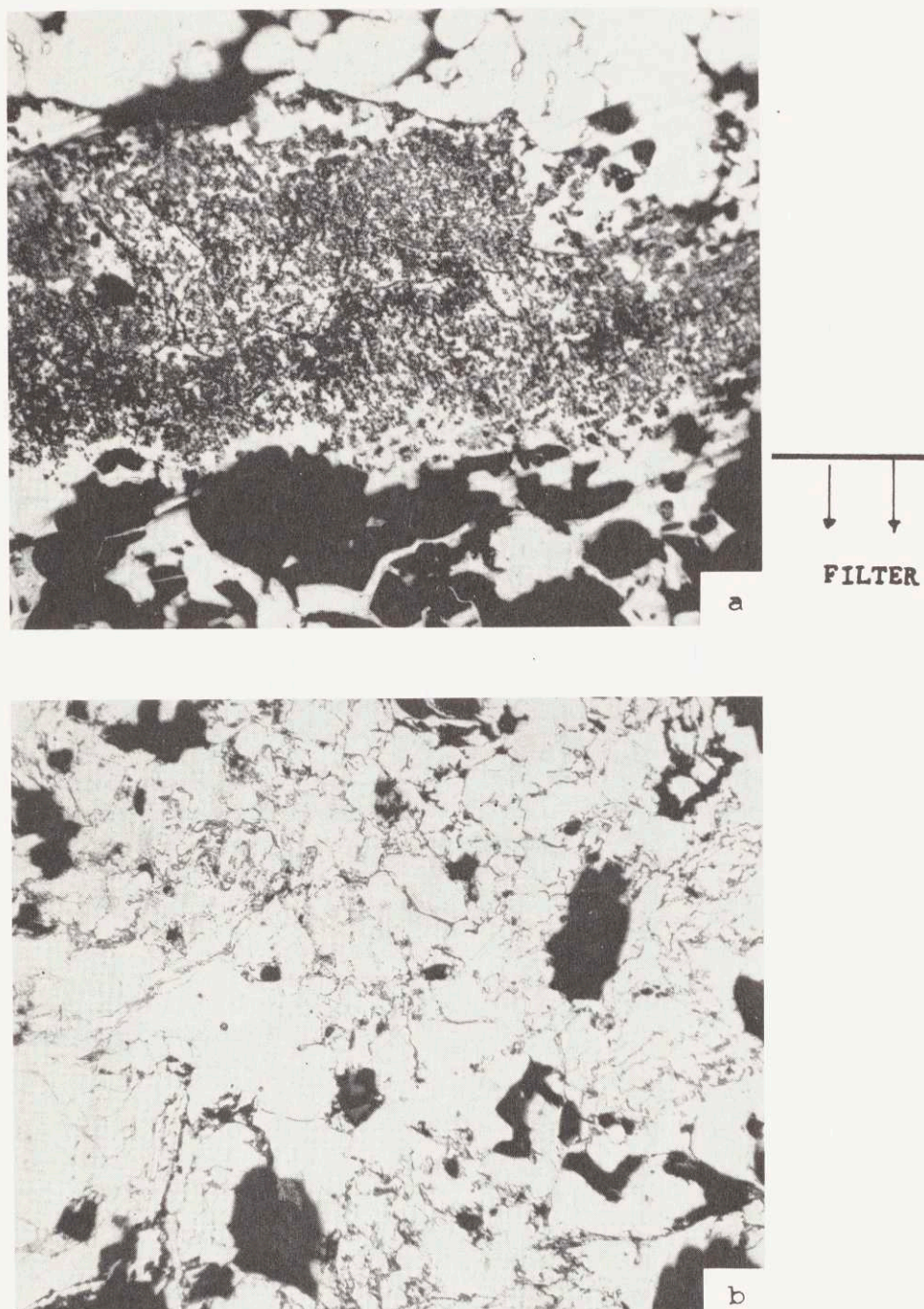
FILTER

Figure 59   Photomicrographs showing filtration of aluminum oxides
from 7075 aluminum alloy melts; (a) oxide "cake"
observed above the SiO_2 filter used in Run #4, 80X,
(b) oxide skins retained above the Al_2O_3 filter used
in Run #16, 100X.
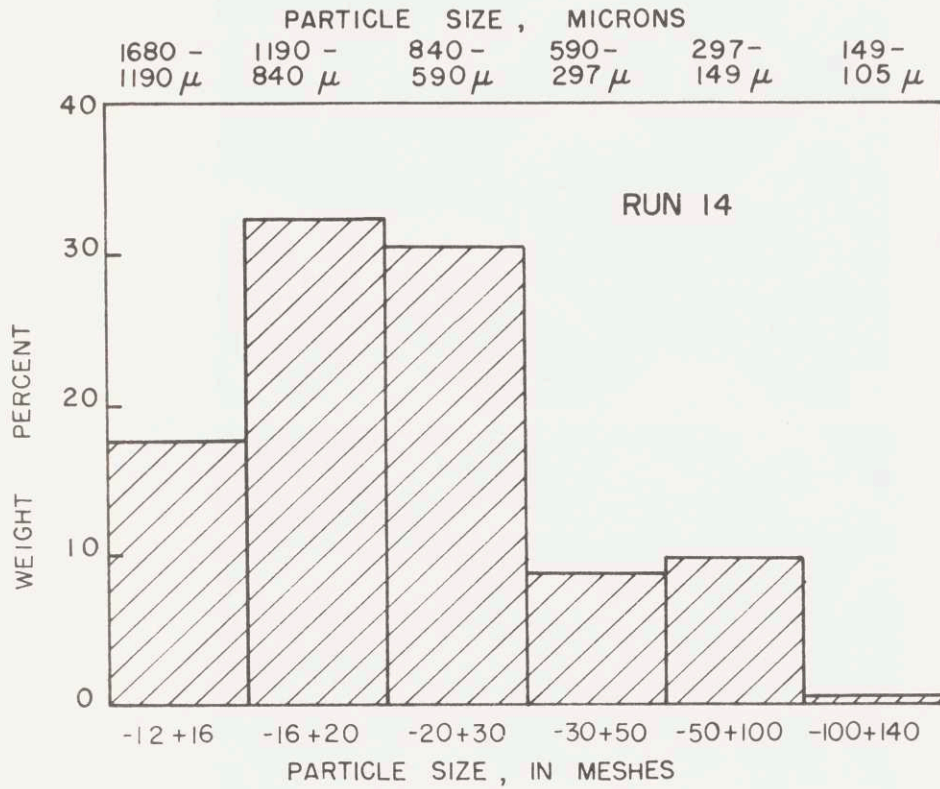
Figure 60   Size distribution of spherical 7075 aluminum alloy powders made in Run #14.
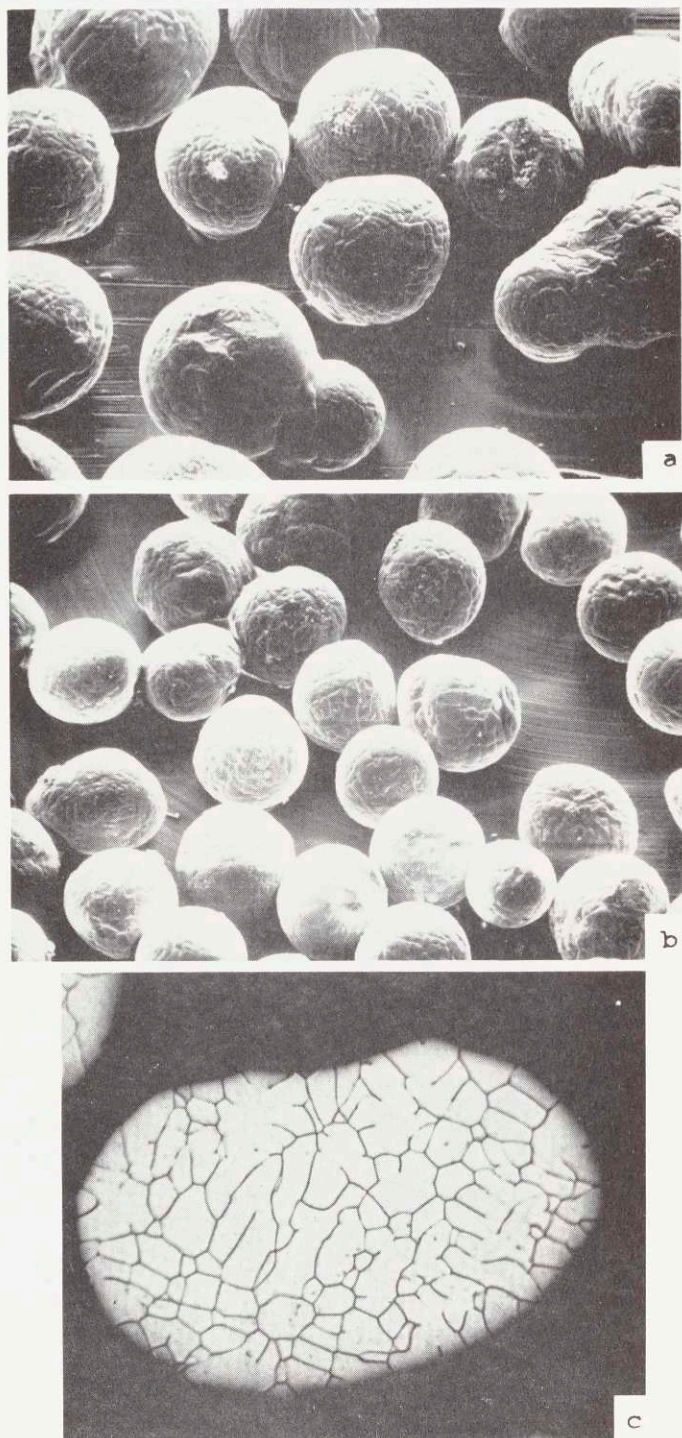
Figure 61: Structures of filatomized pure aluminum powders made in
Run #1; (a) SEM view of ~300μ size powders, 51X, (b) SEM
view of ~150μ size powders, 20X, (c) a representative
microstructure of the powders
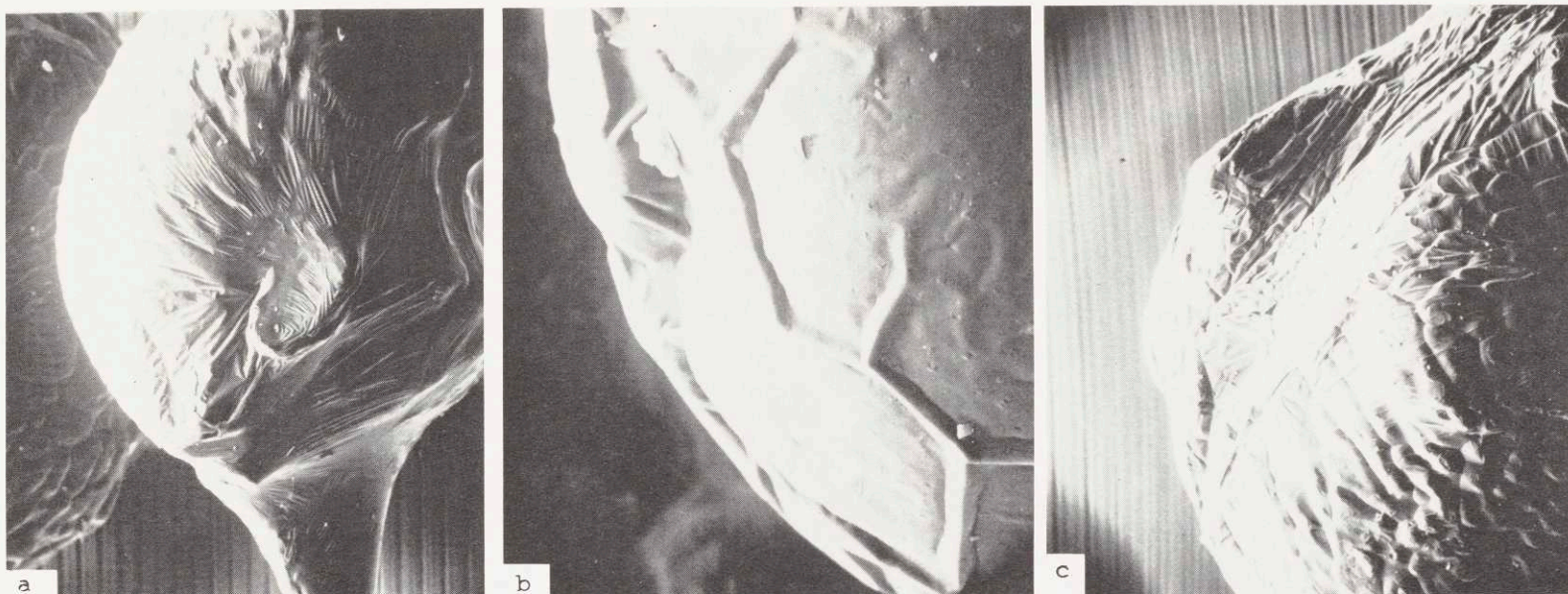
Figure 62. Surface irregularities of filatomized pure aluminum powders; (a) Run #1, 590X, (b) Run #17, 500X, (c) Run #19, 590X.
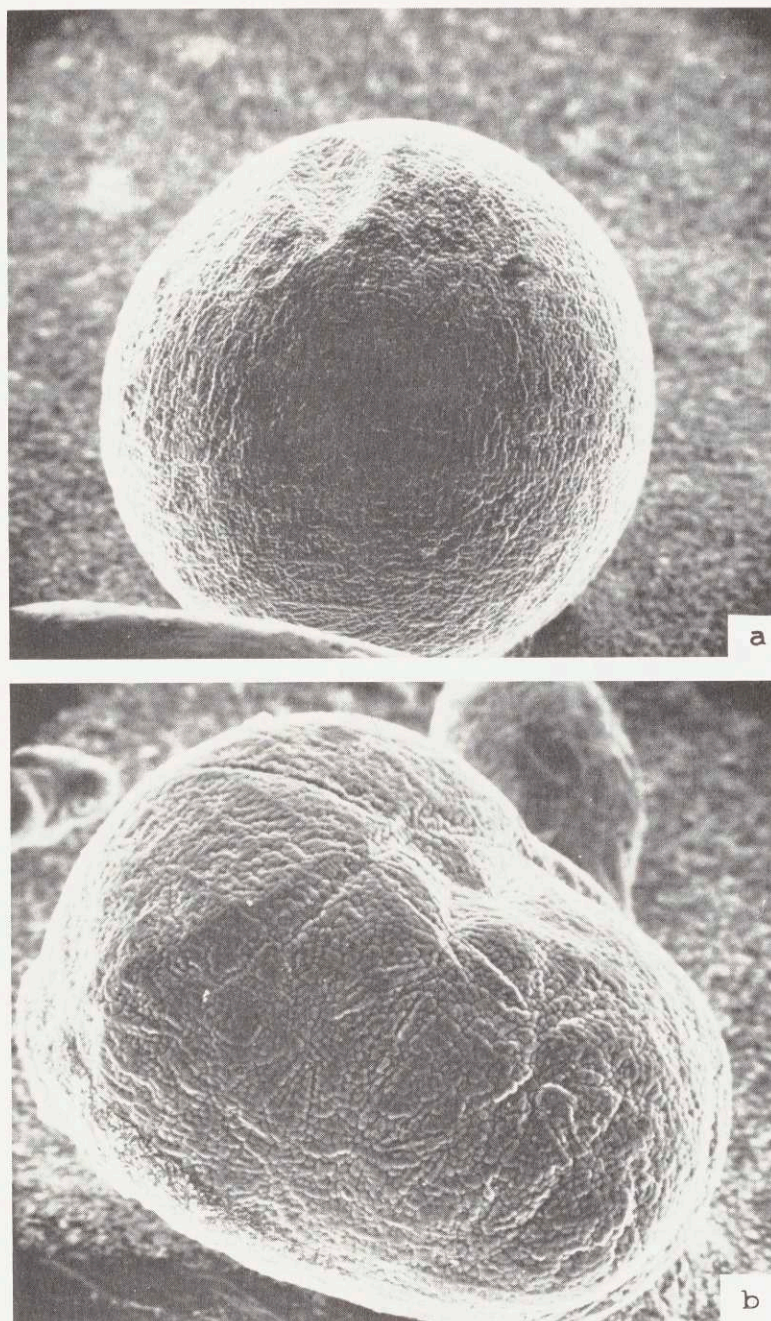
Figure 63: SEM view of filatomized spherical powder of 7075
aluminum alloy made in Run #16; (a) 110X, (b) 200X.
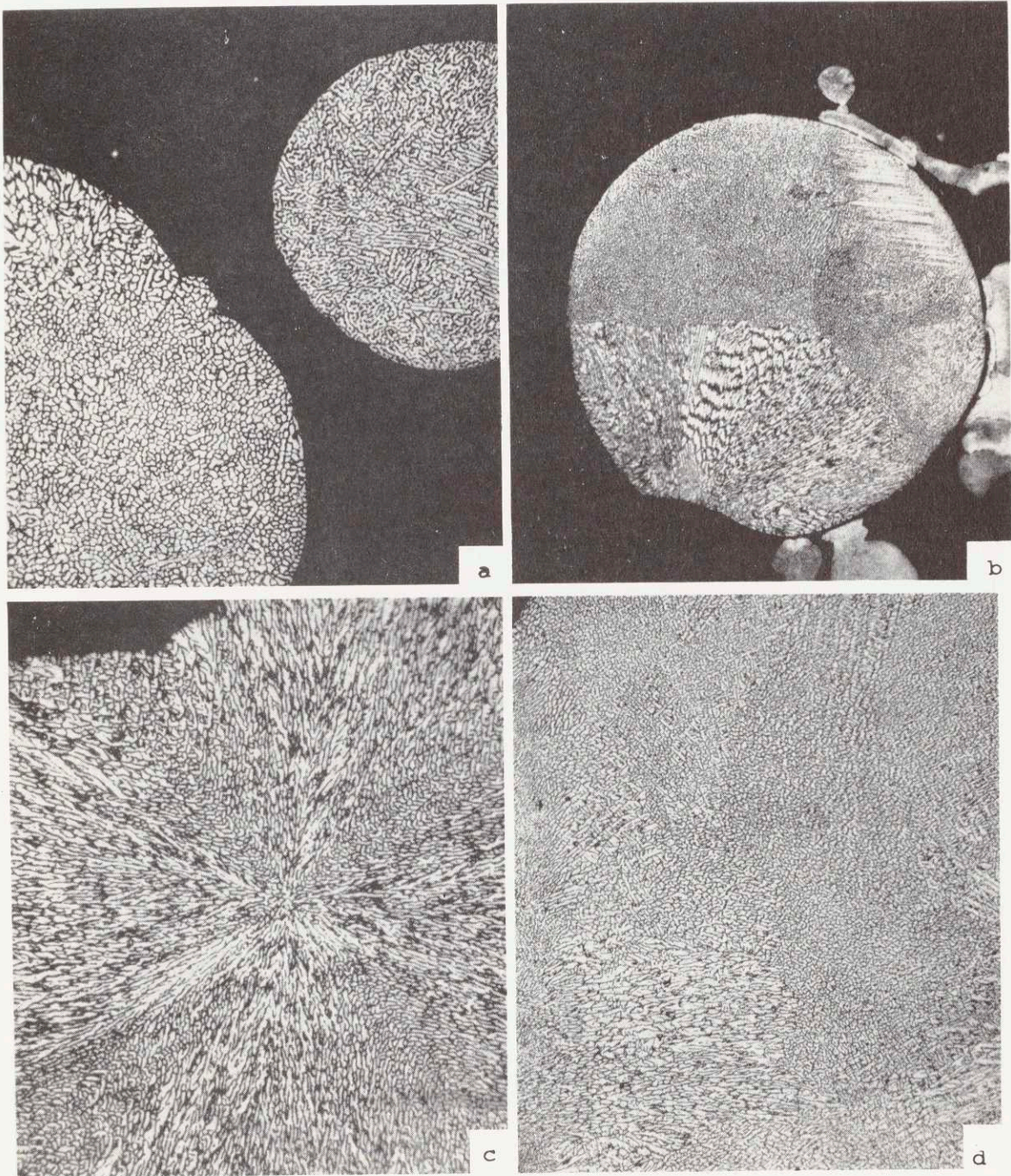
Figure 64   Microstructures of filatomized spherical powders of 7075 aluminum
alloy obtained from different experiments; (a) Run #6, 100X,
(b) Run #11, 100X, (c) Run #18, 200X, (d) Run #16, 100X.
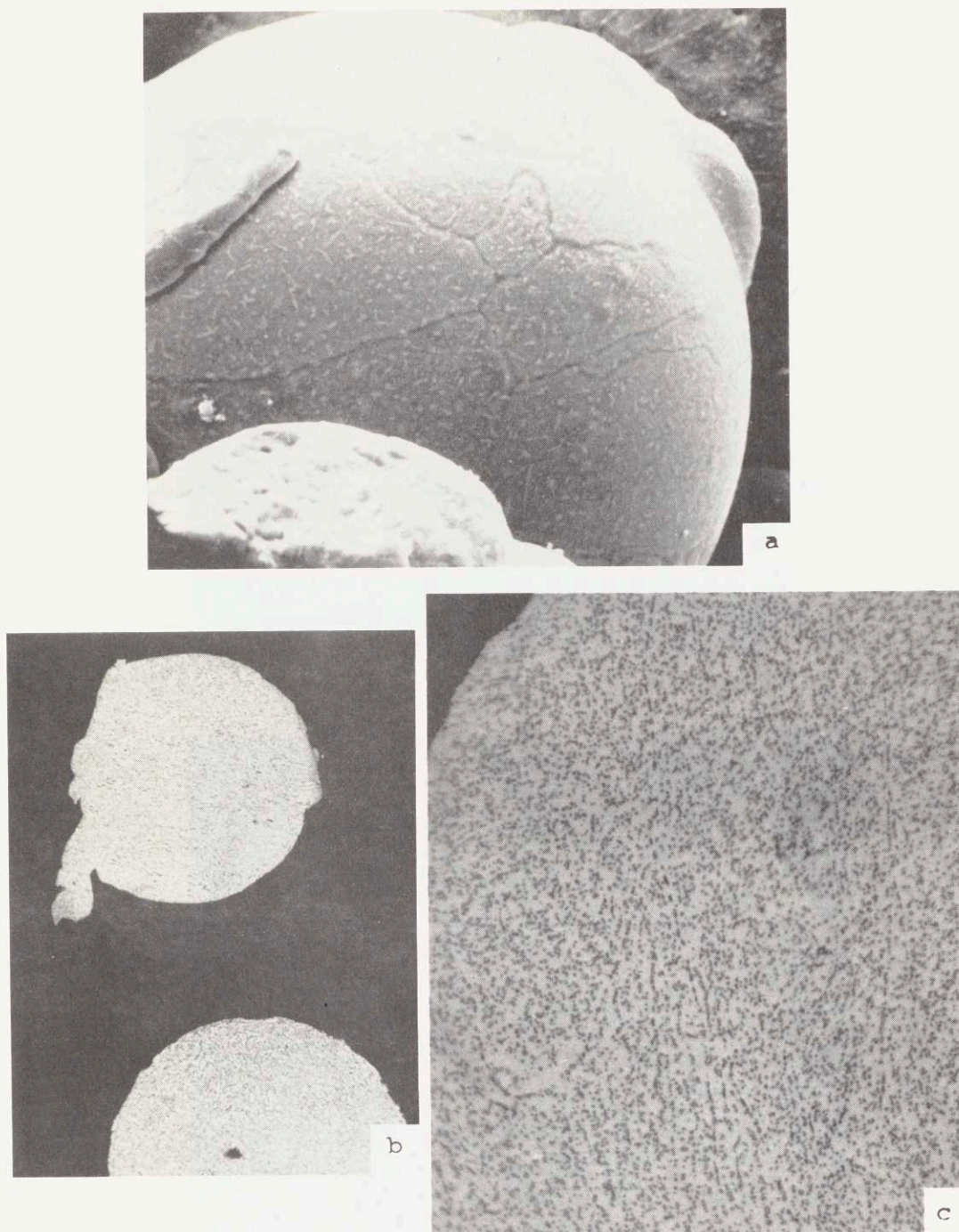
Figure 65: Structure of filatomized spherical powders of 7075 aluminum
alloy made in Run #11, (a) SEM view of a powder, 540X, (b)
and (c) show the microstructure of the powder at 100X and
500X, respectively.
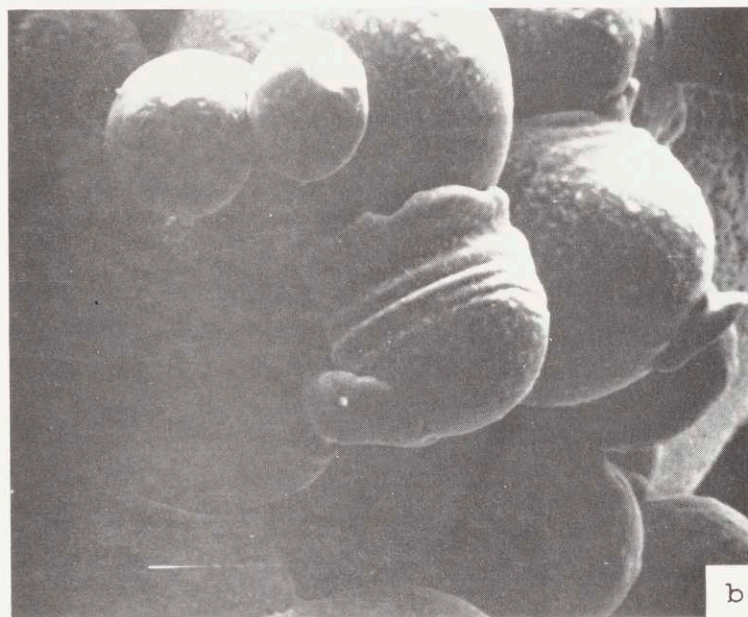
Figure 66. Powders of 7075 aluminum alloy made in Run #11;
(a) 1000X, (b) 500X.
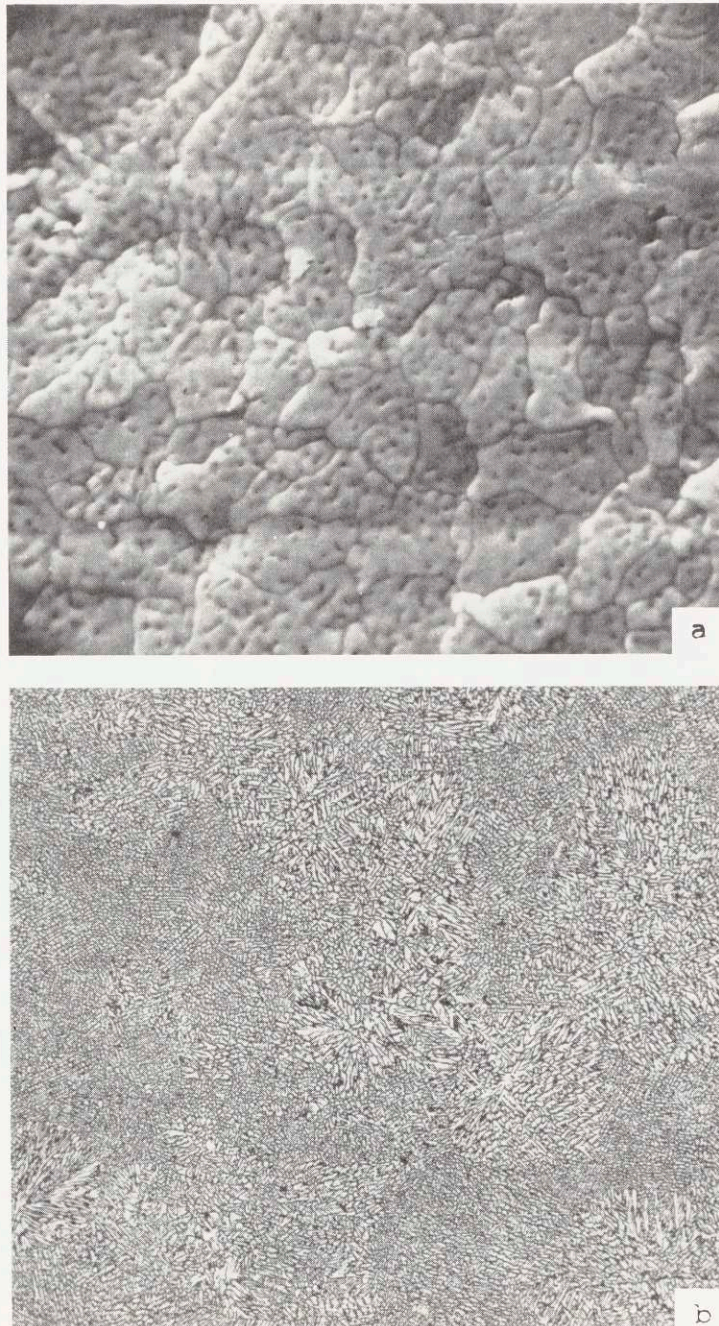
Figure 67   Structure of a filatomized flake of 7075 aluminum
alloy made in Run #8; (a) SEM view, 2300X,
(b) "duplen" dendritic structure due to sudden
variation in cooling rate, 100X.
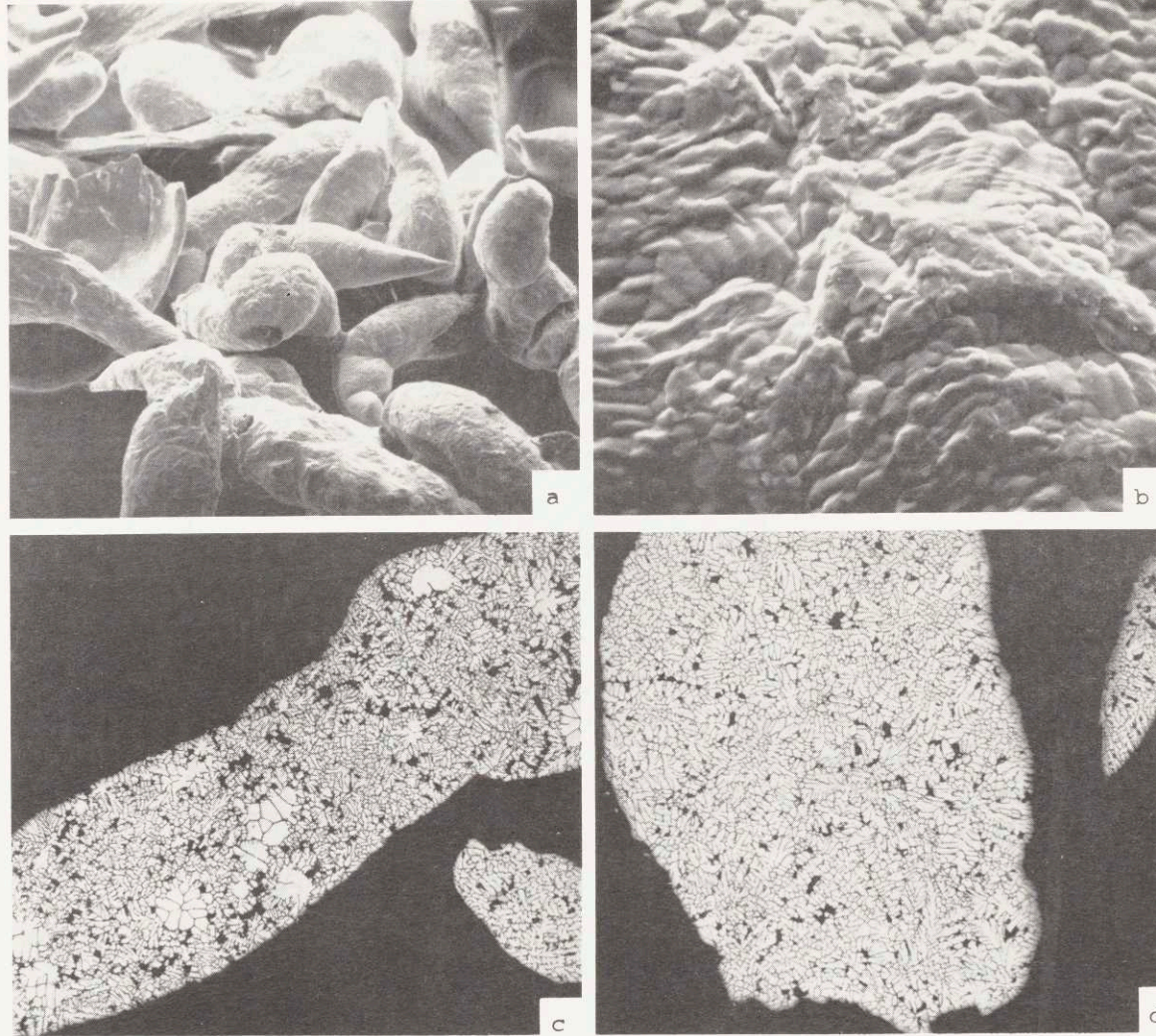
Figure 68: Structure of commercial 7075 aluminum alloy powders; (a) and (b) are SEM views at 24X and 585X, respectively, (c) and (d) show microstructure of the powders at 100X.

PARTICLE SIZE , MICRONS

| 2000- | 1680- | 1190- | 840- | 590- | 297- | 149- | 105- |
| 1680μ | 1190μ | 840μ | 590μ | 297μ | 149μ | 105μ | 74μ |
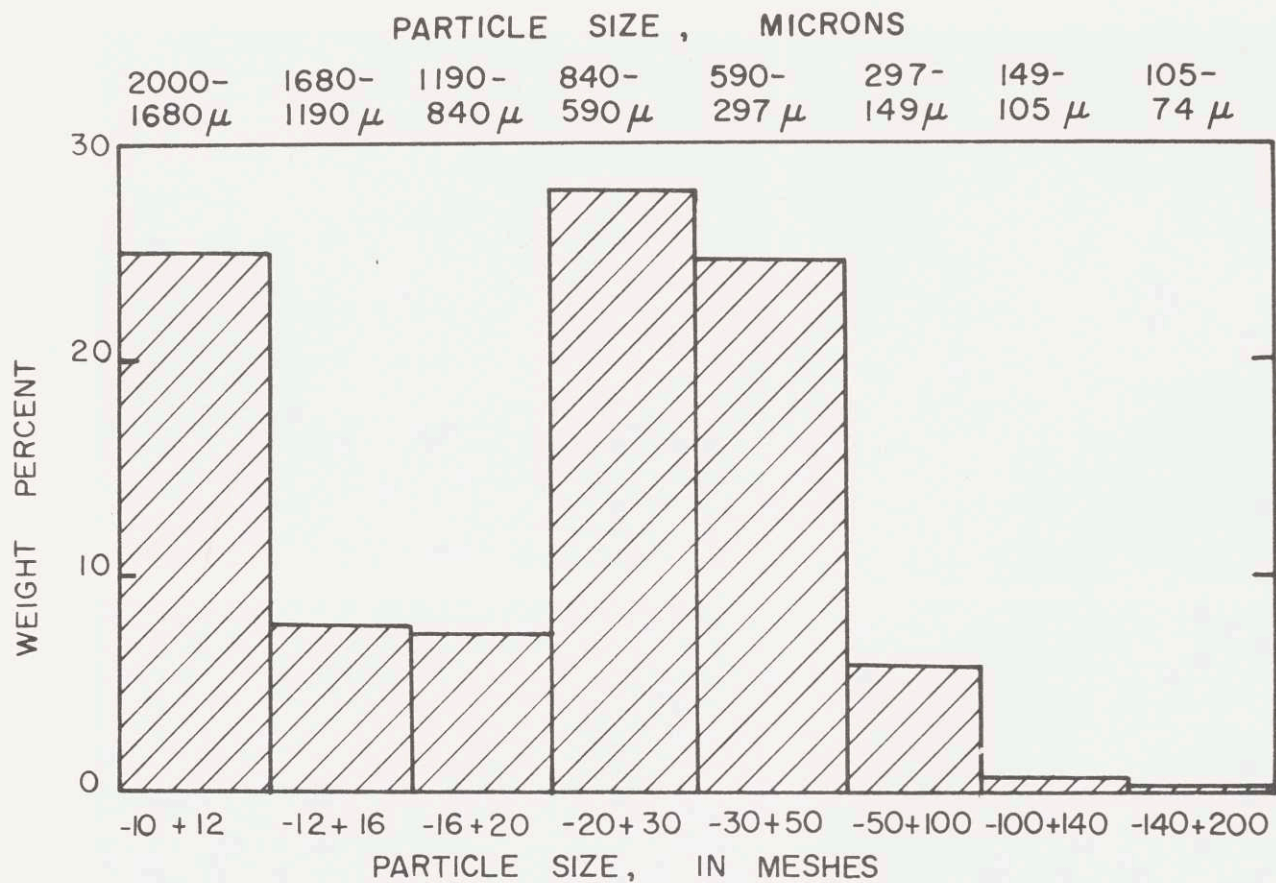
Figure 69.   Size distribution of filatomized 7075 powders used in the extrusions.
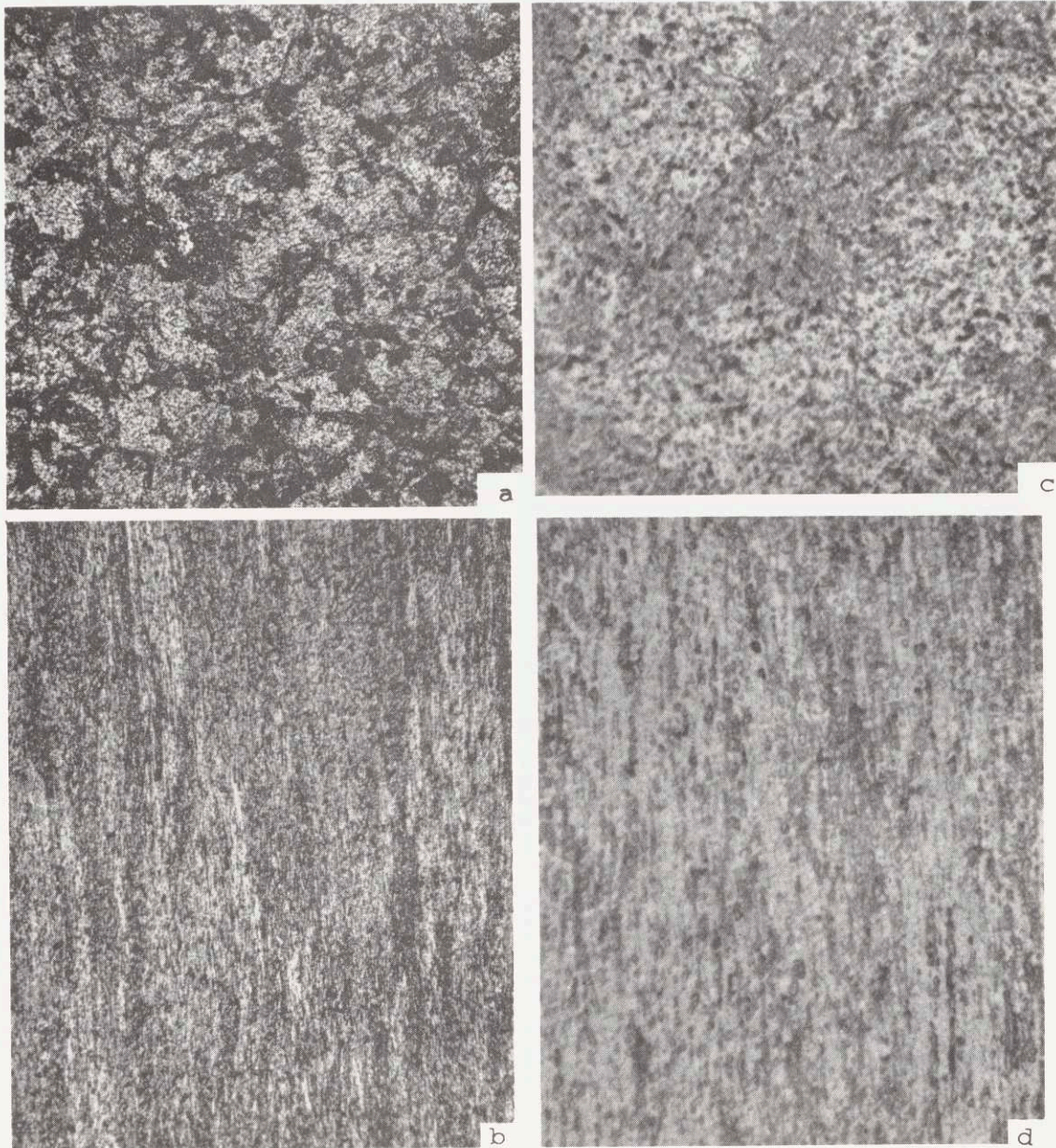
Figure 70 : Structure of extruded billet made from filatomized spherical
powders of 7075 aluminum alloy; (a) and (c) show the trans-
verse microstructure at 100X and 500X, respectively, (b) and
(d) show the longitudinal microstructure at 100X and 500X,
respectively.
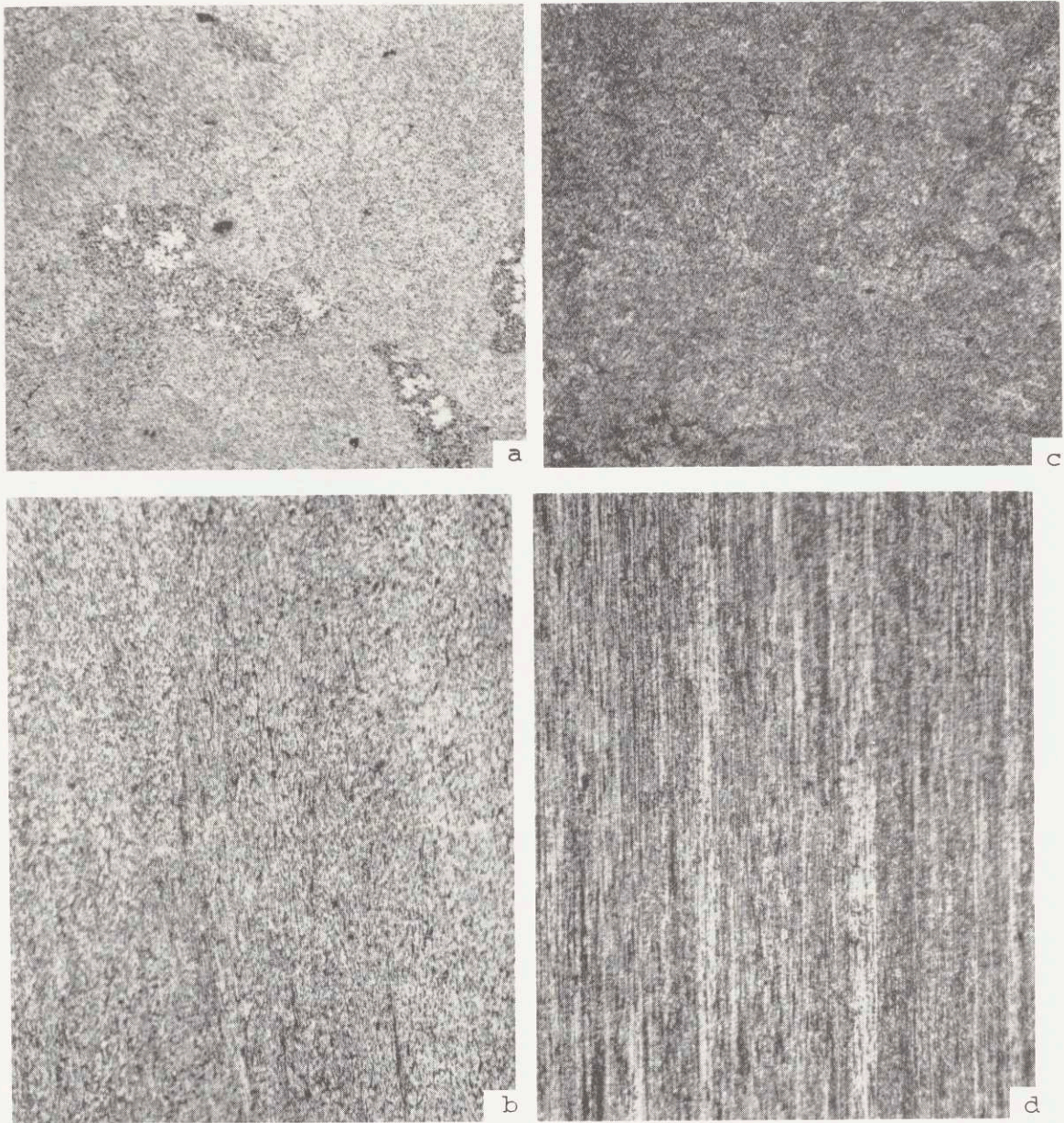
Figure 71: Structure of extruded billets of 7075 aluminum alloy powders;
(a) and (b) show transverse and longitudinal microstructures
of the billet made from filatomized flake, 100X, (c) and (d)
show transverse and longitudinal microstructure of the billet
made from commercial powders, 100X.
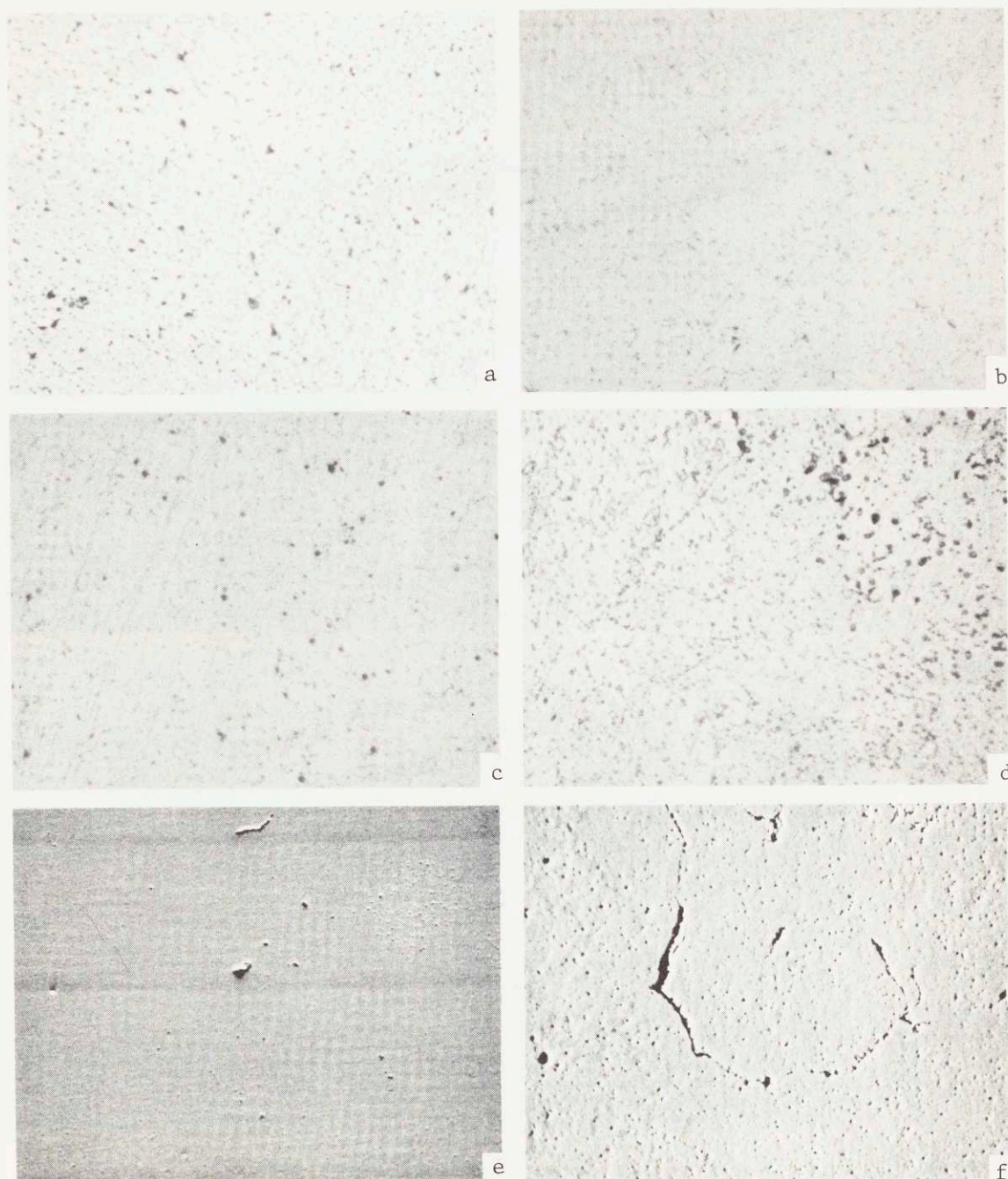
Figure 72. Microstructures of the extruded billet of 7075
aluminum alloy of filatomized spherical powders,
in different solutionized conditions, 500X; (a),
(b), (c), and (d) are from samples solutionized
for 2 hours at 470°C, 475°C, 480°C and 490°C,
respectively; (e) SEM view of solutionized sample
for 2 hours at 475°C, 220X;(f) SEM view of solu-
tionized sample for 2 hours at 490°C, 400X.
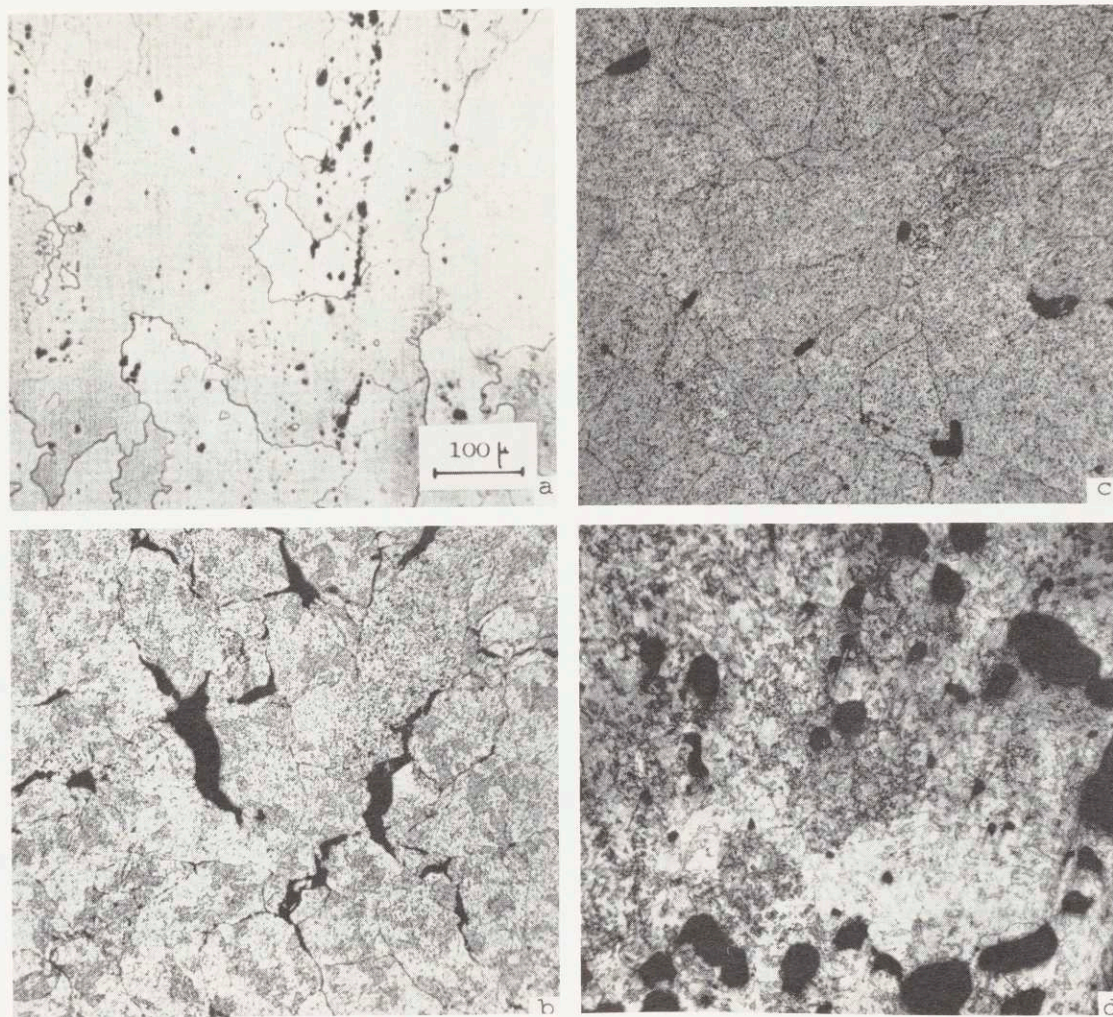
Figure 73: Transverse microstructures of 7075 - T6 extrusions reported
in Table II; (a) commercial bar stock, billet F, 150X, (b)
and (c) are extrusions of commercial powders D and C,
respectively, 100X, (d) extrusion of filatomized flakes,
billet B, 100X.

Figure 74: Microstructure of 7075 – T6 extrusion made from filatomized spherical powders, billet A (Table II), 100X; (a) transverse section, (b) longitudinal section.
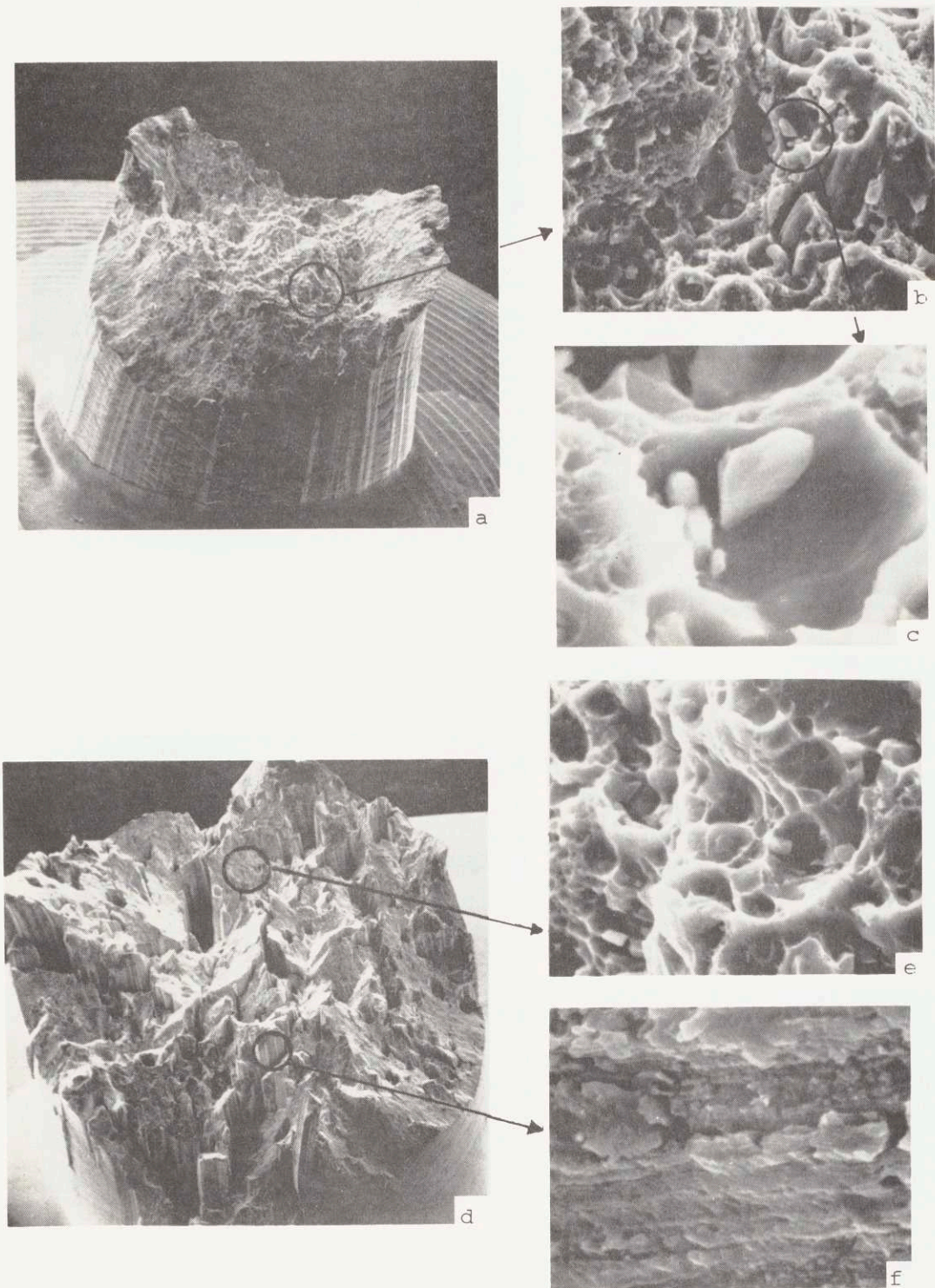
Figure 75: (a),(b),(c) SEM fractographs of 7075-T6 extrusion
          of filatomized spherical powders, billet A (Table II),
          20X,950X, 4750X, respectively.
          (d),(e),(f) SEM fractographs of 7075-T6 extrusion
          of filatomized flakes, billet B (Table II),
          23X,2300X,2300X, respectively.
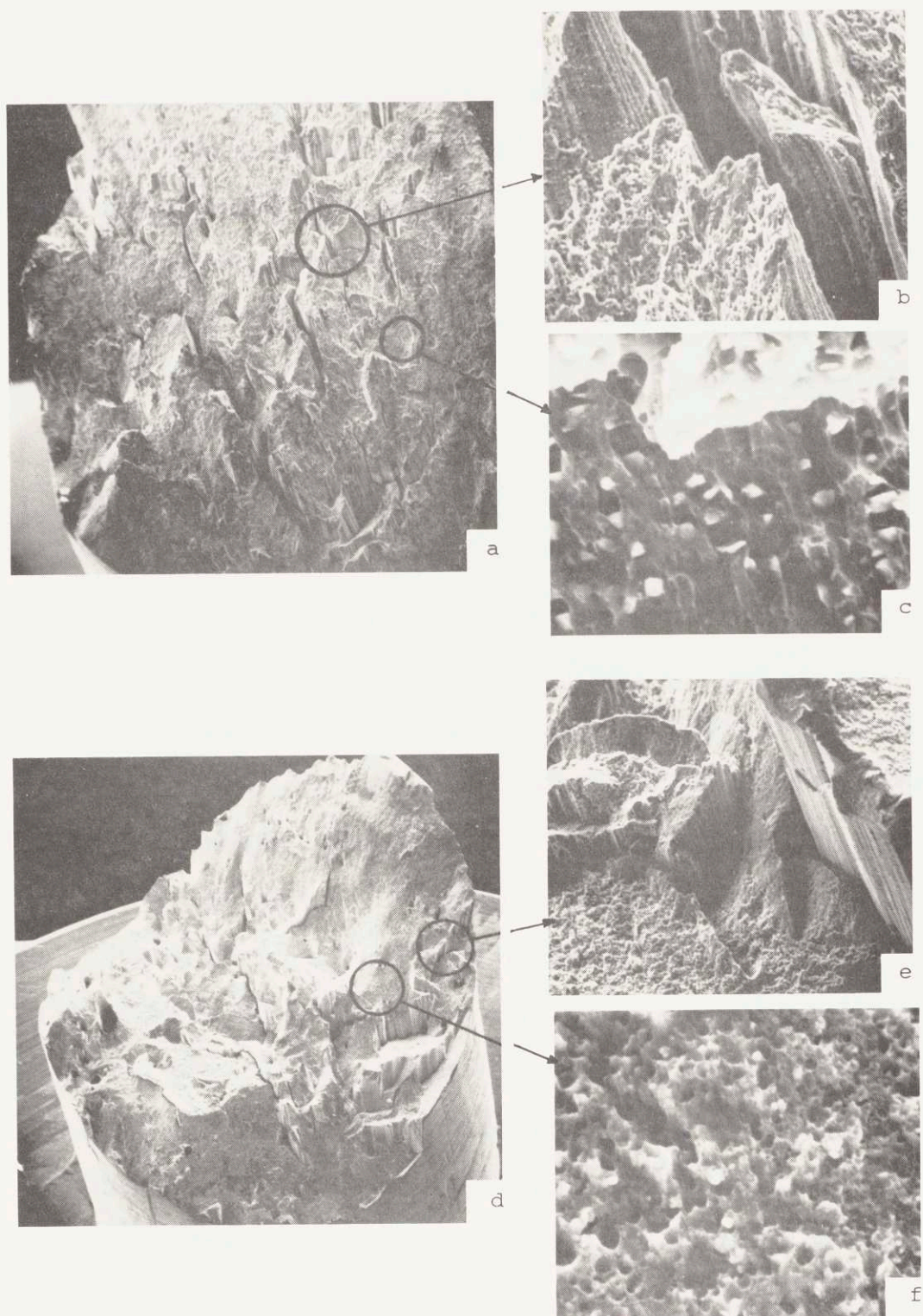
Figure 76: (a),(b),(c) SEM fractographs of extruded commercial
7075-T6 commercial powder, billet C (Table II), 27X,
260X, 2620X, respectively.
(d),(e),(f) SEM fractographs of extruded 7075-T6
splat cooled flakes, billet E (Table II), 22X, 120X,
2080X, respectively.

6. CONCLUSIONS

1. A new type of laboratory filtration apparatus was designed and constructed to study removal of impurities from aluminum melts. The efficiency of various filter media (sintered Al_2O_3, SiO_2, and carbon filters, granular bed filters, woven and non-woven carbon and fiberglass filters) in removing these impurities was evaluated.

2. Platelike $TiAl_3$ "synthetic inclusions", 60μ to 1000μ across by 10μ to 50μ thick, were successfully filtered from the two phase, $L+TiAl_3$, region of an Al-1% Ti alloy at various temperatures. Compositions of the filtered liquid metals, determined by chemical analyses, were those given by the liquidus from the phase diagram.

3. Ultimate tensile strengths and ductilities of commercial purity, 99.5% and 99.9%, aluminums increased when the melts were filtered through a combination filter made of 1.5" high 216μ diameter Al_2O_3 granular bed followed by a 40μ pore size sintered Al_2O_3 disc filter. For example, reduction in area of the 99.9% Al increased from 21.6% to 42.0% after filtration.

4. Granular aluminum was used for initial charge material to introduce large amounts of aluminum oxide to the melt. Effectiveness of sintered disc and granular bed filters in removing oxides was determined by chemical analysis. Al_2O_3 contents of the melts were reduced from ~1.61% to ~0.13%.

5. TiB_2 "synthetic inclusions" of 2-10μ size range were

successfully filtered from an Al-0.5% Ti-0.11% B alloy.

The following observations were made.

(i) The majority of the TiB_2 particles accumulated

above the filter bed and formed a "cake". Some

of the TiB_2 particles were entrapped at various

retention sites (i.e. surface, cavern, and

constriction sites) within the sintered filters.

(ii) Remelting and solidification of the filtered and

non-filtered metals in a centrifuge permitted

concentration of all particles, and thus was

found to be an excellent technique in determining

filtration effectiveness.

(iii) A nine layer fiberglass cloth filter (420 holes/in^2

and 0.00072 in^2/hole) and a 2" thick woven carbon

felt (density 8 lbs/yd^2) reduced the boron content

of the melt to 0.011% and 0.013%, respectively.

(iv) Al_2O_3 sintered disc filters (1" diameter, 1/4"

thick) of 87-100μ and 36-40μ pore sizes reduced

the boron content of the alloy to 0.022% and 0.01%,

respectively. (The boron content of the alloy was

further reduced to 0.006%, when a 1.5" thick

granular bed, Al_2O_3 granules smaller than 200μ,

was used above the 36-40μ pore size sintered Al_2O_3

disc filter.

(v) Pressures required for metal flow through the

various filters utilized was between 3 to 60 psi.)

The combination filter of 36-40μ pore size sintered Al_2O_3 disc coupled with a granular bed made of Al_2O_3 of less than 200μ diameter required the highest pressure for filtration.

6. The filtration apparatus was modified to permit separation of the interdendritic liquid from partially solidified Al-4% Si and Al-4% Si-0.25% Ti alloy samples. It was found that separation of the liquid phase from a solid dendritic network requires the use of a molten flux above the charge to dissolve the impermeable oxide layer.

7. Porous columnar, equiaxed, and grain refined dendritic networks of Al-4% Si alloy with actual volume fractions solid, $g_{SA} > 0.628$ were prepared. Actual volume fractions solid, and efficiencies of the process were determined by two independent techniques.

8. In both the grain refined (Al-4% Si-0.24% Ti) and equiaxed (Al-4% Si) samples, porous channels predominately formed between the primary dendrites (i.e., grains) of the samples. Liquid entrappment occurred in the finer passages between secondary dendrite arms.

9. In the columnar sample with volume fraction solid of 0.794, porous channels formed between both the primary and secondary dendrite arms. This is attributed to the coarser dendritic structure of this sample.

10. Specific permeabilities of the porous dendritic networks were measured with a triaxial cell permeameter. It was found that

(a) flow through the partially solid non-grain refined samples obeys D'Arcy's law and equations derived from the capillaric flow model for volume fraction liquid less than 0.345.

(b) flow through partially solidified grain refined samples is at a slight variance with the predicted capillaric flow model.

(c) measured values of specific permeability were $1x10^{-9}$ and $3.5x10^{-11}$ cm^2 in the Al-4% Si alloy with volume fractions solid of 0.655 and 0.94, respectively. Specific permeabilities in Al-4% Si-0.25% Ti alloy were $5.5x10^{-10}$ and $7.6x10^{-11}$ cm^2 for volume fractions solid of 0.628 and 0.837, respectively.

(d) for equivalent volume fractions solid, the measured specific permeabilities were consistently lower for the grain refined samples. This is due to the higher surface area of available channels for flow in the grain refined samples.

11. A new process for production of powders of metal alloys was developed. The process, called "filatomization", combines filtration of oxides and undesirable second phases with "atomization" of the melt.

12.   Pure aluminum and a 7075 aluminum alloy were filatomized through sintered Al_2O_3 and SiO_2 disc filters with average pore sizes in the range of 40 to 150µ.

13.   The temperature of the melt above the filter influences the size of the drops formed. In a test where the metal was at $700^{\circ}C$, a large percentage of metal drops were in the range of 500-1000 microns, whereas in a run at $742^{\circ}C$, the drops were predominantely in the range of 1500-2000 microns diameter.

14.   A critical pressure range of 3-10 psi was found for successful filatomization through the 40-50µ filters utilized. For pressures below 3 psi, the melt did not penetrate through the filter. For pressures above 10 psi, resulted in the formation of continuous and consolidated streams.

15.   Composition of the filter material influences the size range of metal drops forming below the filter. It was found that Al_2O_3 filters were more amenable to filatomization than the SiO_2 filters, since channeling is less prevelant in the latter.

16.   The microstructures of the filatomized spherical powders of the 7075 alloy were superior to the commercially produced powders. The filatomized powders were free of porosity, had a fine microstructure with measured DAS values between 4-8µ, had low oxide contents.

17. Filatomized spherical powders and falkes, commercial powders, splat cooled flakes, and a 7075 commercial bar stock were all extruded into billets. After a T6 temper treatment, the microstructure of the extruded spherical filatomized powders was superior to all the others.

18. The longitudinal room temperature tensile properties of the 7075-T6 filatomized spherical powder extrusion were: Y.S. - 80,000 psi, U.T.S. - 94,300 psi, R.A. - 42.4%, and elongation - 15.1%. The corresponding values for the commercial powder extrusion were: Y.S. - 75,000 psi, U.T.S. - 87,300 psi, R.A. - 11.5%, and elongation - 7.8%.

7. SUGGESTIONS FOR FURTHER WORK

1. Work on filtration of aluminum alloys should be extended. Identification of particles removed from commercial purity alloys is still a major problem. Forming operations such as rolling the alloys down to very thin sections could be used to verify removal of fine oxide particles. Finally, a pilot plant operation for filtration of aluminum alloys based on work reported in this study could be developed.

2. The technique developed here to permit removal of interdendritic liquid from partially solidified melts can be used for further work in permeability measurements or purification by partial solidification.

(a) Permeability measurements should be extended over a larger range of volume fractions solid. It is also possible to design an experiment where large channels, i.e. freckels, would form in a partially solidified sample. Removal of the interdendritic liquid would then permit direct observation of these channels. Experimental methods of measurement of specific surface area developed for other porous media should be used in dendritic networks. This type of measurement would permit determination of the applicability of Kozney-Carman equation to partially solidified dendritic networks.

(b) Purification of alloys by partial solidification
and subsequent separation of the segregated liquid
is presently used in several processes. The low
pressures necessary for this separation reported
here make this process attractive from a commercial
point of view. Current emphasis on recycling and
refining of alloy scrap should be sufficient
inducement for further study in this area.

3.   The "filatomization" process developed here combines
filtration with atomization. This is an attractive
process for atomization of both low and high temperature
alloys. In low temperature alloys such as aluminum
alloys filtration could have a significant effect on
properties of extrusions made from the powders.
Whereas, in high temperature alloys both filtration and
the fact that gas entrappment in the powders would be
minimized are important considerations. The apparatus
should be modified to study atomization of high
temperature alloys such as nickel-base and cobalt-base
alloys. Finally, larger filters should be tried with
the pressure necessary for "filatomization" being
provided by a constant metal head pressure.

8. APPENDICES

APPENDIX A

Settling Rates for TiAl$_3$ Particles

Stokes(<u>83</u>) assumed that when a spherical particle falling in a viscous fluid attains a terminal velocity, the drag on this particle is due entirely to viscous forces within the liquid, and expressed this drag force by the following:

$$F_D = 3\pi d\mu v_T \qquad (A1)$$

where F_D = drag force

d = diameter of sphere, cm

μ = viscosity of fluid, poise

v_T = terminal velocity attained, cm/sec.

Terminal velocity of the spherical particle is attained when the drag force plus the buoyant force equals weight of the particle.

$$\frac{\pi}{6} d^3 \rho_s g = \frac{\pi}{6} d^3 \rho_f g + 3\pi d\mu v_T \qquad (A2)$$

and thus:

$$v_T = \frac{d^2}{18\mu} (\rho_s - \rho_f)g \qquad (A3)$$

where ρ_s = density of spherical particle, gm/cm^3

ρ_f = density of fluid medium, gm/cm^3

g = acceleration due to gravity, 980 cm/sec^2.

The assumptions made in derivation of Stoke's law of settling velocities are (84):

(1) The particles must be spherical, smooth and rigid, and there must be no slip between it and the liquid

(2) The particle must move as it would in a fluid of infinite extent

(3) The terminal velocity must have been reached

(4) The fluid must be homogeneous compared with the size of the particle

(5) The settling speed must be low so that only viscous forces are brought into play.

TiAl$_3$ particles, which is the impurity phase considered in these experiments, are not spherical, and Stoke's law is modified to take into account derivation of these particles from sphericity. For non-spherical particles falling in a viscous fluid, Stoke's law becomes (84):

$$C_D \pi \frac{d_a^2}{4} \cdot \rho_f \cdot \frac{v_T^2}{2} = \frac{\pi}{6} d_v^3 (\rho_s - \rho_f) g \qquad (A4)$$

where d_a = diameter of sphere having the same projected area as the particle, and thus same resistance to motion as the particle

d_v = diameter of sphere having same volume as particle

C_D = drag coefficient, and equals $24/Re^{\#}$ where Stoke's law applies.

Equation (A4) reduces to

$$v_T = \frac{1}{18\mu} \cdot \frac{d_v^6}{d_a^4} (\rho_s - \rho_f) g \tag{A5}$$

For a TiAl$_3$ platelike particle 60μ across and 10μ thick: $d_v = 1.89 \times 10^{-3}$ cm; $d_a = 6 \times 10^{-3}$ cm; $\rho_s = 3.36$ gm/cm^3; $\rho_f = 2.4$ gm/cm^3, and $\mu = 0.03$ poise. The terminal velocity from equation (A5) is 3.9×10^{-3} cm/sec. For a TiAl$_3$ platelike particle 1000μ across and 40μ thick: $d_v = 3.92 \times 10^{-2}$ cm; $d_a = 0.1$ cm, and the terminal velocity from equation (A5) is 6.3×10^{-3} cm/sec.

For a distance of 4 cm, settling time for these TiAl$_3$ particles range from 1 minute to 17 minutes.

APPENDIX B

Conversion of Weight Fractions to Volume Fractions

Weight fraction liquid, f_L, is expressed in terms of volume fraction liquid, as follows:

$$f_L = \frac{\rho_L g_L}{\rho_S g_S + \rho_L g_L} \tag{B1}$$

where:

ρ_L, ρ_S = densities of liquid and solid, respectively

g_L, g_S = volume fractions of liquid and solid, respectively

Shrinkage, β, occurring during solidification due to density differences between the solid and liquid is defined as:

$$\beta = \frac{\rho_S - \rho_L}{\rho_S} \tag{B2}$$

or

$$\frac{\rho_L}{\rho_S} = (1 - \beta)$$

Substituting equation (B2) in (B1) and rearranging the terms we get:

$$f_L = \frac{g_1 (1 - \beta)}{1 - \beta g_1} \quad ; \quad g_L = \frac{f_L}{(1 - \beta + \beta f_L)} \tag{B3}$$

Generally, shrinkage in aluminum alloys is about 5%, $\beta = 0.05$. Substituting this value in equation (B3) results:

$$g_L = \frac{f_L}{(1 - 0.05 + 0.05g_L)} \qquad (B4)$$

Weight fractions liquid of interest are between $f_L = 0.5$ and $f_L = 0.95$. The volume fractions calculations from equation (B4) for these two values are 0.512 and 0.952, respectively. In this study it is assumed that weight and volume fractions of interest are equivalent, and thus interchangeable.

APPENDIX C

Calculation of Volume Fractions Solid
at the Separation Temperature, T*

A. **Calculation of $\bar{g}_s$ from Equilibrium Lever Rule**

Assuming weight and volume fractions solid to be equivalent as shown in Appendix B, the equilibrium volume fraction solid at a temperature T* is:

$$\bar{g}_s = \frac{C_L^* - C_o}{C_L^* - C_s^*} \tag{C1}$$

where:

C_L^*, C_s^* = equilibrium liquid and solid composition determined from phase diagram, in weight percentage.

Assumptions made in writing equation (C1) include: (1) equilibrium at the liquid-solid interface exists, (2) there is no significant undercooling before nucleation or from effect of radius of curvature, and (3) diffusion in the liquid and the solid is complete.

B. **Calculation of g_s from the Scheil Equation**

Assuming weight and volume fractions solid to be equivalent, as shown in Appendix B, volume fraction solid from the Scheil equation is:

$$g_s = 1 - \left(\frac{C_L^*}{C_O}\right)^{\frac{1}{k-1}} \tag{C2}$$

where:

C_L^* = equilibrium liquid composition from phase diagram, in weight percentage

C_O = initial alloy composition, in weight percentage

k = equilibrium partition ratio, C_s^*/C_L^*

Assumptions made in writing equation (C2) are those listed for the equilibrium lever rule, except that it is assumed that no diffusion takes place in the solid.

APPENDIX D

Calculation of Actual Volume Fractions Solid

A. Determination of g_{SW}

It is assumed here that density is not a function of composition (wt % Si) since density of Al-1% Si to 5% Si ranges from 2.696 to 2.685 gms/cm^3 only (85). Also, it is assumed that for the Al-4% Si alloy used here volume fractions are equivalent to weight fractions. Volume fractions solid remaining were determined from the weight of liquid metal removed by the following expression:

$$g_{SW} = \frac{w_O - w_L}{w_O} \qquad \text{(D1)}$$

where:

w_O = weight of solid plug at the start of experiment

w_L = weight of liquid removed

Values of g_{SW} determined in this manner are listed in Table XI

B. Determination of g_{SA}

In the following calculations, Scheil distribution of solute during solidification is assumed. Appendix C lists the various assumptions used in derivation of this equation. Solute distribution at a temperature T*, in the liquid-solid range is shown in Figure D2. Figure D1 shows the phase diagram used.

At temperature T^*, the average composition of the solid network is:

$$\bar{C}_s = \frac{\rho_s \int_o^{1-g_L} C_s^* dg_s + \rho_L g_L C_L^*}{\rho_s (1 - g_L) + \rho_L g_L} \qquad (D2)$$

where:

$\bar{C}_s$ = average solid composition

ρ_s, ρ_L = densities of solid and liquid, respectively

g_s, g_L = volume fraction solid and liquid (from Scheil equation), respectively.

For all Al-4% Si alloy used here, the difference between ρ_s and ρ_L is negligible($\underline{86}$), assuming $\rho_s = \rho_L$, equation (D2) reduces to:

$$\bar{C}_s = \int_o^{1-g_L} C_s^* dg_s + g_L C_L^* \qquad (D3)$$

If all the interdendritic liquid is removed during the separation (i.e. 100% efficiency), then the average solid composition of the remaining network is:

$$\bar{C}_s = \int_o^{1-g_L} C_s^* dg_s \qquad (D4)$$

However, all of the interdendritic liquid is not removed. The objective here is to find what fraction liquid did remain. Slices of the solid dendritic network were chemically analyzed. The compositions obtained from this analysis, $\bar{C}_s$, are average compositions of the solid network,

and can be represented as follows:

$$\bar{C}_S = \int_0^{1-g_L} C_S^* dg_S + g_L^* C_L^*$$ (D5)

where g_L^* is the fraction liquid not removed, shown in Figure D3.

At a particular temperature T^*, C_S^*, C_L^*, and g_s can be determined from the phase diagram and the Scheil equation, respectively. Thus:

$$g_L^* = \frac{1}{C_L^*} [\bar{C}_S - \int_0^{g_S} C_S^* dg_S]$$ (D6)

g_{SA}, the actual volume fraction solid remaining in the network was then calculated using the following expression:

$$g_{SA} = g_s + g_L^*$$ (D7)

Table XII lists calculated values of g_{SA}.

234
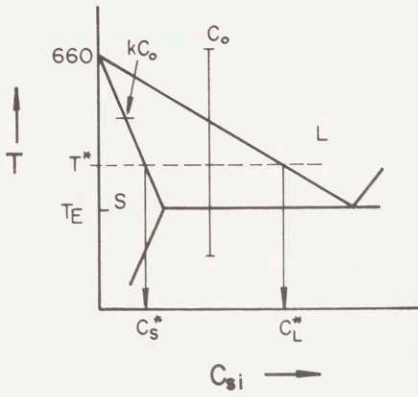
Figure D1: Hypothetical phase
diagram, indicating
temperature of separa-
tion, T*.
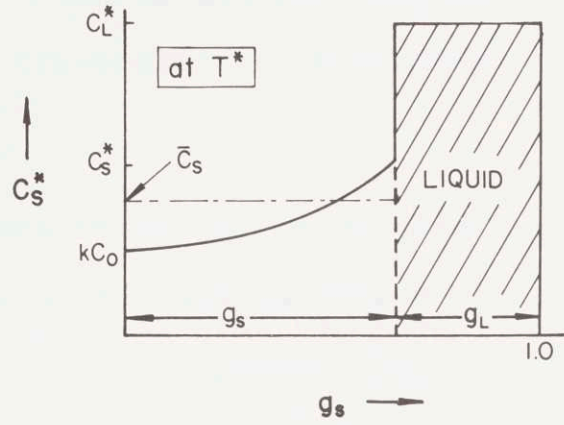
Figure D2: Solute distribution
schematic (Scheil equation),
showing average composition
of solid "network" of volume
fraction, g_S.
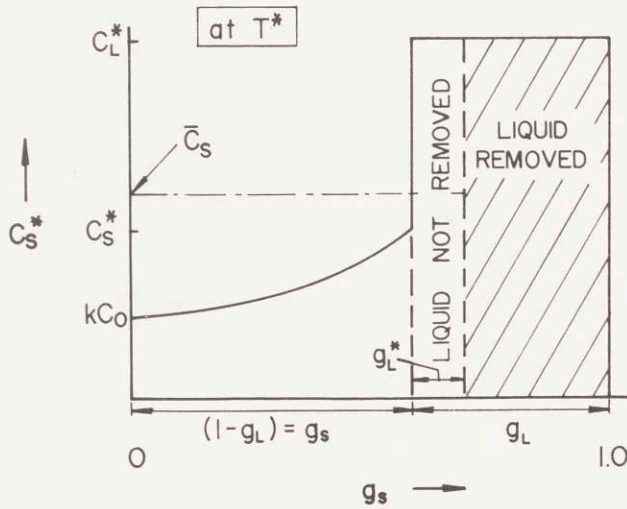
Figure D3: Solute distribution schematic (Scheil
equation), showing average composition
of solid "network" of volume fraction,
$g_S + g_L^*$, (g_{SA}).

APPENDIX E

AGEING KINETICS DATA OF FILATOMIZED POWDERS

Longitudinal and transverse hardness values for various ageing times and solutionizing treatments are tabulated below.

Solutionizing treatment: 2 hours at 485°C, water quench

time	average longitudinal hardness values, $\bar{H}_L$	average transverse hardness values, $\bar{H}_T$
0	31.2	3.6
10 min	32.0	5.8
30 min	34	13
1 hr	39	17.3
2 hrs	46	20.4
4 hrs	54	33.2
18 hrs	61	47.6
24 hrs	64.5	50.0

Solutionizing treatment: 4 hours at 485°C, water quench

time	average longitudinal hardness values, $\bar{H}_L$	average transverse hardness values, $\bar{H}_T$
0	15	off scale
10 min	17.5	off scale
30 min	21.6	1.0
1 hr	29.8	6.0
2 hrs	43.6	11.5
4 hrs	49.1	24.0
16.5 hrs	59.2	34.7
24 hrs	57	52.0

Tensile Test Results of T6-Extrusions of Powders and Flakes

sample		A_o $(10^2$ inch$^2)$	A_f $(10^2$ inch$^2)$	load at yield (lbs)	max load (psi)	yield stress (psi)	UTS (psi)	total elonga- tion (%)	reduc- tion of area (%)	average yield stress (psi)	average UTS (psi)	average total elonga- tion (%)	average reduc- tion of area (%)
A	1	1.99	1.12	1560	1779	78,394	89,407	15.6	43.7				
	2	2.00	1.13	1643	1924	82,160	96,200	14.9	43.5				
	3	1.98	1.18	1573	1926	79,446	97,294	14.8	40.0				
A										80,000	94,300	15.1	42.4
B	1	1.91	1.67	1534	1757	80,312	92,000	8.05	12.5				
	2	1.95	1.72	1521	1745	78,020	89,480	8.15	11.8				
	3	1.93	1.705	1460	1720	75,668	89,120	8.4	11.7				
B										78,000	90,200	8.2	12.0
C	1	2.01	1.75	1527	1783	75,950	88,700	8.4	12.7				
	2	2.01	1.8	1488	1727	74,050	85,900	7.2	10.3				
C										75,000	87,300	7.8	11.5
D	1	2.01	1.79	1650	1889	82,000	94,000	8.14	10.9				
	2	2.01	1.767	1369	1620	68,100	80,600	7.5	12.1				
	3	2.01	1.64	1097	1427	54,600	71,000	11.3	18.6				
D										68,200	81,900	9.0	13.9
E	1	2.00	1.7	1800	2000	90,000	100,000	8.3	15.0				
	2	2.00	1.6	1825	2080	91,500	104,000	8.9	20.0				
E										90,750	102,000	8.6	17.5
F	1	2.00	1.3	1760	1894	88,000	94,714	12.1	35.0				
	2	2.00	1.42	1688	1826	84,400	91,285	10.3	29.0				
F										86,200	93,000	11.2	32.0

9. BIBLIOGRAPHY

1.   German patent DRP 282,894, Appl. 1913, Gebr. Seyboth,
      Munchen.

2.   Austrian patent 128,341, Appl. 1930, Metallgesellschoft
      AG, Frankfurt/Main., H. Klaiber.

3.   A. Buckeley, "The Filtration of Light Metal Melts,"
      Die Giesserei, Vol. 51, 1961, no. 21, pp. 655-659.

4.   Reinacher, "Refining Metal Melts," Metal Industry,
      Sept. 1949, pp. 183-187, 211-213.

5.   "Aluminum Refining" - Review of Recent Developments by
      German Technicians, Metal Industry, Nov. 1947,
      pp. 447-449, 467-469.

6.   A. Buckley, Z. Metallkunde, vol. 48, 1957, pp. 241-245.

7.   K. Schneider, "The Smelting of Aluminum Scrap," 2nd
      Edition, Berlin 1957, p. 178.

8.   U. S. patent 3,006,473, Appl. Nov. 1958, Erwin Gaber,
      ALCOA, Pittsburgh, Pa.

9.   A. G. Spasski, Izv. Vuz, Tsvet. Metall., 1959, no. 3,
      pp. 118-122.

10.   V. S. Kalabushkin, M. V. Pikunov, "Filtering of
      Metals," Liteinoe Proizv., vol. 6, 1960, pp. 30-31.

11.   A. G. Spasski, Liteinoe Proizvodstvo, 1961, no. 12,
      pp. 25-28.

12.   U. S. patent 3,039,864, filed Nov. 1958, Paul D. Hess,
      K. Brondyke, ALCOA, Pittsburgh, Pa.

13.   K. Brondyke, P. D. Hess, Trans. AIME, vol. 230, 1964,
      p. 1542.

14.   K. Brondyke, P. D. Hess, Trans. AIME, vol. 230, 1964,
      p. 1553.

15.   R. B. Miclot, "Filtration of Al Alloys to Reduce Oxide
      Content," Technical Report 67-1507, Rock Island
      Arsenal, June 1967.

16. L. A. Alekseev, I. B. Kumanin, Izv. Vysshikh Uchebnikh
     Zavedenii, Tsvetn. Met., vol. 11, 1968, no. 1, pp.
     155-159. English translation of title: "Change in
     the Structure and Characteristics of an AK6 Alloy
     After Filtering Through Lumpy Filters."

17. British patent 1,148,344, Foseco International Limited,
     George Snow, 1969.

18. British patent 1,152,505, Charles Arthur Sauer,
     Applied June, 1967.

19. H. E. Miller, "Relationship between Inclusion Content
     of Castings and Final Product Quality," Kaiser Aluminum
     Co. Report, 1970.

20. Singleton, Robinson, "Refining of Al-Si Alloys,"
     J. Inst. Met., vol. 99, 1971, p. 155.

21. D. R. Geiger, "Atomization and Refining of Metal Alloys
     Utilizing Partially Solid, Partially Liquid Alloy,"
     M.S. Thesis, Department of Metallurgy and Materials
     Science, M.I.T., June 1972.

22. M. V. Brant, D. C. Bone, E. F. Emley, "Fumeless In Line
     Degassing and Cleaning of Liquid Al," TSM paper No.
     A70-51, Metallurgical Society of AIME.

23. D. B. Purchas, Industrial Filtration of Liquids,
     C. R. C. Press, Cleveland, 1967, p. 14.

24. J. H. Pownall, "Cyclones in the Chemical and Process
     Industries," Chemistry and Industry, Nov. 25, 1961,
     pp. 1888-1896.

25. M. G. Larian, Chemical Engineering Operations,
     Prentice-Hall Inc., Englewood Cliffs, N.J., 1958, p. 585.

26. G. D. Dickey, Filtration, Reinhold Publishing Corp.,
     New York, 1961, p. 27.

27. P. H. Hermans, H. L. Bredee, J. Soc. Chem. Ind.,
     vol. 55, 1936.

28. Graton, Frazer, J. Geol., vol. 43, 1935, p. 785.

29. R. Meldau, J. Stach, J. Inst. Fuel, vol. 7, 1934, p. 336.

30. Hugill, Westmann, J. Amer. Ceramic Soc., vol. 30, 1930,
     p. 767.

31. J. M. Coulson, Trans. Inst. Chem. Engrs. (London), vol. 27, 1949, p. 237.

32. K. Srinagesh, M. R. Seshadri, A. Remachandran, "On Packing Non-Spherical Homogeneous Grains," The British Boundryman, September 1963, p. 411.

33. A. E. Scheidegger, The Physics of Flow Through Porous Media, University of Toronto Press, 1957, pp. 12, 129.

34. T. J. Marshall, "A Relation Between Permeability and Size Distribution of Pores," J. Soil Sci., vol. 9, 1958, no. 1.

35. A. E. Scheidegger, The Physics of Flow Through Porous Media, University of Toronto Press, 1957, p. 115.

36. H. P. G. D'Arcy, "Les fontaines publiques de la ville de Dijon," Victor Dalmont, Paris, 1856.

37. J. Kozeny, Ber. Wien. Akad., vol. 136, 1927, p. 271; Wasserkraft und Wasserwirtschaft, vol. 22, 1927, pp. 67, 86.

38. P. C. Carman, "Fundamental Principles of Industrial Filtration," Trans. Inst. Chem. Engrs. (London), vol. 15, 1937, p. 168.

39. A. E. Scheidegger, The Physics of Flow Through Porous Media, University of Toronto Press, 1957, pp. 114, 115.

40. T. S. Piwonka, M. C. Flemings, TAIME, vol. 230, 1964, p. 1542.

41. H. Pielet, "The Interaction of Dendrites and Flow during Solidification," Ph.D. Thesis, Department of Metallurgy and Materials Science, M.I.T., Cambridge, Mass., 1971.

42. C. A. Calow, C. R. Tottle, "The Measurement and Form of Porosity in the Loose Sintering of Copper Compacts," Powder Metallurgy, vol. 8, 1965, no. 15, pp. 1-19.

43. M. G. Larian, Chemical Engineering Operations, Prentice-Hall Inc., Englewood Cliffs, N.J., 1958, p. 585.

44. D. R. Sperry, Chem. Met. Eng., vol. 15, 1916, p. 198; vol. 17, 1917, p. 161.

45. W. D. Jones, Fundamental Principles of Powder
     Metallurgy, Edward Arnold (London), 1960.

46. J. S. Hirschhorn, Introduction to Powder Metallurgy,
     American Powder Metallurgy Institute, N.Y., 1969.

47. J. P. Lyle, "Properties of Powders and Powder Metallurgy
     Products," Aluminum, vol. I, ASM, 1967.

48. U. S. patent nos. 2,527,009; 2,868,587; and 3,389,733.

49. U. S. patent 3,253,783.

50. U. S. patent 3,428,718.

51. C. R. Adler, W. R. Marshall, Chem. Engr. Progr., vol.
     47, 1951, pp. 515, 601.

52. S. J. Friedman, F. A. Gluckert, W. R. Marshall, Chem.
     Engr. Progr., vol. 48, 1952, p. 181.

53. H. Wilson, G. A. Page, V. W. Cartwright, U. S. Bur.
     Mines Rept. Invest. 3248, 1934.

54. U. S. patent 3,241,948.

55. U. S. patent 3,099,041.

56. U. S. patent 2,544,678.

57. N. J. Grant, "Some Special Powder Production
     Techniques."

58. M. C. Flemings, G. E. Nereo, "Macrosegregation:
     Part I," TAIME, vol. 239, 1967, pp. 1449-1461.

59. R. Mehrabian, M. Keane, M. C. Flemings, "Experiments
     on Macrosegregation and Freckle Formation," TAIME,
     vol. 1, 1970, pp. 3238-3241.

60. J. Bailey, J. Tundermann, "The Effect of Temperature
     on the Dihedral Angle in Some Aluminum Alloys," TAIME,
     vol. 236, 1966, p. 1031.

61. L. A. Willey, "Phase Diagrams," Aluminum, vol. I, ASM,
     1967.

62. F. R. Mollard, J. E. Dore, W. S. Peterson, "High
     Temperature Centrifuge for Studies of Melt Cleanliness,"
     Olin Metals Research Laboratories, New Haven, Conn.

63.   J. H. Durand, "Properties of Splat-Cooled 7075 Aluminum
       Alloys," M.S. Thesis, Department of Metallurgy, M.I.T.,
       Cambridge, Mass., June 1972.

64.   B. I. Edelson, W. M. Baldwin, TAIME, vol. 55, 1962,
       p. 230.

65.   J. A. Marcantonio, L. F. Mondolfo, "Grain Refinement in
       Aluminum Alloyed with Titanium and Boron," TAIME,
       vol. 2, February 1971, pp. 465-471.

66.   J. Moriceau, "Mecanisme de germination heterogene dans
       la coulee continue de l'aluminum," Note Technique No.
       70/7, Pechiney, Centre de Recherches de Voreppe.

67.   I. Maxwell, A. Hellawell, "The Constitution of the
       System Al-Ti-B with Reference to Aluminum Base Alloys,"
       TAIME, vol. 3, June 1972, pp. 1487-1493.

68.   A. Hellawell, Oxford University, private communications.

69.   J. P. Herzig, D. M. Leilerc, P. Le Goff, "Flow of
       Suspensions through Porous Media - Application to Deep
       Filtration," Flow Through Porous Media, American
       Chemical Society Publications, Washington, D. C., 1970.

70.   A. R. Singer, S. A. Cottrell, "Properties of the
       Aluminum-Silicon Alloys at Temperatures in the Region
       of the Solidus," J. Inst. Met., vol. 73, 1947, p. 33.

71.   H. D. Brody, M. C. Flemings, "Solute Redistribution in
       Dendritic Solidification," TAIME, vol. 236, 1966,
       p. 615.

72.   E. Rothwell, J. Inst. Met., vol. 90, 1961/1962,
       pp. 389-394.

73.   E. Gebhardt, M. Becker, J. Dorner, "Properties of
       Metallic Melts, Viscosity of Molten Aluminum and Its
       Alloys," Z. Metallk, vol. 44, 1953, pp. 510-514.

74.   R. Mehrabian, M. Keane, M. C. Flemings, "Experiments
       on Macrosegregation and Freckel Formation," TAIME,
       vol. 1, 1970, pp. 3238-3241.

75.   E. A. Hauser, H. E. Edgerton, B. M. Holt, J. T. Cox,
       Jr., J. Phys. Chem., vol. 40, 1936, p. 973.

76.   W. D. Harkins, F. E. Brown, J. Am. Chem. Soc., vol.
       41, 1919, p. 499.

77.   Professor R. Coble, M.I.T., private communications.

78.   F. W. Keith, A. N. Hixson, Ind. Eng. Chem., vol. 47, 1955, p. 258.

79.   H. Matyja, B. C. Giessen, N. J. Grant, J. Inst. Metals, vol. 96, 1968, p. 30.

80.   Professor H. Edgerton, M.I.T., private communications.

81.   J. P. Lyle, W. S. Cebulak, "Fabrication of High Strength Aluminum Products from Powder," presented at the 18-th Sagamore Army Materials Research Conference: Powder Metallurgy for High Performance Applications, September 1971.

82.   T. F. Bower, S. N. Singh, M. C. Flemings, "Development of High Strength Wrought Aluminum-Bare Alloys," TAIME, vol. 1, 1970, pp. 191-197.

83.   C. Orr, Particulate Technology, The MacMillan Co., New York, 1966, p. 297.

84.   Terence Allen, Particle Size Measurement, Chapman and Hall (London), 1968.

85.   W. A. Dean, "Effects of Alloying Elements and Impurities on Properties", Aluminum, vol. 1, ASM, 1967, p. 167.

86.   C. J. Smithells, Metals Reference Book, vol. II, Butterworths, Washington, 1962, p. 689.

BIOGRAPHICAL NOTE

The author was born in Cairo, Egypt, of Armenian
parentage on October 28, 1945. He lived in Lebanon, Egypt,
Libya and Italy during his childhood because of his father's
business affiliations. In 1960, his family settled in Bryn
Mawr, Pennsylvania, where he attended Haverford High School
and was graduated in 1963. He was awarded a Bachelor of
Science in Metallurgical Engineering from Drexel University
after completing a five-year work-study program. He entered
M.I.T.'s Graduate School of Metallurgy and Materials Science
as a teaching assistant under the supervision of Professor
Merton C. Flemings. He minored in Business Administration
at M.I.T.'s Sloan School of Business.

The author married the former Miss Donna D'Alessio on
July 28, 1968.